

University of Alberta

A Quantitative Analysis of Four Dimensional Computed Tomography

by

Lori Kathleen Noice

A thesis submitted to the Faculty of Graduate Studies and Research
in partial fulfillment of the requirements for the degree of

Master of Science
in
Medical Physics

Department of Physics

© Lori Kathleen Noice
Spring 2010
Edmonton, Alberta

Permission is hereby granted to the University of Alberta Libraries to reproduce single copies of this thesis and to lend or sell such copies for private, scholarly or scientific research purposes only. Where the thesis is converted to, or otherwise made available in digital form, the University of Alberta will advise potential users of the thesis of these terms.

The author reserves all other publication and other rights in association with the copyright in the thesis and, except as herein before provided, neither the thesis nor any substantial portion thereof may be printed or otherwise reproduced in any material form whatsoever without the author's prior written permission.

Examining Committee

Dr. Don Robinson, Department of Physics

Dr. Ron Sloboda, Department of Physics

Dr. Sharon Morsink, Department of Physics

Dr. Terence Riauka, Department of Oncology

Abstract

This project assesses the four dimensional computed tomography (4DCT) capabilities of the Philips Brilliance Big Bore CT scanner (Philips Medical Systems, Cleveland, OH). A mechanical phantom imparts clinically relevant motions to acrylic spheres of various diameters. The size, shape, and position of these spheres, as measured with 4DCT, are compared to their true size, shape, and position. An evaluation of image quality is also performed. Maximum discrepancies between physical and imaged volumes, for all sphere sizes and motion ranges, did not exceed 2.6 mm (mean = 1.2 mm, standard deviation = 0.4 mm). For approximately tissue equivalent density objects, mean CT# in 4DCT images differed from those in standard clinical thoracic images by only a few Hounsfield units. Measured geometric precision along with the accuracy of mean CT#s observed in 4DCT phase images indicate that 4DCT is an appropriate imaging technique for treatment planning.

Table of Contents

Introduction.....	1
Chapter 1: The Role of 4DCT in Radiation Therapy	2
Lungs and Lung Functioning.....	2
Lung Cancer	6
Lung Tumor Motion.....	6
Radiation Therapy in Lung Cancer Treatment.....	8
Margins.....	11
Sources of Error.....	12
Imaging Lung Tumors.....	15
Motion Management.....	16
ICRU62	17
ITV.....	17
4DCT.....	18
4DCT ITV.....	19
Mean Position.....	21
Gating.....	21
SBRT and IGRT.....	22
IMRT.....	23
Chapter 2: 4DCT Imaging... ..	24
CT Image Formation	24
The Sinogram.....	27
Acquisition Geometry.....	28
Artifacts in CT.....	33
Motion Artifacts.....	34

4DCT Techniques.....	39
Helical vs. Axial.....	41
Prospective vs. Retrospective.....	41
Phase-based vs Amplitude-based Sorting.....	41
4DCT Image Formation.....	43
Chapter 3: Quantitative Measurements of Geometric Accuracy.....	49
4DCT Technology.....	49
Bellows.....	49
RPM.....	59
Methods of Quantitative Measurement.....	56
The Motion Phantom.....	56
Imaging Protocols.....	58
Metrics of Geometric Evaluation.....	59
% Volume Difference.....	60
Mean Eccentricity.....	60
Center to Center Distance.....	64
Maximum Distance to Agreement.....	65
The Coincidence Index.....	68
Sources of Error.....	69
Resolution Error.....	69
Thresholding Error.....	71
Phantom Error.....	72
Results of Quantitative Measurement.....	75
Phantom Error.....	75
Catalogue of Artifacts.....	76
3DCT Reference Scans.....	87

4DCT Residual Motion Artifacts.....	96
1 cm Sphere.....	96
3 cm Sphere.....	105
5 cm Sphere.....	114
Summary of Residual Motion Artifacts.....	123
Functional Dependencies of the Metrics.....	124
% Volume Difference.....	125
Mean Eccentricity.....	130
Center to Center Distance.....	136
Maximum Distance to Agreement.....	143
The Coincidence Index.....	147
Summary of Functional Dependencies.....	149
Consolidation of Quantitative Data.....	150
Discussion of 4DCT Geometric Accuracy.....	153
Threshold Sensitivity.....	153
Imaged Volume.....	155
Imaged Shape.....	155
Tracking Ability.....	156
Localization.....	157
Coincidence Index.....	157
Summary and Conclusion of Quantitative Measurements.....	158
Chapter 4: Analysis of Image Quality.....	158
Methods of Image Quality Analysis.....	158
Imaging Protocols.....	159
The Phantoms.....	160

CT# Evaluation.....	161
Noise Measurement.....	162
Low Contrast Resolution.....	162
High Contrast Resolution.....	164
Modulation Transfer Function.....	164
Results of Image Quality Analysis.....	165
CT#.....	165
Noise.....	170
Low Contrast Resolution.....	171
High Contrast Resolution.....	172
MTF.....	176
Discussion of 4DCT Image Quality.....	177
Summary and Conclusion of 4DCT Image Quality.....	179
Chapter 5: Summary and Conclusion.....	180
Summary of Results.....	180
Clinical Implications.....	181
Future Work.....	183
Bibliography.....	184
Appendix A: Additional Comments on 4DCT in RT.....	201
What gate?.....	201
IMRT.....	202
External Markers.....	202
Breath Coaching.....	202
Physiological Variation.....	203
Threshold and Segmentation.....	204
Appendix B: X-ray Formation and Interactions with Matter.....	204

X-rays.....	204
Characteristic Radiation.....	205
Bremsstrahlung.....	207
Photon Interactions with matter.....	212
Rayleigh Scatter.....	212
Compton Scatter.....	217
Photoelectric Effect.....	221
Linear Attenuation Coefficient.....	223
CT#.....	228

List of Tables

Table 1.1: A sample of published margin recipes.....	12
Table 3.1: Philips protocols for 3DCT and 4DCT thoracic acquisitions.....	59
Table 3.2 : Distance between the step and shoot and the calculated phase positions.....	75
Table 3.3: The mean distance between the step-and-shoot data and the dynamic path of the phantom taken from the orthogonal radiographs	76
Table 3.4: The error introduced by the phantom for each phase of motion for each cam size.....	76
Table 3.5: the % <i>volume difference</i> and <i>mean eccentricity</i> metrics calculated for the static spheres.....	87
Table 3.6: The functional dependencies of the five metrics of geometric evaluation....	150
Table 3.7: Results summary table for the metrics of quantitative analysis.....	153
Table 3.8: Average thresholding error in % <i>volume difference</i> measurements.....	154
Table 3.9: Average thresholding error in the mean eccentricity measurements.....	154
Table 3.10: Mean Eccentricities for each sphere size imaged with static 3DCT and dynamic 4DCT.....	156
Table 3.11: The Largest measured <i>maximum distance to agreement</i> for each sphere size and amplitude of motion.....	157
Table 4.1: Clinical protocols.....	159
Table 4.2: Optimized protocols.....	160

Table 4.3: Mean and standard deviation of pixel values in a large uniform density region imaged while stationary with clinical 4DCT.....	165
Table 4.4: Mean and standard deviation of pixel values in a large uniform density region imaged while stationary with clinical 3DCT.....	166
Table 4.6: Mean CT#s for 7 materials measured with 3DCT and 4DCT.....	166
Table 4.7: Summary of measured CT# distributions for clinical & optimized 3DCT and 4DCT acquisitions of a uniform low density plastic cylinder.....	169
Table 4.8: Noise values collected from ten clinical 3DCT scans.....	170
Table 4.9: Noise values collected from ten clinical 4DCT scans.....	170
Table 4.10: Noise values collected from ten optimized 4DCT scans.....	171

List of Figures

Figure 1.1: The basic respiratory system	3
Figure 1.2: The breathing control center of the brain	3
Figure 1.3: The muscles involved in <i>forced</i> breathing	5
Figure 1.4: Muscles involved in compromised breathing	5
Figure 1.5: Lymph nodes of the lung	8
Figure 1.6: Optimal scan range for the staging and planning of lung cancer	9
Figure 1.7: Two 5cm spheres imaged with non-temporally correlated CT	14
Figure 1.8: 3DCT acquisitions of a moving sphere compared to a 4DCT acquisition of the same sphere	19
Figure 1.9: RT margins for targets affected by respiratory motion	20
Figure 2.1: The geometry of CT image acquisition	25
Figure 2.2: A backprojection summation image	26
Figure 2.3: Geometry of a sinogram	28
Figure 2.4: A fan beam and an arced detector bank	29
Figure 2.5: Sinogram data for a fan beam	30
Figure 2.6: Path of a helical CT scan	31
Figure 2.7: Cone beam geometry	32

Figure 2.8: The nutating imaging planes of cone beam geometry	32
Figure 2.9: Geometry of an axial scan using the full detector bank	33
Figure 2.10: Backprojections through a stationary point	35
Figure 2.11: Backprojections through a moving point	36
Figure 2.12: The sinogram, summed backprojection, and filtered summed backprojection for a sphere oscillating about the origin in the imaging plane	38
Figure 2.13: The sinogram, summed backprojection, and filtered summed backprojection of a sphere oscillating about the origin perpendicular to the imaging plane	38
Figure 2.14 : The sinogram, summed backprojection, and filtered summed backprojection of a sphere oscillating both perpendicular to the imaging plane and in it	39
Figure 2.15: Illustration of amplitude- and phase-based sorting: reconstruction of the peak exhale phase	42
Figure 2.16: Shortcomings of amplitude- and phase-based sorting: reconstruction of the end exhale phase	43
Figure 2.17: Illustration of the data sufficiency condition for helical retrospective 4DCT	44
Figure 2.18: The phase function definition of phases. 4 phases	45
Figure 2.19: The breath trace corresponding to Figure 2.17 and a portion of the sinogram from a slice located in 'segment1'	46
Figure 2.20: Image ghosting due to the incorrect classification of phases in adjacent Breaths.....	48
Figure 3.1: Philips Bellow system.....	49
Figure 3.2: Philips screen shot of a respiratory signal	50

Figure 3.3: RPM Camera	50
Figure 3.4: The RPM system	51
Figure 3.5: Recommended marker block position	52
Figure 3.6: The RPM system detecting SI motion.....	53
Figure 3.7: RPM—baseline drift	54
Figure 3.8: The RPM respiratory trace received by Philips: synch pulses or waveform	54
Figure 3.9: RPM Workstation: breath regularity	55
Figure 3.10: Phantom Schematic	56
Figure 3.11: The phantom	57
Figure 3.12: Bellows experiment setup	57
Figure 3.13: RPM experiment setup	58
Figure 3.14: Slices of the 3 cm sphere moving in the SI direction	61
Figure 3.15: Imaging planes intersecting a sphere	62
Figure 3.16: Eccentricity vs slice number for 5 cm sphere undergoing different types of motion	63
Figure 3.17: Imaged and ideal paths	65
Figure 3.18: MATLAB Definitions of Extrema	66
Figure 3.19: Diagram of maximum distance to agreement calculation	68

Figure 3.20: The coincidence index vs fractional overlap	69
Figure 3.21: The step-and-shoot data for the 1 cm cams and the ideal path of the phantom	73
Figure 3.22: Orthogonal radiographs of the phantom's motion in the in the SI-AP-LR direction	74
Figure 3.23: Step-and-shoot data plotted with points taken from the orthogonal radiographs of the moving phantom: 1 cm cams	74
Figure 3.24: 1 cm sphere undergoing motion in the SI direction (Bellows 80% phase, 1.5 cams)	77
Figure 3.25: 3 cm sphere undergoing motion in the SI direction (RPM 30% phase, 1.5 cams)	78
Figure 3.26: 5 cm sphere undergoing motion in the SI direction (RPM 30% phase, 1.5 cams)	79
Figure 3.27: 1 cm sphere undergoing motion in the AP-LR direction (Bellows 20% phase, 1.5 cams)	80
Figure 3.28: 3 cm sphere undergoing motion in the AP-LR direction (Bellows 70% phase, 1.5 cams)	81
Figure 3.29: 5 cm sphere undergoing motion in the AP-LR direction (Bellows 30% phase, 1.5 cams)	82
Figure 3.30: 1 cm sphere undergoing motion in the SI-AP-LR direction (Bellows 20% phase, 1.5 cams)	83
Figure 3.31: 3 cm sphere undergoing motion in the SI-AP-LR direction (Bellows 80% phase, 1.5 cams)	84
Figure 3.32: 5 cm sphere undergoing motion in the SI-AP-LR direction (RPM 20% phase, 1.5 cams)	85

Figure 3.33: Choices of the Philips reconstruction algorithm (3 cm sphere, AP-LR motion, Bellows 20% phase, 1.5 cams)	86
Figure 3.34: Three slices of the stationary 1 cm sphere outlined at 20, 40, 60, and 80% local contrast	88
Figure 3.35: Three slices of the stationary 3 cm sphere outlined at 20, 40, 60, and 80% local contrast	88
Figure 3.36: Three slices of the stationary 5 cm sphere outlined at 20, 40, 60, and 80% local contrast	88
Figure 3.37: Area vs. % local contrast attribute maps for the 1, 3, and 5 cm spheres imaged while stationary with 3DCT	89
Figure 3.38: Volume vs. % local contrast attribute maps for the stationary 1, 3, and 5 cm spheres imaged with 3DCT	91
Figure 3.39: Eccentricity vs. % local contrast attribute maps for the static 1, 3, and 5 cm spheres imaged with 3DCT	93
Figure 3.40: Centroid vs. % local contrast attribute maps for the static 1, 3, and 5 cm spheres imaged with 3DCT	95
Figure 3.41: Three slices of the 1 cm sphere undergoing motion in the SI, AP-LR, and SI-AP-LR directions	97
Figure 3.42: Area vs. % local contrast attribute maps for the 1cm spheres imaged with 4DCT undergoing motion in the SI, AP-LR, SI-AP-LR directions	98
Figure 3.43: Volume vs. % local contrast attribute maps for the 1cm spheres imaged with 4DCT undergoing motion in the SI, AP-LR, SI-AP-LR directions	100
Figure 3.44: Eccentricity vs. % local contrast attribute maps for the 1cm spheres imaged with 4DCT undergoing motion in the SI, AP-LR, SI-AP-LR directions	102
Figure 3.45: Centroid vs. % local contrast attribute maps for the 1cm spheres imaged with 4DCT undergoing motion in the SI, AP-LR, SI-AP-LR directions	104

Figure 3.46: Three slices of the 3 cm sphere undergoing motion in the SI, AP-LR, and SI-AP-LR directions	106
Figure 3.47: Area vs. % local contrast attribute maps for the 3 cm spheres imaged with 4DCT undergoing motion in the SI, AP-LR, SI-AP-LR directions	107
Figure 3.48: Volume vs. % local contrast attribute maps for the 3 cm spheres imaged with 4DCT undergoing motion in the SI, AP-LR, SI-AP-LR directions	109
Figure 3.49: Eccentricity vs. % local contrast attribute maps for the 3 cm spheres imaged with 4DCT undergoing motion in the SI, AP-LR, SI-AP-LR directions	111
Figure 3.50: Centroid vs. % local contrast attribute maps for the 3 cm spheres imaged with 4DCT undergoing motion in the SI, AP-LR, and SI-AP-LR directions	113
Figure 3.51: Three slices of the 5 cm sphere undergoing motion in the SI, AP-LR, and SI-AP-LR directions	115
Figure 3.52: Area vs. % local contrast attribute maps for the 5 cm spheres imaged with 4DCT undergoing motion in the SI, AP-LR, and SI-AP-LR directions	116
Figure 3.53: Volume vs. % local contrast attribute maps for the 5 cm spheres imaged with 4DCT undergoing motion in the SI, AP-LR, SI-AP-LR directions	118
Figure 3.54: Eccentricity vs. % local contrast attribute maps for the 5 cm spheres imaged with 4DCT undergoing motion in the SI, AP-LR, SI-AP-LR directions	120
Figure 3.55: Centroid vs. % local contrast attribute maps for the 5 cm spheres imaged with 4DCT undergoing motion in the SI, AP-LR, SI-AP-LR directions	122
Figure 3.56: Three slices from each sphere size at the 50% phase	124
Figure 3.57: Sphere moving with or against the motion of the scanning plane	125
Figure 3.58: % volume difference vs. phase for different types of motion	126
Figure 3.59: % volume difference vs. phase for different sphere sizes	129

Figure 3.60: Mean eccentricity vs. phase for different types of motion	131
Figure 3.61: Mean eccentricity vs. phase for different sizes of spheres.....	133
Figure 3.62: Mean eccentricity vs. phase for different amplitudes of motion	135
Figure 3.63: Center to center distance vs. phase for different types of motion	137
Figure 3.64: Center to center distance vs. phase for different amplitudes of motion	139
Figure 3.65: Center to center distance vs. phase for different sizes of spheres	142
Figure 3.66: Maximum distance to agreement vs. phase for different amplitudes of motion	144
Figure 3.67: Maximum distance to agreement vs. phase for different sphere sizes... ..	145
Figure 3.68: Maximum distance to agreement vs. phase for different types of motion	146
Figure 3.69: Coincidence index vs. phase for different sphere sizes	147
Figure 3.70: Consolidation of the 5 metrics.....	151
Figure 4.1: Image Quality Phantoms	160
Figure 4.2: Catphan Uniform Solid Water Module (CTP 486)	161
Figure 4.3: Catphan CT# Module (CTP 404)	162
Figure 4.4: The placing of 5 ROIs on the Catphan Uniform Solid Water Module	163
Figure 4.5: Catphan Low Contrast Module (CTP 515)	163
Figure 4.6: Catphan High Contrast Module (CTP 528)	164

Figure 4.7: Cumulative histograms of CT#s in a uniform low density plastic cylinder imaged while stationary with clinical 3DCT	167
Figure 4.8: Cumulative histograms of CT#s in a uniform low density plastic cylinder imaged while stationary with clinical 3DCT and 4DCT, and while in motion with clinical 4DCT	168
Figure 4.9: Cumulative histograms of CT#s in a uniform low density plastic cylinder imaged while stationary with optimized 3DCT and 4DCT, and while in motion with clinical 4DCT	169
Figure 4.10: Low Contrast images acquired with clinical 3DCT, clinical 4DCT, and optimized 4DCT	172
Figure 4.11: High Contrast images acquired with clinical 3DCT, clinical 4DCT, and optimized 4DCT	173
Figure 4.12: Line profiles through a small acrylic high contrast phantom imaged with 3DCT while stationary Figure 4.13: Line profiles through a small acrylic high contrast phantom imaged with 4DCT while moving in the SI-AP-LR direction	174
Figure 4.13: Line profiles through a small acrylic high contrast phantom imaged with 4DCT while moving in the SI-AP-LR direction	175
Figure 4.14: Three slices of a small acrylic high contrast phantom moving in the SI-AP-LR direction, imaged with 4DCT, 80% phase	175
Figure 4.15: Line profiles through the smallest hole pattern of acrylic high contrast phantom undergoing motion in the SI-AP-LR direction, imaged with 4DCT: 3 slices from the same 4DCT phase image	176
Figure 4.16: The MTFs of the clinical 3DCT and 4DCT protocols, and the optimized 3DCT and 4DCT protocols	177
Figure B.1: A simple x-ray tube	204
Figure B.2: The radiation spectrum of an x-ray tube with a tungsten anode	205
Figure B.3: Formation of a characteristic x-ray	206

Figure B.4: Energy level diagram of a tungsten atom showing the emission of characteristic radiation	207
Figure B.5: Vector diagram of a moving charge in a Coulombic field	208
Figure B.6: Impinging electrons interacting inelastically with an atom	209
Figure B.7: Cross section view of the radiation emitted from an accelerating charged particle	210
Figure B.8: Interactions of an impinging electron	211
Figure B.9: Vector diagram of the classical scatter of a photon off a free electron	213
Figure B.10: The classical differential cross section per electron (per unit scattering angle and per unit solid angle) plotted against scattering angle	215
Figure B.11: The effects of incident photon energy and Z of the absorber on the Rayleigh differential cross section per unit scattering angle	217
Figure B.12: Diagram of Compton scatter	218
Figure B.13: The affects of incident photon energy on the Compton differential cross section per unit solid angle	219
Figure B.14: The Classical, Rayleigh, Compton, and incoherent differential cross sections per unit scattering angle plotted against the scattering angle for carbon and 10 keV photons	221
Figure B.15: The photoelectric cross section for water and lead plotted against the incident photon energy	223
Figure B.16: The total atomic cross sections for Water and Lead plotted against the incident photon's energy	224
Figure B.17: Narrow beam geometry	225

Figure B.18: Geometry of an x-rays path through an absorbing medium226

Figure B.19: The total atomic cross sections of water and air for energies between 1 keV and 100 keV228

Scientific Symbols

Z	atomic number
N_A	Avogadro's number: $N_A = 6.022 \times 10^{23}$ atom/g-mole
e	charge of an electron: $e = 1.60 \times 10^{-19}$ C
m_e	mass of an electron: $m_e = 9.11 \times 10^{-31}$ Kg
r_o	classical radius of an electron: $r_o = 2.82 \times 10^{-15}$ m
h	Planck's constant: $h = 6.626 \times 10^{-34}$ Js
c	the speed of light: $c = 3.00 \times 10^8$ m/s ²
ϵ_o	the dielectric constant of the vacuum: $\epsilon_o = 8.85 \times 10^{-12}$ C ₂ /Nm ²
μ_o	the permeability of the vacuum; $\mu_o = 4\pi \times 10^{-7}$ N/A ²
${}_e\sigma_o$	the classical cross section per electron: ${}_e\sigma_o = 66.525 \times 10^{-30}$ m ²
${}_a\sigma_o$	the classical cross section per atom: ${}_a\sigma_o = Z^* {}_e\sigma_o$
${}_e\sigma_C$	the Compton scatter cross section per electron
${}_a\sigma_C$	the Compton scatter cross section per atom: ${}_a\sigma_C = Z^* {}_e\sigma_C$
${}_a\sigma_{inc}$	the Incoherent scatter cross section
${}_a\sigma_R$	the Rayleigh scatter cross section
${}_a\tau$	the photoelectric cross section
${}_a\mu$	the total atomic cross section
μ	the linear attenuation coefficient

List of Abbreviations

3D	Three dimensional
3DCRT	3-dimensional conformal radiation therapy
3DCT	Three dimensional computed tomography (i.e. non-temporally correlated CT)
4DCBCT	Four dimensional conebeam computed tomography: referring to on board imaging
4DCT	Four dimensional computed tomography
4DMRI	Four dimensional magnetic resonance imaging
4DMVCT	Four dimensional megavoltage computed tomography
4DPET	Four dimensional positron emission tomography
AP	Anterior-Posterior directions
bpm	breaths per minute
CBCT	Conebeam computed tomography
COBRA	The true conebeam reconstruction algorithm used by Philips
CT	Computed tomography
CTV	Clinical target volume

CT#	<p>Pixels values of a CT image, defined as</p> $CT\# = \left(\frac{\mu_m - \mu_{water}}{\mu_{water}} \right) \cdot 1000 \text{ HU}$
DIBH	Deep inspiration breath hold
DICOM	Digit Imaging Communications in Medicine: the standard for how medical devices provide services, including: image transfer and storage, printing, formatting, query/retrieve, etc.
DVH	Dose volume histogram
EPI	Electronic portal imaging
FOV	Field of view
GTV	Gross tumor volume: extent of the tumor that is discernable
GUI	Graphical user interface
Gy	Unit of energy absorbed from ionizing radiation per unit mass: 1 Gy = 1 J/Kg
HU	Hounsfield units: the units of CT#
IGRT	Image guided radiation therapy
IM	Internal margin (intended to account for all internal motion of the target)
IMRT	Intensity modulated radiation therapy: a technique of delivering dose while moving the jaws of the radiation beam's collimator. Often multileaf collimators are used.
ITV	Internal target volume (a variation on IM incorporating multiple respiratory phases)

LR	Left-Right directions
mAs	The unit of exposure. Often used as the noun meaning exposure. Sometimes pronounced “mass”.
mAs _{eff}	Effective exposure, defined as $mAs_{eff} = mAs/pitch$
MIP	Maximum intensity projection
MLC	Multileaf collimator
MRI	Magnetic resonance imaging
MTF	Modulation transfer function
MVCT	Megavoltage computed tomography: typically referring to images taken with a tomotherapy machine.
PET	Positron emission tomography
psf	Point spread function
PTV	Planning target volume
ROI	Region of interest
RT	Radiation therapy
SBRT	Stereotactic body radiation therapy
s-HU	Units of grey scale values in CT images (unique to this thesis)
SI	Superior-Inferior directions
SM	Set-up margin (intended to account for all set-up errors)

SRN

Signal to noise ratio

V_{20}

Percent volume of an organ receiving at least 20 Gy of dose

Introduction

Four dimensional computed tomography (4DCT) is a clinically emergent imaging technique capable of creating temporally correlated volumes of moving anatomy, like snapshots in time. The technique was developed for the management of respiratory motion (1), where the act of breathing can cause severe imaging artifacts (2,3) as well as significantly affect the dosimetric coverage of the target (4,5,6,7,8). The intent of 4DCT is to minimize the amount of healthy tissue contained within the treated volume (6). Although 4DCT has wide clinical applications for many disease sites in the thorax and abdomen, lung cancer receives much attention due, in part, to the lack of improvement seen in the local control of lung cancer over recent years (8,9,10,11,12) and to the high contrast of CT in that region. Reduction of the planning target volume (PTV), particularly in light of the increased toxicity associated with concomitant chemotherapies (1,9), is an important factor in improving the long term survival of lung cancer patients (13).

Lung cancer remains the number one cancer killer in North America (11,12) with five year survival rates hovering around 15 % for the last eight years (11,12). Surgical resection is the first choice for curative treatment (14), however, it may be supplanted by radiation therapy (RT) if the patient either refuses surgery or indicates a potential for not tolerating the procedure (e.g. displays frailty, lack of respiratory reserves, has cardiovascular disease, etc.) (15). Large margins, such as those accounting for respiratory motion and uncertainties in target delineation brought about from motion blurring, increase the amount of normal tissue irradiated (16), thus increasing normal tissue toxicity (17,18,6) and, often, necessitating a mitigation of the curative dose (6). Yet, smaller margins which improve tissue sparing (19,17,6) hold the risk of permitting local recurrence of the disease (4). Characterizing and incorporating respiratory motion into the RT process then becomes a crucial component of improving the balance between complications and cure for lung cancer patients.

Respiratory induced motion has been measured for both lung tumors and relevant normal tissues using orthogonal radiographs (16), portal imaging (20), fluoroscopy (21,22), fluoroscopy with fiducial markers implanted in or near the tumor (23), magnetic resonance imaging (MRI) (24), and hyperpolarized He-3 MR (25). Tumor motion on the order of 10 ± 7 mm in the superior-inferior (SI) directions with a maximum of 35 mm (16), 6 ± 3 mm in the anterior-posterior (AP) directions with a maximum of 15 mm (26), and 4 ± 2 mm in the left-right (LR) directions with a maximum of 10 mm (26) can be expected (20,27,28,23,16,26,29,30,24).

When a non-temporally correlated CT scan is used for mobile target delineation, severe motion artifacts leading to systematic errors in target delineation are common (2,3,4). The target is also imaged at an arbitrary phase of motion, and the assumption that this phase represents in some manner the mean position of the tumor can lead to geographic misses (4). Slow CT, which captures multiple respiratory phases per slice, attempts to provide a volume more representative of the area occupied by the tumor over the entire respiratory cycle (13), however, the disadvantages of overestimating the tumor volume (6) and loss of resolution due to motion blurring can also lead to delineation errors (13). A study by Rietzel et al. showed that the slow scanning method simply cannot result in a representative volume, and that fast scanning techniques, which minimize the amount of motion seen in each slice, must be used (2).

The imaging technique of four dimensional computed tomography (4DCT) addresses the issues associated with respiratory motion in target delineation; it uses a fast

tube rotation (i.e. a half second or less (31)) to minimize the motion artifacts (32,33), and provides spatially and temporally resolved volumes of multiple respiratory phases to define the full extent of motion. This information identifies the presence and extent of motion, as well as aids in the determination of a method of motion management appropriate for that patient (16,1).

The spatiotemporal resolution of 4DCT provides useful information on the relationship of the diseased tissue to its surrounding anatomy. Beam angles (e.g. for RT and stereotactic RT delivery) may be optimized or entire phases of motion selected (e.g. for gated delivery) to minimize the involvement of nearby critical structures (1,16). Four dimensional computed tomography affords identification of the true free-breathing end exhale and end inhale positions of the tumor, the true geometric mean position as well as the temporal mean positions for gated RT delivery (1,34). Such a gated delivery may accommodate sufficient reductions in the PTV (24) to enable a safe escalation of the delivered dose (35,36,37). Also, tumor positions from each phase image may be combined to create an accurate representation of the total volume occupied by the tumor over the entire respiratory cycle (38,8,39,40), or the path of the tumor may be tracked (16, 24), facilitating advanced techniques in intensity modulated RT (IMRT)(6,1) and imaged guided RT (IGRT) (41,42,43).

The advantages of patient specific information and flexibility in treatment options have facilitated 4DCT's rapid commercialization (44). Yet, each CT manufacturer supporting 4DCT provides its own proprietary software, and multiple options exist for acquiring the respiratory signal (31,45,46). Each 4DCT system must be individually assessed for accuracy before it may be used in RT treatment planning (47). This project is one such an assessment. The scanner is a Philips' Brilliance Big Bore (Philips Medical Systems, Cleveland, OH). Two respiratory monitoring systems are available: the Philips Bellows (Philips Medical Systems, Cleveland, OH) and Varian's Real-Time Position Management (RPM) Respiratory Gating System (Varian Medical Systems, Palo Alto, CA). To assess the geometric accuracy of the system, a mechanical phantom is used to impart clinically relevant motion to acrylic spheres of various diameters. The size, shape, and position of these spheres, as measured with 4DCT, are compared to their true size, shape, and position. An evaluation of image quality for the 4DCT images with respect to clinically relevant non-temporally correlated CT scans is also performed.

Chapter 1: The Role of 4DCT in Radiation Therapy

Lungs and Lung Functioning

Respiration is the transport of O₂ from the atmosphere into the body and CO₂ from the body into the atmosphere. The lungs are the organs of respiration. The lungs accomplish this gas exchange by providing air conduits into the body (bronchi) and blood vessel-replete membranes for the diffusion of gasses in and out of the bloodstream (alveolar capillaries)(48p3).

Figure 1.1: The basic respiratory system

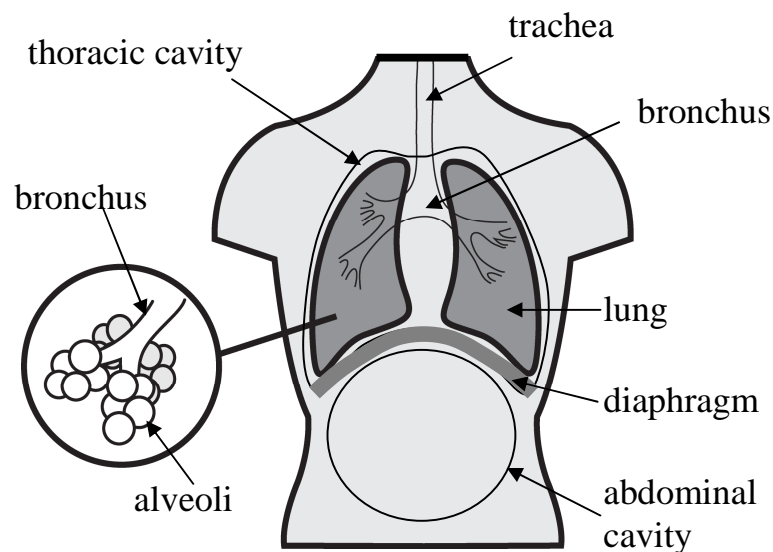


Figure caption: The bronchi provide the pathways for gases in and out of the lungs. At their roots, innumerable small balloon-like sacks called alveolus provide the venue for gas exchange. The walls of the alveoli are replete with alveolar capillaries, through which the gasses diffuse. The lungs reside within the thoracic cavity (i.e. inside the rib cage), and rest on a large dome-shaped muscle called the diaphragm. The diaphragm defines the lower extremity of the thoracic cavity. Below the diaphragm is the abdominal cavity where other vital organs rest, including the large and small intestines, the liver, kidneys, etc.

Ventilation maintains optimal levels of both gasses in the bloodstream (48p103) by adjusting the rate of respiration, the tidal volume of air entering and leaving the lungs, or both (48p45). Metabolic (i.e. involuntary) control of respiration is a function of the brainstem (i.e. pons & medulla, formally known as the respiratory centers)(48p109).

Figure 1.2: The breathing control center of the brain

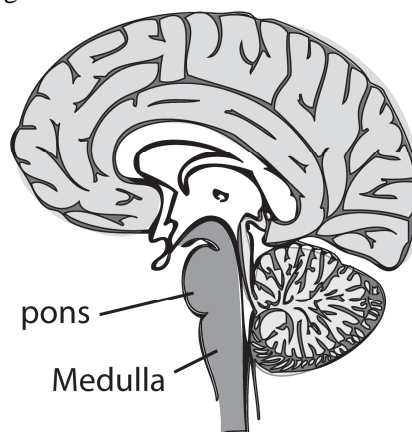


Figure caption: The pons and medulla are a bundle of nerves at the base of the brain responsible for the metabolic regulation of respiration. The pons and medulla are part of the vital life functions of the brain stem, which also regulates the heart beat and blood pressure. These functions are maintained even if one is unconscious or if serious damage has been sustained to other parts of the brain.

Sensory information from various receptors is received by the brain stem (48p104); there are four types of sensory receptors: chemoreceptors, lung receptors, chest wall receptors, and the so called 'other' receptors, referring to nasal, tracheal, laryngeal, arterial baroreceptors, and pain receptors. Chemoreceptors measure the partial pressure of O₂ and CO₂ in the blood as well as the pH (48p107). The partial pressure of CO₂ is strictly maintained within 5.2 -5.4 kPa, whereas quite a bit of latitude is tolerated with the O₂ partial pressure, which does not illicit a regulatory response until it drops below about 6.7 kPa, a level not typically attained under any normal conditions. The kidneys handle variations in blood pH on a much longer time scale and respiration is only minimally involved (48p110-111). Lung receptors monitor the mechanical deformation of lung tissues: stretching, inflammation, irritant receptors, vascular congestion, etc. Responses from these receptors include rapid shallow breathing and the cough reflex. Chest wall receptors monitor rib movement, muscle fibers, the magnitude of muscle contraction in the chest wall, mainly to compensate for any external load (48p109-110). 'Other' receptors respond to irritants and obstructions and also trigger the cough reflex and rapid shallow breathing (48p107). In addition to these involuntary responses, respiration may be willfully controlled as long as one remains conscious --once unconscious, involuntary respiration persists. Behavioral controls includes talking, singing and laughing, for example (48p107). These controls may also be subconscious, however, as in response to nervousness (e.g. a giggle or holding ones breath) or being startled (e.g. yelping or a sudden inhale).

The lungs are void of muscle or any rigid tissues to support or move themselves (48p50). Instead, respiratory muscles external to the lungs induce ventilation by creating pressure gradients between the atmosphere and the lungs via altering the volume of the lung cavity. The primary respiratory muscle is the domed shape diaphragm atop which the lungs rest. (See Figure 1.1.) When contracted, the dome flattens, increasing the intrathoracic volume and drawing air into the lungs (48p6). Intercostal muscles (i.e. the muscles between the ribs: see Figure 1.3), play only a minor role by preventing any contrary deformation of the chest wall (48p55). The contraction of the diaphragm is momentary; relaxation of the diaphragm causes expiration, relying primarily on the elastic recoil of the lung tissues. The elasticity and resistance of these tissue will, thus, affect respiratory functioning (48p45). This is the mechanism of normal *free* breathing, but there are also *forced* and *compromised* breathing mechanisms. In forced breathing, the intercostal muscles actively expand and contract the rib cage to force air in and out of the lungs. The abdominal muscles may perform forced expiration (as when coughing) by contracting and forcing the contents of the abdominal cavity upward against the diaphragm, compressing the thoracic cavity (48p56).

When lung functioning is compromised due to disease or mechanical restriction, breathing involves all the muscles of free and forced breathing, but also utilizes a variety of auxillary muscle groups (48p6). For example, strained inspiration may involve arching the back or, by holding onto a fixed object, flexing the pectoral muscles (48p55). Some accessory muscles involved in compromised breathing are shown in Figure 1.4 and include: the quadratus lumborum, latissimus dorsi, and the serratus posterior.

Figure 1.3: The muscles involved in *forced* breathing

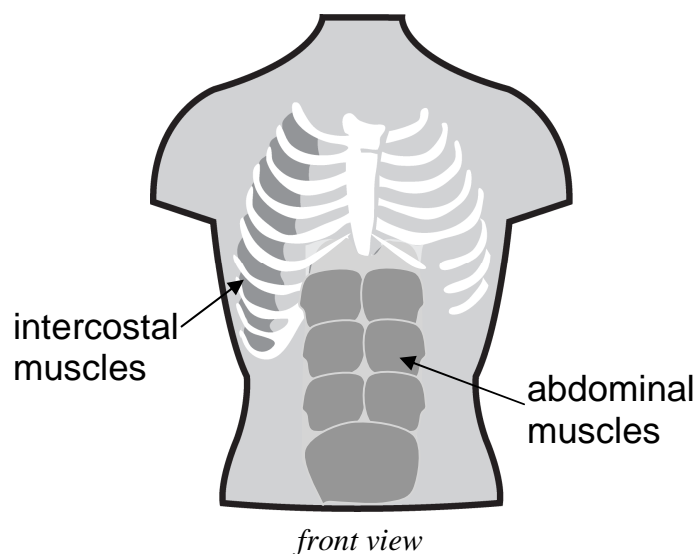


Figure caption: The intercostal muscles lie between the ribs, connecting them together. Interestingly, although these muscles only contract and draw the ribs together, the intercostal muscles perform both forced exhale and forced inhale. In forced exhale, the quadratus muscles in the back lock the lower ribs in place, and compressing the rib cage shrinks the thoracic cavity. In forced inhale, the upper ribs are fixed (held by the scalene muscle), and the intercostal muscles draw the entire rib cage upward, expanding the thoracic cavity (48p53). The abdominal muscles only act in forced exhale. By contracting the abdominal muscles, the contents of the abdomen are forced upward against the diaphragm which presses into the thoracic cavity, thereby shrinking its volume.

Figure 1.4: Muscles involved in compromised breathing

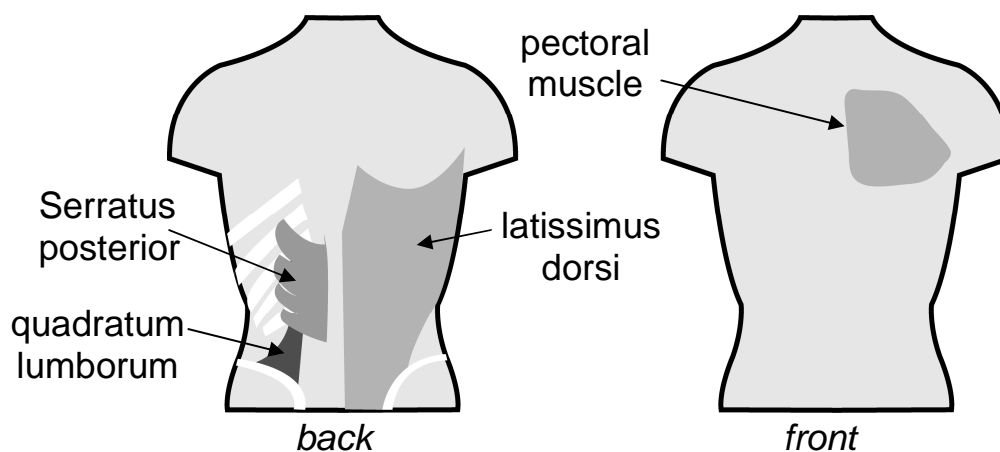


Figure caption: If the arms are held fast (by grasping onto a fixed object), the pectoral muscle contracts the thoracic cavity. In the back, several muscles capable of deforming the thoracic cavity contribute to both forced inhale and forced exhale.

Lung motion as a result of normal ventilation measured by CT (22), MRI (28) , and hyperpolarized He³ MR (25) shows that different portions of the lung extend and contract to different extents. The lower lobe moves about 50 ± 20 mm (28) primarily in the SI direction (25,35), whereas movement in the upper lobe is around 9 ± 4 mm (28) and can be in any direction (25,23). The overall change in lung volume between expiration and inspiration is around 20-26% (48,39,27), with the maximum change occurring in the lower thoracic cavity at end exhale (49) . Other organs also shift around during respiration: heart approximately 5 mm, trachea about 6 mm (27), kidneys close to 12 mm, liver around 15 mm, spleen in the ball park of 14 mm, and the pancreas about 10 mm (50). Of all the organs, not surprisingly, for most patients (49), the diaphragm shows the greatest movement during breathing (32,27) (e.g. 22 mm (27)).

Lung cancer

Lung cancer is the number one cancer killer in North America for both sexes. The estimated number of new cases in Canada for 2008 is 23,900, and in the US, about 10 times that. For all of North America, the estimated deaths due to lung cancer in 2008 are over 18,000, tallying to around 27% of all cancer deaths (11,12). The five year survival rate is only about 15 %, although for women it is slightly higher. While the incidence of lung cancer is down by 2.5 % for men in Canada and an impressive 22 % in the United States, it is up for women by 1.2 % and 9 %, respectively (11,12). There are two forms of lung cancer, small cell and non-small cell, with non-small cell lung cancer (NSCLC) contributing to around 80 % of diagnoses (9). Both types are directly linked to tobacco smoke (51). Curative RT is predominately performed for NSCL, as the small cell variety is particularly virulent and not often caught within the window for curative treatment (52). The non-small cell variety grows slower, and if caught early, localized disease has a 5 year survival rate of nearly 50%. Unfortunately, only about 20% of NSCLC patients present with limited disease (i.e. the disease is localized with no evidence of metastasis at the time of diagnosis (53)). If left untreated, NSCLC is fatal regardless of stage (53). For later stages (i.e. III and IV stage disease) the one year survival rate for NSCLC is about 37%, and only 11% for the two year mark (15).

These statistics have remained relatively unchanged since the turn of the last century, despite every effort to improve the long term survival of lung cancer patients (14,9). For limited disease, surgical resection is the treatment of choice (53). For the other 80%, adjuvant and neoadjuvant¹ chemotherapy and radiotherapy are increasingly included in both small cell and non-small cell lung cancer treatment plans (53,54,56,56). Patients may be treated solely with radiotherapy if suffering from the infirmament of old age, cardiovascular disease, or some form of respiratory impairment making surgery intolerable (53,15). Although there is strong evidence that aggressive radiotherapy is effective on both types of lung cancer (55,57,58,59), normal tissue toxicity inevitably imposes dose restrictions that often lead to limiting the curative intent of the radiotherapy treatment (6,60,17).

Lung Tumor Motion

As the lung deforms by pressure gradients causing it to fill and deflate, so the lung tumor may move. Lacking any rigid structure, what connectivity exists between the tumor and the lung consists of soft elastic tissues which allow the tumor to respond to the

¹ i.e. Rx doses not in themselves curative administered either sequentially or concomitantly

external forces of respiration with complex 3-dimensional (3D) movement. A fluoroscopy study by Ekberg et al. found that tumor motion in patients ranged from 0 -12 mm (35). Weiss et al., using 4DCT, measured a mean tumor movement of 7.1 mm with a maximum of 24 mm (27). Several investigators have focused on evaluating tumor motion based on its position within the lung. Plathow et al. used dynamic MRI and found the mean tumor motion in the upper lobe to be 3.4 mm and for the middle and lower lobes, 4.5 mm and 7.2 mm, respectively (28). In an extensive study by Seppenwoolde et al., a mean distance of 4.1 mm in the upper lobe was measured, 3.3 mm in the middle lobe, and 7.2 mm in the lower lobe, with the maximum movement occurring near the diaphragm (23). Plathow observed that SI motion was most significant in the lower lobe and least in the upper lobe, suggesting a connection between diaphragm motion and tumor motion (28). Chen et al. measured diaphragm motion with fluoroscopic video, and found an average displacement of only 2.6 mm (61). Stevens et al. found tumor motion in some patients that had no diaphragm motion, including one with a 22 mm tumor displacement (16). In fact, in general, tumor motion cannot be reliably linked to the functioning of the respiratory muscles. In a study by Ross et al. using ultrafast CT, one tumor attached to the chest wall in the upper lobe displayed no movement at all (29). Interestingly, Plathow noted that the mobility of the lung was reduced in regions containing tumors (28).

Using electronic portal imaging, Erridge et al. evaluated tumor motion based on its direction, finding a mean motion in the AP direction of 9.4 mm with a standard deviation of 5.2 mm. For the LR direction, a mean of 7.3 mm with 2.7 mm standard deviation was recorded, and in the SI direction, the mean was 12.5 mm with a standard deviation of 7.3 mm (20). In Seppenwoolde's study, a mean of only 2.2 mm with a standard deviation of 1.9 mm was measured in the AP direction. The maximum, however, was 8.2 mm. For the LR, again, Seppenwoolde's results are smaller than Erridge, with a 1.2 mm mean and 0.9 mm standard deviation. The maximum displacement in the LR direction was only 2.8 mm. For the SI direction, Seppenwoolde measured a mean displacement of 5.5 mm with a standard deviation of 6.0 mm and a maximum displacement of 24.6 mm (23). It may be argued that Seppenwoolde's method of using fluoroscopy to track gold fiducial markers implanted in or near the lesions may be more accurate than electronic portal imaging (EPI), but another important paper by Shimizu et al. using a method similar to Seppenwoolde, found a maximum AP motion of 14.6 mm, 10 mm in the LR and 15.9 mm in the SI (26). Using MRI, Lui et al. measured motion only in the AP and SI directions, resulting in a mean of 6.9 mm with a standard deviation of 2.6 mm in the former, and 13.4 mm with a standard deviation of 7.4 mm for the latter (24).

The cardiac beat can also significantly contribute to tumor motion (35). Seppenwoolde observed 1 - 4 mm of motion due to heartbeat (23). Ross saw a 1.2 mm mean in the AP direction, 2.0 mm in the LR, and 1.5 mm in the SI direction due to the heart (29). Both investigators noted the greatest motion due to cardiac functioning occurred when the tumor was attached to either the heart or the aorta. However, in general, the greatest amplitudes were always observed when the tumor was attached to the diaphragm (29,23). One of the most important outcomes of Seppenwoolde's study was the observation of hysteresis in many lung tumors. Forty eight percent of the patients exhibited hysteresis, with differences in the trajectories from end inhale to end exhale ranging from 1 - 5 mm (23).

The motion of mediastinal and hilar lymph nodes is also a concern for radiation therapy as distant metastases tend to form in these locations (see Figure 1.5)(35). In a study by Piet et al., 47 nodes in 25 patients were measured using 4DCT. The mean motion in the AP direction was 2.4 mm with a standard deviation of 1.8 mm. In the LR

direction, the mean and standard deviations were 2.8 mm and 1.9 mm, respectively. For the SI direction, they were 4.7 mm and 2.3 mm, respectively. More than twenty five of the nodes exhibited motion greater than 5 mm, five nodes had motion greater than 1 cm, and one node had motion larger than 1.4 cm (62).

Figure 1.5: Lymph nodes of the lung

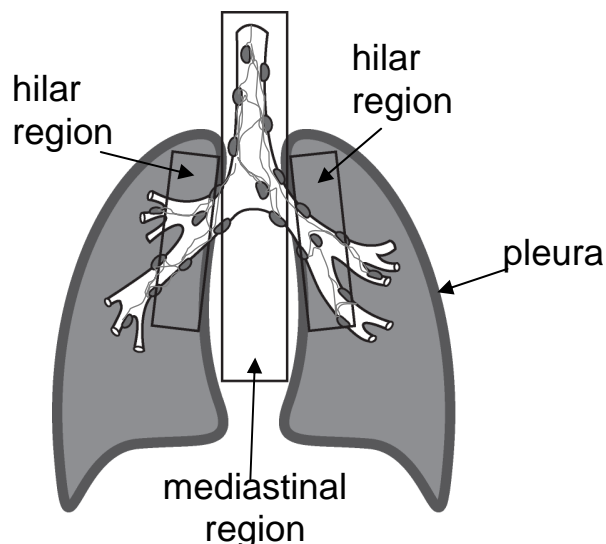


Figure caption: Distant metastases tend to form in the lymph nodes near the lung. The mediastinal region constitutes the space between the right and left lungs—the region is shared by the heart, esophagus, and the trachea. Hilar regions refer to the entry point of the lungs, where the bronchus, arteries, and veins penetrate the pleura (i.e. the sack containing the lungs).

This wide range of observations only serves to illustrate that tumor motion cannot be assumed or predicted by the size of the tumor, rib or diaphragm motion, its location, or even pulmonary functioning. Each patient must be individually assessed for the presence and extent of tumor motion (16).

Radiation Therapy in Lung Cancer Treatment

A typical staging for lung cancer may involve 2 CT scans and a positron emission tomography (PET) scan. The first CT is performed without contrast to acquire the electron densities of the relevant anatomy. These values are used by the treatment planning system to calculate the dose distribution of the radiation treatment and to act as a correction map for the PET scan (63). The second CT is performed after injection of an iodinate contrast agent to improve the soft tissue contrast, as some lung tumors may be adjacent or attached to more dense structures in the mediastinum (e.g. esophagus, aorta, heart, etc.) or the chest wall. Contrast also helps identify metastases in the lymph nodes (7). A typical technique for both CT scans would be 120 kV and 250 mAs. The slice thickness remains small, around 2-5 mm in order to resolve the lymph nodes (see Figure 1.5)(6). The entire lung must be included in these scans, from cricoid cartilage just below the adam's apple in the neck to the second lumbar vertebra (see Figure 1.6), to assure that

the metrics used in evaluating treatment plans (such as dose volume histograms² (DVH) and V_{20} ³) are accurate (7,64).

Figure 1.6: Optimal scan range for the staging and planning of lung cancer

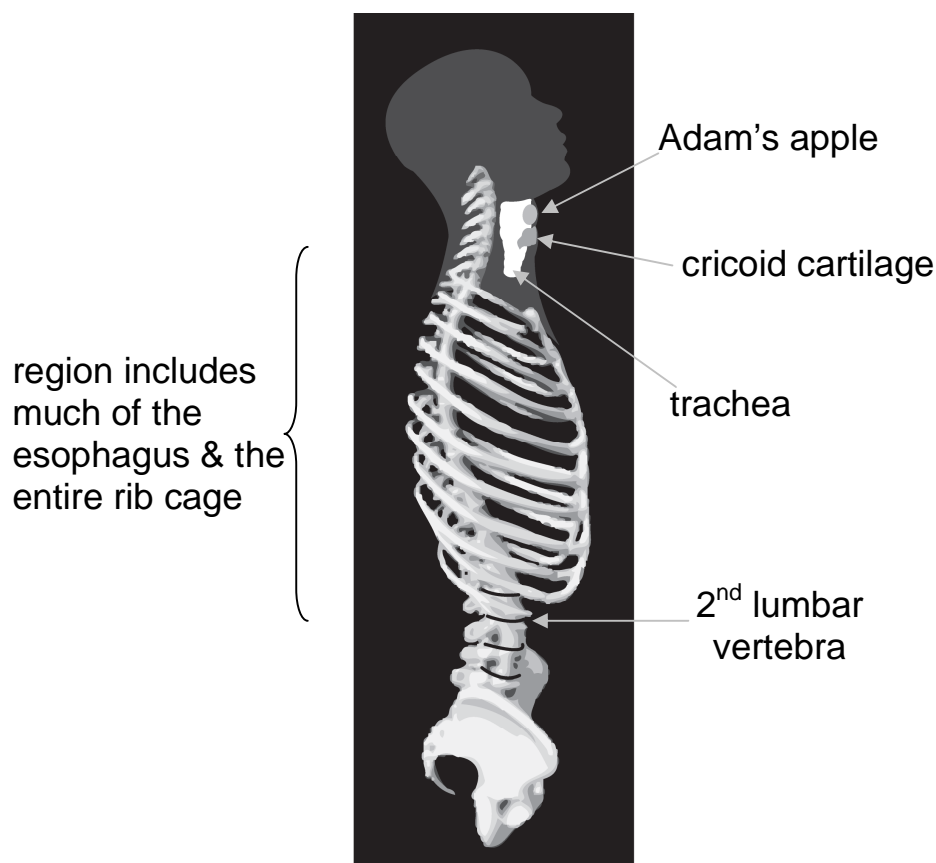


Figure caption: Inclusion of all the anatomy between the cricoid cartilage and the 2nd lumbar vertebrae insures that the entire lung and rib cage are imaged, as well as much of the esophagus, liver, and other nearby vital organs.

A PET scan provides metabolic information by picking up evidence of positron emissions from F^{18} tagged sugar (i.e. fludeoxyglucose, or just FDG). Cancer cells have an accelerated FDG uptake, helping to identifying nodal involvement⁴ and distinguishing tumors from other confounding physiological conditions, such as portions of collapsed lung due to bronchial blockages (i.e. atelectasis) or inflamed lung tissue (i.e. pneumonitis) (65,66). The resulting image is blurred by respiratory motion (typical scan requires approximately 5 minutes at each table position (6)), and is almost completely void of landmarks, and thus, is ill suited for delineation. However, the high sensitivity⁵

² Cumulative DVH: a histogram showing the % volume of the target (or organ at risk) receiving at least the dose specified by each dose bin.

³ the percent volume of an organ receiving more than 20 Gy

⁴ The size of lymph node has been used to indicate metastatic involvement (i.e. ≥ 1 cm on the short axis), however, this is not a sensitive indicator unless excluded by PET (7).

⁵ proportion of true positives correctly identified

and specificity⁶ of PET contributes additional information in 41 % of patients (68) and reduces inter-observer variations in GTV delineation (68,66). Using PET and CT together provides the functional and anatomic information for optimal staging of lung cancer (65,69,66), and has been shown to reduce the rate of regional and systematic failure (70).

Local control of lung cancer is usually determined from subsequent CT scans acquired 3 to 6 months after completion of RT. A positive outcome entails a complete disappearance of the malignancy with no further evidence of the disease for at least another 6 months (7). Although other factors (e.g. the patient's overall strength and wellness) contribute to an individual's outcome, dose to the planning target volume (PTV) is the only definitive factor of local control (59). Unfortunately, RT impacts normal as well as the diseased tissues, and treatment planning inevitably involves balancing the curative effect to the tumor with the toxic dose delivered to the surrounding anatomy. Organs at risk⁷ in the vicinity of the lung include the heart, esophagus, spinal cord, and the lung itself; near the diaphragm, the liver and kidneys may also be at risk depending on beam angles (6). Dose limiting toxicities include bronchitis⁸, fibrosis⁹, pericardial effusion¹⁰, hypoxia¹¹, esophagitis¹², and pneumonitis¹³ (58,6,40,71), all of which are strongly correlated to high radiation doses (17,72,6,71,18,73,74,19,16). Even at low doses, pneumonitis can still result when large volumes of lung tissue are irradiated (17). In order to assess the risks to normal tissues, evaluation of treatment plans typically involves dose volume histograms for each of the involved organs, mean biological doses¹⁴, and indices such as normal tissue complication probabilities¹⁵ (64,18,17,75). For instance, the limit for the volume of lung receiving 20 Gy (V_{20}) or 25 Gy (V_{25}) may be specified. A typical value for this constraint is 30% (7). Also, each organ at risk may be assigned a maximum accumulated dose, such as no more than a total of 18 Gy to the spinal cord, 36 Gy to the trachea, 27 Gy to the esophagus, etc. (76). Strict adherence to these normal tissue sparing protocols can easily lead to dosimetric compromises, particularly in the region near the tumor's boundary, reducing the probability of local control (77) or even mitigating the curative intent of the procedure (6). And still, the high incidence of local and distant recurrences indicates a need to increase tumor doses for lung cancer patients (67). There is compelling evidence that escalating the dose received by the tumor improves local control (6,15,37,78,59,67), and if the treatment volumes can be reduced, the dose to the tumor may be safely increased (36,35,79). Including the hilar and mediastinal lymph nodes in the GTV without evidence of involvement, so-called 'elective nodal irradiation', although controversial, has been the standard of care until just recently (67). There is about a 7 % chance of nodal failure without elective nodal irradiation (7,67), but obviously, foregoing irradiation the lymph nodes reduces the field

⁶ proportion of true negatives correctly identified

⁷ Normal tissues with a sufficient radiosensitivity to affect the prescribed dose and/or other aspects of treatment planning (80)

⁸ Inflammation of the bronchi (i.e. the bronchial tubes)(81)

⁹ The development of scar tissue—with pulmonary fibrosis, the lung tissue becomes hard and stiff (82)

¹⁰ Fluid in the sack that surrounds the heart (83)

¹¹ A deficiency in the amount of oxygen reaching tissues (84)

¹² Inflammation of the esophagus (85)

¹³ Inflammation of lung tissue

¹⁴ The sum of all partial volumes (for a given organ) receiving x dose, multiplied by the total dose delivered to that volume over complete RT course, $NTD_{mean} = \sum_i v_i NTD_i$. (17)

¹⁵ An NTCP curve is a plot of the probability for a normal tissue complication (where the complication is specified and a time frame for development is given) vs. the prescribed dose.

size and thus, the extraneous irradiation of the esophagus and pulmonary normal tissues (10,67). Another issue is the increased use of pretreatment and concomitant chemotherapy, which not only increases the toxicity of RT, but also poses target delineation issues as well. Pretreatment chemo can reduce the tumor volume (7,67). One option is to use the pre-chemo volume in treatment planning (7), as it is uncertain how many clonogenic cells remain in the area of regression. However, treatment plans using the post-chemo tumor volume give marginal reductions of V_{20} (160), potentially supporting dose escalation (86,7). For those patients receiving concurrent chemo, there is a significant increase in the risk of pneumonitis at any given V_{20} (7), meaning particular care must be given to margins and the prescription dose (67). The trend is currently leaning towards replacing elective nodal irradiation with pretreatment chemotherapy (67).

Margins

The International Commission on Radiological Units (ICRU) issued report ICRU 50 recommending a geometric system of assigning and evaluating the safety margins around the visible/palpable gross tumor volume (GTV) seen during staging (87). These guidelines give unambiguous definitions of volumes and doses which are widely accepted (6), providing a common language between institutions (80) and promoting consistency in the delineation and treatment of all cancers (4).

Beginning with what can be seen of the tumor (the GTV) in the planning CT, a margin is added around the volume to account for microscopic extension of the disease. The result is called the clinical target volume (CTV), and is intended to encompass every clonogenic cell of the disease. Another margin is then added, referred to as the integrated planning margin, to account for the various uncertainties in planning and in treatment; everything from tumor delineation and the unknown extent of the subclinical spread of the tumor, to organ position and setup errors throughout the entire course of the RT are included (87). These uncertainties may be systematic or random, occurring on an intra-fractional or inter-fractional time scale, normally or anisotropically distributed, correlated or independent (35,4). The result is the planning target volume (PTV), designed to completely encompass the CTV in every foreseeable circumstance. The PTV is the target for radiotherapy.

The geographical limit of the subclinical extent of the disease is invisible (65), and expansion of the GTV margin to include the microscopic spread of the tumor is deduced from pathological specimens (67,63). A study of 70 resected tumors found the maximum extent of microscopic disease for the two prominent forms of NSCLC, adenocarcinoma and squamous cells, to be 3 cm and 2 cm, respectively (75). A histologic study of another 70 lung tumors indicated a $GTV \rightarrow CTV$ margin of 8 mm is sufficient for adenocarcinoma and 6 mm for squamous cell (67). The CTV may enclose just a rind around the GTV or it may include physically distinct regions if metastatic disease is suspected. The CTV is the volume that must receive adequate treatment in order to achieve the intended therapeutic goal, which may be either curative or palliative (87). In most instances, for radiotherapy to be effective, more than 99 % of the CTV must receive greater than 95 % of the prescription dose (87). The dose given to the target (i.e. the PTV) is high in order to insure that the CTV receives the intended treatment (4). Typically, conforming the 95% isodose¹⁶ line to the PTV results in an adequate dose to the CTV (67).

¹⁶ On a 2D or 3D map of dose distribution, the line or contour defined by a single dose value

The margin added to the CTV to create the PTV encompasses all systematic and random errors (4) and is derived from the oncologist's personal experience and/or published margin recipes (88). If the uncertainties are based on probabilities or biological models, distributions must be well known and the margins are added in quadrature, as these represent the width of the probability distributions (4,89). However, if the margins are defined as percent coverage of minimum dose, then the systematic and random error margins are added linearly (4). A popular recipe for constructing the PTV comes from van Herk (4)

$$\text{Margin} = 2.5\Sigma + 1.64\sqrt{(\sigma^2 + \sigma_p^2)} - 1.64\sigma_p, \quad 1.1$$

where Σ is the standard deviation of all the systematic error, σ is the standard deviation of all the random error, and σ_p is the standard deviation of the dose gradient (i.e. the beam penumbra (8)). This formula should deliver 95 % of the prescription dose to the CTV for 90 % of the population (8). Table 1.1 gives a modified version of the summary of published margin recipes from the van Herk paper "Errors and Margins in Radiotherapy"(4).

Table 1.1: A sample of published margin recipes

Author	Application	Recipe	Assumption
Bel et al (90)	target	0.7σ	Random errors only (linear approximation) Monte Carlo
Antolak & Rosen (91)	target	1.65σ	Random errors only
Stroom et al (92)	target	$2\Sigma + 0.7\sigma$	95% dose to 99% CTV—tested in realistic plans
van Herk et al (2000) (93)	target	$2.5\Sigma + 1.64\sqrt{(\sigma^2 + \sigma_p^2)} - 1.64\sigma_p$	95% dose to CTV for 90% of patients. Analytical solution for perfect conformation
Parker et al (94)	target	$\Sigma + \sqrt{(\sigma^2 + \Sigma^2)}$	95% min dose & 100% dose to 95% of volume
van Herk et al (2002) (95)	target	$2\Sigma + 0.7\sigma - 3\text{mm}$	Monte Carlo-based test of 1% loss in tissue control probability due to geometrical errors
van Herk et al (2003) (96)	target	M – 2 mm M – 5 mm	Correction for nonuniform cell density
McKenzie et al (2000) (97)	respiration	A_o	Margin for respiration on top of other margins (respiration dominates other errors)
van Herk et al (2003) (98)	respiration (lung)	0.25 A_o (caudally) 0.45 A_o (cranially)	random respiration combined with 3 mm random stdev, when respiration dominates other errors ($A_o > 1\text{cm}$)
McKenzie et al (2002)(99)	organ at risk	$1.3 \Sigma \pm 0.5\sigma$	Margins for small and/or serial organs at risk in low or high dose region
Mutaf & Brinkmann (2008) (100)	respiration (lung)	$IM_{\text{symetric}} = 0.37A_o - 2.00 \text{ mm}$ $IM_{\text{asymetric}} = 0.72A_o - 2.5 \text{ mm}$	Assessed under simulations of phantom and patient data

Table caption: Σ is the standard deviation of systematic errors, σ is the standard deviation of random errors, σ_p is the width of penumbra (Gaussian fit), A_o is the peak-to-peak amplitude of respiratory motion, and M is the margin before adjustment (4).

Sources of error

There are three basic sources of treatment error: delineation, internal motion, and setup error; the latter two produce both random and systematic uncertainties while the former engenders purely systematic error (4). Systematic errors can affect a single fraction of treatment or the entire RT course, while random errors affect only a single fraction (80,4).

Random uncertainties result from daily setup errors (1) and variations in patient physiology. Changes in physiology may be intra-fractional, such as pulmonary and cardiac functioning, inter-fractional, due to normal biological functioning (e.g. fullness of the bladder or rectum, weight loss, daily variation in respiratory motion), or a result of treatment (e.g. shrinking of the tumor or the re-inflation of the lung after atelectasis) (1). All tumor motion during RT is random. Random errors in the thoracic region range from about 2.3 mm to 5.4 mm (80). Since the magnitude of respiratory induced tumor motion is not isotropic, it is reasonable to calculate these errors by direction, that is $\sigma = \sqrt{(\sigma_{\text{motion}}^2 + \sigma_{\text{setup}}^2)}$ may equal, for example, 5.3 mm in the SI direction, 3.8 mm in the AP direction, and 4.2 mm for LR (35).

Systematic uncertainties begin with the delineation of the GTV. Delineation is limited by the imaging system's resolution, the ability of the oncologist to distinguish the tumor amidst various confounding physiological conditions (e.g. atelectasis, pleural infusion, pneumonitis, and motion) as well as to interpret and integrate disparate sources of information (4,67). Even with CT/PET, the boundary between the tumor and normal tissues may not be visible (63), particularly if the tumor is adjacent or attached to another structure of similar density or biological activity. Such residual uncertainties always exist, and are handled by a safety margin (4) included in the integrated planning margin. Delineation of the GTV and CTV, being subject to the discretion of the physician, are susceptible to inter- and intra- physician variation, and so contribute another source of systematic error (65). Motion of any kind hinders accurate GTV delineation as it blurs the boundaries between the tumor and normal tissues as well as creates artifacts (6). Many tumors demonstrated shape deformation (54), but the problem is particularly severe for tumors in the thoracic cavity due to respiration. For CT, respiratory motion induces random distortions resulting from the dynamic interplay between the moving anatomy and the image acquisition (2,88). Depending on the initial CT tube angle (3) as well as the phase relationship between the target motion and the advancing scan plane, a myriad of non-representative shapes and volumes are possible. Known objects undergoing clinically relevant motions have appeared elongated and shortened (3). A sphere can be imaged as lozenge-, pear-, or barrel-shaped; it can appear as a truncated cone or all twisted around like taffy (3); straight edges look wavy; even identical objects of fixed relationship to one another can exhibit distinct and dissimilar artifacts (3). Some examples of these artifacts are shown in Figure 1.7.

These motion artifacts are most severe where motion is largest and at high density gradients, such as near the diaphragm where the act of respiration can create discontinuities in the imaged anatomy, introducing non-physical structures into the data set (2,3,101) (see Figure 1.7). Motion artifacts lead to probable systematic errors in both the GTV and normal tissue delineation, affecting the shape, position, and volume of these structures (88), all of which are detrimental to dose escalation (49). In addition to delineation errors, other systematic errors include mechanical uncertainty (e.g. light/radiation field alignment, laser alignment, isocenter, etc.) and translation errors (i.e. the transferring of coordinates from the internal reference frame of the patient to the external reference frame of the room) (1). Typical combined systematic errors measured in the thoracic region range from 1.8 mm to 3.5 mm (80).

Figure 1.7: Two 5 cm spheres imaged with non-temporally correlated CT

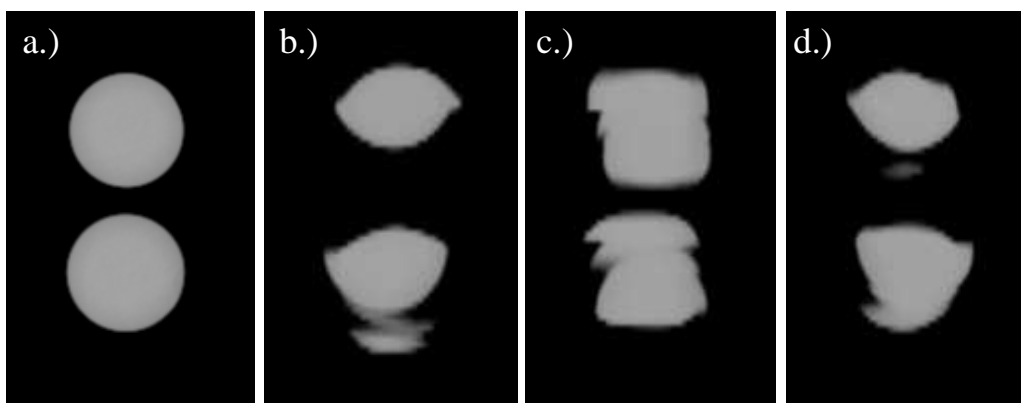


Figure caption: Four images of two 5 cm diameter spheres with a fixed spatial relationship to one another. All four images were acquired with 3DCT (120 kVp, 400 mAs). a.) the spheres are stationary, b-d.) the spheres are undergoing motion in the SI direction with an amplitude of 2.5 cm. Note: a portion of the upper sphere in d.) is imaged as a separate object.

Towards the goal of minimizing the amount of normal tissue irradiated, patients with lung cancer suffer an additional disadvantage in that, even at end exhale, there is still air in the lungs, making lung tissue very low density. The range of secondary electrons¹⁷ in this low density tissue broadens the penumbra of the treatment beam and necessitates larger field margins between the target and the edge of the radiation field to achieve a homogeneous dose coverage of the target (102). Higher energy beams (i.e. anything over 10 MV) require extra care so that the penumbra does not become intolerably large (7) and that the scattering of electrons out of edges of tumor does not result in an under dose of the target (7). In addition, breathing during treatment can move both the tumor and critical structures in, out, and around the radiation field (101), causing additional uncertainties in the dose distribution (6).

Random errors, like respiratory motion, blur the dose distribution in a predictable fashion (4,5). Physiological movement during treatment manifests as blurring of the static dose distributions along the path of motion. With conventional RT, where the beam is static, dose gradients in the center of the beam are small, and this blurring essentially increases the beam's penumbra (1) by reducing the size of the high-dose region of the treatment field (4,5). Compensation by either enlarging the beam portals (16,5) or escalating the dose (which is problematic due to penumbra issues) is required (8). The quantity of high-dose region lost depends on the shape of the field in the high-dose fall-off region, which in turn, depends on the tissue density and beam characteristics (5). A similar effect is seen in the cumulative dose distribution over many fractionations, resulting in inter-fraction random errors (5).

Systematic errors arising from inter-fraction organ motion, setup, and delineation errors shift the cumulative dose distribution relative to the position of the target (4,1). In the worst case scenario, the shift leads to geographic misses, needlessly irradiating normal tissues and failing to deliver a tumorcidal dose to the CTV (8,4). When fractionation is used, as in lung RT, the relative difference between the impact of random and systematic errors increases (4), and systematic errors end up having a much larger effect on the total delivered dose (4).

¹⁷ Secondary electrons are the products of ionizations.

Imaging Lung Tumors

Traditionally, clinics performed a *fast CT* (i.e. a fast tube rotation for a fast acquisition) to minimize the amount of motion captured in each CT scan. Without knowledge of what respiratory phases are recorded, oncologists were forced to assume that the tumor was imaged at, or at least near, its temporal mean position (8). A margin recipe was chosen, for example

$$\text{Margin} = 2.5\Sigma + 0.7\sigma, \quad 1.2$$

(4), where both systematic and random errors associated with tumor mobility were taken from population statistics (67). There are a couple of problems with the fast CT method. The first of these is the hope that the tumor was captured in its temporal average position (67). The location of the GTV in a fast CT is arbitrary, and the undefined displacement of the tumor from its true temporal mean position inevitably introduces systematic errors (8,4). McKenzie treats the systematic errors arising from target deformation due to motion artifacts, Σ_s , and displacement from the true mean position, Σ_d , separately. The faster the CT scan, the less the GTV is distorted and the smaller Σ_s , but the uncertainty in its position with respect to the temporal mean Σ_d is increased. The slower the scan, the more motion is captured, and Σ_s increases while Σ_d decreases since the sampling time increased. McKenzie claims that, to a first order approximation, the linear sum of these two uncertainties is not only constant (i.e. $\Sigma_s + \Sigma_d = \Sigma$), but is approximately equal to the standard deviation of the tumor's amplitude of motion A_o (103). Wolthaus attests that both the systematic and random errors associated with tumor motion can be estimated by this same standard deviation Σ (8), which van Herk et. al show to be approximately one third of the peak amplitude of motion (i.e. $\frac{1}{3}A_o$) (4). Using statistically derived margins, the results appear reasonable (e.g. AP = 9 ± 6 mm, SI = 10 ± 7 mm, LR = 8 ± 5 mm), however the errors are problematic. These margins may be appropriate for some patients, yet they would significantly under-dose many tumors, especially in the lower lobe where motion can be quite large (104,102), while needlessly irradiating healthy tissues in patients whose tumors move very little. This is the second problem: use of population-based margins. Often a 1 cm uniform margin is chosen, but in general, uniform margins overestimate the PTV, and in some cases, quite counter intuitively, they can miss the GTV entirely, especially for small peripheral tumors (49, 54). Such fear of geographic misses has even compelled the mechanical suppression of motion over 8 mm via an external load (40). In a 20 patient study by Ekberg et. al, going from the margins required to adequately cover 90% of the population to cover 95 % of the population, the SI margin increases by 13.9%, the AP margin by 31.7 %, and for the LR, 20.3 %, suggesting a need for individualized motion margins (54).

In order to acquire patient specific information on amplitude and direction of tumor motion, fluoroscopy is often used (2). Yet, this is a two dimensional technique and tumor motion is 3D; thus, at least two orthogonal views are required to accurately characterize the motion (32,54,2,7). Ideally, motion of the GTV itself would be measured, but the contrast of fluoroscopy is poor without radio opaque markers (2). Tiny gold fiducial markers (e.g. ~ 1.5 mm diameter (105)) must be inserted into or near the GTV (e.g. within 5 or 6 cm (89)). When implanted transcutaneously¹⁸, estimates of incidences of pneumothorax¹⁹ fall between 20 to 30% (106). Bronchoscopic²⁰

¹⁸ Inserted through the skin

¹⁹ Collapsed lung due to air in between the two layers of the sack encasing the lung (i.e. the pleura).

implantation is less invasive (105,106), but the markers have a tendency to drift from their implanted location or fall out of the tumor (46,107,89). A week or so after implantation, a slight fibrosis and hyperplasia²¹ occurs around the gold bead, stabilizing it. Thus, imaging and treatment should not begin before 5 days after bronchoscopic insertion (46). Once confident in the location of these fiducial markers, their position and phase relationship to the tumor must be determined (21). Other than the risks associated with the implantation and migration of the marker, the gold appears harmless to normal lung tissues (105).

Motion management

Under the hypothesis that the poor long term survival rates for NSCLC treated with RT are due to the geometric errors arising from a target delineated using fast CT (107) and the dose mitigating toxicity of the large margins needed to cover population-based estimates of tumor motion (6), researchers and clinicians began exploring a new tack where tumor motion is accounted for and incorporated into RT planning and treatment. The first attempts were to image the tumor using *slow CT*. With slow CT, the patient breaths freely, and the acquisition time of the CT scan is sufficiently long to capture multiple phases of respiratory motion in a single image (4); preferably, the entire extent of the tumor's motion is captured (e.g. ~ 4 s per CT slice (108)) (1). The rationale for this approach is that dose calculations based on the geometry seen in slow CT are more representative of the dose received by the patient during treatment (3,1). The gross tumor volumes produced by slow CT are more reproducible than those of fast CT, but overestimate the volume of the tumor (108,6). According to Senan et al., the volume of a single slow CT is equivalent to approximately 6 fast CT scans combined (7). The loss of resolution due to increased motion blurring exacerbates the potential for error in tumor delineation. For this reason, slow CT is decidedly inferior for the delineation of tumors adjacent or attached to structures with similar density (1). Due to motion blurring, a typical slow CT, on average, provides only 80 % geometric coverage. Even combining two slow CT scans with a 3 mm uniform margin would still give inadequate coverage for some patients (107). In fact, it has been shown that a slow CT cannot produce volumes representative of the full extent of the tumor's motion, particularly underestimating motion in the transverse plane (2).

To get around the uncertainties introduced into the RT process by breathing, breath hold techniques attempt to arrest respiratory motion entirely (108) and hope to allow margin reductions sufficient to afford dose escalation (46). Ideally, the tumor and its surrounding anatomy are imaged while stationary, facilitating the accurate delineation of the tumor and other critical structures at a specific phase of respiration. Breath hold techniques do significantly reduce tumor motion (46), but residual motion may still exist, for example, due to the heart beat (7).

The deep inspiration breath hold (DIBH) technique capitalizes on the inflated lung to reduce the percentage of lung volume receiving a significant dose (e.g. can reduce V_{20} by 30% (109,108)) and to create a buffer for critical structures like the heart or the spinal cord. In DIBH, the patient is coached into a comfortable maximum inspiration breath hold. This maneuver is then repeated during treatment for each treatment field (46), and a respiratory monitoring system is required to assure consistency from breath hold to breath hold (110, 1).

²⁰ Inserted through the bronchus

²¹ Enlarged by an increase in cell number

All breath hold procedures require compliance and some considerable effort on the part of the patient (111,46)—up to 30 breath holds may be required for a single treatment session (111). Roughly half of all patients are unable to perform DIBH, and screening for tolerance is necessary prior to implementation of the technique (7, 46). Typically, capable patients can hold their breath for a maximum of ~ 20 s (61), however, towards the end they may tremble from the effort, potentially causing the target to swing a couple millimeters. Thus the duration of the hold should be kept shorter than the absolute tolerance of the patient (61). Most patients are comfortable holding their breath for only 12 to 16 seconds up to 10 - 13 times in one session (112). Attempts have been made to image patients while holding their breath at different inspiration levels in the hopes of achieving images at different phases of respiration (21). However, the lack of reproducibility has focused efforts on maximum inhale and maximum exhale breath holds. For cases where the patients have been incapable of performing a breath hold, abdominal compression has been used to immobilize the tumor—a procedure of considerable discomfort to the patient (113).

ICRU 62

In keeping with the philosophy of motion management, in 1999 the ICRU released a supplement to ICRU 50, suggesting an alternative method of delineating the PTV. Rather than defining the integrated planning margin by distinguishing components of systematic and random errors, uncertainties derived from the internal motion of the target are grouped together to form an internal margin (IM), then an additional margin is added for setup errors (SM) to achieve the PTV; that is (114)

$$\text{CTV} + \text{IM} + \text{SM} = \text{PTV}. \quad 1.3$$

All the same systematic and random errors apply, and the ICRU 62 system produces the same PTVs as the ICRU 50 system, but by clarifying what portion of the PTV is attributed to anatomical motion uncertainties, it provides a framework for optimizing the patient specific component of the PTV (i.e. the IM) (115).

The IM accounts for both inter- and intra-fractional variations in the anatomy due to respiration, weight loss, tumor shrinkage, variations in the relationship between the target's motion and respiratory pattern, etc. (80,114,21). The SM accounts for patient setup errors, variations in daily positioning, mechanical uncertainties, etc (38,114). The SM margin is, thus, clinic and treatment machine specific, and should be assessed for each beam of the treatment (114,7,35,4). A simple linear addition of the IM and SM as seen in Equation 1.3, can easily result in an intolerably large treatment volume (114), and often necessitates a complete or partial reversion back to the ICRU 50 method of grouping systematic and random errors, e.g. (21)

$$\text{Margin} = 2.5\sqrt{(\Sigma_{\text{IM}}^2 + \Sigma_{\text{SM}}^2)} + 1.65\sqrt{(\sigma_{\text{IM}}^2 + \sigma_{\text{SM}}^2)}. \quad 1.4$$

ITV

The internal target volume (ITV) is a concept for the definition of an IM. The ITV encompasses the CTV throughout every phase of the respiratory cycle seen by the treatment beam (114). Creation of an ITV is a common approach (116) that comes at the problem of motion management from the tack that it is better to provide 100 % dose coverage (8,114) than worry about reducing the size of the PTV (8). The size of the ITV depends on the imaging technique used (i.e. fast CT, slow CT, breath hold CT, or 4DCT (115)).

One of the benefits of using an ITV is that it incorporates any temporal asymmetry as well as hysteresis; since all respiratory motion is encompassed, there is no error associated with time, and so all respiratory motion is treated as purely systematic error (8). However, other motion uncertainties may still be of a concern, for example the inter-fraction changes in respiration such as baseline drift (i.e. changes in the tumor's mean position over time), or anatomical variations as a direct result of treatment, like the opening of once blocked airways with tumor recession. In such cases, an additional margin can be added to the ITV (50,114).

People have used slow CT to derive an ITV (67), yet, as mentioned earlier, this cannot create a volume which encompasses the entire tumor motion (2). One solution has been to combine multiple slow CT scans (107), but delineation issues due to blurring are still problematic. Another method of obtaining an ITV entails acquiring two breath hold images: one at maximum inhale and one at maximum exhale; the two images may be simply combined using a maximum intensity projection (MIP²²) (54,1). Again, the patient must be capable of holding his or her breath, only in this case, just twice during the imaging session –treatment is performed under free breathing. Due to hysteresis, however, this composite volume may not encompass the volume occupied by the tumor throughout its entire motion (113). In addition, the maximum inhale and exhale positions in a breath hold overestimate the extent of tumor motion seen during free breathing (16,2,1). From a treatment planning point of view, the lung volume at a deep inspiration is three or four times that of a free breathing inhale (1). Attempts at capturing a more representative end inhale still result in lung volumes 25 – 46 % larger than what is seen in free breathing (64).

4DCT

In many cases, an ITV can be unreasonably large (35) and many patients are either incapable or cannot tolerate the demands of breath hold techniques. As a result, the method of 4DCT was developed. Like fast CT, 4DCT utilizes a fast tube rotation speed to minimize the amount of motion captured in each image. Like slow CT, the 4DCT technique acquires data over the full respiratory cycle to capture the full range in motion. The result is a set of temporally correlated images, like snapshots of multiple respiratory phases. Figure 1.8 compares the spatiotemporal resolution of 4DCT to non-temporally correlated CT (3DCT).

Four dimensional computed tomography identifies motion (46), the extent of that motion, and whether hysteresis is present. The true free breathing end inhale and end exhale phases may be imaged. The geometric or temporal mean position can be resolved for gated RT (34,1). All the phases of motion may be combined to create an ITV that actually encompasses the volume occupied by the tumor over the full range of motion (38,8,39,40). Also, the path of the tumor can be tracked, having implications for IMRT, IGRT, as well as modeling tumor motion (16,117). From the information provided by 4DCT, the best, most appropriate treatment for the individual patient may be ascertained (54); this could be just identifying beam angles that minimize the amount of motion from the beam's perspective (16) or determining the optimal IM for that particular tumor (54,1,16).

²² A single image that is formed from multiple images by assigning each pixel the maximum value out of all the images.

Figure 1.8: 3DCT acquisitions of a moving sphere compared to a 4DCT acquisition of the same sphere

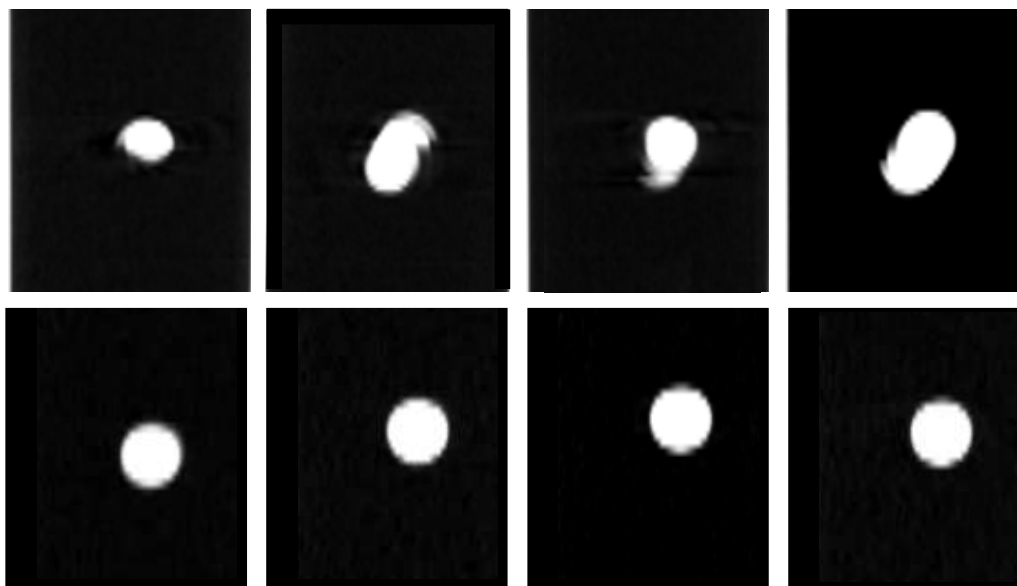


Figure caption: Top row, 3DCT acquisition (120 kVp, 400 mAs, helical with 2 mm slice thickness) of a 2.5 cm sphere undergoing motion in the SI-AP-LR direction with an amplitude of 1 cm. Bottom row, a 4DCT acquisition (also 120 kVp, 400 mAs, helical with 2 mm slice thickness) of the same sphere undergoing the same motion. The 3DCT images capture the sphere at arbitrary phases of motion, and each image suffers significant motion artifacts. The 4DCT images are much more sphere-like and capture distinct sequential phases of motion.

The size and shape of 4DCT generated margins depend on the chosen treatment option (21). Figure 1.9 shows several margin options derived from 4DCT image sets.

4DCT ITV

An ITV may be created from multiple phase images reconstructed from a single 4DCT scan –typically, ten 3D volumes are combined together (6,67). The resulting ITV is larger than a slow CT ITV by an average of 24.8 % (range of 4.4% to 72.6%) (49), and even though in general, larger margins are undesirable, this same study found the V_{20} reduced. With an accurate ITV, the only uncertainties contributing to the ITV \rightarrow PTV margin are baseline and setup errors (24,8). Compared to a target delineated with fast CT, the 4DCT ITV can reduce the PTV as much as 23 % by simply avoiding inappropriate population based margins (118). In most cases, however, the PTV obtained from a 4DCT ITV is larger, increased by an average of 3 ± 8 % in the SI direction, 7 ± 4 % in the AP direction, and 8 ± 3 % for the LR direction (8). Not insignificantly, the systematic error generated from capturing the tumor at an arbitrary phase of motion (rather than its temporal mean position) is eliminated with the 4DCT ITV –no geographic misses assures 100 % dose coverage and significantly reduces the unnecessary irradiation of normal tissues. It is the reduction of this kind of systematic error that has the greatest potential impact on the delivered dose and so too treatment outcomes (46,119).

Figure 1.9: RT margins for targets affected by respiratory motion

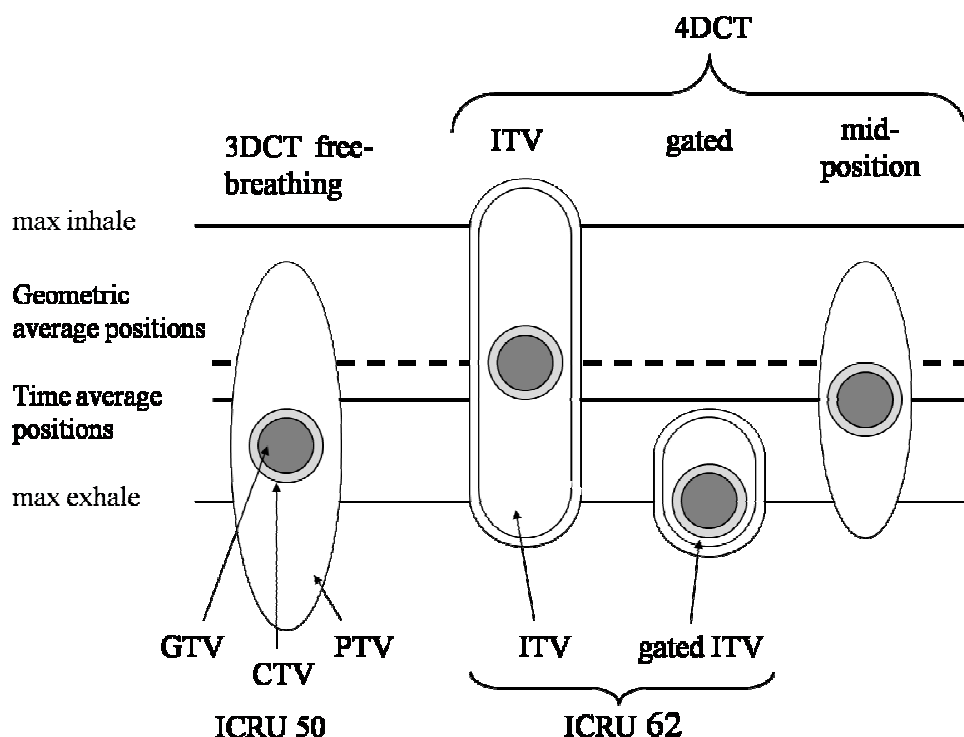


Figure caption (adapted from (8)): In the traditional 3DCT free breathing method, the tumor is imaged at a random phase of motion. Assuming it is the mean position, population-based margins are applied symmetrically—portions of the tumor's path go untreated while normal tissues are needlessly irradiated. With the 4DCT scan, all the imaged phases of motion may be combined to form an ITV that actually covers the full range of the tumor's motion. For a gated delivery, all the phases irradiated in the gate are grouped together to form a gated ITV. Finally, irradiating the temporal mean position with reduced margins can still provide effective dose coverage (8).

A typical recipe for constructing an ITV-based PTV may involve reconstructing anywhere from 8 to 25 phases from a single 4DCT acquisition (1). A maximum intensity projection (MIP) constructed from each phase image is used to contour the GTV (38,8, 120), which is then transferred to a free-breathing CT scan (to retain the relevant electron densities). An 8 mm margin is then added to form the CTV for each phase (119). These CTVs are combined into the ITV, then a uniform margin is added for setup errors and other inter-fractional uncertainties, resulting in the final PTV (119). The choice of algorithm used for adding the uniform margins can be shape sensitive (e.g. rolling ball method), and can significantly affect the resulting shape of the PTV (32). Since MIP images are not immune to motion artifacts (120), just the end inhale and end exhale phases may be chosen for the ITV, minimizing the inclusion of any residual motion artifacts. Caution should be exercised with this approach, however. In a 10 patient study by Reitzel et al., the target volume defined by the union of the two extreme CTVs only encompassed the entire area occupied by the tumor throughout its motion 93 % of the time. Due to hysteresis, the average distance the 10-phase ITV protruded outside the 2-

phase ITV was 1.7 mm (88). In addition, 4DCT ITVs can still underestimate the full range of motion if the breath period is irregular (120) or if an insufficient number of phase images are reconstructed. Either case can cause the 4DCT acquisition to miss the true turn-around points in the tumor's trajectory (121,122).

Mean Position

For a mid-ventilation RT plan, the treatment planning and delivery are the same as for fast CT, only the planning CT is derived from a single phase of the 4DCT acquisition. Since the true amplitude of motion is discernable from the 4DCT data set, the PTV can be tailored to the individual patient using a margin recipe (See Table 1.1). However, geometric coverage of the target and dosimetric coverage are not equivalent. Besides geometric placement, dosimetric coverage is also determined by the beam's characteristics: its penumbra and how it scatters in tissue (116). Because of the wide beam penumbra in lung, the tumor can still receive adequate dose coverage even though the GTV may not reside within the PTV for a fraction of the breathing cycle (102,5). In a study by Mutaf & Brinkmann, when compared to a static reference plan, a 3 cm sphere undergoing 1 cm motion was significantly underdosed with the IM = 0 mm. With full geometric coverage (i.e. IM = ITV = 5mm), the target was overdosed. For the 3 cm sphere undergoing 1 cm motion to achieve the same dosimetric coverage it received while stationary, an IM of only 1.5 mm should be applied. Mutaf and Brinkmann found that the optimal IM for adequate dosimetric coverage is linear and a function of the sphere's amplitude of motion A_0 (116)

Symmetric margins $IM = 0.37A_0 - 2.00$ mm 1.5

Asymmetric margins $IM = 0.72A_0 - 2.5$ mm 1.6

In the same study, the optimal IM for a group of patients with ~ 10 mm tumor motion was 1.3 ± 0.4 mm (based on a DVH and equivalent uniform dose analysis). The assignment of 1.5 mm IM to all patients resulted in irradiating 10 % less lung tissue on average than the ITV plans; the average target volume covered by the minimum prescription dose was 99.8%, and the absolute difference in minimum target dose compared to a static plan was 0.2% (116). Since some commercial treatment planning systems provide measures for modeling intra-fraction motion and dose calculations, optimization of the IM based on dosimetric coverage is possible (116).

The geometric mean position is relatively easy to implement (8). However, if using the time-averaged position instead, the required margin for respiratory motion can be made quite small (4), some even advocate an IM = 0 mm compensated by dose escalation (4,123,124). The random error due to respiration for both mid-ventilation techniques is identical to that of a free breathing scan since respiration is still present, but the systematic contributions are reduced to nearly zero. Even the small residual error due to hysteresis can be eliminated when using the time-weighted mean position (8). The resulting mid-ventilation PTV is, on average, 9% smaller than for conventional fast CT methods -- 12% smaller in the SI direction (8).

Gating

Gating the RT beam has been in clinical practice since 1996 (125). It is reliable (36) and well tolerated by both patients and therapists (46). The treatment beam can be gated at end inhale, end exhale, the mid-ventilation position (geometric or temporal average), or any phase of motion imaged with 4DCT (1). Ideally, the beam should be turned on and off according to a direct monitoring of the GTV, however, since this is

very difficult, either fluoroscopic observation of an implanted fiducial marker or an external respiratory signal is used (8). Even if an internal marker is chosen (46), some form of respiratory monitoring is still required to verify the consistency of the gate and that the patient is breathing normally (1).

One common strategy is to gate on the end exhale phase. The length of the gate (or time window) is typically between 20 – 65 % of the respiratory period (8,112,46). The residual motion within that window generates the IM (i.e. the gated ITV. See Figure 1.9). Using a 4DCT data set, the phases of motion corresponding to the temporal window are combined, either through a MIP or by taking the envelope of all the CTVs. Note: rather than accounting for baseline error (i.e. error in the tumor's mid position), the uncertainty of the end exhale position is used. Although the magnitude of these errors may be essentially the same (8,126), the intra-fraction variability in end expiration will have more of an impact on gating than inter-fraction baseline drift.

As with the mid-ventilation method, since the phases included in the gate are known and motion artifacts are all but eliminated with the 4DCT acquisition, the systematic errors due to respiratory motion are significantly reduced (8). The random errors included in the gated IM

$$\sigma_{IM}^2 = \sigma_{interfraction}^2 + \sigma_{intrafraction}^2 \quad 1.7$$

consist of $\sigma_{interfraction}^2$, relating to shifts in the relationship between the target and the surrogate signal (i.e. fiducial marker or external respiratory signal), estimated at be about 2 mm (21), and $\sigma_{intrafraction}^2$ which is dependant on the size of the gating window (21). Thus, the size of the IM is dependant on the gating duty cycle.

Choice of duty cycle is a compromise between minimizing the amount of motion seen in the gating window and delivering the treatment in a reasonable amount of time (46). A linear relationship exists between the amount of residual motion in the gate and the size of the IM (8). Depending on the amount of tumor movement, the duty cycle may or may not be critical to the PTV (21). For example, in a study by Vedam et al., for one patient, when the duty cycle was between 0 % and 40 %, setup errors dominated the PTV. From 40 - 60 %, both setup errors and residual motion captured within the gating window contributed significantly to the PTV, and when the duty cycle exceeded 60 %, internal motion dominated (21). To ensure the efficacy of gated RT, the number of phases included in the gate must be determined for each individual patient (24,127). First, a tolerable amount of residual motion should be determined and the IM compared to the SM. If the IM for the chosen window is less than the SM, then the gate is too small, and all that is being accomplished is extending the time it takes to deliver the treatment. To maximize the efficiency of gating, a phase interval that keeps tumor motion approximately within the setup margin is optimal (127). Therefore, gating only brings a significant advantage to patients with relatively large tumor motion (8). Otherwise, the mid-ventilation technique is preferable (128).

Reported decreases in the size of gated PTVs compared to those derived from fast CT range from 11-27 % (8,24,129), with margin reductions in the SI direction as much as 36 ± 15 % (24). With smaller margins, the volume of lung receiving a significant dose declines as well (109), and in most cases, the prolonged treatment time can be compensated for by increasing the dose delivery rate (46).

SBRT and IGRT

Stereotactic body RT (SBRT) uses multiple non-opposing beams to deliver a high dose to the target in each fraction. The number of fractions can range from 1 to 10 with 5 - 20 Gy delivered per fraction (113). Due to the large doses, a high degree of

accuracy as well as complete volumetric information of all organ motion is required (2). Individualized target volumes for SBRT derived from 4DCT phase images lead to improved normal tissue sparing, and include treatment plans based on the ITV, mid-ventilation, gating, and tumor tracking strategies (113,89,130,102,46,78).

Unlike conventional RT, the prescription dose is delivered to the 80 % isodose level, not 95 %. Correspondingly, the chosen margin recipe must be modified. For example, the margins of Eq. 1.1 become (8)

$$\text{Margin} = 2.5\Sigma + 0.8\sqrt{(\sigma^2 + \sigma_p^2)} - 0.8\sigma_p. \quad 1.8$$

High doses demand a high level of accuracy in their delivery. Inter-fraction setup errors may vary from institution to institution depending on the protocol for immobilization, localization, and equipment (113), but typically equate to SMs on the order of 1 or 2 mm (113,78). Multiple beams in each fraction means prolonged treatment times (for gated SBRT, a single fraction can last 1 to 2 hours) and intra-fractional baseline variations become more significant (i.e. 1.5 mm to 2 mm) (8,78). Also, the demand for high precision means that the dosimetric impact of tumor and normal tissue deformation (i.e. geographic misses and, to a lesser extent, small alterations in the radiological pathlength) cannot be ignored (2,89). Still, even using the ITV method, SBRT plans based on 4DCT images give clinically acceptable plans with SM = 0 mm (78).

Tumor tracking is possible (6,1), but still poses major challenges (89) including adequate motion predictive algorithms to interpolate anatomy between the discrete phases captured by the 4DCT (88). No matter how sophisticated the predictive software, movement of the treatment beam must not be dictated by the static planning images due to the variability of respiration, baseline drifts, and the many possible alterations in gross anatomy throughout the course of RT. Image guided RT (IGRT) requires not only temporally correlated images and sophisticated imaging tools, but onboard imaging devices that are registered to the treatment units (63).

The precious, patient-specific spatiotemporally resolved data available from 4DCT is helping to move RT toward true 4DRT via improving planning images, dose calculation, and onboard imaging. For treatment planning, 4DCT data sets are being used to generate patient specific motion models to predict the anatomy at arbitrary phases of motion (131), develop automated contouring algorithms (132), and automated registration of various other temporally correlated data sets (e.g. 4DMRI, 4DCBCT, 4DPET) (133). In addition, the dose delivered to moving anatomy is not equal to the same prescription delivered to stationary anatomy (70); there are significant differences (134) between dose distributions calculated on 3DCT images and those calculated on 4DCT images (e.g. 3 – 5%). Motion estimation algorithms derived from 4DCT images can be used to score the dose throughout the respiratory cycle (135) and quantify the influences of the extent and type of motion on the distribution of dose (136,132). Such enhanced imaging techniques, motion estimations, and sophisticated dosimetric information, all tailored to the patient, facilitate selection of the optimal 4DRT treatment (136). It should be noted that motion estimators and other models based on 4DCT images will contribute some error that must be accounted for in the resulting SBRT or IGRT margins (89).

IMRT

Intensity modulated RT (IMRT) can create significant normal tissue sparing by generating concave dose distributions with strong gradients to constrict the penumbra and restrain the highest doses to the PTV (6). It is often used when the margins prescribed using the conventional 3D approach are intolerably large due to extensive disease (119).

Intensity modulation also allows for dose gradients within the field defined by the primary collimators. Thus, when the target is moving and so blurring the dose gradient, unanticipated hot and cold spots may result from the interplay between the modulating beam and the moving anatomy (4,137). However, when the motion of the multileaf collimator is synchronized with the tumor motion, the beam's penumbra is reduced (49). Several groups report progress in tumor tracking with IMRT (138,139,140,141), although issues remain. Predictive algorithms are needed for the time delay between the sensing the tumor's position and the mechanical response (142). It is also vital that the breathing pattern remain consistent in order to minimize geometric errors, and rapid optimization strategies are required to compensate for any perceived variations (138). Beam hold interlocks are needed to stop irradiation if the target loses synchronization, moves outside of a predefined tolerance (49), or passes beyond the mechanical range of the MLCs (41). Gating for IMRT at a reliable phase can reduce the likelihood of such events as well as any unintended hot and cold spots (21).

Chapter 2: 4DCT Imaging

This chapter covers the basics of 4DCT imaging, beginning with the principles of CT image formation. Computed Tomography creates 3-dimensional radiological images from x-rays. Unlike simpler forms of radiological imaging, where the image is acquired in an instant and the true dimensionality of the object is reduced to a 2D projection of density, CT takes time, building up the lost dimension of depth by stepping along the object and acquiring projection images at multiple angles. Not only does CT provide depth information, but the fact that all the overlaying layers of anatomy are not superimposed atop one another gives CT improved contrast over 2D radiological images (143). For information on x-rays, their formation and interactions with matter, see Appendix B.

CT Image Formation

In a CT scan, only a thin slice of the object is examined at one time. Consider a heavily collimated pencil-shaped beam of x-rays translating across the object opposite a likewise translating detector. The detectors record the radiological image (i.e. the variation in exiting fluence ϕ across the object), called an *intensity profile* (See Figure 2.1). Then, the tube and detector are rotated in the same plane, and the slice is examined again from another angle (144). This process is repeated until a sufficient number of intensity profiles have been collected such that, by a process called *filtered backprojection*, the 2D map of linear attenuation coefficients $\mu[x,y]$ for that slice can be constructed.

Figure 2.1: The geometry of CT image acquisition

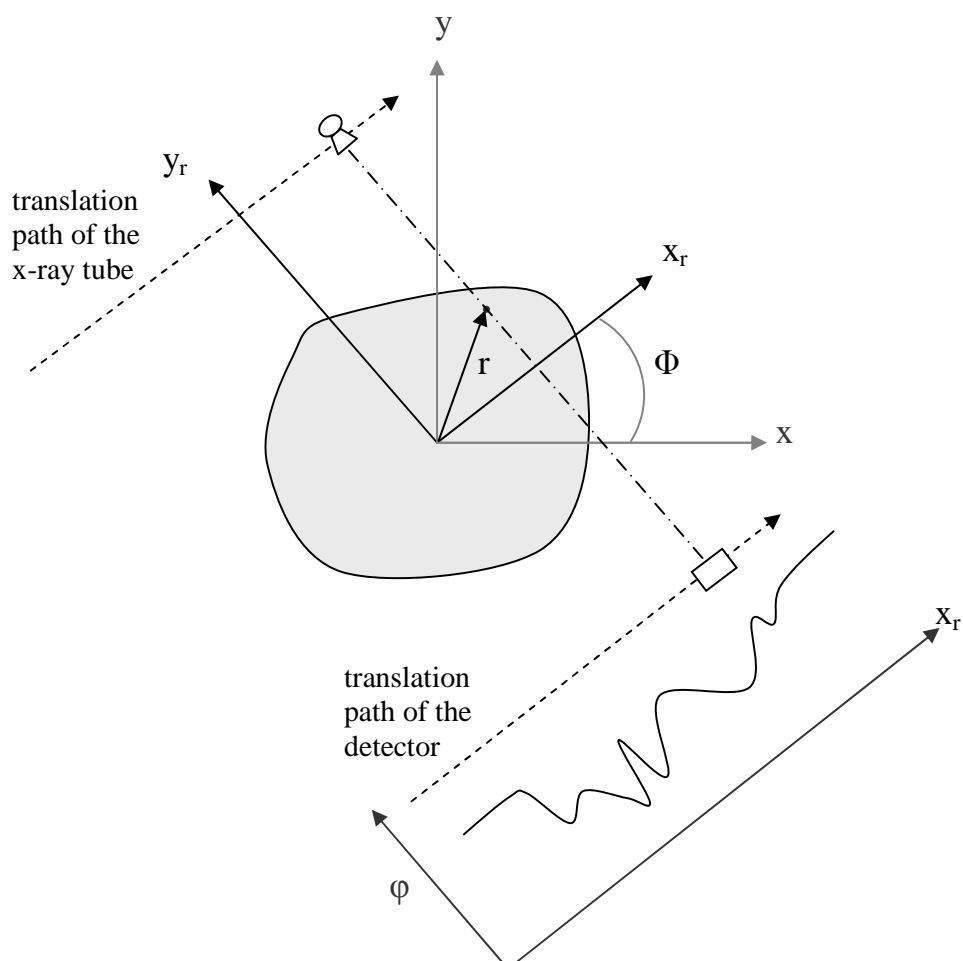


Figure caption (after (144)): The x-ray tube and detector translate across the object, and the exiting fluence is collected. Then, the tube and detector are rotated by some angle Φ with respect to the stationary reference frame of the CT scanner (x,y) . At each rotation angle, the pencil beam of photons is parallel to y_r of the rotational reference frame, and the path of the detector lies along x_r . Any point in the object may be described by vector \mathbf{r} .

The first step in creating the μ map is to convert the intensity profiles from each projection angle Φ into a plot of μ values called a *line integral* or a *projection* λ_Φ

$$\lambda_\Phi(x_r) = -\ln\left(\frac{\varphi}{\varphi_0}\right) = \int \mu[x_r, y_r] dy_r, \quad 2.1$$

where x_r and y_r refer to the cartesian coordinates of a rotating reference frame depicted in Figure 2.1 (144). For each x_r value across the object, the projection represents the line integral of all μ values along the path of the x-rays through the object, from the source to the detector. Since this path is always parallel to y_r , the 2D information of $\mu[x_r, y_r]$ has

been reduced to 1D information about just x_r . The lost y_r information must then be reconstructed. This is accomplished by simply reassigning all the y_r values along the path of the x-rays to $\lambda_\Phi(x_r)$, that is

$$g_\Phi[x_r, y_r] = \lambda_\Phi(x_r). \quad 2.2$$

This process is called backprojection, and $g_\Phi[x_r, y_r]$ is the backprojected image at acquisition angle Φ . The resulting 2D image would look something like a barcode, and not particularly representative of the object's true μ distribution. The solution is to build up the image by acquiring multiple projections from many different angles. An approximate map of $\mu[x, y]$ is then reconstructed by summing all the backprojections from each projection angle Φ

$$b[x, y] = \sum g_\Phi[x_r, y_r], \quad 2.3$$

creating an image similar to what is depicted in Figure 2.2.

Figure 2.2: A backprojection summation image

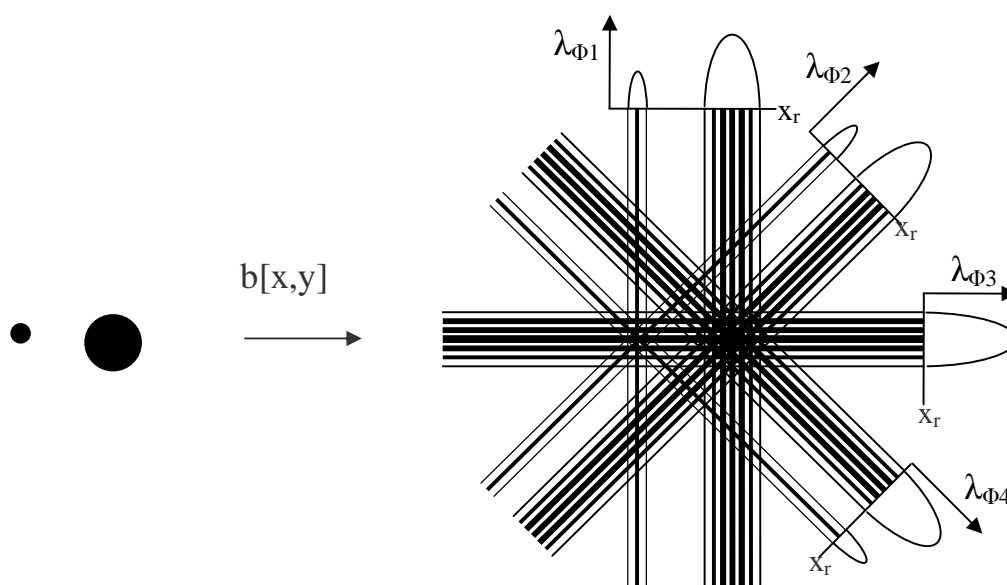


Figure caption (after (144)): The process of backprojection and summation transforms a couple of circles into an image of two radially diverging patterns. The plots of $\lambda_{\Phi_1}, \lambda_{\Phi_2}, \dots$ etc. are the line integrals taken at different acquisition angles Φ_1, Φ_2, \dots . If a fifth projection were acquired directly opposite λ_{Φ_1} , it would contribute no new information to the data set.

It is obvious that the summation of backprojections blurs the μ map. This blurring can be described by a point spread function psf , that is

$$b[x, y] = \mu[x, y] ** psf \quad 2.4$$

(where $**$ is a 2-dimensional convolution) which, in turn, can be compensated for with a filter function. The psf may be calculated from the backprojection and summation of an

impulse object, and is equal to $1/\pi r$, where r is the length of vector \mathbf{r} in Figure 2.1. Since convolution is equivalent to multiplication in Fourier space, Equation 2.4 can also be expressed as

$$B[\gamma, \zeta] = M[\gamma, \zeta] \cdot \frac{1}{\pi\rho}, \quad 2.5$$

where γ and ζ are the Fourier space coordinates associated with x and y , respectively, and ρ is the Fourier transform of r . It seems obvious to define the filter function in Fourier space, FF , as the inverse of the Fourier transform of the *psf* $1/PSF$, where $PSF = 1/\pi\rho$, so that

$$B[\gamma, \zeta] \cdot FF = M[\gamma, \zeta] \cdot \frac{1}{\pi\rho} \cdot \pi\rho = M[\gamma, \zeta]. \quad 2.6$$

However, a perfect filter is not needed. There is a limit to the required resolution, and such a filter will only serve to amplify the noise in the image. To address this, an apodizing function $A(\rho)$ minimizes the high frequency contributions of the filter function. The new filter function $Q(\rho)$

$$Q(\rho) = \pi\rho \cdot A(\rho), \quad 2.7$$

is such that

$$B[\gamma, \zeta] \cdot Q(\rho) = M[\gamma, \zeta] \cdot \frac{1}{\pi\rho} \cdot \pi\rho \cdot A(\rho) = M[\gamma, \zeta] \cdot A(\rho). \quad 2.8$$

From Equation 2.8, it can be seen that the point spread function of the backprojected summation filtered CT image is the inverse Fourier transform of the apodizing function. (Since backprojection, summation, and filtering are all linear operations, typically, the filtering is done prior to backprojection, so that the convolution is only over a single dimension, (i.e. $\lambda_{\Phi}(\mathbf{x}_r) = \lambda_{\Phi}(\mathbf{x}_r) * q(\mathbf{x}_r)$ (144).

The Sinogram

A convenient method of depicting the raw data of a CT acquisition is a *sinogram*. Instead of having numerous 2D plots of $\lambda_{\Phi}(\mathbf{x}_r)$, one for each projection angle, a sinogram plots all the line integrals for all angles on a single cartesian plot $\lambda_{\Phi}(\Phi, \mathbf{x}_r)$. On the ordinate axis are all the projection angles, from 0 to 360, and on the abscissa are the \mathbf{x}_r values covering the entire imaging field. The value of each line integral $\lambda_{\Phi}(\Phi, \mathbf{x}_r)$ is proportional to the intensity at point (Φ, \mathbf{x}_r) in the sinogram (145). For all line integrals λ_{Φ} which pass through point \mathbf{r} , the \mathbf{x}_r value equals the projection of \mathbf{r} onto the \mathbf{x}_r -axis, that is $x_r = r \cos(\theta - \Phi)$ (See Figure 2.3a). Thus, for a single, uniform density, point-like object in an empty field, the sinogram is a simple cosine curve (see Figure 2.3b).

Figure 2.3: Geometry of a sinogram

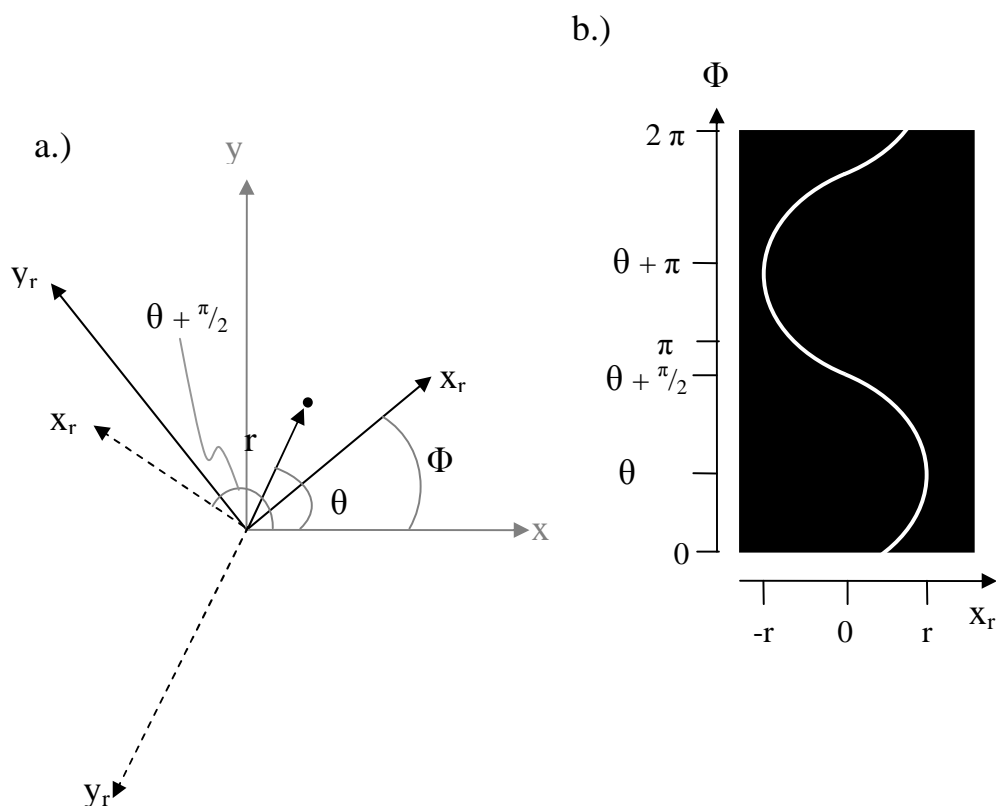


Figure caption: A point-like object located at \mathbf{r} , traces out a sine wave in sinogram space. The distance of the point from the center of rotation is the projection of r onto the x_r -axis. In the rotational reference frame, that is $r \cos(\Phi - \theta)$. When $\Phi = \theta$, $x_r = r$, when $\Phi = \theta + \pi/2$, $x_r = 0$, and at $\Phi = \theta + \pi$, $x_r = -r$ (144). The intensity of the sinogram is proportional to the line integral at each projection angle Φ (145): for empty space, $\phi = \phi_0$ appears black, whereas when x-rays have passed through the point object, $\phi < \phi_0$ appears white here. With real data, the sinogram contains many such waveforms, all at different phases and of different intensities (i.e. shades of grey).

Only projection angles $\Phi=0$ to 180° are necessary to acquire the complete μ map, since any two projections 180° apart will contain data from x-rays that have traversed the same path through the object, just heading in opposite directions (143).

Acquisition Geometry

The discussion up to this point has entailed a pencil-like beam and a single, perhaps well collimated detector for an assumed narrow beam geometry. However, the Philips Big Bore CT scanner does not follow this geometry. The tube does not translate across the object as in Figure 2.1, but rotates around it. The detector rotates with the tube, directly opposite of it, and in order to expedite the imaging process, the x-rays are collimated into a fan shape, wide enough to image the entire breath of the object at once. The detector is actually a bank of detectors spanning the arc of the fanned-out x-ray beam (143). See Figure 2.4.

Figure 2.4: A fan beam and an arced detector bank

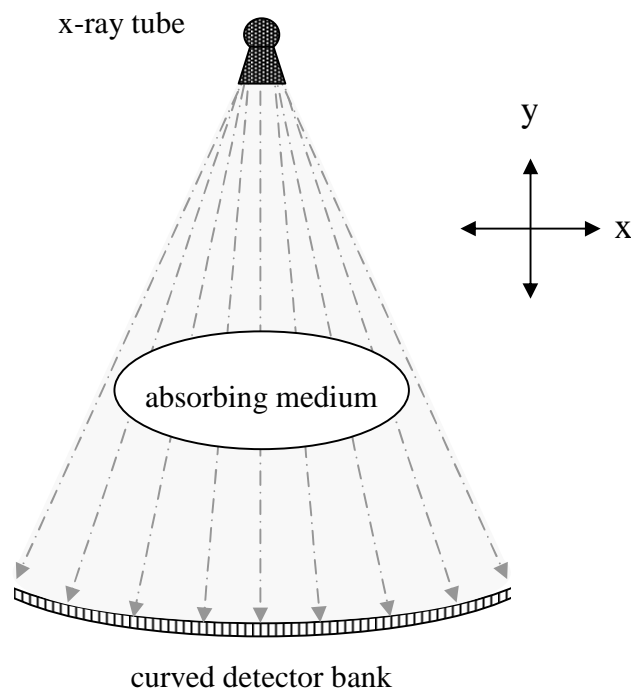


Figure caption: In a fan beam geometry, the source is collimated wide enough to allow a fan shaped beam of x-rays to reach the detectors. The span of detectors is wide enough to collect data over the entire beam.

Yet with a fanned-out beam, the line integrals through the object diverge, and the method of reconstruction just discussed no longer applies. There are two solutions, however. The fan data can be re-ordered into a parallel geometry or the backprojection itself can be weighted to compensate for the divergent rays through the object (146). As a consequence of fan beam geometry, more angular projections are necessary to acquire the same amount of data. Figure 2.5 depicts sinograms of data collected with fan beam geometry. In parallel beam geometry, the data collected over 180° fills a rectangular region of sinogram space. However, the data collected with a fan beam over 180° forms a parallelogram in sinogram space, leaving a portion of the required data unfilled (Figure 2.5a). In order to adequately reconstruct a μ map for that slice, the acquisition must be extended by $1/2$ the fan angle on both sides (Figure 2.5b). Thus, when using a fan shaped beam, the minimum amount of projection data is now 180° plus the fan angle (146).

Figure 2.5: Sinogram data for a fan beam

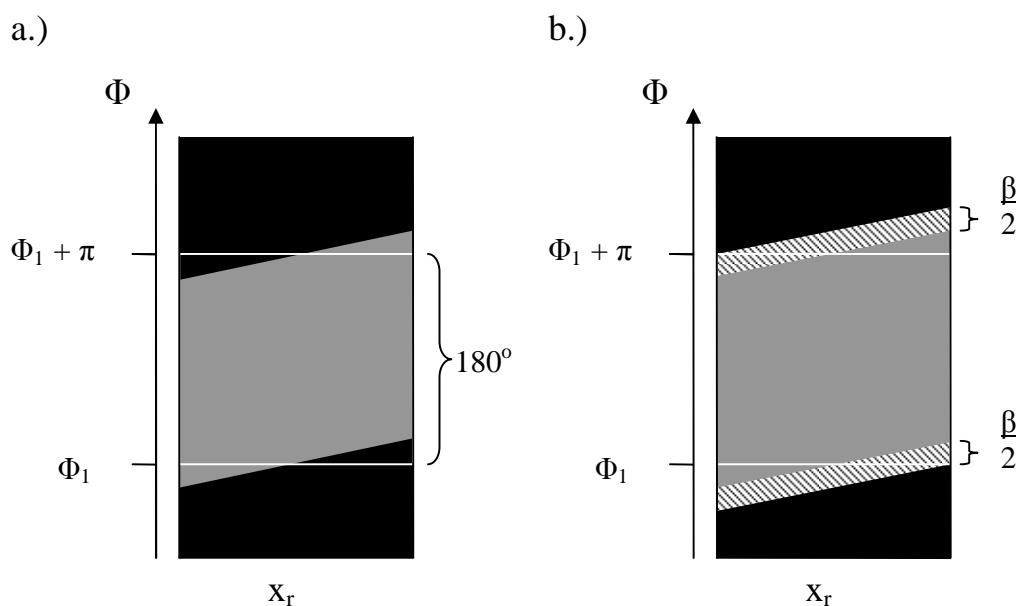


Figure caption (after (146)) In a parallel beam geometry, acquiring all of x_r at each Φ fills up a rectangular region of sinogram space. With a fan beam, every splaying ray through the object is its own little parallel beam geometry described by some Φ and x_r . When these individual parallel beam geometries are mapped onto sinogram space, they fill up a parallelogram shaped region. Figure (a) shows 180° degrees of data collected between Φ_1 and $\Phi_1 + \pi$ with a fan beam (grey area). Portions of the sinogram space required for reconstruction are missing. Figure (b) shows the extra data (hatched region) that must be acquired to fill sinogram space for reconstruction. The extra projection angles each equal one half of the fan beam angle β . Thus, the minimum amount of angular data that must be acquired for a complete image is 180° plus the fan angle.

So far, only the acquisition of a single 2D slice of CT data has been addressed. In order to build up a 3D volume, more slices are necessary. There are two ways of going about acquiring more slices. One is to acquire a single slice at a time, stepping the patient forward to the next slice location in between turning the tube on and off. In this method, called *axial* scanning, the patient is stationary during each image acquisition. The other method is to turn the tube on only once, and slowly move the patient through the imaging plane. In this method, the tube traces out a helical path around the patient (see Figure 2.6), and so is called *helical* or *spiral* scanning. The resulting projections are no longer in a planar geometry (143). The speed at which the table slowly advances through the imaging plane relative to the width of the detectors is called the *pitch* p

$$p = (T_m / T_s) t_r, \quad 2.9$$

where T_m is the speed of the table movement, t_r is the time it takes the x-ray tube to complete one full rotation, and T_s is the total collimated width of the beam (147, 148). The collimated width of the beam, for multislice CT scanners is defined as the total number of detectors illuminated divided by the width of each detector (i.e. the average

collimated width of a detector) (148).²³ The pitch dictates whether there will be overlapping information or gaps in the reconstructed volume (143).

Figure 2.6: Path of a helical CT scan

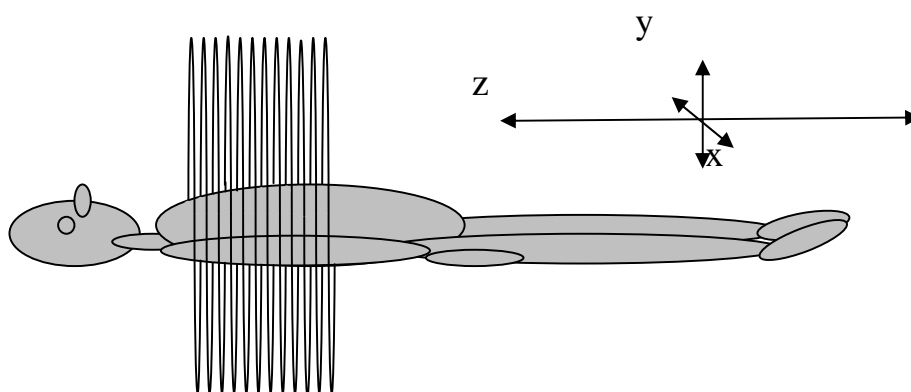


Figure Caption: The tube and detector rotate in the scanning plane as the patient passes through the plane continuously. The result is a non-planar geometry, however, slices may be reconstructed at any point along the patient's longitudinal axis. These slices may be overlapping or gaps in the resulting volume are also possible (143).

In order to collect even more data with every rotation of the tube, the beam of x-rays is allowed to fan out along the longitudinal axis of the patient as well, creating a cone-shaped beam. The detector bank is extended by adding additional rows to cover the full area exposed to the beam. The more detector rows, the fewer tube rotations are needed to cover the region of interest, dramatically reducing acquisition times (13) and lessening the demand on the x-ray tube (147). The Philips Big Bore has 24 detector rows, allowing up to 16 slices of data to be acquired per tube rotation (31). See Figure 2.7. Now, however, not only are the line integrals through the object diverging in the imaging plane, they are also diverging perpendicular to this, along the axis of rotation (149). See Figure 2.8. Many schemes exist to compensate for these angled trajectories, involving interpolation and weighting similar to those for fan-beam geometry (147, 149).

²³ Definitions of pitch vary. The definition presented here is the one adopted by the International Electrotechnical Commission (IEC) (138)

Figure 2.7: Cone beam geometry

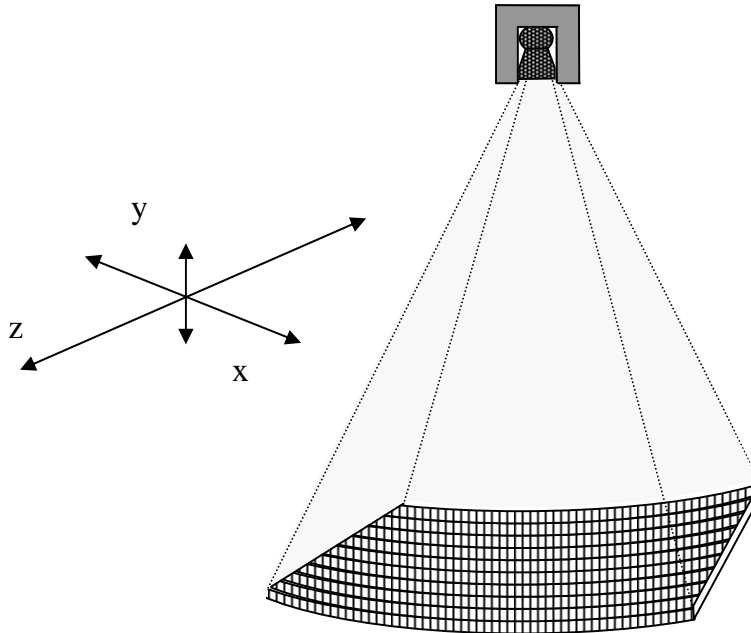


Figure caption: To increase the data acquisition of every rotation of the x-ray tube, the source is collimated into a cone and the detector bank is extended in the z-axis direction as well.

Figure 2.8: The nutating imaging planes of cone beam geometry

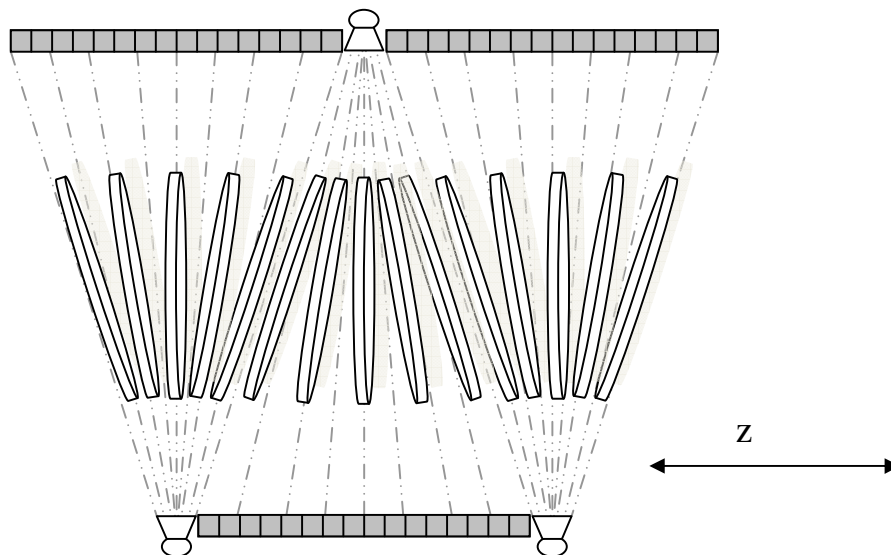


Figure caption (after (147)): As the cone of x-rays and the detector bank expand in the z-axis direction, so the imaging planes become more skewed. The angle of the plane depends on tube position (i.e. Φ) (149).

All such schemes, however, produce a radial artifact which becomes increasingly severe as the span of the beam's cone increases to encompass more and more detector rows (147, 148). Philips' solution, instead, has been to develop a true cone-beam reconstruction algorithm (COBRA) (149) based on the n-Pi method algorithm (149). The 'n-Pi' is a variant of the 'Pi' method, which just refers to a sufficiency condition that any point of the object being imaged must be illuminated by the beam for at least Pi rotations of the tube (150). In the cone-beam geometry, λ_ϕ does not provide μ maps of parallel slices since all the line integrals through the object diverge (150). Thus, rather than a direct reconstruction, all Pi-method algorithms introduce an intermediate step of calculating the first derivative of λ_ϕ with respect to the distance between the diverging image plane and isocenter, which can be found from these angled projections. Reconstruction then becomes a problem of finding the $\mu[x,y]$ of each slice from these derivatives (150). Philips' COBRA algorithm is proprietary. It should be noted, also, that full use of all 24 rows of the detector bank and the n-Pi method can only be applied to helical scanning (147). If the entire bank were utilized when the table is stationary, as when performing an axial scan, the peripheral rows of the detector bank would not collect any data about that slice location. See Figure 2.9. For axial scans, interpolation, averaging, and weighting reconstruction schemes must be used (147).

Figure 2.9: Geometry of an axial scan using the full detector bank

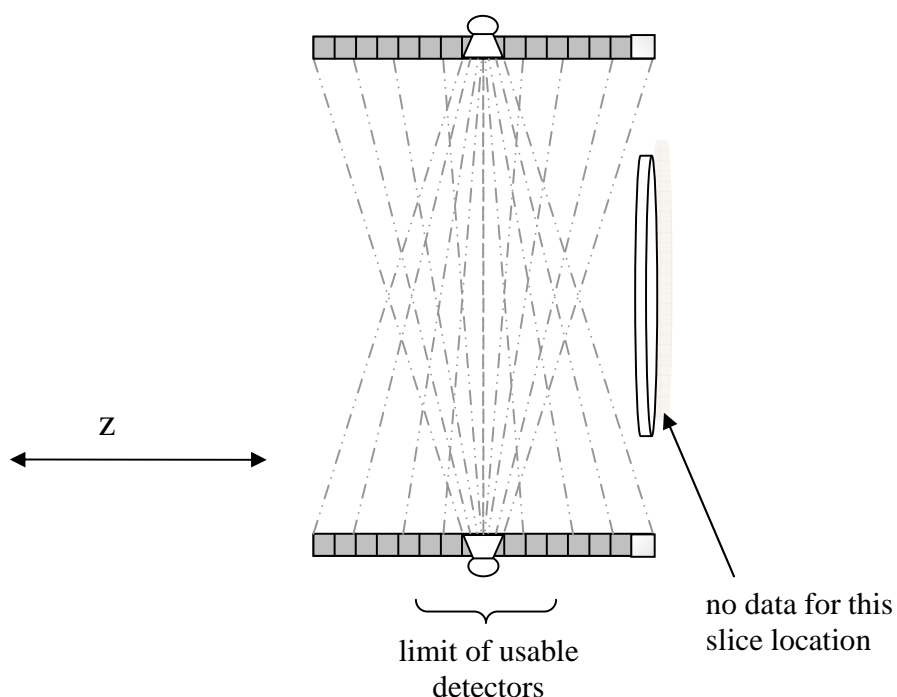


Figure caption (after (147)): If the full detector bank were utilized for axial scanning, the end detectors would contain no information about their slice location. Thus, for axial scanning, the number of reconstructed slices per tube rotation is limited.

Artifacts in CT

One of the several artifacts that are inherent to CT image reconstruction is the partial volume effect (151). The fluence collected by each detector is a single value that is assigned to its entire area. Although in CT, detector size does not necessarily dictate

the voxel size ('voxel' being a 3D pixel, (x,y) dimensions in the imaging plane and (z) along the longitudinal axis of the patient), the uniform distribution of a single CT# for each voxel is analogous. Any pattern of fluence variation smaller than a voxel will be lost. A common occurrence is when a physical object protrudes part way into a voxel, but not enough to fill it. The resulting density of the voxel is a weighted average (by spatial extent) of the object's density and the background's density. This causes high density objects to appear fuzzy as their peripheral extent inevitably shares some portion of each voxel with the background (101,148). The partial volume effect can also be caused by motion if an object occupies part or all of a voxel for only a portion of the time required for imaging. The resulting value of the voxel will be a spatiotemporally weighted average object and surrounding background densities.

Motion Artifacts

To understand the nature of motion artifacts (152) in CT imaging, consider an empty field with only a single point-like object located at $\mathbf{r} = (r\cos\theta, r\sin\theta)$. See Figure 2.10. The location of the x-ray tube, or more precisely, the apparent origin of the x-rays (i.e. the effective focal spot) within the non-rotating reference frame is

$$\mathbf{R}(\Phi) = (-R \cos \Phi, R \sin \Phi), \quad 2.10$$

where R is the distance between the focal spot and the axis of its rotation, and here again, Φ is the projection angle. Only those backprojections passing through point \mathbf{r} have a non-zero value, say equal to one; that is $\lambda_\Phi(x_r) = g_\Phi(x_r, y_r) = 1$ at $x_r = r\cos\Phi$, and equal to 0 everywhere else. Thus, for each projection angle, the backprojection $g_\Phi(x_r, y_r)$ can be thought of as a subset of points lying along the line $y_\Phi = m x + b$, passing through points $\mathbf{R}(\Phi)$ and \mathbf{r} , where

$$m = \frac{(r \sin \theta - R \cos \Phi)}{(r \cos \theta - R \sin \Phi)} \quad 2.11$$

and

$$b = \frac{(R \sin \Phi r \cos \theta + R \cos \Phi r \sin \theta)}{(r \cos \theta + R \sin \Phi)}. \quad 2.12$$

Figure 2.10: Backprojections through a stationary point

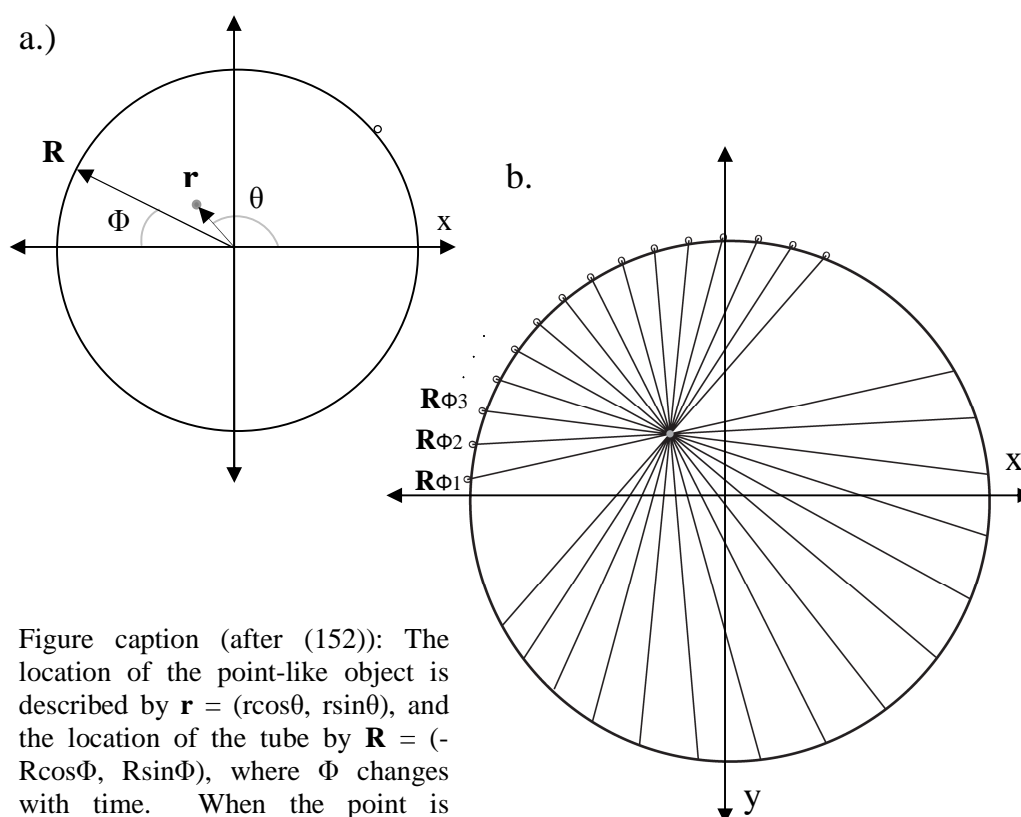


Figure caption (after (152)): The location of the point-like object is described by $\mathbf{r} = (r\cos\theta, r\sin\theta)$, and the location of the tube by $\mathbf{R} = (-R\cos\Phi, R\sin\Phi)$, where Φ changes with time. When the point is stationary, all the lines $y_\Phi = m x + b$ connecting the point-like object and the source intersect at \mathbf{r} .

As seen earlier, the image of this point-like object results from the sum of all the backprojections as they build up density at the intersection of the lines y_Φ passing through \mathbf{r} . The coordinates of the point of intersection p of any two backprojections y_{Φ_1} and y_{Φ_2} are

$$x_p = (b_2 - b_1) / (m_1 - m_2) \quad 2.13$$

and

$$y_p = (m_1 b_2 - m_2 b_1) / (m_1 - m_2). \quad 2.14$$

Without plugging any values into Equations 2.13 and 2.14, we know by definition that all backprojections intersect at \mathbf{r} , i.e. $(x_p, y_p) = \mathbf{r} = (r\cos\theta, r\sin\theta)$. However, if we now look at the intersection of backprojections when the point-like object is moving during image acquisition, i.e. $\mathbf{r}(\mathbf{r}(t), \theta(t))$, as in Figure 2.11, the build up of densities no longer converges on a single point. Instead, it is smeared out in space.

Figure 2.11: Backprojections through a moving point

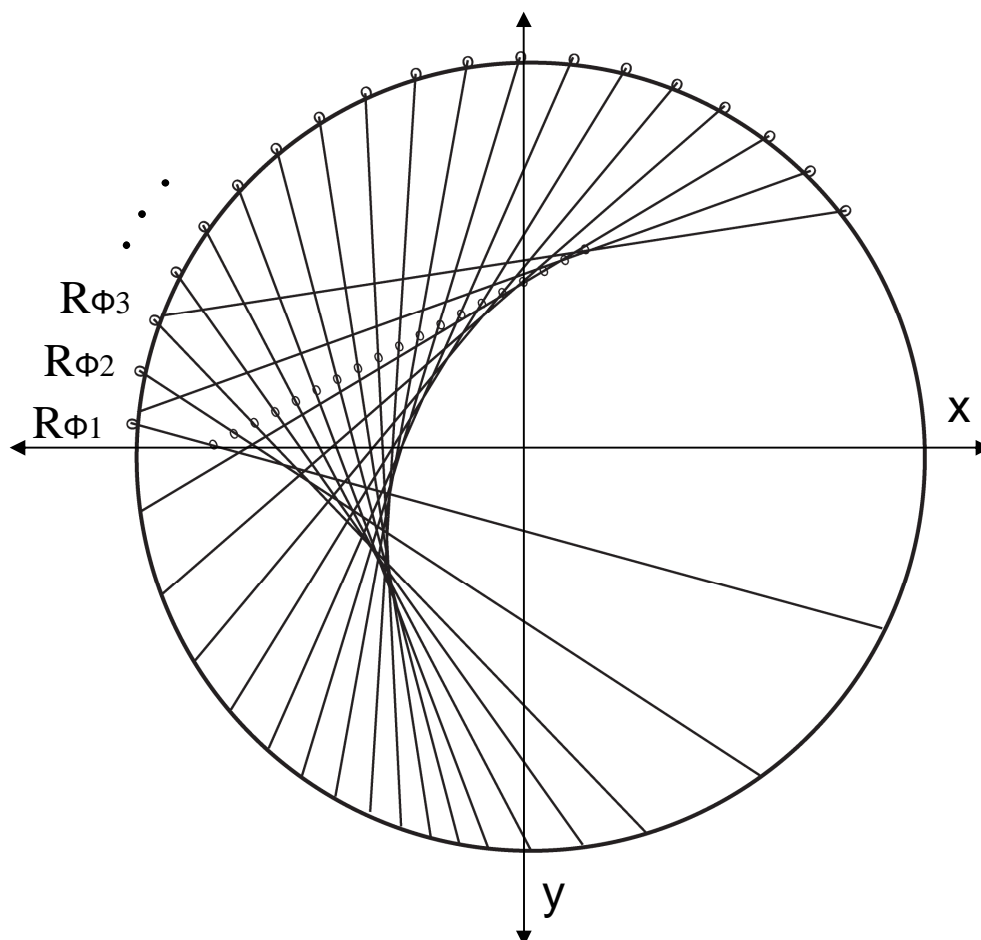


Figure caption (after (152)): When the point is moving (i.e. \mathbf{r} is a function of time: $\mathbf{r}(r(t),\theta(t))$), the lines connecting the point-like object and the source no longer intersect at a single point.

For simplicity, consider that the point-like object is constrained to motion along the x-axis of the non-rotational reference frame, such that $\mathbf{r}(t) = \mathbf{r}(r(t),\theta(t))$ reduces to just $\mathbf{r}(r(t))$. For the sake of relevance to respiratory motion, let's say that the point-like object also oscillates within its trajectory about the axis of rotation with frequency ω_r . Then

$$\mathbf{r}(t) = r\cos(\zeta + \omega_r t), \quad 2.15$$

where ζ is the initial phase of motion. The x-ray source is also rotating with a frequency of ω so that

$$\mathbf{R}(\Phi(t)) = (-R\cos(\Phi_0 + \omega t), R\sin(\Phi_0 + \omega t)). \quad 2.16$$

where Φ_0 is the initial phase of motion (i.e. the first projection angle). The intersection of any two consecutive backprojections described by lines $y_{\Phi_1} = y_{\Phi}(t_1)$ and $y_{\Phi_2} = y_{\Phi}(t_2)$ is $p = (x_p(t_1, t_2), y_p(t_1, t_2))$, where now

$$x_p = (b_2 - b_1)/(m_1 - m_2) =$$

$$\frac{r \cos(\zeta + \omega_r t_2) \sin(\Phi_0 + \omega t_2) [r \cos(\zeta + \omega_r t_1) + R \cos(\Phi_0 + \omega t_1)] - r \cos(\zeta + \omega_r t_1) \sin(\Phi_0 + \omega t_1) [r \cos(\zeta + \omega_r t_2) + R \cos(\Phi_0 + \omega t_2)]}{\sin(\Phi_0 + \omega t_2) [r \cos(\zeta + \omega_r t_1) + R \cos(\Phi_0 + \omega t_1)] - \sin(\Phi_0 + \omega t_1) [r \cos(\zeta + \omega_r t_2) + R \cos(\Phi_0 + \omega t_2)]}$$

2.17

and

$$y_p = (m_1 b_2 - m_2 b_1)/(m_1 - m_2) =$$

$$\frac{R \sin(\Phi_0 + \omega t_1) \sin(\sin \Phi_0 + \omega t_2) [r \cos(\zeta + \omega_r t_1) - r \cos(\zeta + \omega_r t_2)]}{\sin(\Phi_0 + \omega t_2) [r \cos(\zeta + \omega_r t_1) + R \cos(\Phi_0 + \omega t_1)] - \sin(\Phi_0 + \omega t_1) [r \cos(\zeta + \omega_r t_2) + R \cos(\Phi_0 + \omega t_2)]}$$

2.18

The fact that Equation 2.18 does not equal zero confirms what is seen qualitatively in Figure 2.11 –when the object is moving during data acquisition, density values are assigned to locations never occupied by the object. Also, from these two equations, the functional parameters of the motion artifact are revealed:

- R –the radius of the tube's rotation
- r – the amplitude of the object's oscillation
- ω –the rotational frequency of the tube
- Φ_0 –the initial acquisition angle of the tube
- ω_r –the frequency of the object's oscillation
- ζ –the initial phase of the object's motion.

Since, in general, $\mathbf{r}(t) = \mathbf{r}(r(t), \theta(t))$ and $x_r = r \cos(\theta(t) - \Phi(t))$, the phase relationship between θ and Φ also affects the nature of the artifacts.

Figure 2.12 (33) shows the sinogram (a) and a few backprojections (b) of a sphere undergoing the same motion described above. For illustrative purposes, the amplitude of motion r is much greater than the radius of the sphere, and its frequency of oscillation is half that of the tube's rotation (i.e. it travels once across the path from $-r$ to r in one full rotation of the tube). In Figure 2.12c, the summed backprojected image reveals that not only is the sphere's density assigned to locations not representative of its true locations along its path, the blur of the summed backprojection beyond the boundaries of the object (i.e. the density assigned to empty space) is no longer radially symmetric. Application of the filter function, designed to remove this radial blur, only serves to enhance the artifact and the asymmetry of empty space (33,2).

Now, imagine the sphere located at the center of the imaging field, but undergoing motion perpendicular to the imaging plane. Its sinogram is depicted in Figure 2.13a (33). As its cross section changes in the imaging plane, the width and intensity of the sinogram changes as a function of projection angle. The curve of the sinogram, however, is similar to that of a stationary object, but due to this angular dependence of the sinogram intensity, the blur of the summed backprojected image is also not symmetric (33,2).

Figure 2.12: The sinogram, summed backprojection, and filtered summed backprojection for a sphere oscillating about the origin in the imaging plane

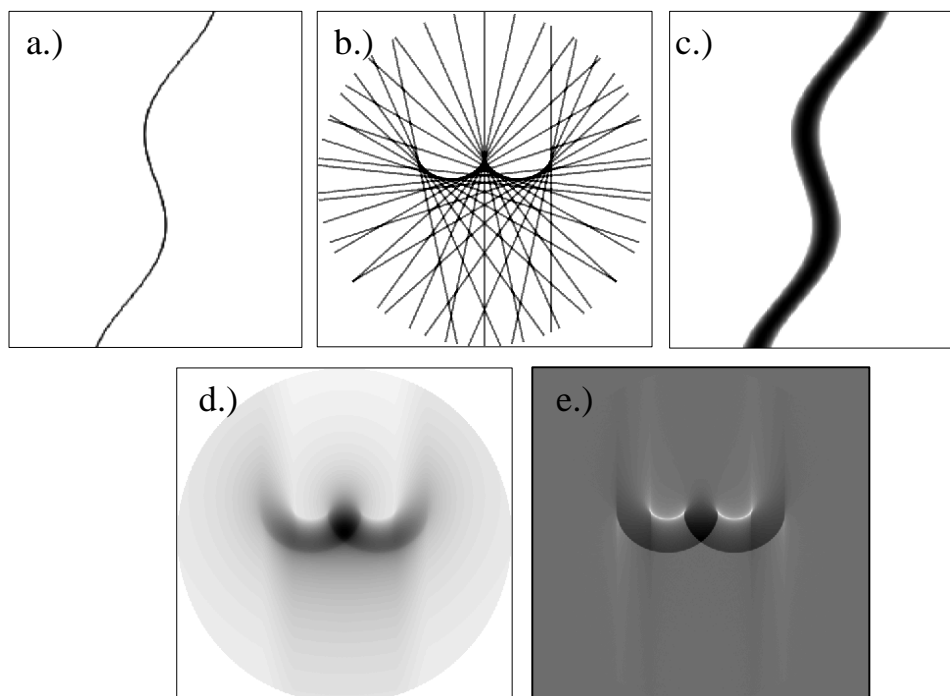


Figure caption (33): a.) The sinogram of a point-like object moving along the x-axis of the non-rotational reference frame drifts (here the color assignment is: object black: background white). b.) Several backprojections of the point-like object show the build up of density orthogonal to the object's motion. c.) The sinogram of a sphere moving with the same motion; the sphere consists of many point-like objects. d.) The summed backprojection of the moving sphere does not resemble the circle due to the misassignment of density. e.) The filtered summed backprojection accentuates this misassignment.

Figure 2.13: The sinogram, summed backprojection, and filtered summed backprojection of a sphere oscillating about the origin perpendicular to the imaging plane

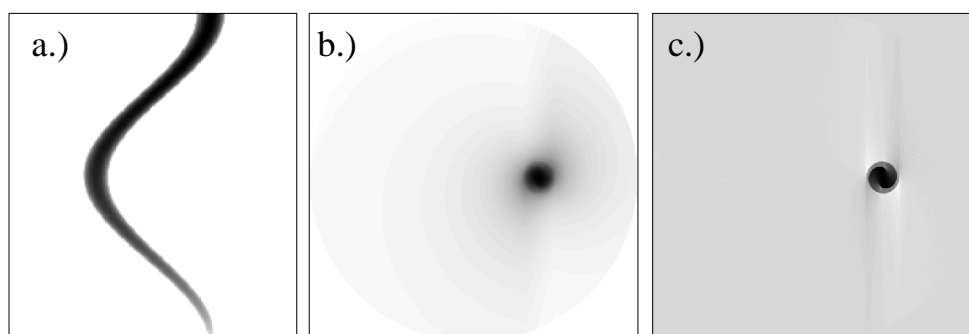


Figure caption (33) a.) The sinogram of a sphere moving orthogonal to the imaging plane diminishes as the sphere moves out of the imaging plane, presenting a smaller and smaller cross section. b.) The summed backprojection of the moving sphere is circular, however, the densities both inside the boundary of the sphere and outside of it are affected. c.) The filtered summed backprojection accentuates the artifacts; the densities spiral out from the center of the sphere, and again, the density of the background is no longer radially symmetric.

Although not as extreme as the in-plane motion case, this asymmetry is, again, accentuated by the filter function designed for stationary objects. The result is an inhomogeneity of densities both within and exterior to the sphere (33). When helical scanning is employed, if the motion of the sphere along the longitudinal axis is with the advancement of the imaging plane, the sphere's cross section remains in the imaging plane longer, resulting in an apparent elongation of the sphere. If instead, the sphere moves against the advancement of the imaging plane, its cross section leaves the plane too early, and the sphere is imaged as squashed in the z-direction (2).

For in-plane motion, increasing the amplitude of motion will likewise increase the extent of the artifact, and for motion orthogonal to the imaging plane, densities decrease. Different combinations of initial phase of motion and tube rotation alter both the radial and angular allocation of the object's density in sinogram space. When all else is the same, even changing the orientation of motion produces new artifacts (33). Three-dimensional motion results in a combination of these artifacts, altering the width, intensity, and position of the sinogram intensities (33) (see Figure 2.14). In general, the physiological motion of breathing and the respiratory induced tumor motion are three dimensional, and may well include rotation, deformation (153), and hysteresis (23). In addition, the phase relationship between the respiratory induced motion and the tube rotation will be random and potentially dynamic. Thus, the artifacts seen clinically are unpredictable and unique. Any pause in the patient's breathing, however, say at end inhale or end exhale, will lessen the motion of the tumor and allow the backprojections to build-up more localized densities (33), and the faster the x-ray tube can rotate around and collect the data, the smaller the motion artifact will appear (67).

Figure 2.14 : The sinogram, summed backprojection, and filtered summed backprojection of a sphere oscillating both perpendicular to the imaging plane and in it.

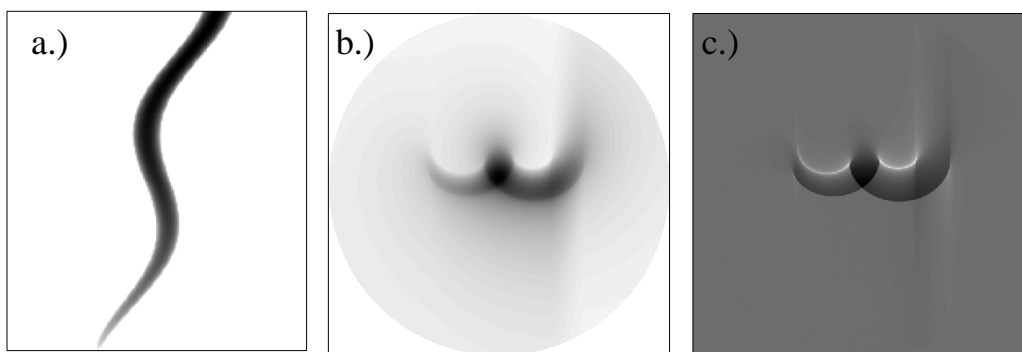


Figure caption (after (33)): A sphere moving both orthogonal to the imaging plane and across it shows features of both types of imaging artifacts. a.) the sinogram both drifts and fades. b.) The summed backprojection resembles that of the sphere moving across the imaging plane, yet the symmetry is diminished by the changing cross section seen by the imaging plane. c.) Again, the filtered summed backprojection accentuates the artifacts.

4DCT techniques

The method of 4DCT addresses respiratory motion because, unlike other physiological motion affecting RT such as the filling/emptying of stomach and bladder, or the constant unglugulation of the bowels, breathing is fairly periodic, and therefore, the motion caused by respiration is somewhat predictable. This is the foundation of 4DCT.

Four dimensional computed tomography works on the presumption that, for any given phase of motion, an object of interest will occupy the same volume with the same physical relationship to the surrounding anatomy during each respiratory cycle. When this is true, gating the x-ray beam by turning the tube on and off (within a sufficiently short temporal window) captures a single reproducible phase of motion with each breath. Another 4DCT technique entails collecting data on all phases of motion into the sinogram of each slice, then only reconstructing images for the desired phase or phases. This process is called *sorting*. Both methods require a respiratory signal to inform the CT scanner and reconstructive software of the various phases of motion (13,154,45,31).

There are four distinct 4DCT techniques: *prospective axial*, *prospective spiral*, *retrospective axial*, and *retrospective spiral*. *Axial* refers to the scanning techniques in which the patient bed remains stationary throughout the x-ray tube's rotation and the patient table is advanced to the next image location between image acquisitions. *Spiral* scanning refers to the helical scanning technique, where the patient bed is moving continuously throughout image acquisition.

With *prospective axial*, the patient is asked, or sometimes physically manipulated (113) to hold his or her breath during an axial acquisition (38). This arrests respiratory motion for the duration of the image acquisition. The process is then repeated for each slice of the desired volume. This technique, of course, does not halt the motion associated with the cardiac beat, which will contribute motion artifacts to the final image in the vicinity of the heart. Also, each patient's ability to hold the position as well as reproduce it for the numerous slice locations required for adequate coverage of the target affects the quality of the resulting 4DCT volume. The prospective axial technique gives a single phase of motion corresponding to the position of the breathhold (38,49).

For situations where breathhold may not be tolerated (38) and/or manipulation is either unavailable or also intolerable, *prospective spiral* allows the patient to breath normally. Instead of arresting the motion, this technique relies on gating the x-ray beam, acquiring images only during a specific and predetermined phase of motion (38), typically, but not limited to the end inhale or exhale position. A respiratory monitoring system is required to signal the scanner when the chosen phase has been obtained by the patient (38). This technique can also be used during a breathhold as well—in this case, the distinguishing aspect from *prospective axial* being that the entire volume is collected during a single breathhold. The breathhold phase has particular importance for situations where an inflated lung is desirable for creating a buffer between the target and critical structures during RT (e.g. protecting the heart during treatment of the breast (38)). The choice of using either the prospective axial or prospective spiral can depend on the axial dimensions of the required imaged volume and the patient's ability to hold his or her breath.

For both types of prospective 4DCT scans, the desired phase of motion must be determined before data acquisition. With *Retrospective axial*, the phases imaged are not predetermined. The data for all phases of motion are collected continuously at each slice location (2). The duration that the x-ray tube must rotate about the same slice location to insure that all phases are captured must equal or exceed one full breath period plus the time it takes to acquire a single image (13,154,155). This continuous irradiation of each slice location in excess of a full breath period can increase the patient dose by an order of magnitude if no other parameters are altered to mitigate the exposure (13).

Retrospective spiral also acquires a large amount of data to reconstruct an arbitrary phase or multiple phases (38). The patient table moves at sufficiently low pitch to ensure that, like *retrospective axial*, motion over the entire respiratory cycle is captured at each slice location (38). Both *retrospective axial* and *retrospective spiral*

require a respiratory signal to identify and correlate the various phases of motion to each reconstructed image.

Helical vs Axial

Although axial reconstruction is limited to a specific table position and spiral offers the freedom to reconstruct at any slice location within the volume investigated (143), spiral reconstruction typically involves interpolation between adjacent detectors, which reduces the spatial resolution in the axial direction (154, 156). Also, with axial scans, every bit of the patient's exposure goes into the image's formation, resulting in 100% dose efficiency (154). Spiral scans have reduced dose efficiency as the tube must turn on earlier and turn off later to acquire the same data (154) (see Figure 2.5), and the dose to the patient is the same whether 1 or 10 phase images are reconstructed. For small coverage, spiral scans take longer as the table must move farther and the tube must be on longer compared to an axial scan to capture the same data. However, the advantage goes to the spiral scans for larger volumes, such as those in thoracic imaging; the efficiency of the spiral scan to acquire data and translate the table simultaneously results in a significant time savings (154).

Prospective vs Retrospective

Prospective scans are fairly easy to acquire at end exhale or end inhale (32), in that with a capable patient, no sophisticated respiratory monitoring system is required. Any other desired phase, however, requires a respiratory monitoring system capable of both communicating with the CT scanner and interpreting the breath period. With prospective 4DCT scans, only a single phase of motion is captured, meaning a quick processing time and minimal dose to the patient (38). The down side is that prospective techniques provide no information on either the target's or surrounding anatomy's actual movement (2). Also, any additional desired phases require repeating the entire scan (32), and so increase the amount of time spent on and the dose to the patient by a factor equal to the number of total phases reconstructed.

Retrospective scans enable the reconstruction of any number of arbitrary phases (31), providing precious patient-specific temporospatial information on the motion of the full anatomy (38). Yet, the large amount of data (on the order of 1000 images per thoracic exam (39)) requires increased data storage needs (39), sophisticated contouring algorithms (32), as well as consideration of the increased dose to the patient (157,38). Also, the image quality of retrospective methods depends heavily on the reliability of the respiratory monitoring system and the degree of periodicity of the patient's respiratory signal (32,31). A major benefit to retrospective methods, however, is the opportunity to manually inspect the respiratory signal and phase correlation information from the respiratory monitoring system. This affords the ability to edit the phase correlation information prior to reconstruction (31), easing the demand on the patient for perfect periodicity in their breathing pattern and minimizing the incorporation of technique-specific artifacts in the resulting images (38). As well, with retrospective methods, new phases may be reconstructed from the raw data indefinitely without any additional dose to the patient (38,39), providing much needed flexibility in phase options for treatment planning.

Phase-based vs Amplitude-based Sorting

There are two methods for identifying the phases of motion in the respiratory signal: one based on amplitude and the other based on phase. The phase-based method defines a monotonically increasing function of time, straddling each complete breath cycle (see Figure 2.15). The respiratory monitoring system is responsible for identifying

a point in the respiratory cycle (e.g. end inhale or end exhale) to define the beginning and ending of each breath and then defining the phase function for that breath (2). The phases of motion chosen for reconstruction are located by a simple linear interpolation of the phase function.

Figure 2.15: Illustration of amplitude- and phase-based sorting: reconstruction of the peak exhale phase

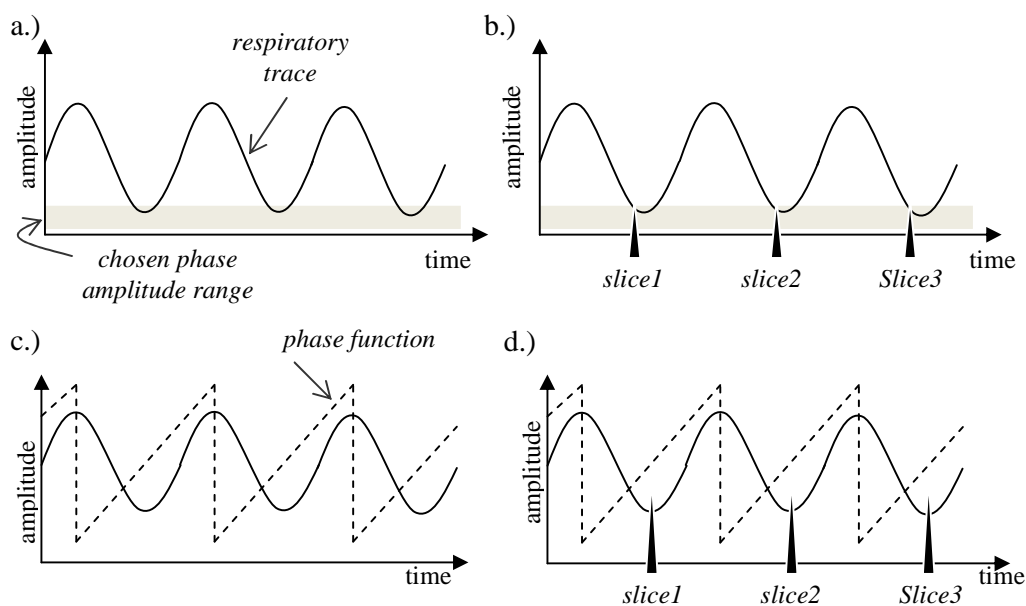


Figure caption: a.) The respiratory monitoring system records the amplitude of the breath signal with time. b.) The peak exhale phase is selected for reconstruction with amplitude based-sorting. When the respiratory trace enters the selected amplitude range, the phase is chosen for reconstruction. c.) With phase-based reconstruction, the respiratory monitoring system defines a phase function for each breath period. The phase function is a monotonically increasing function of time going from peak inhale to peak inhale (peak exhale to peak exhale could also be used) d.) The peak exhale phase is chosen by selecting the midpoint of the phase function..

Because the phase function is not sensitive to amplitude, a breathing pattern which is not sufficiently periodic will introduce artifacts in the resulting reconstructed volume (155). Identical phases of motion can differ in physical location due to variations in slope, period, and amplitude of the respiratory signal from cycle to cycle (155). Phased-base sorting of the phases of motion from such a respiratory pattern is depicted in Figure 2.16. When end exhale is desired, the phase function inadvertently selects other phases of motion (see Figure 2.16a), resulting in *stepladder artifacts*, where the edges of the anatomy show discontinuities from one slice to the next.

Amplitude-based sorting, depicted in Figure 2.16b, distinguishes the different phases of motion based on their amplitude. This method significantly reduces the stepladder artifact by choosing the moment of imaging based on the physical location of the anatomy in each breath cycle (2). However, if the breath pattern is irregular to the point where the desired amplitude is not attained for any given breath (see Figure 2.16c), no image will be reconstructed for that slice of the 4DCT volume (155).

With phase-based sorting, the ability to edit the phase function for the true temporal location of the desired phase of motion helps insure that any two contiguous slices in the resulting 4DCT volume will have continuous edges. There is no analogous

editing procedure that can correct for the missing slice resulting from the amplitude-based sorting of an irregular breathing pattern.

Figure 2.16: Shortcomings of amplitude- and phase-based sorting: reconstruction of the end exhale phase

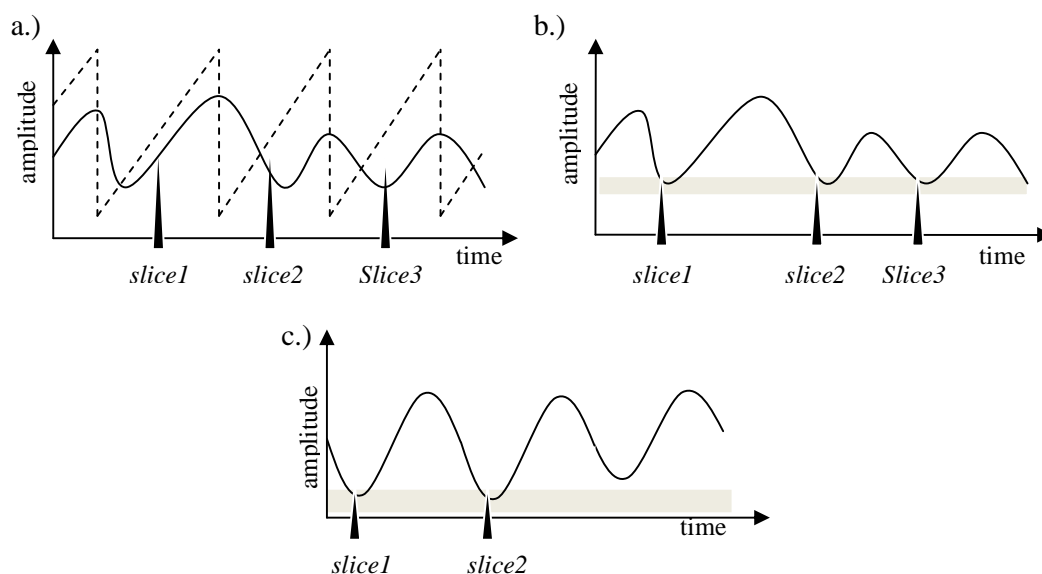


Figure caption: a.) With phase-based sorting of an irregular breath pattern, slices 1 and 2 fail to identify the peak exhale; only slice 3 correctly captures the desired phase. When these three slices are placed contiguous to one another in the resulting volume, the slight differences in amplitude (as well as any phase dependent artifacts due to motion) result in disjointed edges called stepladder artifacts. However, the amplitude-based sorting (b) correctly identifies peak exhale in all three slices. Yet, even if the breathing pattern is quite regular (c) amplitude-based sorting can still fail to identify the desired phase of motion. In (c), the third slice will fail to be reconstructed, and the resulting 3D volume will have a slice missing.

4DCT image formation

This project utilizes the *retrospective spiral* method with *phase-based* sorting exclusively. As described above, retrospective spiral 4DCT is a two step process. First, data for all phases of motion is collected at each reconstructed slice location. Then, only the desired phases of motion are reconstructed from the oversampled sinogram (154). In order to assure that every phase of motion is captured at each slice location, the tube must rotate around the same slice for a minimum of one full breath period t_b . The pitch p must be chosen so that this data sufficiency condition is met, (154)

$$t_r / p \geq t_b, \quad 2.19$$

where t_r is the period of the tube rotation (39). Since it takes a finite amount of time to acquire a single image t_i (i.e. half a rotation plus fan angle), this time must be added to the right side of Equation 2.19 (39,154,155)

$$t_r / p \geq t_b + t_i. \quad 2.20$$

If the detectors move past any slice location before the time required for one complete breath plus image acquisition, a portion of the respiratory cycle will be absent from the sinogram. If such a phase is chosen for reconstruction, the phase-based sorting algorithm will fail to reconstruct an image for that slice (39,154,155). A low pitch and many detector rows for maximum instantaneous longitudinal coverage help prevent missing data (39,154,32). Figure 2.17 illustrates the data sufficiency condition. The shaded region indicates the data contributing to the reconstructed volume between z_1 and z_2 , which equals the z-extent of a 16 slice detector bank. For a tube rotation time t_r equal to 0.5 s, $t_b = 4$ s, $t_i = 2/3(t_r) = 0.3$ s (i.e. 180° data acquisition plus a 60° fan angle is $2/3$ of a complete rotation) the detectors must collect data at each slice location for 4.3 s, i.e. $t_b + t_i$ (154).

Figure 2.17: Illustration of the data sufficiency condition for helical retrospective 4DCT

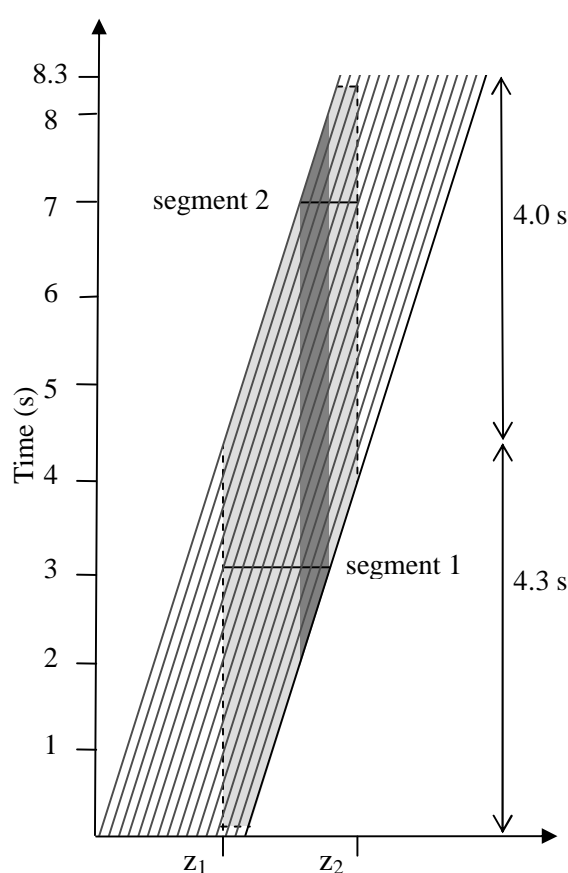


Figure caption:(after (154)): The 16 grey lines represent the path of the detectors in the z-direction with time. The shaded region indicates the data contributing to the reconstructed volume between z_1 and z_2 , which equals the z-extent of a 16 slice detector bank. For a 4 s breath period, the data sufficiency condition dictates that data over 4.3 s must be collected at each slice location. By the time the first slice location has seen 4.3 s of data collection, the last slice has only been illuminated for 0.3 s, thus another 4 seconds of data acquisition are required, totaling 8.3 s to meet the data sufficiency condition. Note, the shaded region of data acquisition cannot start at 0 s nor end right at 8.3 s due to the time needed for the gantry to rotate through the fan angle (154). Segment1 and segment2 represent data collected at the same respiratory phase for two consecutive breaths. Since these segments overlap in the z-direction, data from either segment may be used to reconstruct the phase image for those slices, or an average of both (154).

The total acquisition time, however, is 8.3 s due to the time required for the table to translate; by the time the first slice location has been illuminated for 4.3 s, the last slice location has only been illuminated for 0.3 s. An additional 4 s are needed to insure each slice sees at least 4.3 s of data collection. The data collected before z_1 and after z_2 do not contain all the phases of respiration, but are still necessary for data sufficiency within the shaded region.

From Figure 2.17, it is clear that data collected from a single slice location may contain data from more than one breath. With a 4 s breath period, the data collected at $t = 3$ s and $t = 7$ s (labeled segment 1 and segment 2, respectively) correspond to the same respiratory period in two consecutive breaths. Since these two segments overlap in the z -direction (darker shaded region), either segment could be used to reconstruct a slice within this range, or an average of both (154). This oversampling at each slice location exacerbates the heat load on the x-ray tube, and the mA may need to be reduced or the z-extent of the exam limited to prevent damaging the tube (32).

The respiratory monitoring system is responsible for detecting the breathing cycles, calculating their periods, defining the phase function, and sending tags to the CT reconstruction algorithm indicating the beginning and ending of each cycle (39,45). Based on the phase function, the CT reconstruction algorithm determines the temporal location of the desired phases of motion, and reconstructs the phase images. Typically, the respiratory monitoring system tags peak inhale or peak exhale as these phases are the easiest to identify (39,31). To avoid a time lag between detection and when the CT scanner receives the tag, respiratory monitoring systems require predictive algorithms that must first learn the breathing pattern. This allows anticipation of the beginning of each breath cycle as well as recognition of irregular breathing. A 100 ms discrepancy has been reported in the predicted and tagged peak inhale position of a phantom with Varian's Real-Time Position Management (RPM) Respiratory Gating System, possibly due to an electronic delay between the system and the CT scanner (39). Such a delay is unlikely to affect image quality²⁴.

Figure 2.18: The phase function definition of phases. 4 phases

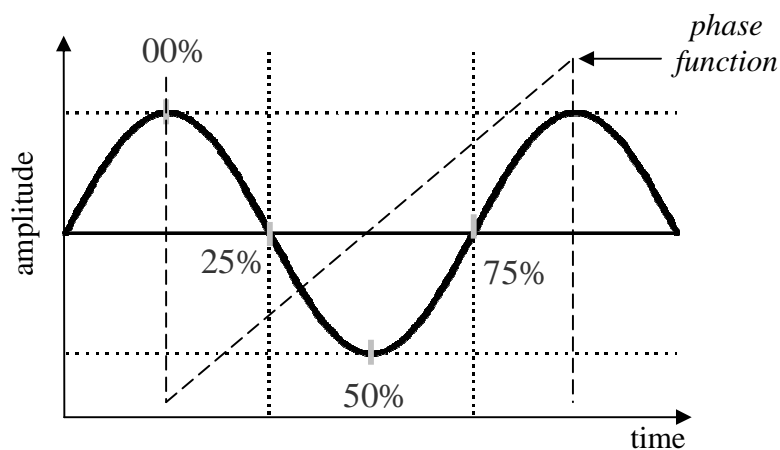


Figure caption: The phase function is a monotonically increasing function of time spanning one complete breath cycle. The phases of motion are defined by dividing the phase function into equal parts. Here, four phases of motion have been defined. The 00 % phase, corresponding to peak inhale, the 50% phase is peak exhale, and the 25% and 75% phases are the halfway points between peak inhale and peak exhale.

²⁴ A time delay of 100 ms may be relevant to IGRT or IMRT.

Figure 2.19: The breath trace corresponding to Figure 2.17 and a portion of the sinogram from a slice located in 'segment1'

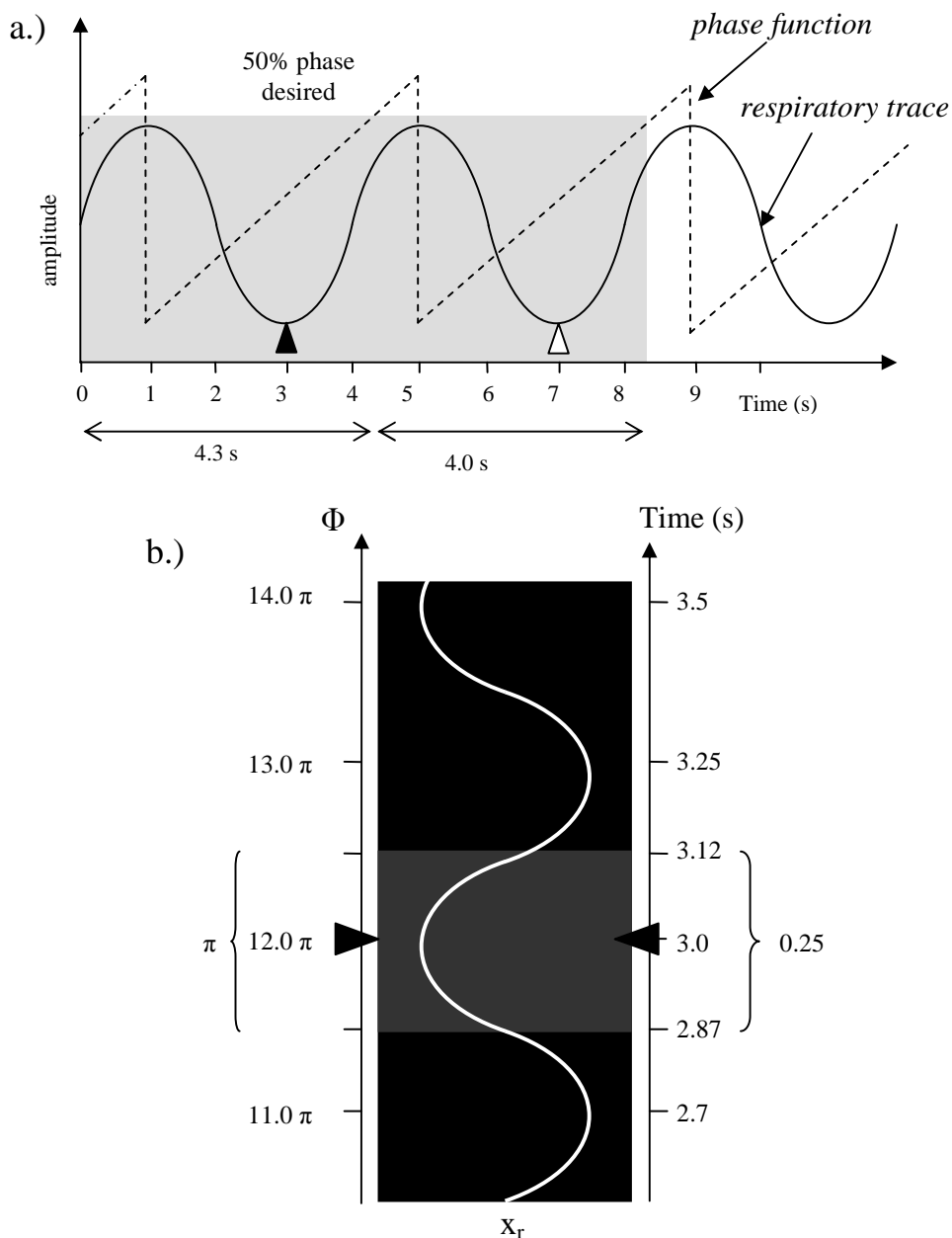


Figure caption: a.) The recorded respiratory trace and phase function corresponding to the acquisition depicted in Figure 2.17. The portion of trace collected during the 8.3 s of data collection is shaded grey. During that time, two 50 % phases (i.e. peak exhales) were recorded, corresponding to 'segment1' (black marker) and 'segment2' (white marker) in Figure 2.17. b.) A portion of the sinogram collected for a single slice from 'segment1'. The temporal resolution is a half tube rotation; 180° worth of data equates to 0.25 s (with 0.5 s rotation time). Thus, to avoid temporal overlap, the sinogram can only be chopped-up into a limited number of $\Delta\Phi = \pi$ chunks.

Knowledge of the beginning of the CT acquisition is combined with the respiratory monitoring signal to select the correct phases of motion for reconstruction

based on the time stamp on each image (32,154). The phase function for each breath period is a monotonically increasing function of time, typically from peak inhale to peak inhale. Each desired phase of motion is linearly interpolated from the phase function, thus, peak exhale is defined at halfway between two adjacent peak inhales (32,39). Typically the phases are described as a percentage of the period of each cycle (32,155), thus, if 4 equally spaced phases of motion are reconstructed, these would be the 00%, 25%, 50%, and 75% phases (see Figure 2.18). The 00% phase corresponds to the tagged phase of motion (e.g. peak inhale). The 50% is peak exhale, and the 25% & 75% phases are half way between peak exhale and two consecutive peak inhales. The portion of sinogram corresponding to each desired slice location contains temporal information concerning the duration of its acquisition. This information may be based on an absolute internal clock or relative to the onset of the CT acquisition. For each slice, the temporal location of the desired phase (from the respiratory signal as determined by the phase function) is then matched up with the sinogram's time stamping. That is, the moment in time where that phase occurs at that slice location is flagged on the sinogram. The reconstruction algorithm then selects 90° of data on either side of the flag to reconstruct the phase image (32,39,155). See Figure 2.19. This allows any arbitrary phase or number of phases to be reconstructed from the same data (155). Also, the sinogram data can be accessed again indefinitely to reconstruct different phases of motion (38,39). The number of phases that can be reconstructed at a single slice location are limitless, yet if no temporal overlap is desired, the number of temporally distinct phases is dictated by the speed of the x-ray tube's rotation (39). The temporal resolution corresponds to one half the tube rotation, i.e. 180° of the sinogram data (154).

As mentioned earlier, phase-based sorting is susceptible to stepladder artifacts resulting from slope, period, and amplitude variations in the respiratory signal (155). It is important to realize that the respiratory monitoring system only recognizes a single phase of motion, typically peak inhale. This is the only phase that is based on the *true* phase of the respiratory signal; all other phases of motion are interpolated from this single phase. Therefore, it is wise to retain access to the full respiratory signal, so that the phase function and/or phase flags can be retrospectively modified prior to any reconstruction. This helps to insure that every phase of motion is accurately identified and that the resulting volume is free of stepladder artifacts (39).

A single image may be formed by averaging the data acquired from two contiguous breaths. If these two breaths are not identical, blurring or ghosting similar to that shown in Figure 2.20 results (154). This image, however, was produced from a phantom moving with perfect periodicity. The respiratory monitoring system requires time to learn the respiratory pattern, and in this instance, CT acquisition began before the learning period was complete –adjacent breaths were assigned different periods. The resulting phase function inadvertently selected portions of sinogram from two different phases for reconstruction. Thus, not only is it important that the patient's breathing be as periodic as possible, but also that the respiratory monitoring system be given adequate time to learn the respiratory pattern. Such an image, when placed in the 3D volume, would result in a stepladder artifact. Stepladder artifacts result from the incorrect classification of phase between two adjacent breaths (32); they occur when adjacent breaths are out of phase (39,157), or they could also be due to insufficient time for the monitoring system to learn the breathing pattern. This type of artifact is most noticeable where the amplitude of motion is the greatest, such as near the diaphragm (157).

Figure 2.20: Image ghosting due to the incorrect classification of phases in adjacent breaths

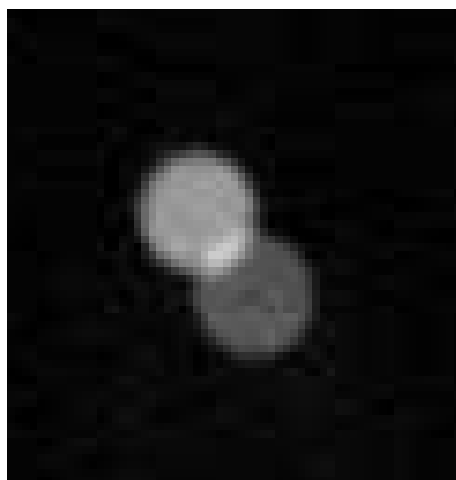


Figure caption: A single slice of the 4DCT phase image constructed from two breaths. The motion imparted to the sphere was periodic, thus, the two adjacent breaths should have had the same period and amplitude. Yet the Bellows respiratory monitoring system was not given sufficient time to learn the phantom's true period, and so incorrectly assigned the phase function for the two breaths. The contributions from each breath do not appear to be equally weighted.

Since respiration is not purely periodic, but governed by metabolically driven involuntary responses as well as the patient's will, stepladder artifacts are common in patient data. Being startled by the beginning of the CT acquisition can cause the patient to catch their breath; excitement or relaxation during the acquisition can progressively quicken or slow successive respiratory cycles; indeed, it can be difficult to attain sufficiently regular breathing from many patients (16,7,46,113). Even if regular breathing is attained, the relative amplitude of inspiration/expiration can drift slowly during the acquisition; this is known as baseline drift (46,111). Various techniques to improve the regularity of the patient's respiration, including audio, audiovisual, or just visual coaching (45,31,30), have been shown to improve the quality of the 4DCT (39,30,158,46,89).

Chapter 3: Quantitative Measurements of Geometric Accuracy

4DCT Technology

Philips recognizes only the Philips Bellows and Varian RPM respiratory monitoring systems, and is capable of performing prospective axial, prospective spiral, and retrospective spiral 4DCT (31p13-1). It is the respiratory monitoring system's responsibility to detect the breathing pattern, identify the phases of respiration, and in the case of the RPM system, measure the amplitude of motion. Philips requires that the method of respiratory monitoring be chosen prior to image acquisitions (31p13-4).

Bellows

The Bellows system (Philips Medical Systems, Cleveland OH) is a pressure transducer that looks like a rubber belt. It plugs into the CT gantry and, when wrapped around a patient's chest or abdomen, generates a breathing signal correlated to lung volume (31,38). Figure 3.1 shows the Philips/Bellows configuration. For prospective acquisitions, there is choice of gating the tube on end inhale, end exhale, or a user defined phase (ranging between 0 and 1, where 0 is the average valley and 1 is the average peak height of the respiratory trace) (31p14-4). Figure 3.2 shows a screen shot of the Bellows respiratory trace as seen on the Philips workstation. If either prospective method is chosen, Philips must first learn the relative amplitudes of the breath trace, a process spanning several breaths. There is no provision for indicating to the user when it has accomplished this task, so patience is required. The Bellows system cannot measure motion amplitude nor can it amplitude sort; the amplitudes depicted in the waveform of the respiratory trace correlate to tidal lung volume. However, when the internal pressure of the Bellows is normalized to the tidal volume of the lungs recorded using a spirometer, White et al. claim that the Bellows system is capable of quantitative measurements (159). The breath phases are marked in percent of respiration from peak-to-peak (31p13-2). For retrospective scans, the user must indicate before acquisition the desired phases to be reconstructed, up to 10 (31p13-4). Once acquisition is complete, any number of phases of motion may be reconstructed off line from the raw data (31p13-21).

Figure 3.1: Philips Bellows system

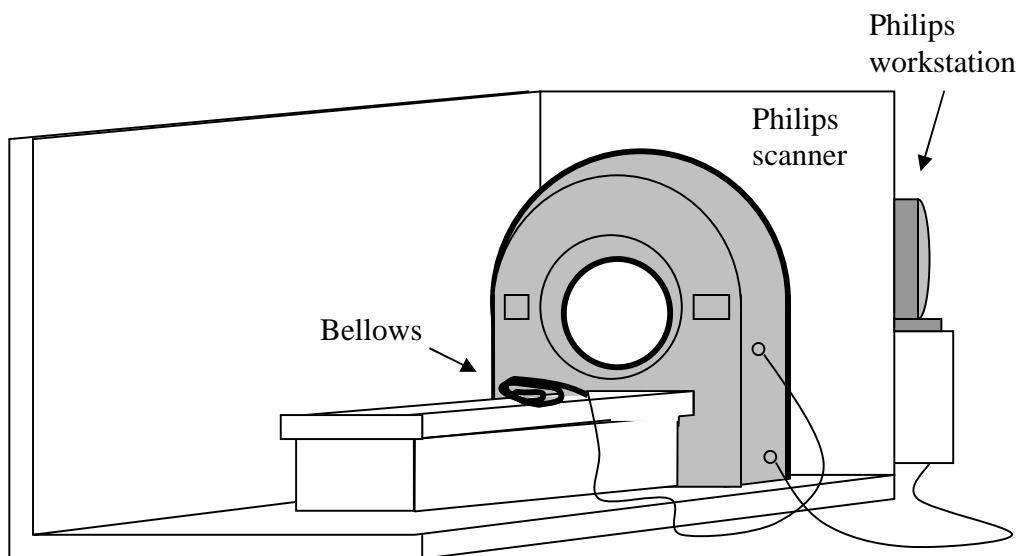


Figure caption: The Philips Bellows plugs directly into the gantry. The signal it generates is transmitted to the Philips workstation over the same hard line connecting the CT scanner to the workstation.

With the respiratory trace, one can rescale the time axis, observe the location of the desired phases and move them, as well as retrieve their statistics. It is possible to record a respiratory cycle without acquiring image data (31p13-6). Breath statistics are available off-line; these include the scan length, the number of breath cycles recorded, the breath rate in breaths per minute (bpm), and the relative amplitude data. The amplitude is expressed in terms of % phase—the average end exhale phase, for example could be 49%

and the average end inhale, 99 %. The range of recorded amplitudes is also available (31p11-13).

Figure 3.2: Philips workstation screen shot of a respiratory signal

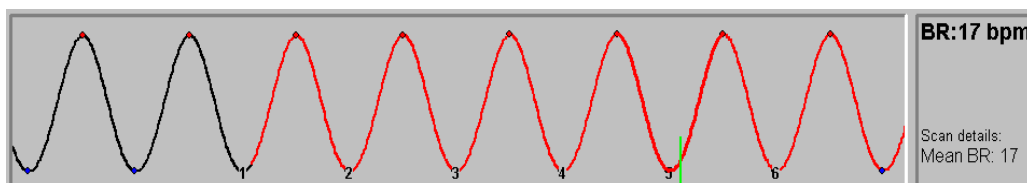


Figure caption: The Philips workstation display of the respiratory trace collected with Bellows. This trace is artificially generated. The green tag indicates placement of the 60% phase.

RPM

The Real time Position Management system (Varian Medical Systems, Palo Alto, CA, USA) is designed for use with CT, PET, MRI, fluoroscopy video segment, in-room portal vision and onboard kV imagers (45p7), as well as treatment machines. The system uses the motion of the chest wall or abdomen as a surrogate for the respiratory induced motion of the target and surrounding anatomy (45p7,22). It captures the amplitude and phase of each breath in real time (32) by tracking a marker block placed on the patient's skin. The block is constructed of light weight plastic and has two small circular reflective markers. A video camera imbedded in a ring of infrared lights (See Figure 3.3) monitors the block at 30 frames/s. The IR light reflected off the block appears in the video signal sent by the camera to the RPM Respiratory Gating System software (version 1.7) installed on a Varian RPM workstation (45p9). The system is capable of tracking 6 - 25 breaths per minute (45). Figure 3.4 shows the RPM system with the Philips scanner.

Figure 3.3: RPM Camera

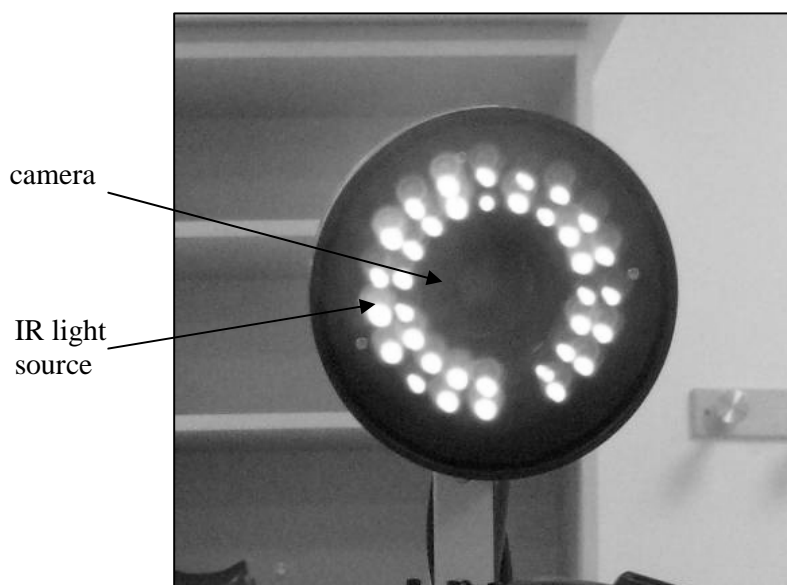


Figure caption: The RPM camera consists of an IR sensitive charged couple device (CCD) tracking camera surrounded by rings of IR sources.(45p9)

Figure 3.4: The RPM system

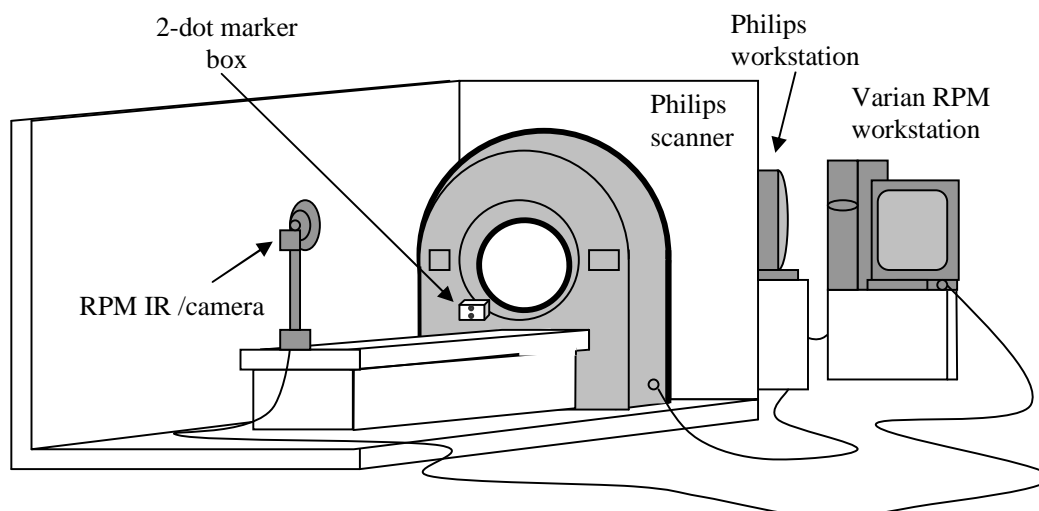


Figure caption: The RPM camera is physically connected to the RPM workstation, which receives the video signals and converts them into a respiratory waveform. The RPM workstation sends synchronizing pulses to the Philips scanner through a hardwire connection to the Philips workstation.

The RPM software translates the video images into a respiratory waveform (50) by sensing end exhale (45p21). Only motion perpendicular to the surface vector of the camera face is recognized (21). However, a more sophisticated software package is available to track a six dot marker block (RPM Respiratory Gating System version 1.7), and is capable of recognizing motion in any direction, but this software has not yet been installed at The Cross. Once installed, the six dot marker block software will still recognize the two dot marker block, but will only track it in 1D (45p11).

Positioning of the marker block depends on the treatment prescription and the patient's physique (45p10) –often it is chosen to produce the best (i.e. maximum or most reproducible) signal (45p10, 160). The suggested location is midway between xyphoid and umbilicus (45p10) (i.e. halfway between base of the sternum and the belly button) (see Figure 3.4), a position often corresponding to maximum abdominal movement (161). The RPM system is limited by the patient's ability to produce a detectable and reliable respiratory signal (46, 45p11). It should be noted that the location of the marker block may be removed from the region of interest (160) and that shifts in both the physical and phase relationship between the marker and the target have been observed (21,162,129,88,24).

Figure 3.4: Recommended marker block position

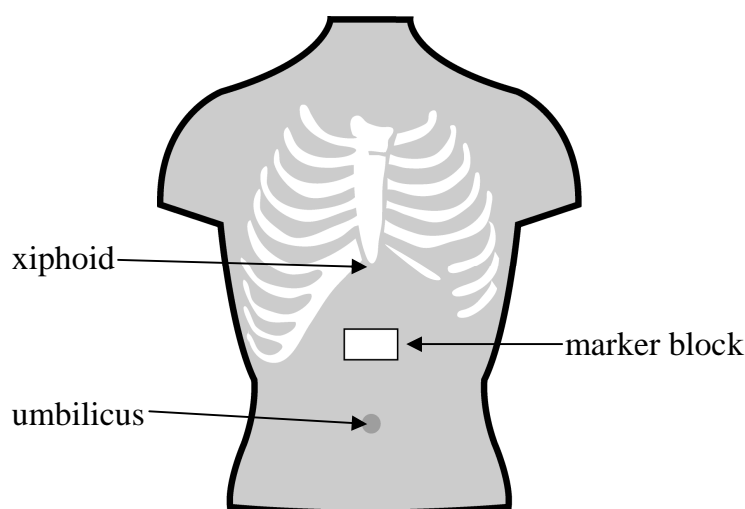


Figure caption: Placement of the marker block is usually chosen to provide the best signal. The recommended starting point for determining this optimal location is midway between the base of the sternum (xiphoid) and the belly button (umbilicus), along the midline of the body.

Unlike the Bellows respiratory tracking system, the RPM system is designed for quantitative measurement, down to 0.1 mm accuracy if properly calibrated (45p17). Calibration is usually performed at installation, and the RPM system comes equipped with calibration checking software. Calibration is not necessary with the two dot marker block for just qualitative tracking of the respiratory phases (like the Bellows system). However, if the six dot marker block is utilized, the camera must be calibrated to establish the required coordinate system for any kind of tracking (45p11). The camera will be unable to track either marker block with some other sufficiently reflective object in the room (e.g. the patient's watch, or reflective patterns on the patient's clothes) (45p4). If the camera is already tracking when another reflective object enters its field of vision, however, the system should be able to continue unless this object breaks the line of sight between the camera and the block (45p4). Any disruption in the video signal, whether mechanical, electrical, or just someone stepping in front of the camera will stop the tracking (45p19).

Since the camera should remain in a fixed relationship to the marker block during CT acquisition, the camera is mounted on the patient bed, moving, as the block moves, with the table. Because of the 1D tracking limitation of the two dot marker block, the RPM system has difficulty detecting SI motion. For motion of 1 cm amplitude in the SI direction, the stand of the camera must be telescoped to its maximum height to capture the motion (See Figure 3.6). However, the system was simply unable to detect 0.5 cm amplitude SI motion without removing the camera from the patient table and placing it at a higher vantage. Removing the camera from the bed, however, creates a baseline drift in the respiratory signal; as the bed moves through the bore of the CT, the block moves away from the camera. Figure 3.7 shows what such a baseline drift looks like on the Varian workstation.

Figure 3.6: The RPM system detecting SI motion.

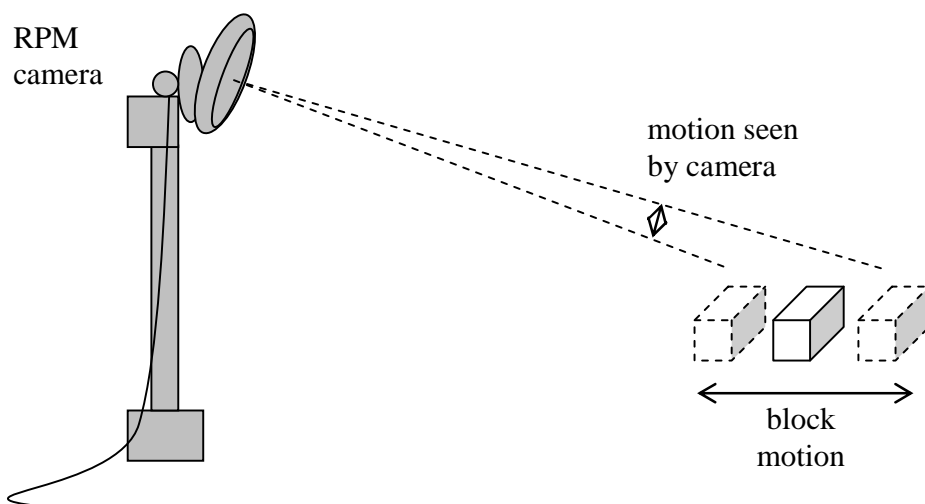


Figure caption: With the two marker block, the camera sees AP motion only. Thus, the actual SI motion is only detected by the reflector's apparent motion parallel to the face of the camera.

In the treatment room, where the target is fixed at isocenter relative to the entire room, the vantage of the RPM camera could be altered to optimize the signal. During both treatment and imaging, the marker block should never be moved, since the relationship between the surrogate and the target must be maintained.

Figure 3.7: RPM—baseline drift

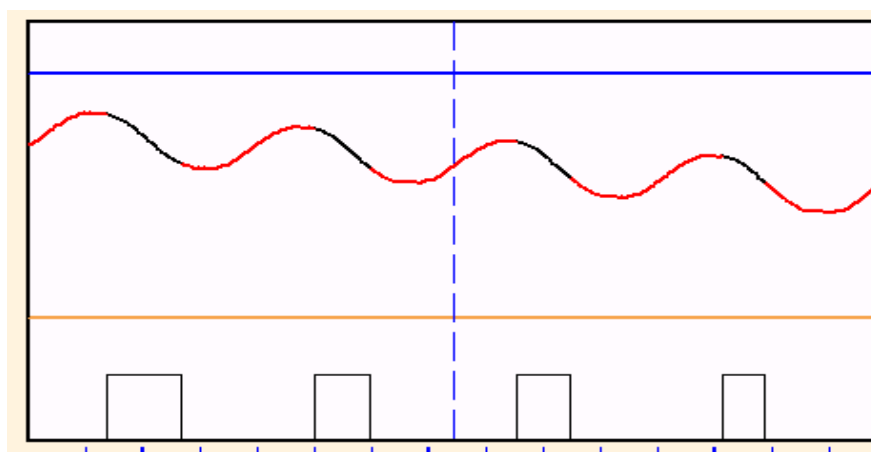


Figure caption: A respiratory trace from the RPM Workstation GUI. The red portions of the trace indicate that the RPM system has detected abnormal breathing and is unable to gate, while the black means the trace is behaving as expected (45p35). The rectangles at the bottom show the potential gating windows, however, the system will not allow gating unless the entire trace is black. Here, the camera is placed on a stationary cart, and as the patient table moves away from the camera, the signal of the retreating marker block is perceived as a drifting of the mean position of the marker.

The RPM system software creates the phase function from the respiratory signal (45p8), and sends synchronizing pulses to the Philips scanner over a hardwire connection

between the RPM and Philips workstations (45p37). These pulses may be initiated at end inhale, end exhale, or a user defined phase (45p32). When these signals are used to gate the CT tube for prospective acquisitions (45p8), the pulses themselves or the timestamp of the beginning and ending of the acquisition may be used to temporally correlate the phase images; thus, the RPM system also captures data from the scanner over the same hardware connection (45p37).

Whether doing a prospective or retrospective acquisition, the respiratory signal must be sent to the Philips workstation for reconstruction. In addition to the waveform itself, the exported RPM respiratory trace contains the phase information and time stamps (45p8). Transfer of the respiratory trace is via the computer network, although a removable storage device may also be used (45p34). If the option of automatic export of the respiratory trace is not selected, the respiratory trace must be manually exported to the folder where the Philips system may retrieve it prior to image reconstruction. If Philips does not receive the respiratory trace, it will phase sort and reconstruct the images using the synchronizing pulses (see Figure 3.8a). Figure 3.8b shows a true RPM breath trace as displayed by the Philips system. Once the respiratory data is transferred to the Philips workstation, the same manipulations are available as for the Bellows signal (31,45).

Figure 3.8: The RPM respiratory trace received by Philips: synch pulses or waveform

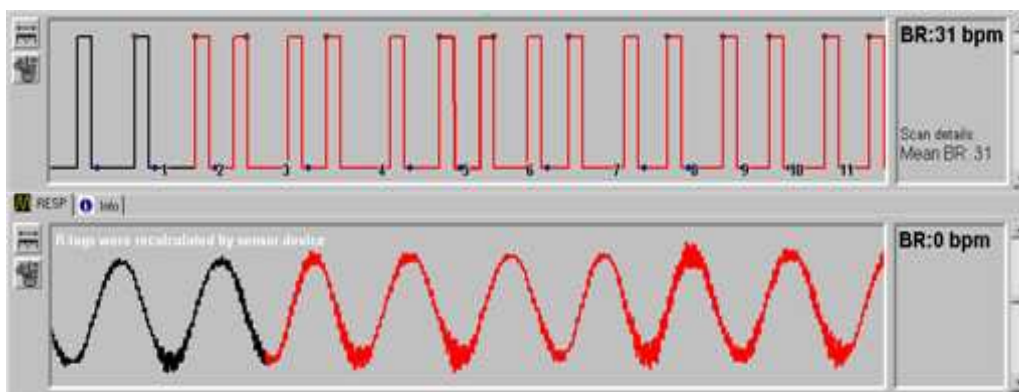


Figure caption: The RPM respiratory traces as shown on the Philips workstation. Top: Without exporting the RPM file properly, the respiratory signal received from the RPM system is just the synchronizing pulses sent by the RPM system to the CT scanner for gating the x-ray tube. Bottom: With the file transferred to the proper folder for pick up, Philips receives the actual breath trace.

The RPM system is also designed to gate radiation treatment beams. It monitors the consistency of the respiratory pattern, and if the breathing becomes too irregular, RPM will cease to send synchronizing/gating pulses. The user witnesses this monitoring on the Varian RPM workstation by observing a bar of blue boxes in the upper left hand corner of the RPM session GUI. See Figure 3.9.

Figure 3.9: RPM Workstation: breath regularity

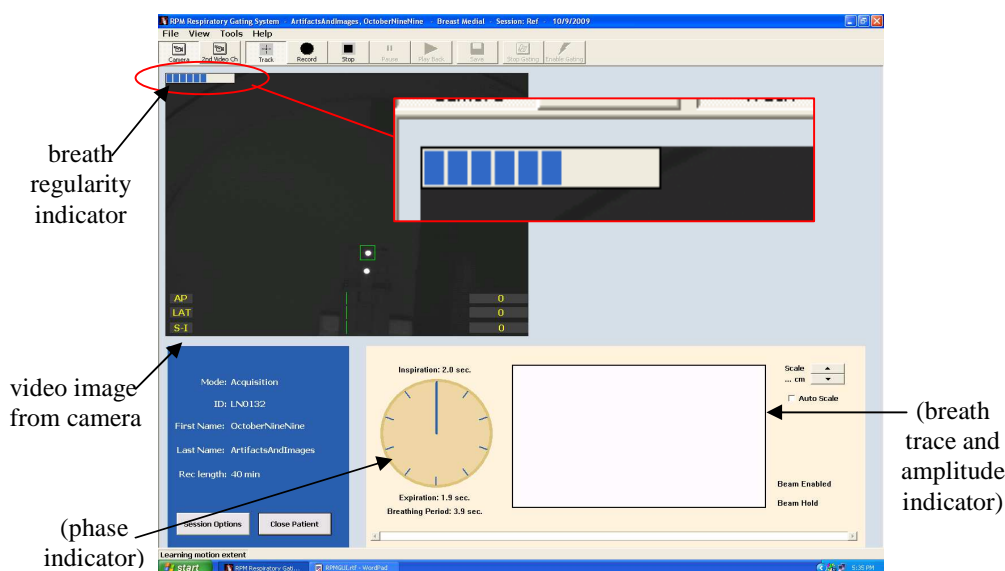


Figure caption: The full RPM workstation GUI; prior to recording the breath trace, the RPM system must first learn the patient's breathing pattern. A row of blue boxes in the upper left hand corner of the GUI indicates to the user when the RPM system has recognized that the breathing is regular enough to record the trace and gate the beam safely. (The Bellows system does not provide such indications, and allows the x-ray beam to be turned on before it has learned the breathing pattern.) Also shown are the basic components of the RPM GUI. Many of these components are not activated in this image as the RPM system has not begun recording the breath signal. Recording should not commence until the number of blue boxes has reduced to 5 or less.

A full row of 10 boxes indicates that a new breath period has been measured and/or that the system is adjusting to a new range of motion. The RPM software assumes periodicity and monitors the variation between the current breath and previous breaths. The number of boxes reduces as the software perceives the breathing becoming more consistent. Anything under 5 boxes indicates the system considers the breathing periodic (45p16-17). It is possible to adjust RPM sensitivity to variations in the breath pattern by specifying its *normal breathing predictive filter* (45p17). The filter is based on a percentage similarity to past breaths –the synchronizing/gating pulse stops if the current breath does not meet the expected percent similarity, such that a value of 100 % means every breath must be identical to all past breaths in order to proceed, and a value of 0 % essentially disables the filter (45p18).

If phase correlation between the marker and the GTV is required for a specific treatment option, this relationship must be determined and monitored, as phase differences between marker and GTV can occur both intra- and inter-fractionally (21,2,129,88,24). The RPM software also provides audio and adjustable video coaching (45p24).

Methods of Quantitative Measurement

Patient data is not appropriate for quantitative measurements since the absolute size, shape, and location of a tumor are indeterminable (2). Instead, a mechanical phantom is used to impart clinically relevant motion to acrylic spheres during 4DCT acquisition. The measured size, shape, and position of these spheres in each phase image are compared to their true size, shape, and position.

The Motion Phantom

The phantom used to move the acrylic spheres is capable of motion in the SI, AP, and LR directions. Electrically driven circular cams with center offsets provide smooth sinusoidal motion in each orthogonal direction. The specific motions produced by the phantom are $z = -A_0 \cos(\omega t)$ for the SI direction only, $x = y = -A_0 \cos(\omega t)$ for AP-LR motion, and $x = y = z = -A_0 \cos(\omega t)$ for the SI-AP-LR motion, where A_0 is the offset of the cams. Each of these motions produces a linear translation path. Three sets of cams enable amplitudes of 0.5 cm, 1.0 cm, and 1.5 cm in each of the three orthogonal directions. Close adherence to this intended motion is assured by the mechanically robust construction of the phantom. Figure 3.10 shows a schematic of the phantom, and Figure 3.11 is a digital photograph of the phantom set up on the patient couch of the Philips CT scanner.

Figure 3.10: Phantom Schematic

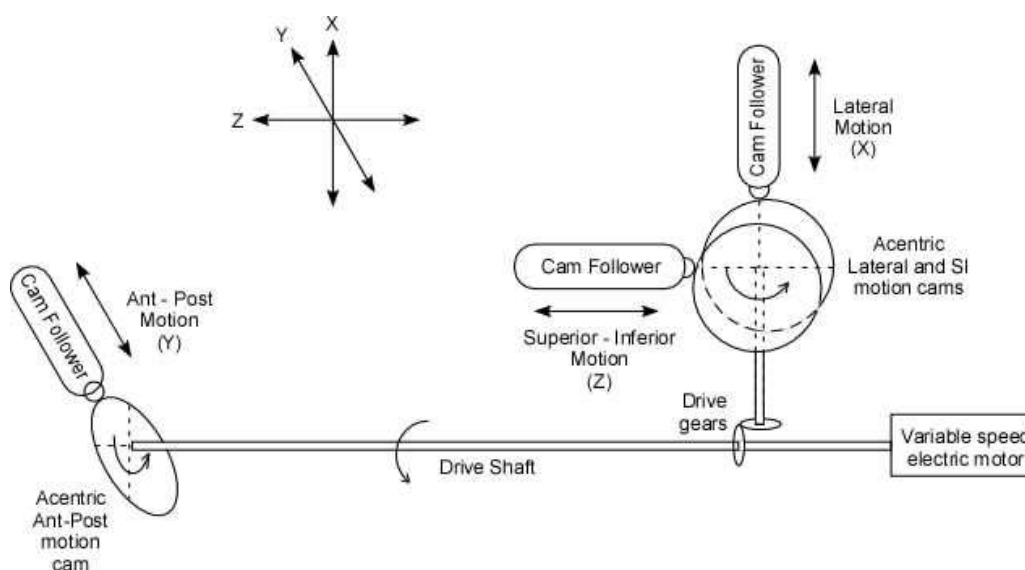


Figure caption: The specific motions produced by the phantom are $z = -A_0 \cos(\omega t)$ for the SI direction only, $x = y = -A_0 \cos(\omega t)$ for the AP – LR combined motion, and $x = y = z = -A_0 \cos(\omega t)$ for the SI-AP-LR motion. Here, A_0 is the offset of the cams (i.e. 0.5 cm, 1.0 cm, and 1.5 cm). Each of these motions produces a linear translation path.

Figure 3.11: The phantom

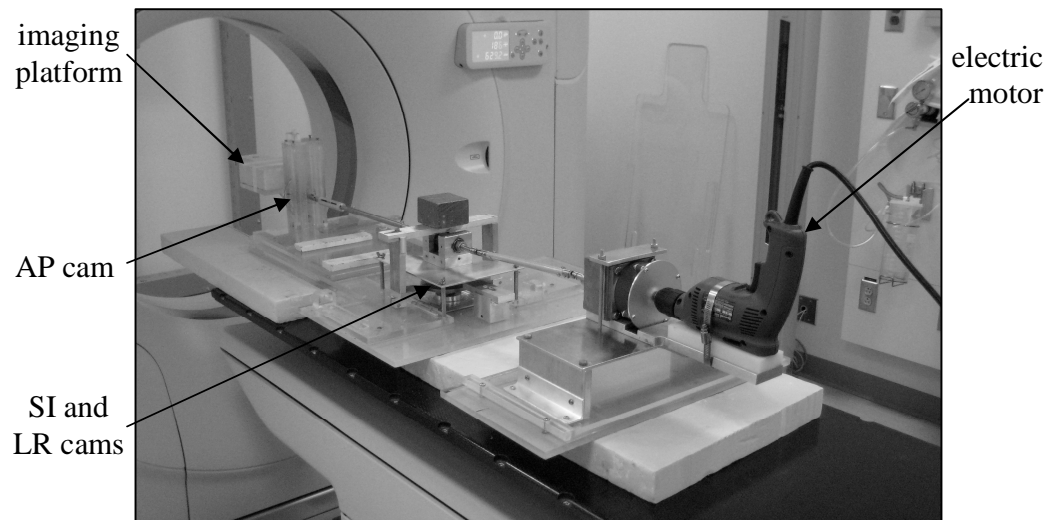


Figure caption: The acrylic spheres rest on the imaging platform. The platform is capable of movement in the SI, AP, and LR directions via electrically driven cams.

Figure 3.12: Bellows experiment setup

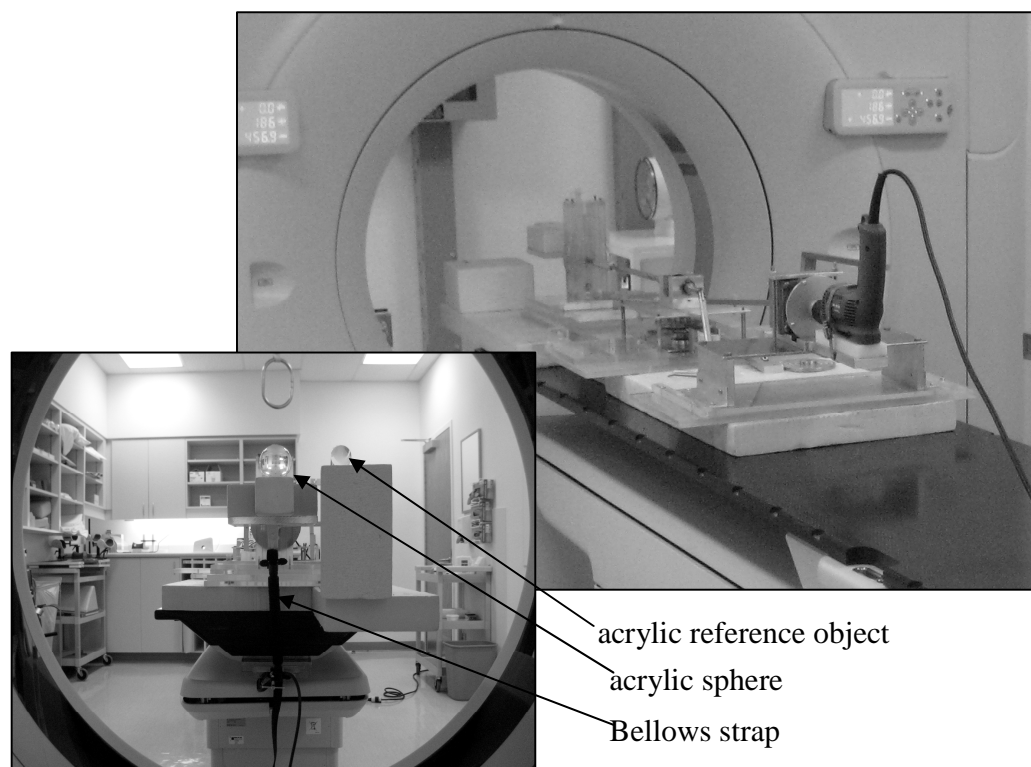


Figure caption: The Bellows strap is not wrapped around the phantom as it would be for a patient because tension in the elastic Bellows could influence the phantom's motion. Instead, the Bellows are suspended from the center of the motion platform with the other end attached to the patient couch. Care was taken to stretch the Bellows the minimum amount necessary to adequately acquire the signal.

Figure 3.13: RPM experiment setup



Figure caption: The marker block is set atop the motion platform and the camera is mounted at the end of the patient bed. The lightness of the plastic box and the remote detection of the reflectors does not interfere with the phantom's motion.

Acrylic spheres of 1, 3 and 5 cm diameters (representing a small, medium, and large tumor, respectively (16)) are imaged while undergoing motion in the following directions: SI direction only, AP-LR combined, and SI-AP-LR combined. All three amplitudes of motion are utilized. A stationary reference object (i.e. an acrylic cylinder 3 cm in diameter) placed within the field of view and near the moving sphere is used to aid in segmentation. A variable transformer controls the period of motion, which is confined to 3.6 to 4.0 s (equating to 15 to 17 bpm). Each permutation of sphere size, amplitude of motion, and type of motion are imaged using both the Philips Bellows and Varian RPM respiratory monitoring systems. Figures 3.12 and 3.13 are digital photographs of the complete experimental set up with the Bellows and RPM respiratory monitoring systems, respectively.

Imaging Protocols

The imaging protocols used are clinical standards for thoracic CT scans. The helical-retrospective 4DCT protocols along with those for standard clinical 3DCT scans are given in Table 3.1. The default of 10 phases of motion (i.e. 00% through 90%) are reconstructed per 4DCT acquisition. Thus, for each 4DCT acquisition, 10 spatially and temporally distinct 3D volumes are reconstructed.

Table 3.1: Philips protocols for 3DCT and 4DCT thoracic acquisitions

protocol	Static (3DCT)	Pulmo (4DCT)
<i>Filter type</i>	B	B
<i>Scan type</i>	Helical	Helical
<i>FOV</i>	400 mm	400 mm
<i>Slice thickness</i>	2 mm	2 mm
<i>Tube potential</i>	120 kVp	120 kVp
<i>Reconstruction</i>	180°	180°
<i>Detector collimation</i>	16 x 1.5 mm	16 x 1.5 mm
<i>Voxel size</i>	0.78 x 0.78 x 2.00 mm ³	0.78 x 0.78 x 2.00 mm ³
<i>Exposure/ detector</i>	400 mAs	401 mAs
<i>Pitch</i>	0.688	0.081
<i>Tube current</i>	275 mA	65 mA
<i>Rotation speed</i>	1 s	0.5 s

Table caption: The protocols specified are the clinical standards for both 3DCT and 4DCT scans.

Metrics of Geometric Evaluation

Each slice of the phase image is converted to a binary image through a thresholding segmentation algorithm performed in MATLAB (version 7.6.0.324, The MathWorks, Inc., <http://www.mathworks.com/>). Various attributes of the binary image (e.g. centroid, eccentricity, and area) are then used to create the metrics by which the accuracy of the 4DCT system is analyzed.

Data processing begins by importing into MATLAB each slice of the phase image containing a cross sectional image of the sphere (as determined by manual inspection using ImageJ (version 1.40, <http://rsb.info.nih.gov/ij/>). The default pixel values of the imported image matrix are grey scale, 0 to approximately 1200. As the conversion function to Hounsfield units (HU) is linear and the same for all the images (i.e. from the DICOM header, $y = a + bx$, where $a = -1024$ and $b = 1$), all image manipulation is performed using these grayscale values, referred to here as pseudo-Hounsfield units (s-HU). The grayscale image matrix is converted to a binary image matrix using a threshold segmentation algorithm –each pixel value equal to or greater than a specified threshold is cast to a boolean 1, while each pixel value below this threshold is cast to boolean 0.

The threshold applied to each slice of each phase image is chosen from the segmented diameter of the stationary reference object as follows. The 3 cm diameter acrylic cylinder is located near, but not on the phantom's moving platform. Beginning with a threshold of 120 s-HU, each slice of the image is segmented and the diameter of the reference object found using the MATLAB function "STATS.Majoraxis", which returns the major axis of a labeled binary image in number of pixels. This value is converted to millimeters and stored in an array along with the threshold. The threshold is then increased by 10 s-HU and the process repeated until the threshold becomes too large to segment the reference cylinder as a single object. This occurs, typically, around 1000 s-HU. The array is then examined to identify the threshold at which the diameter of segmented reference object equals, as closely as possible, its true diameter, and this threshold is then chosen to segment the cross sectional image of the sphere at that slice location. This process results in a different optimal threshold for each slice of the phase image; typically, the thresholds used to segment the phase images range from around 40 - 45 % local contrast of the sphere.

Various attributes of each phase image are also collected at each threshold which are then used to create attribute maps, revealing each attribute's sensitivity to threshold. These maps are also used in error calculations (see Threshold Error-Attribute mapping). The attributes of these segmented images are direct returns from functions found in the MATLAB imaging toolkit, such as "STATS.Centroid" or "STATS.Area", which return, respectively, the center position and the number of pixels of a binary image. The various metrics used to evaluate the accuracy of the 4DCT imaging system are all derived from these attributes. These metrics are:

% volume difference:

Using the MATLAB function "STATS.Area", the number of pixels contained in the segmented area of each cross sectional image of the sphere are summed over the entire phase image, and then converted to units of mm³ by multiplication by the volume of a single voxel (i.e. 0.78 mm x 0.78 mm x 2 mm = 1.217 mm³). This produces the sphere's imaged volume. The percent volume difference between the imaged sphere and the true sphere is then

$$\% \text{ volume difference} = [\text{imaged volume} - \text{known volume}] / \text{known volume} * 100 \quad 3.1$$

Note: absolute value signs are neglected to retain the nature of the discrepancy (i.e. too large or too small.)

Since multiple spheres are used for each sphere size, the "true" volume of each sphere size is taken from the average radius of all spheres of that size. This radius is determined by acquiring multiple caliper measurements (i.e. six measurements, separated by approximately 30°) from three orthogonal planes passing through the center of each sphere. All the measurements from spheres of the same nominal size are averaged and the "true" volume calculated. The error in this measurement is calculated using the standard deviation of these measurements

The *% volume difference* is a metric of how well the 4DCT system is able to capture the true volume of a moving object.

mean eccentricity:

The eccentricity of any given cross sectional image of the sphere, defined here as the ratio of the distance between the two foci of an ellipse and the length of its major axis, is sensitive to residual motion artifacts, especially for slices near the edges of the sphere. This sensitivity arises from residual motion artifacts that, when convolved over a smaller area, may have a greater impact on the overall shape of the imaged cross section (33). In addition, for spheres undergoing motions with an SI component, the cross section seen in the imaging plane changes more rapidly at the edges, generating larger partial projection artifacts (see Figure 3.14) (33,2). Thus, rather than select a single cross sectional image to represent the shape of the entire sphere, the *mean eccentricity* of all identifiable cross sections is calculated.

Figure 3.14: Slices of the 3 cm sphere moving in the SI direction

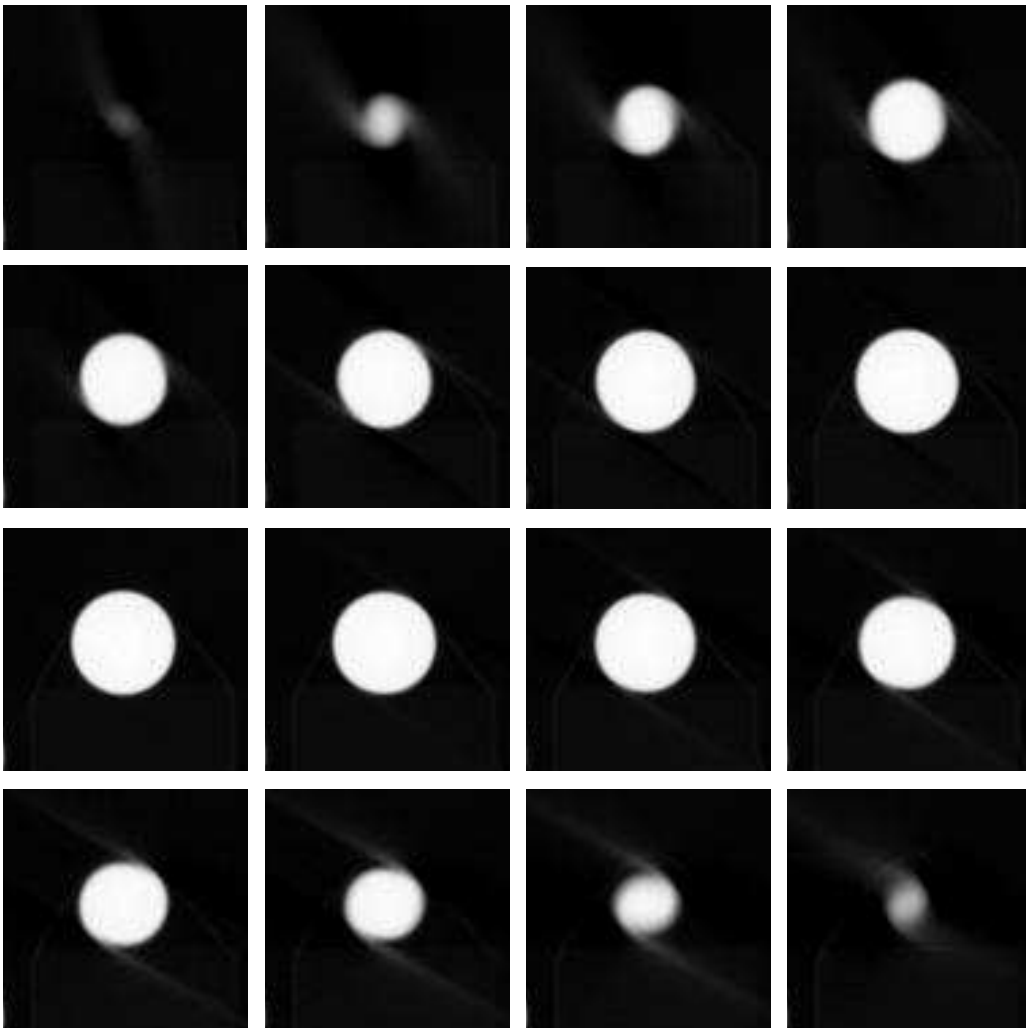


Figure caption: The edge slices show increased residual motion artifacts because, for SI motion, the cross section of the sphere seen in the imaging plane changes more quickly at the edges.

Figure 3.15 shows different ways equally spaced imaging planes may slice through a sphere. Depending on where the sphere happens to land in relationship to the slice planes, the eccentricity of the cross sectional images in the first and last slices of the sphere can vary greatly.

Figure 3.15: Imaging planes intersecting a sphere

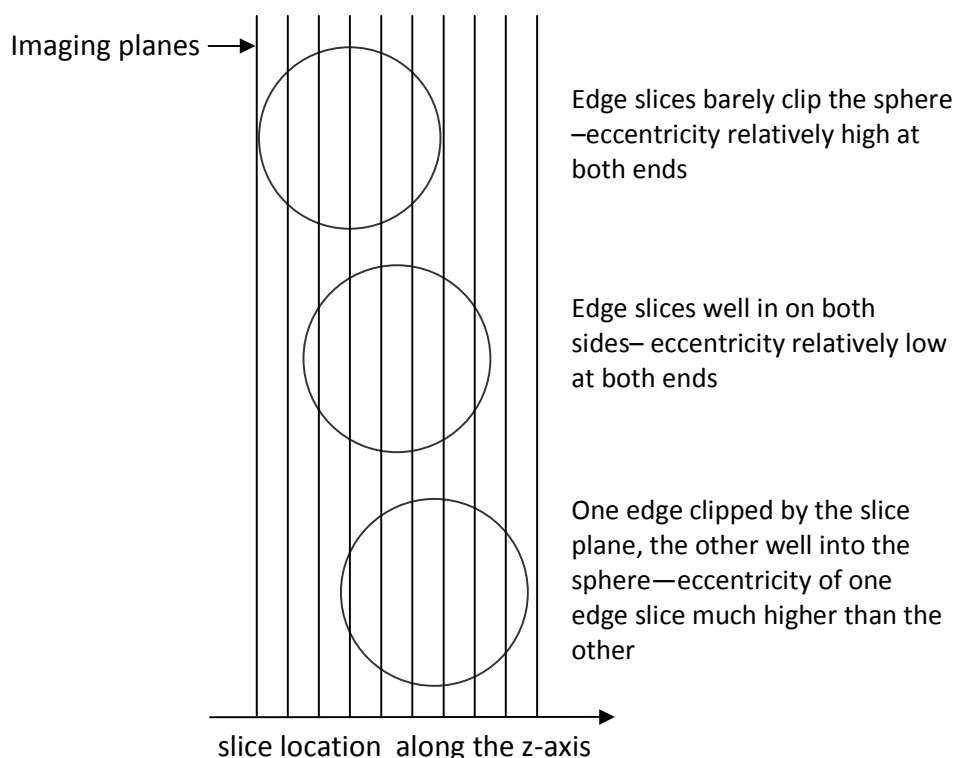
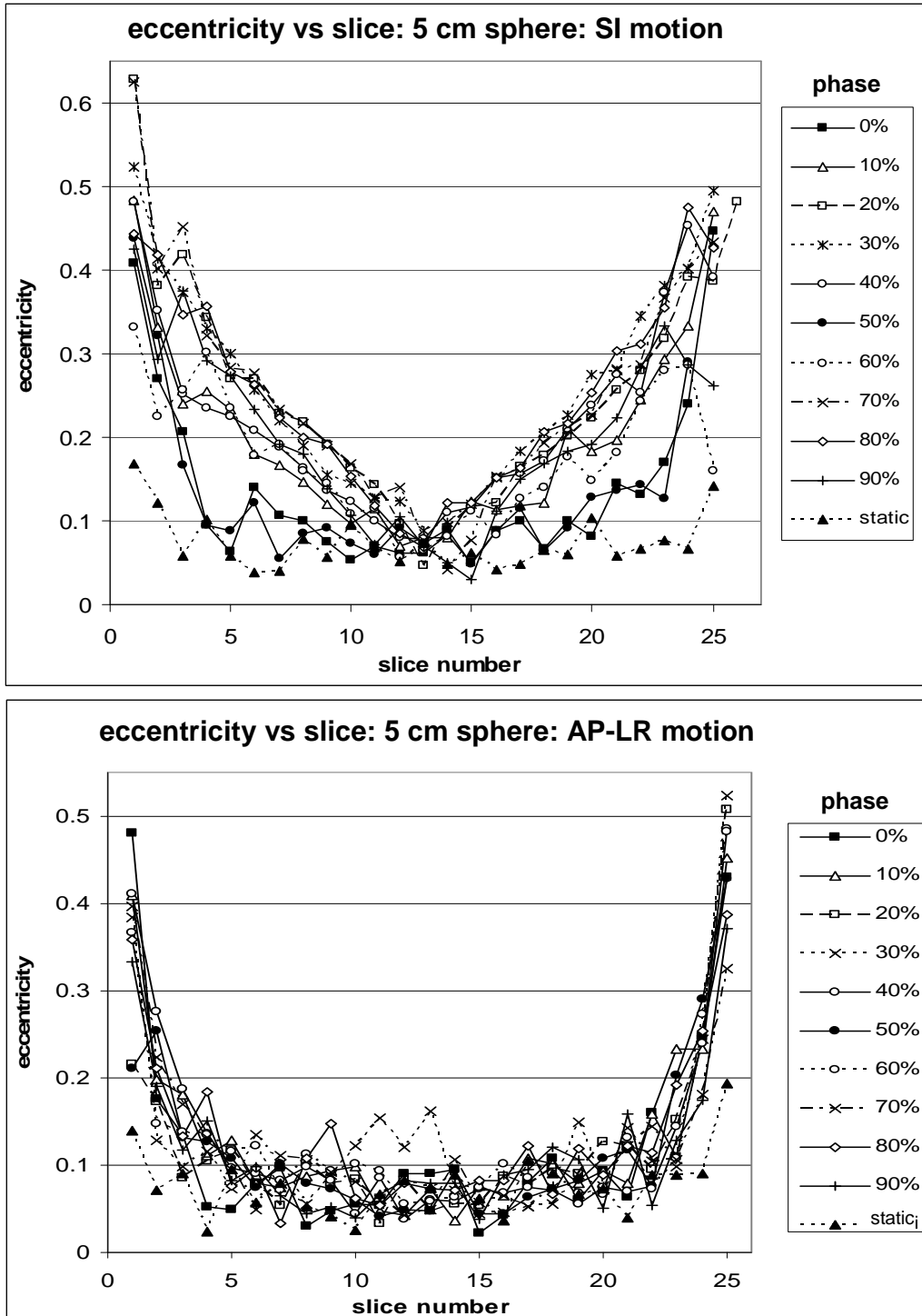


Figure caption: Medio-lateral view of how equally spaced imaging planes may cut through different cross sections of the same sphere, depending on the sphere's location along the z-axis of the CT scanner.

Figure 3.16 shows plots of the eccentricity vs slice number for each of the 10 phase images resulting from the 4DCT acquisition of the 5 cm sphere undergoing motions in the SI direction only, the combined AP-LR direction, and combined SI-AP-LR direction. Also depicted in each graph is the eccentricity vs slice number of the 5 cm sphere imaged while stationary with 3DCT. To produce Figure 3.16, the MATLAB function "STATS.Eccentricity" for a labeled binary image returns the eccentricity from each segmented cross sectional image. Despite the variability of the eccentricity seen in the first and last slices, phase dependant patterns appear for each type of motion. In each graph, the mean eccentricity of the stationary sphere remains low compared to its moving counterparts. For the mobile spheres, eccentricity increases with distance from the sphere's center for all motions and phases. There is a manifest difference between the SI and AP-LR motions. For SI motion the increase in eccentricity begins much closer to the sphere's center for all but the 00% and 50% phases, where motion is minimal. The eccentricities observed with AP-LR motion remain relatively small for the majority of slice locations and rise dramatically only for the smallest cross sections nearest the edges of the sphere. When the sphere is moving in all three directions at once, the eccentricity vs slice number graphs undulate, as if alternating between the SI and AP-LR shaped graphs. These motion specific patterns exert an influence over the *mean eccentricity*, indicating the metric is indeed meaningful.

The mean eccentricity is a metric indicating how well the 4DCT system is able to capture the true shape of a moving object.

Figure 3.16: Eccentricity vs slice number for 5 cm sphere undergoing different types of motion



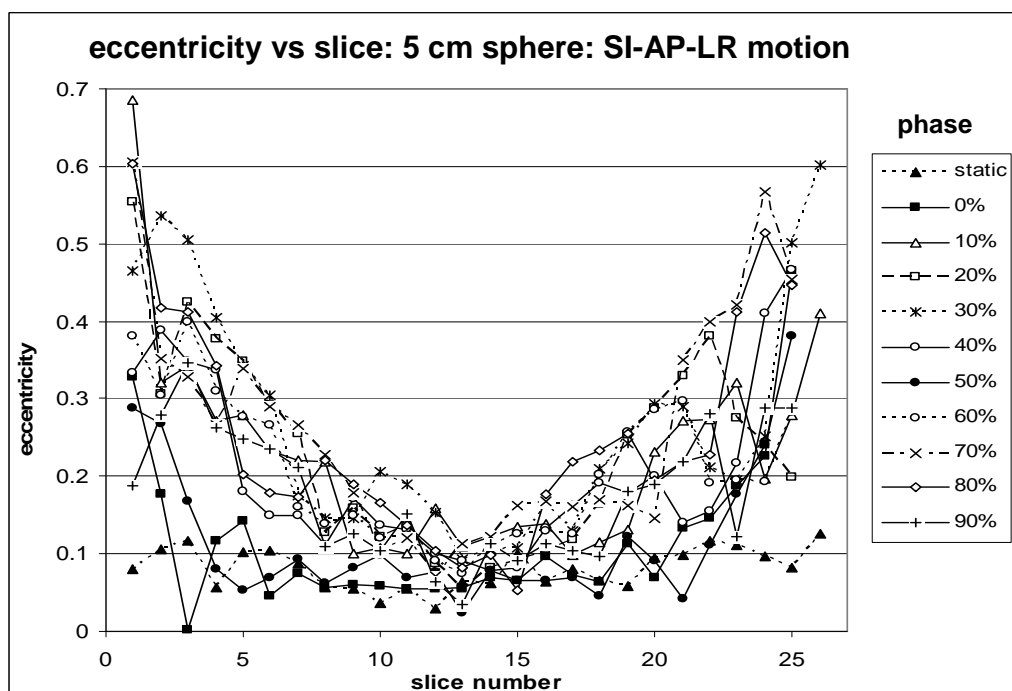


Figure caption: The slice number is the order of slices containing the phase image of the sphere, 1 being the first slice containing a cross sectional image of the sphere, 2 being the second slice of the phase image, 3 the third, and so on. Phase images of the 5 cm sphere consist of 24 - 26 slices. a.) For the SI motion, a 'V' shape appears for all phases except end inhale (00%) and end exhale (50%). b.) The eccentricity of the AP-LR motion is low for all phases of motion, and c.) when the sphere is moving in all three directions at once, the eccentricity vs slice graphs undulate, as if alternating between the SI and AP-LR shaped graphs. These motion specific patterns exert an influence over the mean eccentricity.

center-to-center distance:

Finding the center of the sphere (x, y, z) in each phase image entails a different approach for the transverse coordinates than for the axial coordinate. Within the Cartesian coordinates of the CT scanner, the z -axis coordinate is given in millimeters, with an arbitrarily defined reference point based on the scan bed position. Using ImageJ, the axial coordinate of the sphere's center z is located by manually identifying the slice containing a fiducial marker placed 3 cm from the center of the sphere on the phantom's moving platform. Thus, $z = z_{fid} + 30$ mm. For the transverse plane, the MATLAB function "STATS.Centroid" returns the center of mass coordinates of the cross sectional image on the middle slice of the segmented sphere. The pixel coordinates are then converted to millimeters to give the center of the phase image (x, y, z).

For each 4DCT acquisition, a static 3DCT image is acquired with the phantom parked in the 00% phase position (i.e. end inhale.) The center of the stationary sphere in this image (as determined above) provides a known position on the mechanical path of the sphere. From this position, the true phase locations may be determined mathematically. For ten reconstructed phases $i = 1, 2, 3, \dots, 10$, with a maximum total displacement of s , the advancement ds per phase in any of the three orthogonal directions (i.e. x , y , or z) is given by

$$ds = \frac{s}{2}(1 - \cos(i\pi/5)). \quad 3.2$$

Figure 3.17 shows the path of the 5 cm sphere moving in the SI-AP-LR directions with an amplitude of 1.5 cm in each of the three orthogonal directions. The calculated center positions are given as squares and the measured positions from the 4DCT phase images as circles. Thus, the *center to center distance* for each phase of motion i is simply the distance between the squares $(a,b,c)_i$ and the circles $(x,y,z)_i$,

$$d_i = \sqrt{(a_i - x_i)^2 + (b_i - y_i)^2 + (c_i - z_i)^2}. \quad 3.3$$

The *center-to-center distance* is a metric indicating how well the 4DCT system is able track the path of a moving object.

Figure 3.17: Imaged and ideal paths

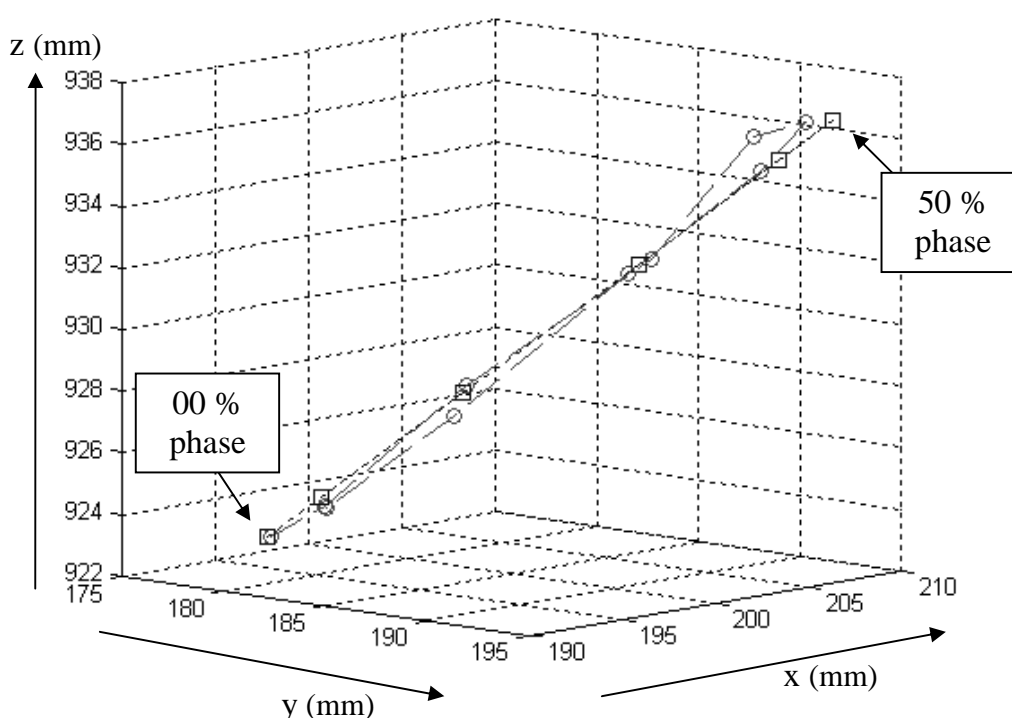


Figure caption: The calculated path is shown as squares and the imaged path (i.e. the center positions of the sphere in each phase image) is shown as circles. The only measured data point on the calculated path is the 00% phase, all other points are mathematically derived based off the mechanical motion of the phantom.

maximum distance to agreement:

The *maximum distance to agreement* between the segmented volume and the ideal volume is defined as the point to point distance between “like” locations on the surfaces of the segmented and ideal spheres. This is found by looking at each cross sectional image of the sphere and finding a point (m,n,o) on the perimeter of the segmented area furthest from the sphere’s center (x,y,z) . Angles ϕ and θ , which orient the point to the center of the segmented sphere, are then used to find the “like” point on the surface of the ideal sphere (e,f,g) (See Figure 3.19). The distance between the points (m,n,o) and (e,f,g) is determined for each slice of the segmented sphere (see Figure

3.19c), and the largest value is taken as the *maximum distance to agreement* for the entire volume. If the imaging system were perfect, (m,n,o) would coincide with (e,f,g). Thus, the maximum distance to agreement is another measure of how well the 4DCT system can localize a moving object. A more in depth description follows.

First, a binary image of the sphere is created in MATLAB using the threshold segmentation algorithm described earlier. The centers of the sphere (x,y,z) and its corresponding ideal sphere (a,b,c) are determined as above for the center to center distance. On each slice containing a cross sectional image of the sphere, the location of the furthest point on the segmented area's perimeter from the sphere's center (m,n,o) is found using the MATLAB function "STATS.Extrema". This function returns the eight extrema of a labeled binary image as shown in Figure 3.18.

Figure 3.18: MATLAB Definitions of Extrema

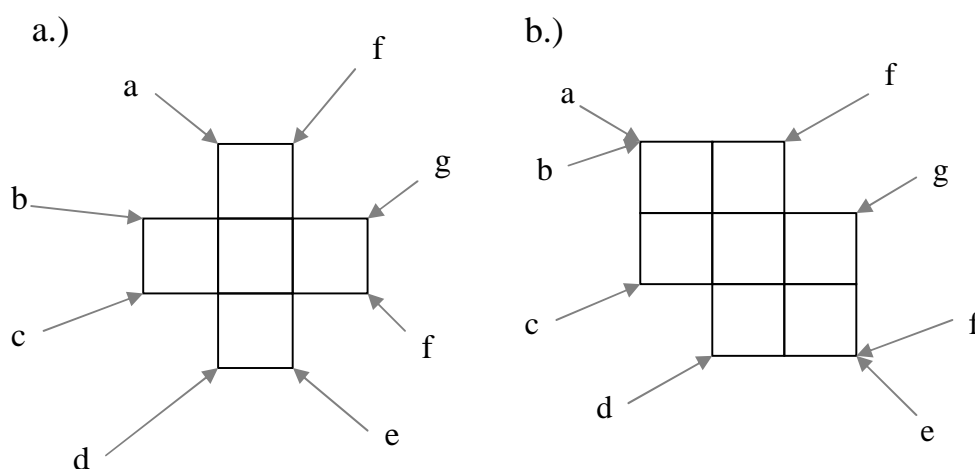


Figure caption: This figure illustrates the definition of extrema/return coordinates of the MATLAB function "STATS.Extrema" for two different labeled binary images: a.) each extremum is distinct, b.) some extrema points (e.g., top-left and left-top) are identical.

Each set of returned coordinates is examined to determine which one gives the largest distance d from the center of the segmented sphere using

$$d = \sqrt{(m-x)^2 + (n-y)^2 + (o-z)^2} .^{25} \quad 3.4$$

Once the point (m,n,o) is located, the angle φ created between this point, the center of the segmented sphere, and the center of the segmented cross sectional area on the slice containing (m,n,o) is calculated using

$$\varphi = \cos^{-1}\left(\frac{z-o}{d}\right). \quad 3.5$$

²⁵ Although a calculation of distance between the point (m,n) and the center of the segmented slice at (x,y) would have sufficed, the distance between (m,n,o) and (x,y,z) reveals the same coordinates for (m,n,o) while its value is also used to find φ .

Please see Figure 3.19b. The angle θ created by the point, the center of the segmented area and the y-axis is

$$\theta = \tan^{-1}\left(\frac{m}{n}\right). \quad 3.6$$

These angles are then applied to the center of the ideal sphere (a,b,c) to find the “like” location (e,f,g) on its surface.

If r is the radius of the ideal sphere centered at (a,b,c), to find the point (e,f,g), the axial coordinate g is simply

$$g = c - (r \cos(\theta)). \quad 3.7$$

To locate the transverse axis coordinates (e,f), the radius l of the ideal cross sectional area at g must be found

$$l = \sqrt{|r^2 - (g - c)^2|}. \quad 3.8$$

Since the segmented sphere and the ideal sphere may be in any orientation with respect to one another:

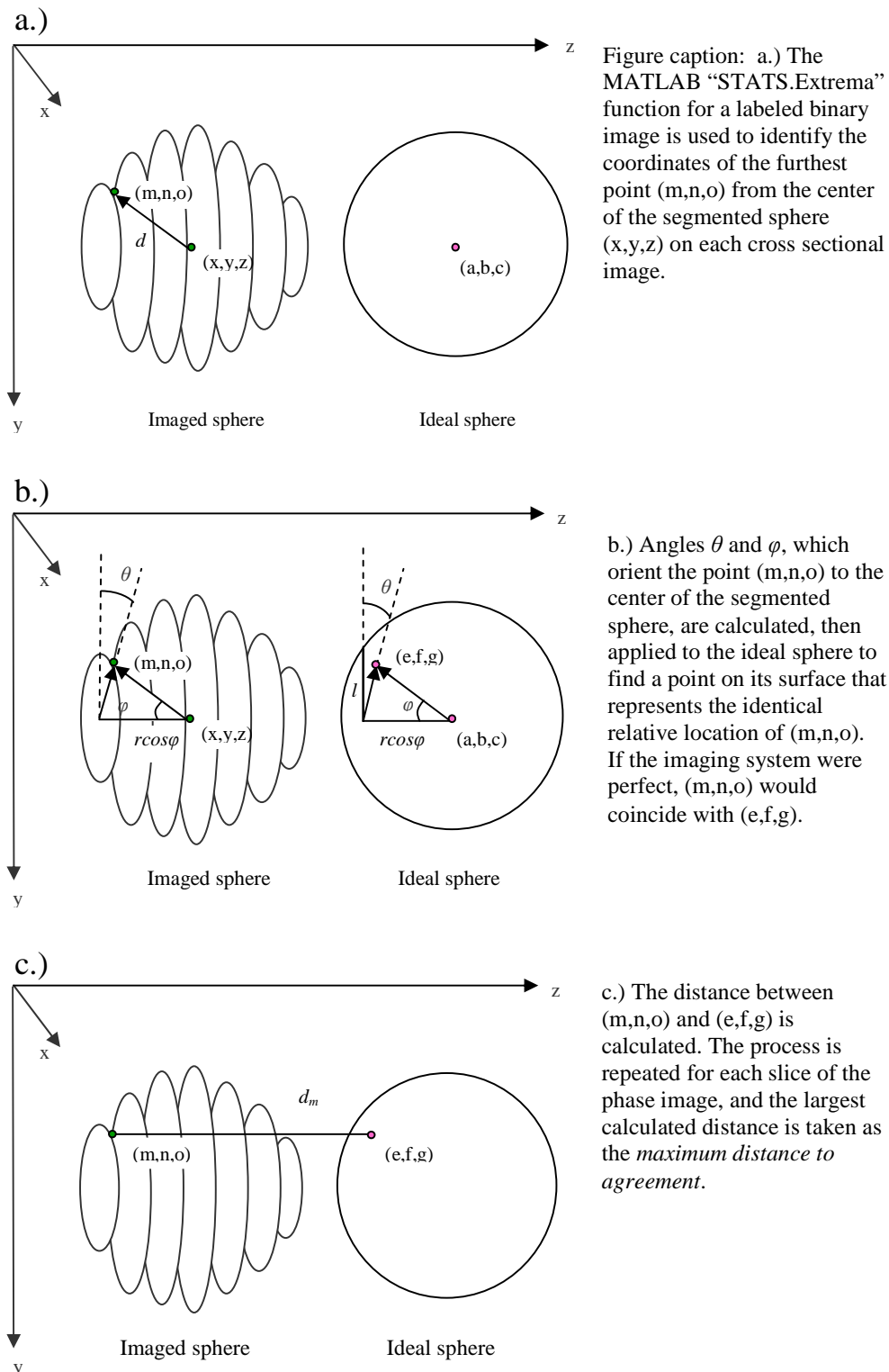
$$\begin{aligned} e &= a + l \sin(\theta) \\ f &= b + l \cos(\theta) \end{aligned} \quad \left\{ \text{for } n < 0, \right. \quad 3.9$$

and

$$\begin{aligned} e &= a - l \sin(\theta) \\ f &= b - l \cos(\theta) \end{aligned} \quad \left\{ \text{for } n \geq 0. \right. \quad 3.10$$

The distance between (m,n,o) and (e,f,g) is then calculated (as above for d). This is done for every slice of the volume. The largest distance for the entire volume is then taken as the maximum distance to agreement for that phase image.

Figure 3.19: Diagram of maximum distance to agreement calculation



The coincidence index (24):

The *coincidence index* is the ratio of the intersection of the ideal sphere and the segmented sphere to the union of the two

$$\frac{A \cap B}{A \cup B}, \quad 3.11$$

where A is the imaged sphere, and B is the ideal sphere (see Figure 3.20). A binary mask of the ideal sphere is constructed by creating a circular mask of radius l for each slice location intersecting the ideal sphere (where l is determined as above (see Figure 3.19b) from Equation 3.8 where g is simply the slice location). For each slice of the 4DCT phase image, the intersection of the binary segmented image and the binary ideal image is calculated, then, all the intersections are summed over all slices containing the imaged sphere and the binary mask of the ideal sphere to create the numerator of the index. Likewise, the union of the segmented and ideal cross sections are calculated and summed to create the denominator. Ideally, if the imaging system works perfectly, the index equals unity.

The *coincidence index* is a metric indicating how well the 4DCT system is able to capture the size, shape, and position of a moving object.

Figure 3.20: The coincidence index vs fractional overlap

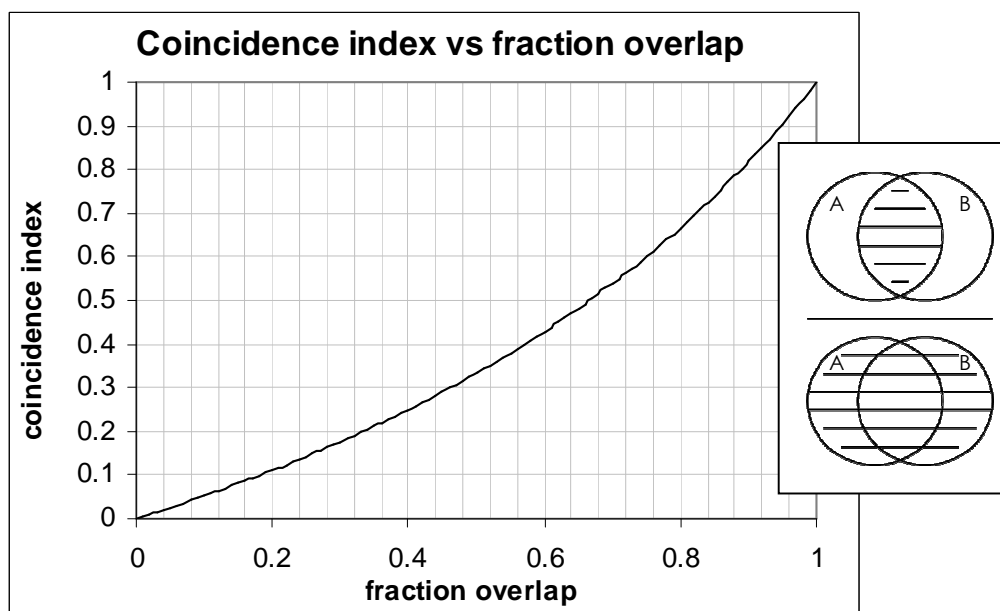


Figure caption: The relationship between the fractional overlap of areas and the coincidence index is not linear. Insert: A is the imaged sphere and B is the ideal sphere. It is irrelevant which is which.

Sources of Error

There are three potential sources of error in each metric: resolution error (e_r), threshold error (e_t), and phantom error (e_p). For those metrics which are independent of location within the cartesian coordinates of the CT scanner, only resolution and threshold errors contribute uncertainties, and these are added in quadrature

$$error = \sqrt{(e_r^2 + e_t^2)}. \quad 3.12$$

For those metrics calculated with respect to a specific location within the CT scanner, the uncertainty introduced by the phantom must be included

$$error = \sqrt{(e_r^2 + e_t^2 + e_p^2)}. \quad 3.13$$

Resolution Error:

All of the data acquired from the 4DCT data sets are taken from binary images derived by segmenting the data sets using MATLAB. The attributes of these segmented images are direct returns from functions found in the imaging toolkit, such as “STATS.Centroid” or “STATS.Area”. Since the segmented shape of a 4DCT phase image is constructed from discrete pixels or voxels, the resolution error is the uncertainty in each attribute due to the finite size of these pixels or voxels. The size uncertainties are therefore propagated through to the metric used to evaluate the accuracy of the 4DCT imaging system.

For eccentricity, an assumption is made that the semi-major and semi-minor axes (d_{max} and d_{min} , respectively) bisect one another:

$$ecc = \sqrt{1 - \left(\frac{d_{min}}{d_{max}}\right)^2}. \quad 3.14$$

The error in eccentricity is

$$\partial ecc = \frac{\left(\frac{d_{min}}{d_{max}}\right)^2 \sqrt{\left(\frac{\partial d_{min}}{d_{min}}\right)^2 + \left(\frac{\partial d_{max}}{d_{max}}\right)^2}}{ecc}. \quad 3.15$$

Here, the error contributions of the independent measurements of the semi-major and semi-minor axes are added in quadrature. The resolution error in each of these measurements ∂d_{min} is half a pixel dimension (i.e. $1/2 (0.78) = 0.39$ mm). The metric of evaluation is *mean eccentricity*, so the metric's error due to resolution is simply the mean of the eccentricity errors.

With the *center to center distance*, the centroid of the center slice (x,y) is calculated by center of mass. Since every pixel is assigned an identical value (i.e. a weight of boolean 1), this reduces to a simple calculation of the mean x and y coordinates of all the pixels included in the cross sectional image. For example, the mean x coordinate is

$$x_{mean} = \frac{1}{N} \sum x_i. \quad 3.16$$

With the error in each x coordinate being $1/2$ of a pixel dimension, the error in this calculation is also $1/2$ of a pixel dimension (i.e. 0.39 mm). The uncertainty in the z-axis coordinate is $1/2$ slice thickness (i.e. ± 1 mm). Since the *center to center distance* is

calculated between two points with identical resolution uncertainties, the error introduced by resolution in the *center to center distance* is

$$\partial_{ccd} = \frac{|(a-x)|(\sqrt{2}\partial a) + |(b-y)|(\sqrt{2}\partial b) + |(c-z)|(\sqrt{2}\partial c)}{ccd}. \quad 3.17$$

For the maximum distance to agreement, the uncertainty in pixel size affects the true location of the extrema to $\pm 1/2$ of a pixel. Propagation of this error through the calculation steps to find the like point on the ideal sphere (i.e. Equations 3.5 - 3.10) has a tendency to “blow up” due to multiple divisions by small numbers arising from the trigonometric functions. Thus, the resolution uncertainty in locating the extremum point (m,n,o) is simply translated directly to the uncertainty of the like point (e,f,g), with the error in the distance between the two points being

$$\partial_{dist \max} = \frac{|(m-e)|(\sqrt{2}\partial m) + |(n-f)|(\sqrt{2}\partial n) + |(o-g)|(\sqrt{2}\partial o)}{dist \max}. \quad 3.18$$

The error introduced into the coincidence index due to resolution uncertainty is found by moving the location of the ideal sphere + 1 mm in the z-direction and calculating the index, then the ideal sphere is moved -1 mm in the z-direction and the index is calculated again. This procedure is also performed by moving the ideal sphere 0.39 mm up and down in the x and y directions, although the error introduced by this in-plane maneuvering does not significantly affect the total error. The error due to resolution is then taken as plus or minus one half of the extreme index values.

With the % volume difference, the measured volume of the sphere is acquired by counting up all the voxels included in the segmented image of the sphere, N , and multiplying this number by the dimensions of a single voxel. When voxels are used to make distance measurements, the location of any point within the voxel is uncertain. However, the location of any point, and indeed, the location of the voxels themselves is inconsequential in the calculation of volume occupied by all the voxels included in the segmented phase image. This is because the volume of a voxel is a known mathematical construction. Therefore, there is no resolution error in this measurement of volume. The only question is whether any given voxel is included in the segmented image or is not included, and this is a thresholding issue.

Threshold Error –Attribute Mapping:

Since the segmented shape and volume of a 4DCT phase image are sensitive to thresholding, the error contribution due to thresholding for each attribute as well as the metrics utilizing these attributes are calculated by mapping each attribute’s response to threshold.

To find the error in a given attribute with respect to threshold, first, select slices of the image (see below) are segmented with a range of thresholds. Beginning with 120 s-HU and incrementing by 10 s-HU, the slices are segmented until the threshold becomes too high to segment the sphere as a single object. For each threshold, the attribute and percent local contrast of the sphere are graphed to create a map of the value of each attribute as a function threshold. Next, the attribute’s maximum and minimum values within the small range of thresholds actually used to segment the 4DCT image (e.g. ~ 40 - 45% local contrast) are found. The error for each attribute is taken to be the difference in these values divided by two (i.e. $\pm (\max - \min)/2$).

The slices selected for attribute mapping are the first slice (or edge slice) of the sphere, the slice in the middle of the sphere, and the slice halfway between the center and the edge of the sphere. The attribute of eccentricity varies greatly depending on which slice is mapped due to motion artifacts and partial volume effects. For this attribute, the error is calculated from the attribute map of the slice halfway between the edge and the center slices of the segmented sphere, as this slice is the most representative of the entire sphere. It should also be noted that for many of the attributes, the response to thresholding on this slice is quite similar to that of the center slice. The error in the sphere's center position is, of course, taken from the attribute map of the center slice. For the attribute of volume, the entire sphere is segmented and the cross sectional areas from all the slices are summed to create the attribute map of volume as a function of threshold; the error in volume is then calculated as above.

For the maximum distance to agreement, thresholding error is determined in a similar fashion. In order to avoid the error propagation issues mentioned earlier (i.e. finding the threshold uncertainty in the extrema (m,n,o), then propagating this uncertainty through Equations 3.5 -3.10), a slightly different tack is adopted. The entire sphere is segmented to one threshold and the distance to maximum agreement is calculated. This is done repeatedly over the specific range of thresholds used to segment that phase image for the metric measurements (i.e. typically 40 - 45% local contrast). The error in maximum distance to agreement due to thresholding is then just the range of these distances divided in half (i.e. again, $\pm (\max - \min)/2$). This approach is also employed for the coincidence index –the center index is calculated with the sphere segmented to a single threshold, and this is done repeated for all the thresholds used in the metric measurement. The error due to threshold is again, just the difference in the two extreme values divided in half.

Phantom error:

For those metrics which are calculated against the location of the ideal sphere (i.e. *center to center distance*, *maximum distance to agreement*, and the *coincidence index*), some error is introduced by the phantom's inability to place the sphere exactly at the correct phase location as determined by the respiratory monitoring system. The error in the dynamic phase positions of the phantom are estimated for each set of cams by calculating the distance between the center positions of a sphere imaged with 3DCT while the phantom is parked at each of the 10 phase locations (i.e. manually cranked to each phase position, creating a step-and-shoot phase image) and the ideal position of each phase calculated from the mechanical motion of the phantom. This calculation is identical to the *center to center distance* metric, producing a distance of discrepancy between the true position of the phantom and its supposed position for each of the ten phase locations.

These measurements utilized the 5 cm sphere, and rather than determine this error for each specific type of motion (i.e. SI, AP-LR, and SI-AP-LR), just the SI-AP-LR motion is chosen, as the dynamic interplay of all the phantom's moving components should induce maximum variability. Figure 3.21 shows the step-and-shoot phase positions (circles) compared to the calculated path of the phantom (squares) for the 1.0 cm cams.

The distance between the measured phase locations $(x,y,z)_i$ and the ideal phase positions $(a,b,c)_i$ is simply

$$p_i = \sqrt{(a_i - x_i)^2 + (b_i - y_i)^2 + (c_i - z_i)^2} . \quad 3.19$$

Figure 3.21: The step-and-shoot data for the 1 cm cams and the ideal path of the phantom

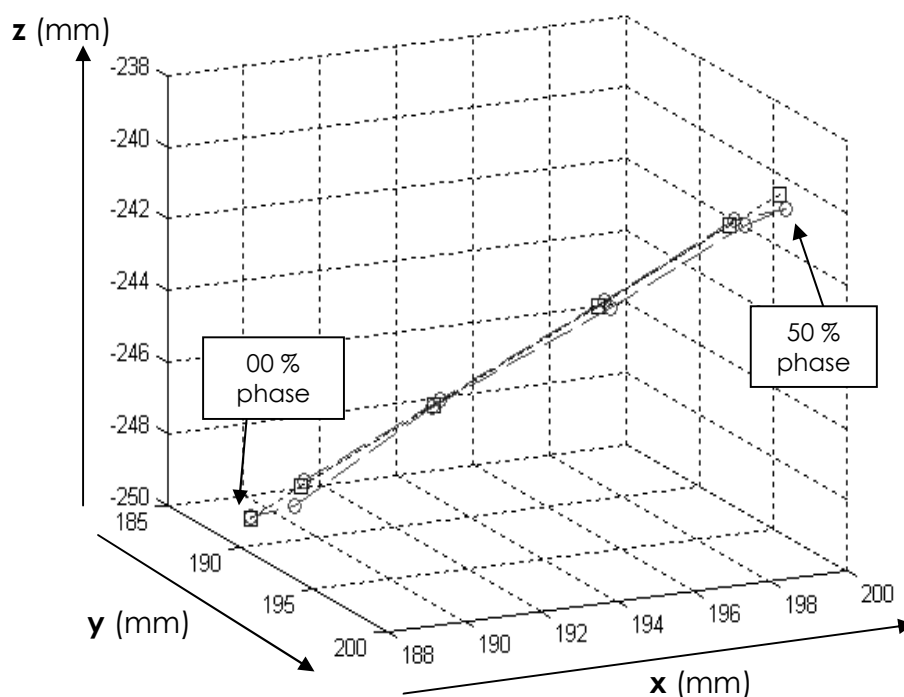


Figure caption: The step-and-shoot path is shown as circles and the ideal path with squares. All points on the ideal path are mathematically calculated based on the mechanical motion of the phantom in reference to the measured 00% phase point.

Errors in this calculation are due to locating the centers of the ideal and imaged spheres due to resolution and thresholding (just as discussed earlier for the *center to center distance*). However, there is a third source of error in this measurement: the uncertainty arising from differences in phase position between when the phantom is parked and when it is in motion. The error arising from the dynamic phantom e_m is estimated by measuring the mean orthogonal distance between the step-and-shoot path of the phantom and its dynamic path. Figure 3.22 shows the orthogonal radiographic projections (i.e. AP (the xz plane) and LR (the zy plane)) of the path produced with all three 0.5 cm cams working together (i.e. SI-AP-LR motion). Small radio-opaque markers are placed on the phantom's imaging platform, and, with the phantom in motion, radiographs are taken with the x-ray capabilities of an Oldelft Simulix-MC radiotherapy simulator (Oldelft Corp of America, Fairfax, VA, USA) using a technique of 40 kVp and 63 mA for a duration of 6.3 s, sufficient time to capture in excess of one complete period of motion. The images are recorded using Agfa CR RT 1.0 (low dose) computed radiography imaging plates (Agfa Corporation, Ridgefield Park, NJ, USA). Figure 3.23 shows 10 locations along the path traced out by the moving phantom in the orthogonal radiographs (squares) plotted with the 10 phase locations of the step-and-shoot data for the 1 cm cams (circles).

Figure 3.22: Orthogonal radiographs of the phantom's motion in the in the SI-AP-LR direction

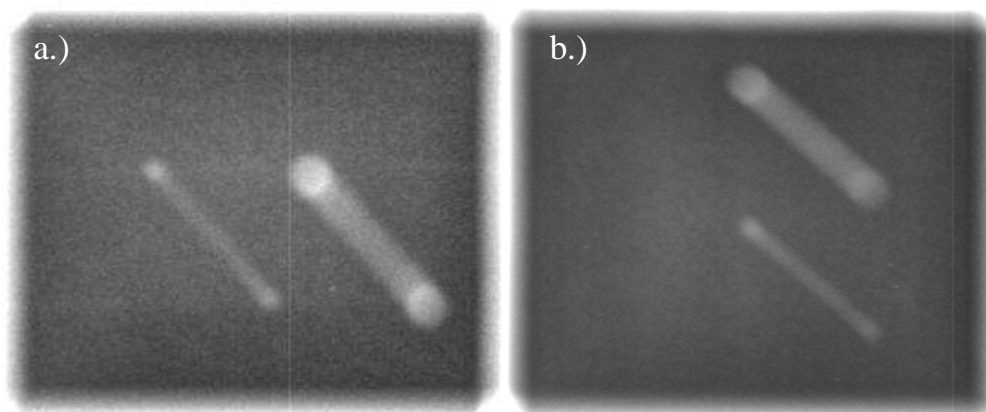


Figure caption: Radiograph of two fiducial markers on the moving platform of the phantom. a.) AP (xz plane (coronal view)), b.) LR (zy plane (medial view)). The lengths of these paths appear to differ only due to differences in magnifications. Magnification factors necessary for a quantitative analysis of the radiographic images are obtained by measuring the total displacement of the motion platform in each dimension with a dial gauge accurate to ± 0.01 mm (Mitutoyo Corporation, Mississauga, Ontario, Canada).

Figure 3.23: Step-and-shoot data plotted with points taken from the orthogonal radiographs of the moving phantom: 1 cm cams.

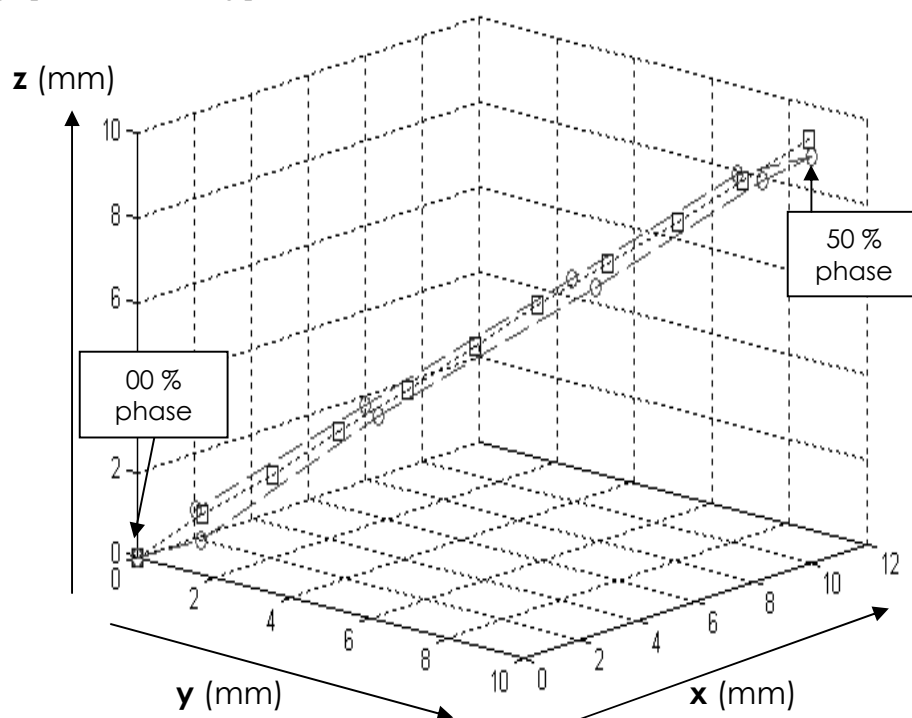


Figure caption: The squares are data points from the radiograph of the moving phantom, and the circles are the step and shoot data. The error in phantom motion arising from discrepancies in phase positions between when the phantom is parked and when it is in motion are estimated by the average distance between these two lines, measured orthogonal to the radiograph trace.

The total error in phantom motion is then

$$e_p = p \pm \sqrt{(e_r^2 + e_t^2 + e_m^2)}, \quad 3.20$$

but is simply taken as $p + \sqrt{(e_r^2 + e_t^2 + e_m^2)}$ to overestimate the error introduced by the phantom.

For the *center to center distance* and *distance to maximum agreement* metrics, this error is added in quadrature with the resolution and threshold errors. For the *coincidence index*, the error due to phantom uncertainty is found by moving the location of the ideal sphere e_p in the direction of the imaged sphere's centroid and calculating the index, then the ideal sphere is moved e_p away from the imaged sphere and the index is calculated again. The error due to phantom motion is then taken as plus or minus one half of these values. This error is then added in quadrature to the *coincidence index's* resolution and thresholding errors.

Results of Quantitative Measurement

The full set of data for all three spheres undergoing all types of motion using both respiratory monitoring systems, not including the static reference scans, comes to 540 images (i.e. 3D volumes). The RPM system was unable to detect the SI motion with the 0.5 cm cams, reducing the number of acquired scans to 510. In addition, due to mechanical failure of the phantom, acquisition of data for the 3 & 5 cm spheres moving in the SI-AP-LR direction using the 1.5 cm cams with the RPM system was abandoned, bringing the total number of inspected images down to 490. This should not cause concern, however, since acquisition with both the Philips' and Varian's respiratory monitoring systems is redundant.

Phantom Error

Estimates of the error introduced by the motion phantom are calculated from step-and-shoot measurements of the 5 cm sphere undergoing motion in the SI-AP-LR directions.

Table 3.2 : Distance between the step and shoot and the calculated phase positions

	distance from ideal position p (mm)		
	0.5 cm cams	1.0 cm cams	1.5 cm cams
00%	0.03 ± 0.77	0.06 ± 0.59	0.01 ± 0.56
10%	0.04 ± 1.6	0.26 ± 0.99	0.46 ± 1.52
20%	0.38 ± 1.43	0.35 ± 0.93	0.58 ± 1.17
30%	0.55 ± 1.28	0.34 ± 0.97	0.42 ± 1.28
40%	0.57 ± 0.70	0.37 ± 0.91	0.15 ± 2.65
50%	0.58 ± 0.72	0.29 ± 0.77	0.78 ± 1.68
60%	0.63 ± 0.71	0.62 ± 0.86	0.30 ± 1.70
70%	0.24 ± 2.42	0.61 ± 0.88	0.66 ± 1.42
80%	0.14 ± 3.00	0.48 ± 0.90	0.85 ± 1.79
90%	0.37 ± 0.79	0.38 ± 0.91	0.64 ± 1.21

Table captions: Errors are due to uncertainties in imaging the stationary sphere (i.e. thresholding and resolution errors). The largest errors arise from significant discrepancies in the z-axis direction (i.e. when the center of the segmented sphere in the step-and-shoot phase image is on a different slice than the calculated location.)

The distance between the measured phase locations from the step-and-shoot data and the ideal phase positions based on the mechanical motion of the phantom are given in Table 3.2. Additional error in this measurement arises from discrepancies between phase positions when the phantom is stationary and when it is in motion. For each of the three cam sizes, the mean distance of all ten step-and-shoot phase positions from the path traced out by the moving phantom in orthogonal radiographs is given in Table 3.3. Table 3.4 gives the total phantom error e_p for each phase of motion for each cam size.

Table 3.3: The mean distance between the step-and-shoot data and the dynamic path of the phantom taken from the orthogonal radiographs

	motion error e_m (mm)		
	0.5 cm cams	1.0 cm cams	1.5 cm cams
distance (mm)	0.55	0.43	0.68

Table caption: Errors arising from the differences in phase positions between the stationary step-and-shoot images and the moving phantom. For the 0.5 cm cams, the largest difference occurs near the 20 and 90 % phases. For the 1 cm cam data, it is the 20% and 50% phases. With the 1.5 cm cams, the largest distance corresponds to the 80% phases.

Table 3.4: The error introduced by the phantom for each phase of motion for each cam size

	e_p (mm)		
	0.5 cm cams	1.0 cm cams	1.5 cm cams
00%	0.97	0.78	0.89
10%	1.73	1.34	2.12
20%	1.91	1.37	1.93
30%	1.94	1.40	1.87
40%	1.46	1.37	2.89
50%	1.48	1.17	2.59
60%	1.53	1.58	2.13
70%	2.71	1.59	2.24
80%	3.19	1.48	2.76
90%	1.33	1.39	2.03

Table captions: The total phantom error for each phase of motion and each cam size are the values from Table 3.2 plus the errors. For the 0.5 cm cams, the greatest phantom error occurs in the 80% phase, and for the 1 cm cams, the 20% and 50% have the largest phantom errors. For the 1.5 cm cams, it is the 40% and 70% phases.

Catalogue of Artifacts

It is not the intention of this study to directly quantify the artifacts of 4DCT, however, some introduction to the artifacts seen in the data is warranted. Recall the functional parameters of motion artifacts for a point-like object when motion is constrained to the imaging plane:

R –the radius of the tube’s rotation

r – the amplitude of the sphere’s oscillation

ω –the rotational frequency of the tube (i.e. $2\pi/\tau$, where $\tau = 0.5$ s)

Φ_0 –the initial acquisition angle of the tube

ω_r – the frequency of the object’s oscillation

ζ –the initial phase of the object’s motion

In this experiment, R , ω , and ω_r are fixed, Φ_0 and ζ are random, and only r is a controlled variable (i.e. the different cam sizes). Since the frequency of oscillation remains fixed, increasing r essentially increases the object’s speed and, thus, the small portion of its amplitude captured by the image acquisition. Obviously, the spheres are not point-like, and their size will affect the relative severity of the residual motion artifacts. In-plane and transverse plane motions produce distinctive artifacts, however, the path of the phantom fixes the relationship of these motions. Thus, the resulting menagerie of possible shapes is constrained with respect to their general shape, but not in orientation (which is a function of Φ_0). The following examples are all fast phases taken from 1.5 cm cam data sets, and are windowed and leveled for clarity.

In pseudo-Housefield units, the density of the static acrylic spheres is about 1150 s-HU, empty space is around 25 s-HU, and the Styrofoam blocks on which the spheres and the reference object sit are about 50 s-HU. Figures 3.24, 3.25, and 3.26 are slices through the 1, 3, and 5 cm spheres, respectively, imaged while undergoing SI motion only. The partial projections resulting from the changes in cross section seen in the imaging plane create this distinctive pinwheel artifact. In all three figures, the spiraling-out of density is greatest for slices near the edge of the spheres where the cross section changes the quickest (2). As labeled in Figures 3.24, 3.25, and 3.26, the density of each arm of the pinwheel is the same, reflecting the symmetry of the objects. The center slice of the 1 cm sphere (Figure 3.24) is much blurrier than those of the 3 and 5 cm spheres (Figures 3.25 and 3.26, respectively). This is due to the extent of motion captured in the phase image, which although the same for each sphere, is larger compared to the diameter of the 1 cm sphere.

Figure 3.24: 1 cm sphere undergoing motion in the SI direction (Bellows 80% phase, 1.5 cm cams)

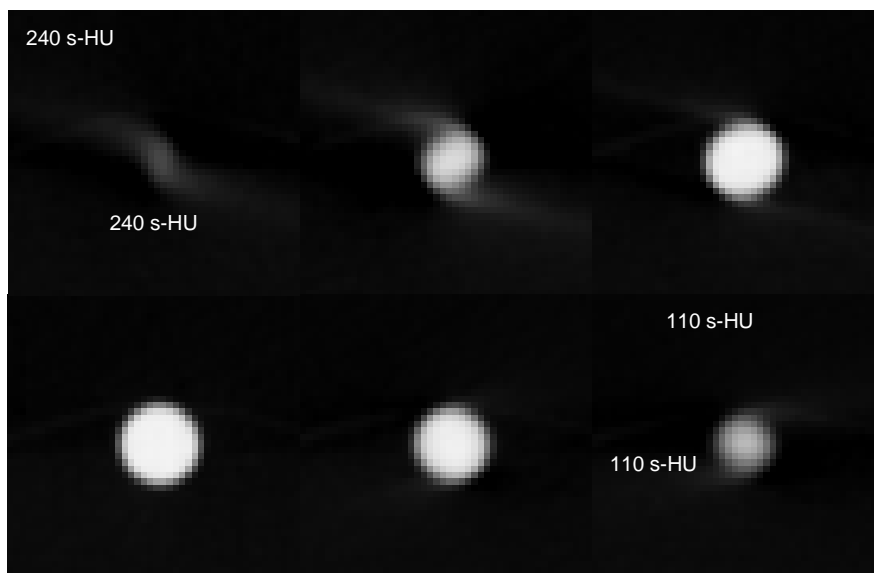


Figure caption: Slices through the 1 cm sphere undergoing SI motion imaged with 4DCT. The density of the pinwheel artifacts are symmetric because the object is symmetric.

Figure 3.25: 3 cm sphere undergoing motion in the SI direction (RPM 30% phase, 1.5 cm cams)

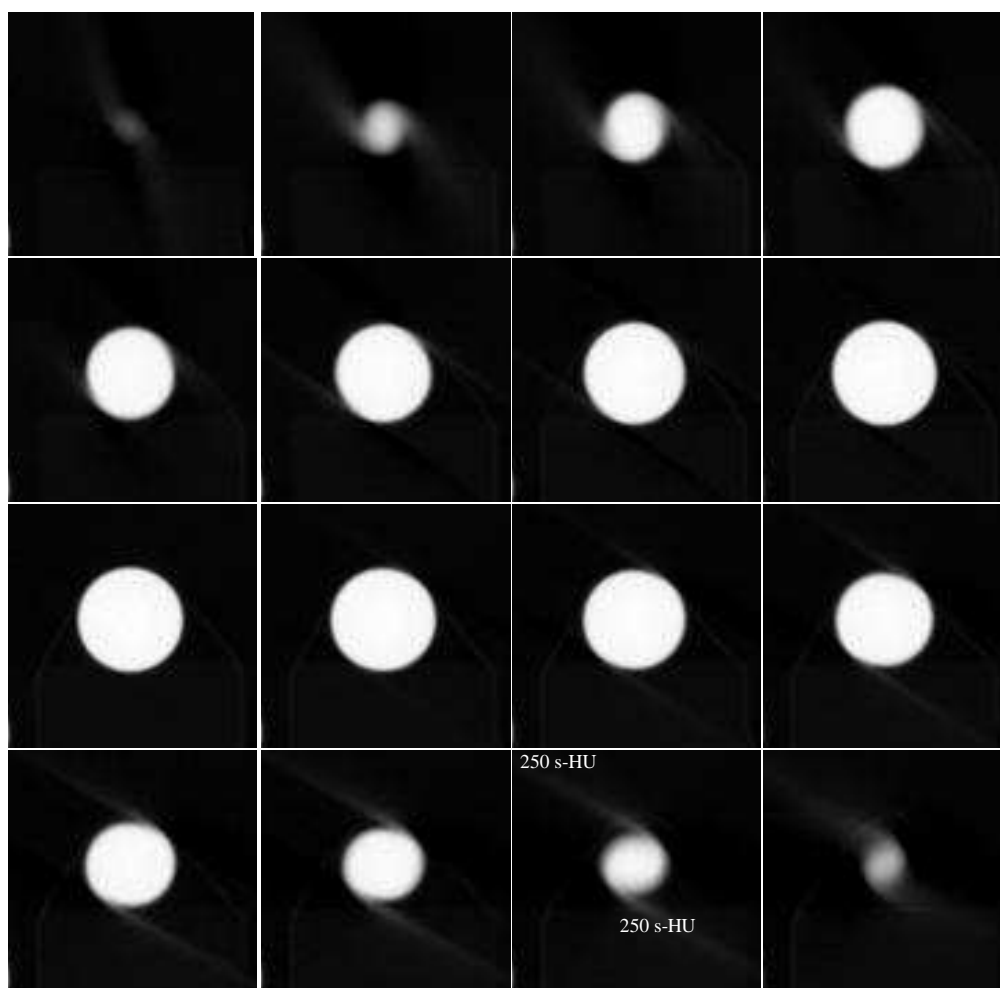


Figure caption: Slices through the 3 cm sphere undergoing SI motion imaged with 4DCT. The severity of the artifact is greatest at the edges due to the rapidly changing cross section of the sphere in the imaging plane.

Figure 3.26: 5 cm sphere undergoing motion in the SI direction (RPM 30% phase, 1.5 cm cams)

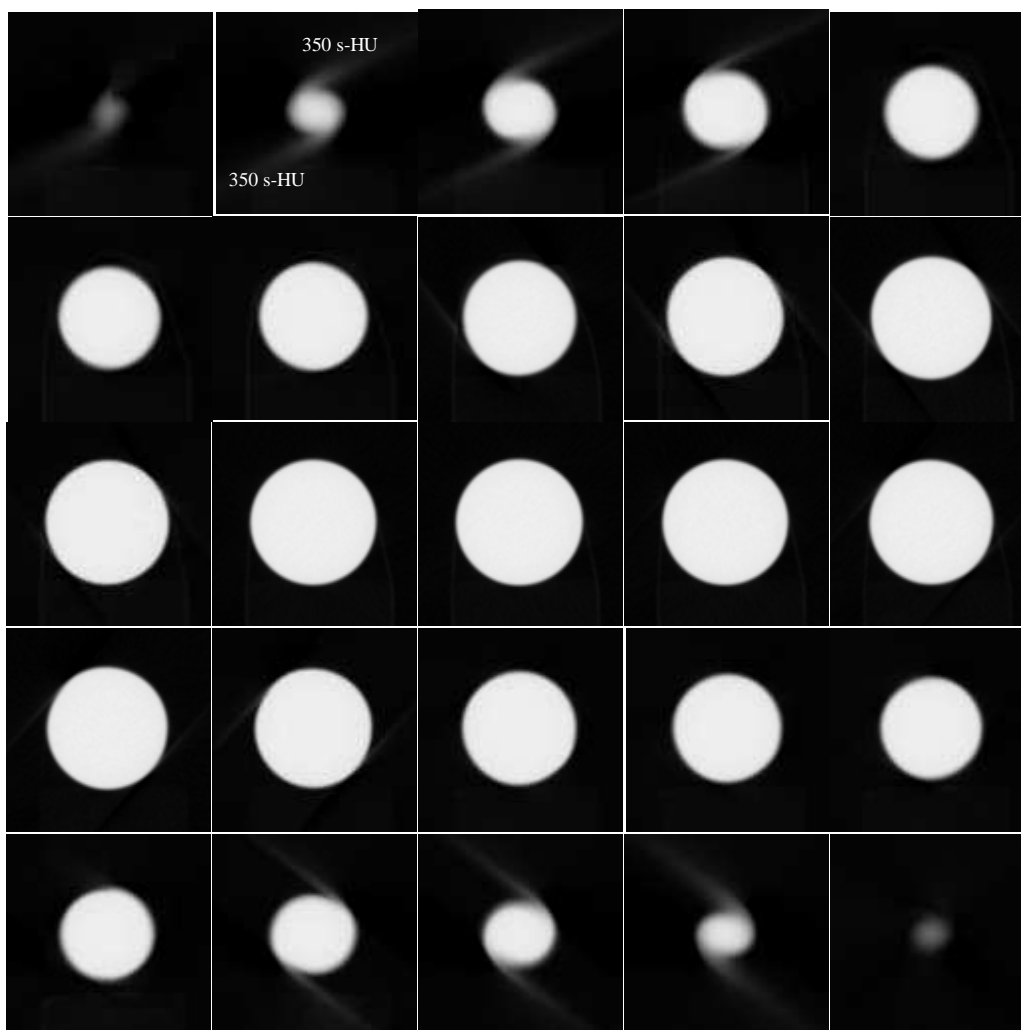


Figure caption: Slices through the 5 cm sphere undergoing SI motion imaged with 4DCT (one of the center slices has been removed for convenience). There are plenty of crisp center slices because the motion captured in each image is small compared to the extent of the object. The pinwheel artifact is larger for the big sphere just because its cross section is changing faster at the edges.

The center slices of the 5 cm sphere are the crispest since its residual motion is small compared to its diameter. The size and density of the pinwheel artifact increases with sphere size due to the increasingly rapid change in cross section towards the edges. The orientation of the spiraling arms is determined by the initial acquisition angle Φ_0 , which is random for each slice of the reconstructed volume. Although not shown, these partial projection artifacts are absent in the static images (157).

Figures 3.27, 4.28, and 3.29 show the 1, 3, and 5 cm spheres undergoing AP-LR motion. The residual motion artifacts shape the sphere like a horseshoe crab. For each sphere, a density shadow of 0 s-HU, about 25 s-HU below background, is a direct result of the filter function optimized for static objects (33,2). In each of the AP-LR phase images shown here, at least one slice has the density shadow overlaying the supporting

Styrofoam block, making the shadow a full 50 s-HU below background in this region. It has been noted that this mis-assignment of density is more severe for small spheres (32), which is certainly true in this study as well. Figure 3.27 shows a background density of 150 s-HU opposite the shadow for the 1 cm sphere, while Figures 3.28 and 3.29 show densities opposite the shadow of 110 s-HU for the 3 cm sphere and 90 s-HU for the 5 cm sphere, respectively. Inspection of these background discrepancies in the 5 cm sphere slices shows that the smaller cross sections have greater asymmetry. (Please see Figure 3.29).

Figure 3.27: 1 cm sphere undergoing motion in the AP-LR direction (Bellows 20% phase, 1.5 cm cams)

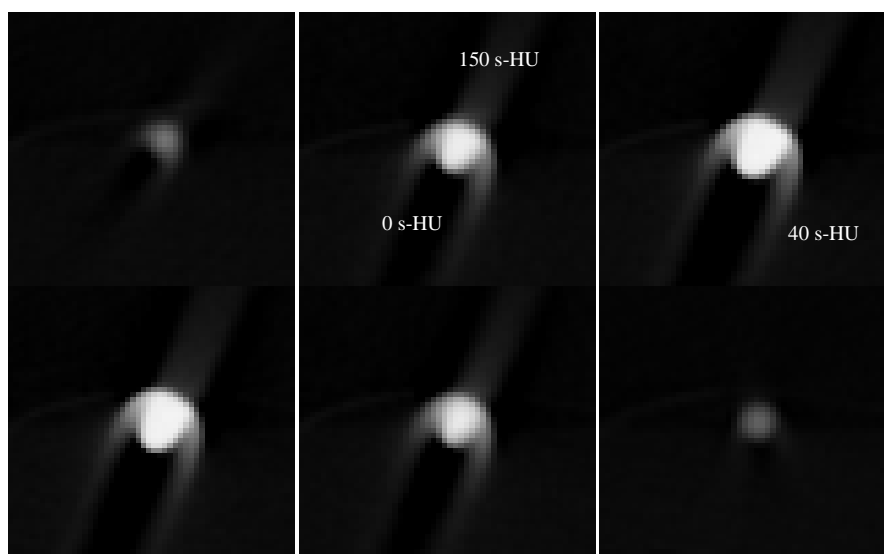


Figure caption: Slices through the 1 cm sphere undergoing AP-LR motion imaged with 4DCT. The distinctive horseshoe crab-shaped artifact is most noticeable for the smaller sphere. The disparity in background values between the shadow and the face of the crab is 150 s-HU (i.e. 150 HU).

Figure 3.28: 3 cm sphere undergoing motion in the AP-LR direction (Bellows 70% phase, 1.5 cm cams)

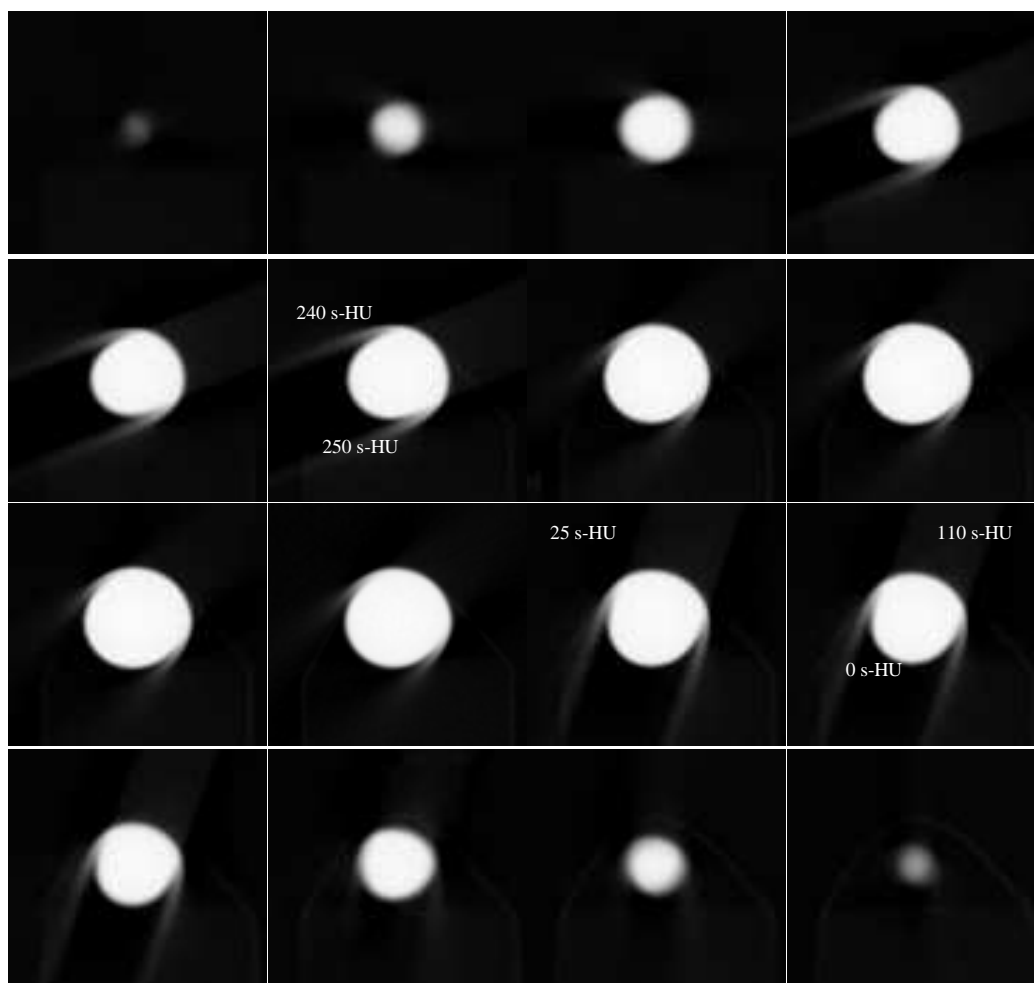


Figure caption: Slices through the 3 cm sphere undergoing AP-LR motion imaged with 4DCT. The slices for the larger sphere are more circular, and the disparity in background values is only about 110 s-HU. The densities of the horns of the artifact are not completely symmetric like they are for the pinwheel artifact. However, the horn densities are still very similar.

Figure 3.29: 5 cm sphere undergoing motion in the AP-LR direction (Bellows 30% phase, 1.5 cm cams)

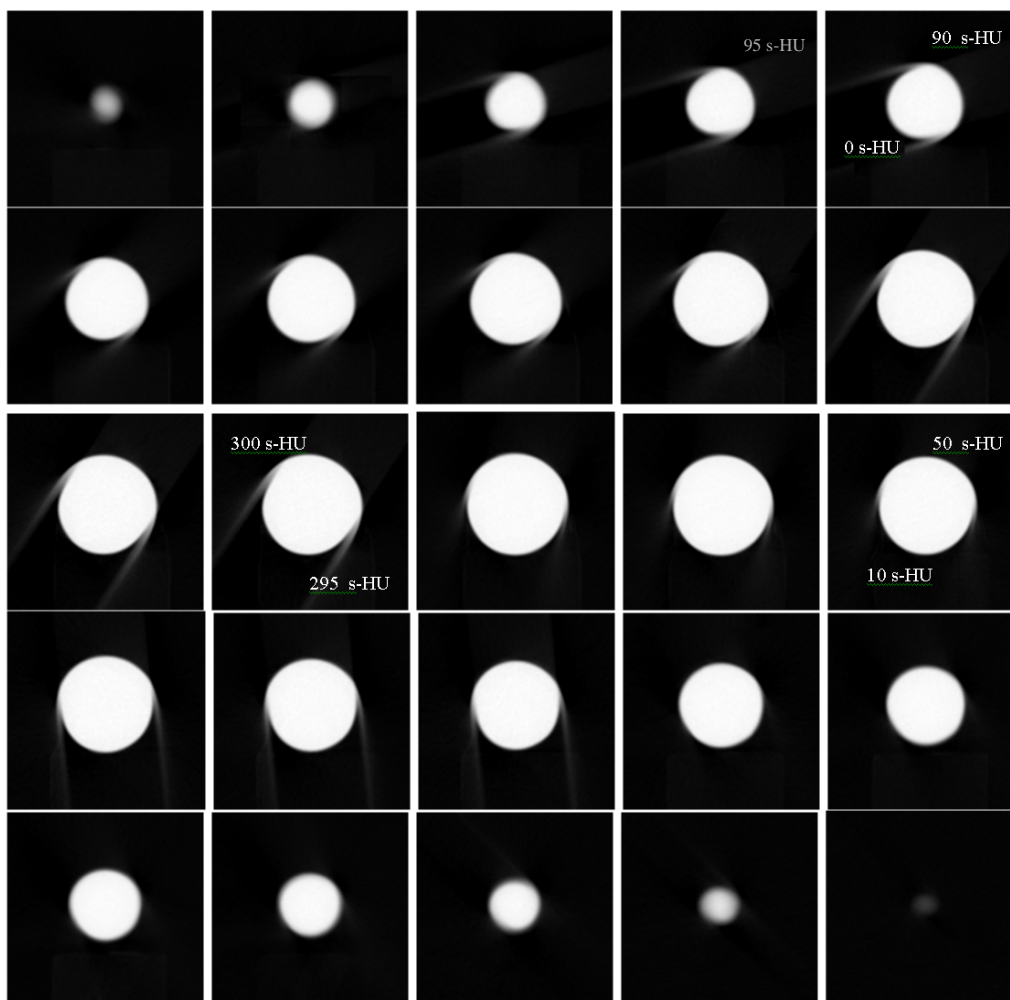


Figure caption: Slices through the 5 cm sphere undergoing motion in the AP-LR directions imaged with 4DCT. The AP-LR motion induced horseshoe crab artifacts have the least impact on the largest sphere; at its worst, the asymmetry in background values is only about 95 s-HU.

The severity of the artifact derives from both the disparity of densities between the object and its background and the size of the cross sectional image. If the motion of the object is large compared to the cross section image, the displacement of densities is accentuated. Partial volume effects which decrease the contrast between object and background diminish the severity of misplaced densities. Thus, for spheres, the largest artifacts appear in slices towards the edges, but not the edge slices themselves. Unlike the arms of the pinwheel artifact, the horns of the horseshoe crab are not always symmetric, although they are usually within 20 s-HU of one another.

Motion in the SI-AP-LR direction results in a convolution of the artifacts arising from SI and AP-LR motions. Figures 3.30, 3.31, and 3.32 show images of the 1, 3, and 5 cm spheres undergoing motion in all three directions at once. At the edges of the spheres, where the partial projection artifacts are strongest, one spiraling arm of the pinwheel cancels one horn of the horseshoe crab artifact, while on the other side, the two reinforce

one another (See Figures 3.30, 3.31, and 3.32). The disparity in background values caused by the AP-LR component of motion does not appear to be affected by the inclusion of an SI component. For the 3 cm sphere (Figure 3.31) near the center, the horseshoe artifact seems to dominate. However, towards the trailing end of the sphere, the SI-motion artifacts begin to dominate; the center slices start to look nearly circular and symmetric pinwheel artifacts appear at the edge. For the 5 cm sphere, the two types of artifacts seem to balance one another, except for the last slice, where evidence of an AP-LR motion artifact is completely absent (See figure 3.32).

Figure 3.30: 1 cm sphere undergoing motion in the SI-AP-LR direction (Bellows 20% phase, 1.5 cm cams)

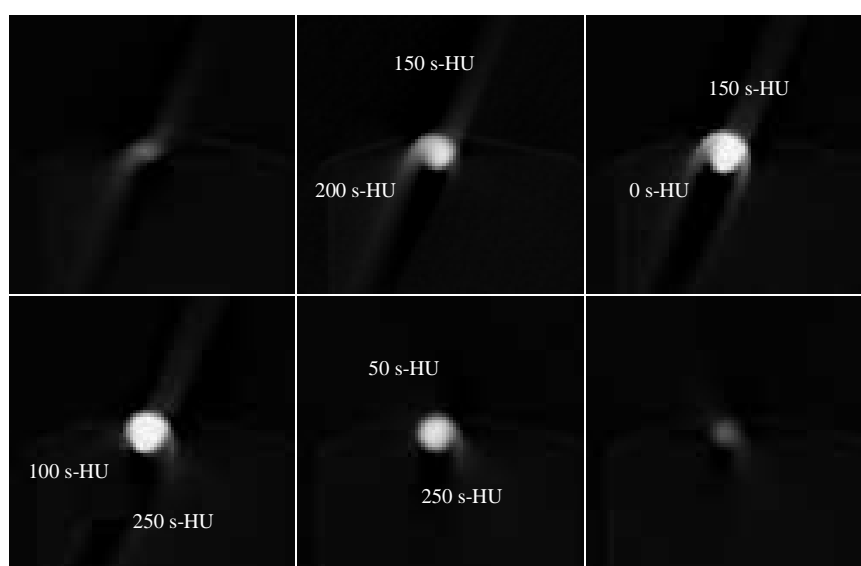


Figure caption: Slices through the 1 cm sphere undergoing motion in the SI-AP-LR directions imaged with 4DCT. The arms of the pinwheel artifact are no longer symmetric, however, the asymmetry of background densities persists.

Figure 3.31: 3 cm sphere undergoing motion in the SI-AP-LR direction (Bellows 80% phase, 1.5 cm cams)

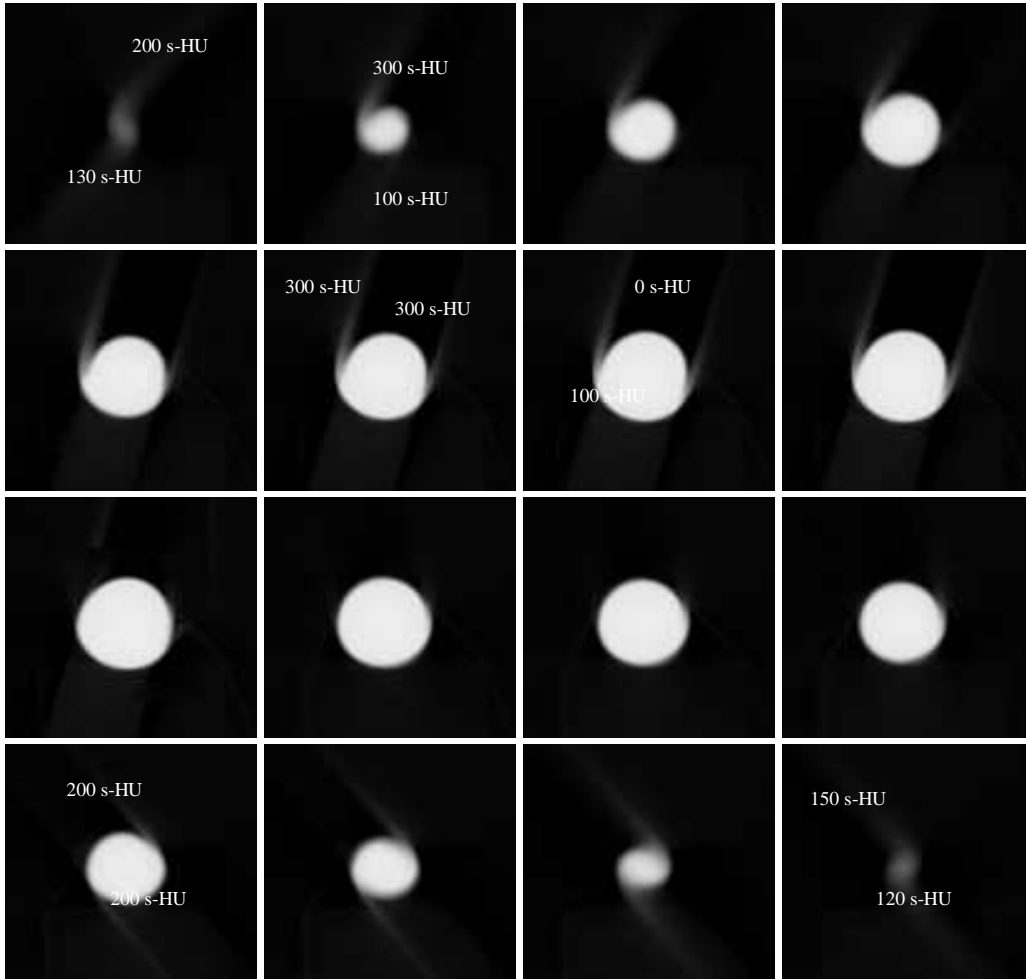


Figure caption: Slices through the 3 cm sphere undergoing SI-AP-LR motion imaged with 4DCT. Towards the center of the sphere, AP-LR motion artifacts appear to dominate, but as the slices progress through the sphere, SI motion artifacts begin to balance them. Towards the trailing edge of the sphere, SI motion artifacts dominate.

Figure 3.32: 5 cm sphere undergoing motion in the SI-AP-LR direction (RPM 20% phase, 1.5 cm cams)

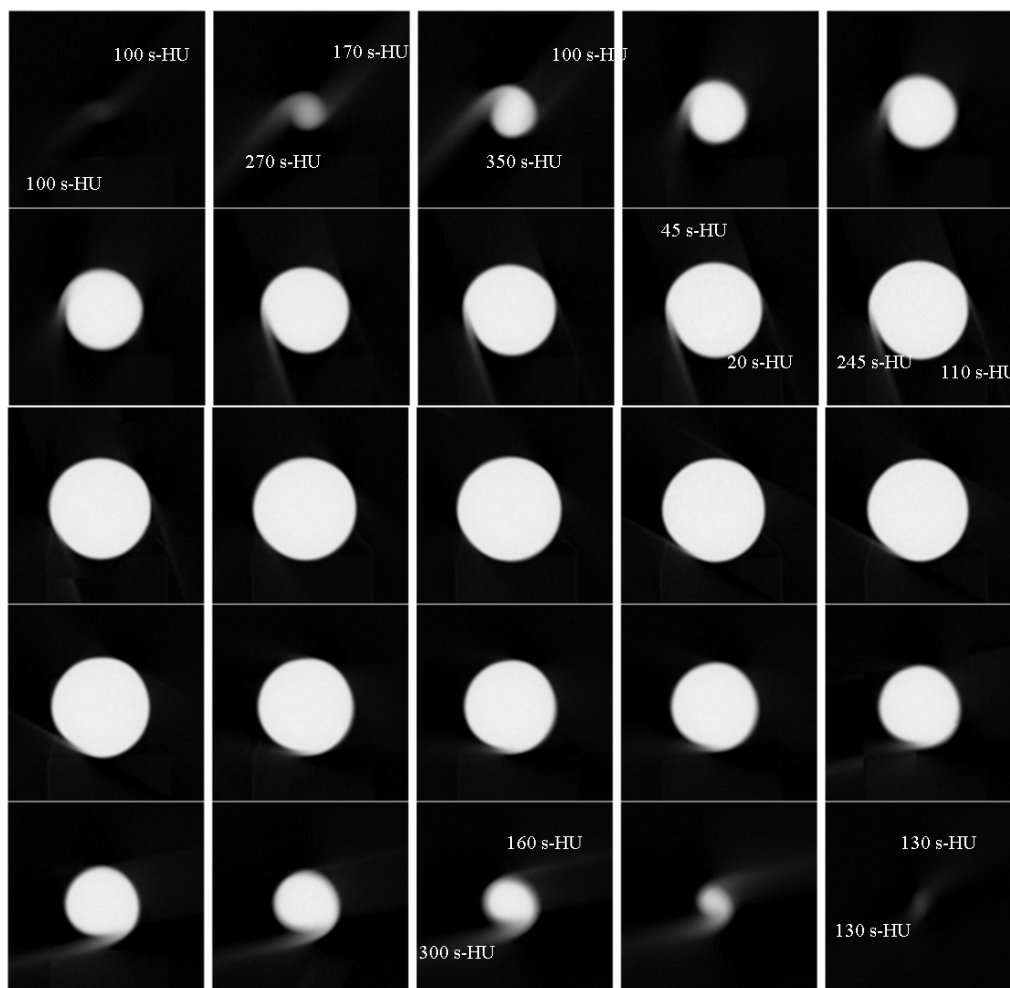
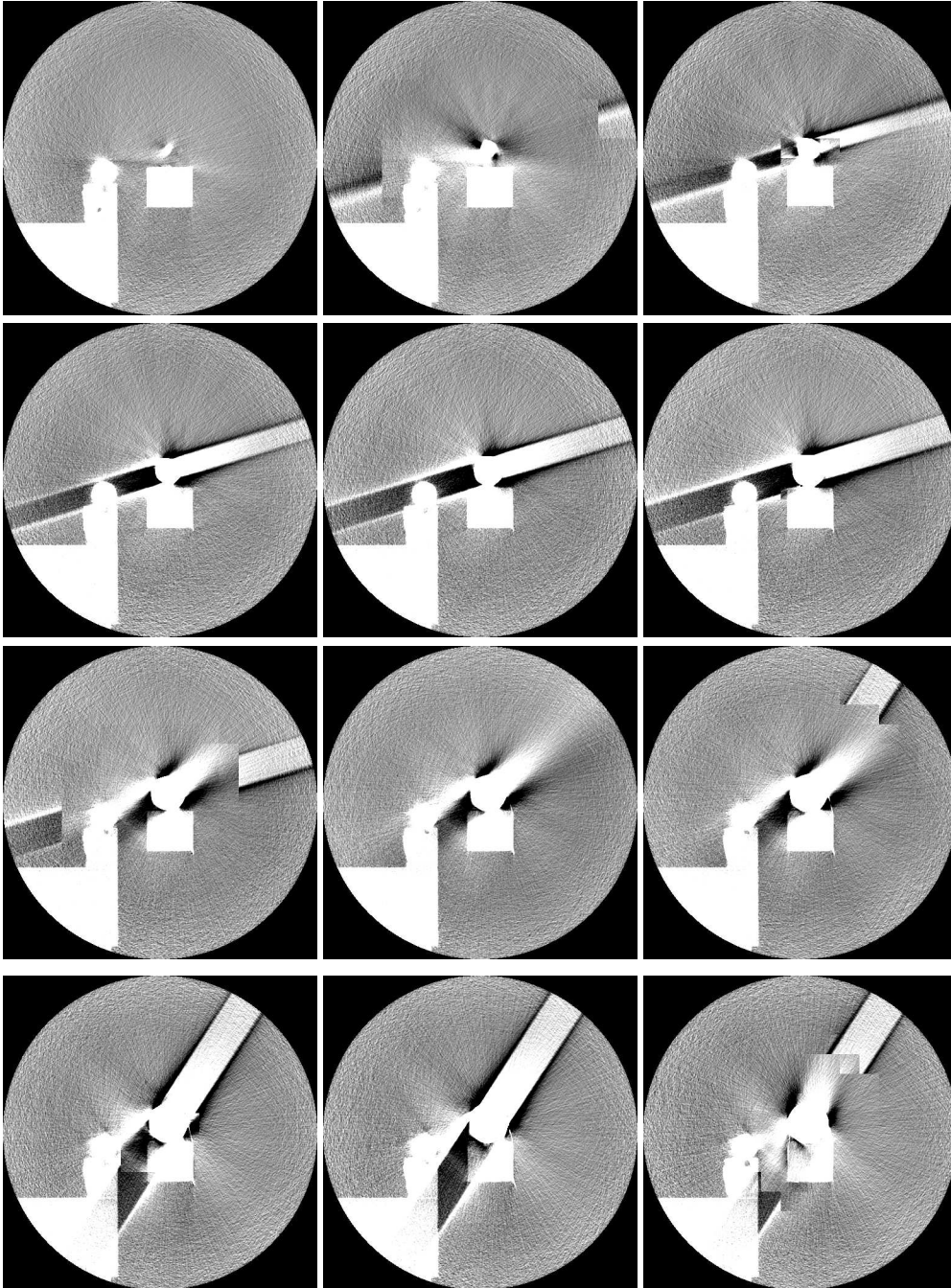


Figure caption: Slice through the 5 cm sphere undergoing motion in the SI-AP-LR direction imaged with 4DCT (two of the center slices have been removed for convenience.) In all but the edge slices, the AP-LR and SI residual motion artifacts appear balanced.

Philips' 4DCT reconstruction algorithm is unknown, and as seen in Figure 3.33, is making some complex decisions about density allocation in each reconstructed slice, particularly around the center of the field of view. Figure 3.33 has been windowed and leveled to reveal very low density structures. Unlike the images shown up to this point, these images are not cropped around just the sphere, but include the reference object as well as the Styrofoam supports. The motion is in the AP-LR direction, and it is clear that the asymmetric density of empty space extends throughout the full field of view. Yet, in some way, the Philips algorithm compensates by blocking out regions of artifact affected space. How these regions are chosen and where the replacement data originates is unknown, although it appears that data from two adjoining slices may be cobbled together. It is possible that data sharing between slices is occurring in every slice, however, note the three images in the second row; the artifact is widening and slowly rotating with no discernable patchwork affect.

Figure 3.33: Choices of the Philips reconstruction algorithm (3 cm sphere, AP-LR motion, Bellows 20% phase, 1.5 cams)



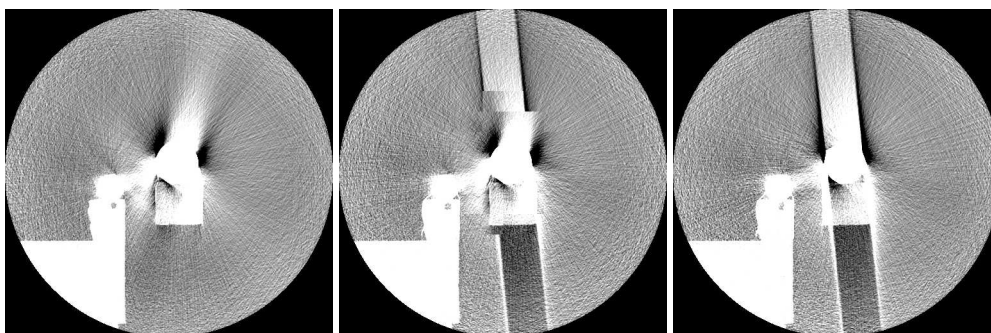


Figure caption: Slices of the 3 cm sphere undergoing motion in the AP-LR direction imaged with 4DCT. The entire FOV is shown and the window and level set to 25/30 s-HU, revealing the very low density objects in the image, including the residual motion artifacts. It appears that in some instances, Philips is replacing or partially replacing the inner portion of one image with data from an adjacent slice. However, the Philips algorithm is unknown.

3DCT Reference Scans

From caliper measurements of the acrylic spheres, the average diameter of the 1 cm spheres is 9.99 mm, giving a volume of 522.03 mm^3 . The maximum eccentricity calculated from any combinations of measurements from a single sphere was 0.133. For the 3 cm spheres, the average diameter is 30.03 mm, giving a volume of 14165.46 mm^3 . The maximum eccentricity is 0.086. The 5 cm spheres have a mean diameter of 49.98 mm, yielding an average volume of 65371.34 mm^3 . The maximum measured eccentricity for the 5 cm spheres is 0.057.

Recall that a static 3DCT image is required to locate a point on the mechanical path of a sphere from which all the actual phase positions are calculated. Many of the metrics used to evaluate the phase images have no equivalent in the static images since they are calculated relative to an ideal position (based on the position of the static image.) However, the *% volume difference* and *mean eccentricity* can be calculated for these static images, and so serve as a reference for these metrics. The average *% volume difference* for the stationary 1 cm sphere imaged with 3DCT is 1.06 % too small with standard deviation of 1.69 %. For the 3 cm sphere, the average *% volume difference* is 0.10 % too big, with a standard deviation of 0.47 %. The 5 cm sphere is an average of 0.03 % too small, standard deviation of 0.19 %. The average of the *mean eccentricities* for the 1 cm is sphere is 0.270, with a standard deviation of 0.049. For the 3 cm sphere, the average *mean eccentricity* is 0.121, standard deviation of 0.012. The static 5 cm sphere has an average *mean eccentricity* of 0.084 with a standard deviation of 0.008. These quantities are summarized in Table 3.5.

Table 3.5: The *% volume difference* and *mean eccentricity* metrics calculated for the static spheres

	1 cm sphere (17)	3 cm sphere (16)	5 cm sphere (16)
% volume difference	$-1.06 \pm 1.69 \%$	$0.10 \pm 0.47 \%$	$0.03 \pm 0.19 \%$
mean eccentricity	0.270 ± 0.049	0.121 ± 0.012	0.084 ± 0.008

Table caption: The average measured % volume differences and mean eccentricities of the stationary spheres. The numbers in parentheses are the number of inspected images. The error is one standard deviation of the measured values.

Figure 3.34: Three slices of the stationary 1 cm sphere outlined at 20, 40, 60, and 80% local contrast

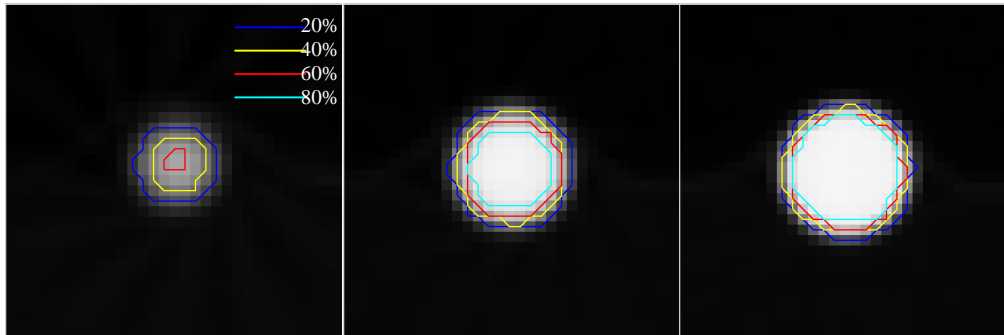


Figure caption: Stationary 1 cm sphere imaged with 3DCT. From left to right: the edge slice, the slice halfway to the middle, and the center slice. As the % local contrast increases, more peripheral pixels are eliminated from the segmented area. The 80% threshold is too high to select any pixels from the edge slice.

Figure 3.35: Three slices of the stationary 3 cm sphere outlined at 20, 40, 60, and 80% local contrast

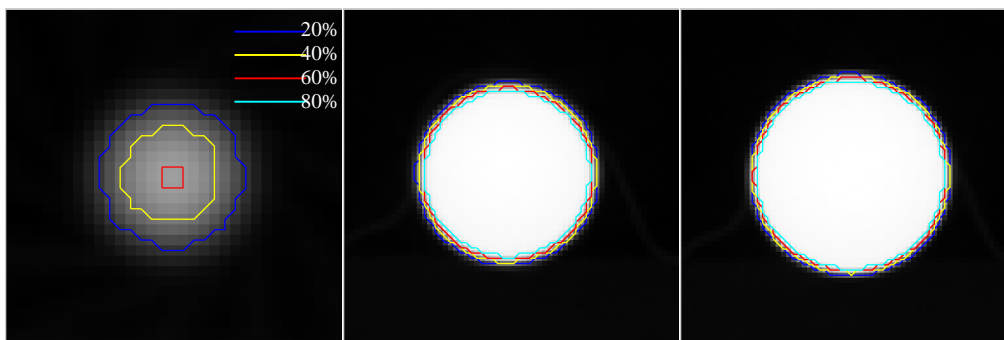


Figure caption: Stationary 3 cm sphere imaged with 3DCT. Again, the 80% threshold is too high to select any pixels from the edge slice.

Figure 3.36: Three slices of the stationary 5 cm sphere outlined at 20, 40, 60, and 80% local contrast

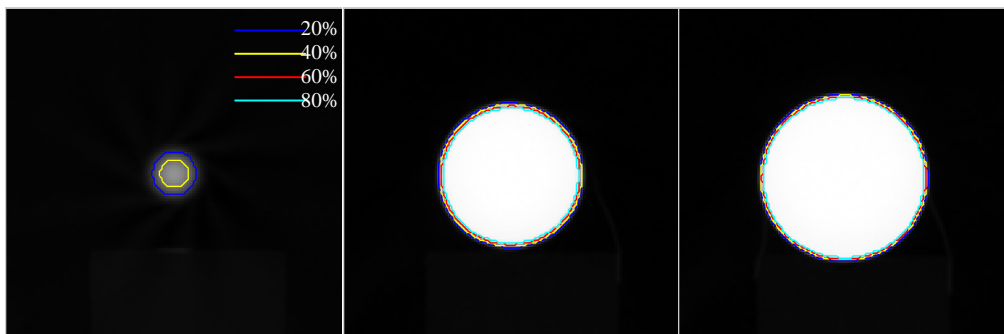
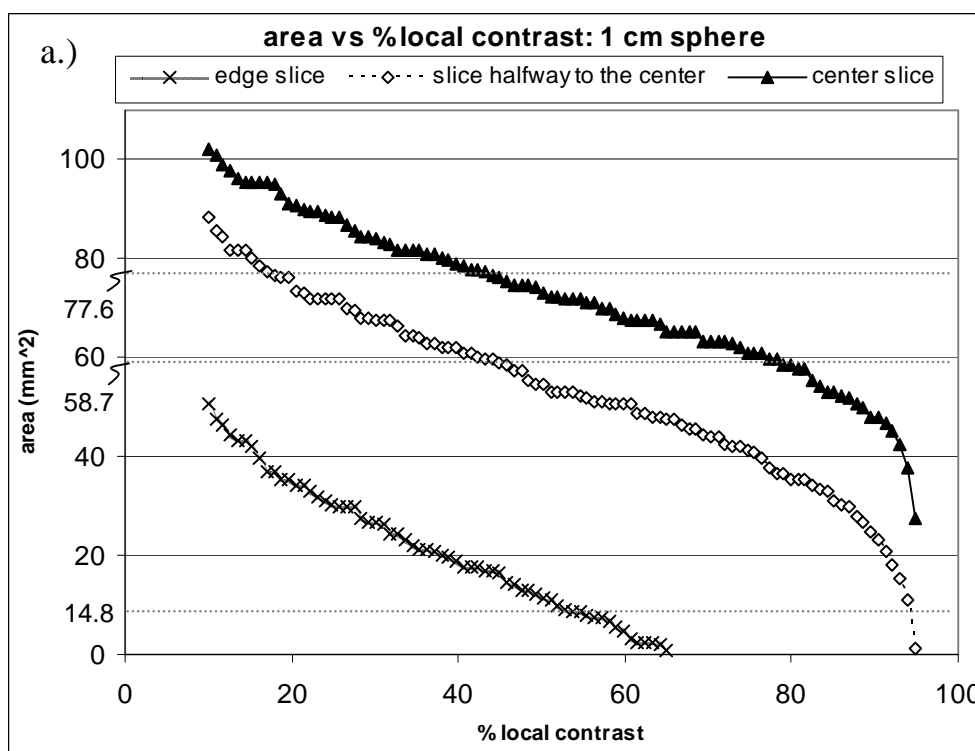


Figure caption: Stationary 5 cm sphere imaged with 3DCT. The 60% and 80% thresholds are too high to select any pixels from the edge slice. This sphere is not displayed at the same magnification as the 1 and 3 cm spheres, and so appears smaller.

Figures 3.34, 3.35, and 3.36 display select slices of the stationary spheres imaged with 3DCT. For each sphere, the edge slice, the slice halfway to the middle, and the center slice are shown. Also included are their outlines using 20, 40, 60, and 80 % local contrast as the threshold value. These outlines represent the area that would be included in the cross sectional image of the sphere if segmented at these thresholds.

Figure 3.37 gives the area versus % local contrast attribute maps for the slices shown in Figures 3.34-3.36. To create these graphs, the threshold is increased until the sphere cannot be imaged as a single object; edge slices, sharing nearly every pixel with some degree of background, have a lower overall density due to the partial volume effect, and break up at lower thresholds than do the more central slices. Thus, for each size sphere, the graph associated with the edge slice does not extend over as large of a threshold range. This is true for every attribute mapped. The shapes of these graphs are fairly linear over a wide range of thresholds. In all area attribute maps, the cross sectional area in the vicinity of thresholds used to segment the sphere for metric measurement (i.e. ~ 40 - 45 % local contrast) matches well with reality. The values of the inner most pixels fluctuate a little due to noise; it is not until the threshold reaches nearly 100 % local contrast that the vast majority of pixels are excluded and the area drops quickly. Figure 3.38 shows the analogous volume vs. % local contrast attribute maps for each sphere.

Figure 3.37: Area vs. % local contrast attribute maps for the 1, 3, and 5 cm spheres imaged while stationary with 3DCT



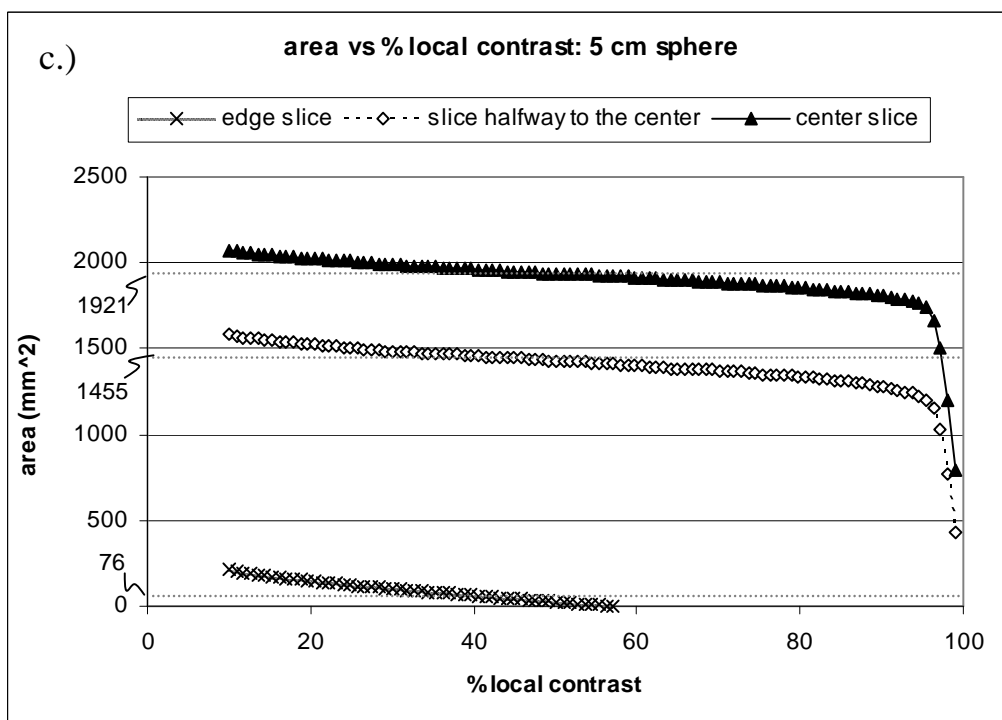
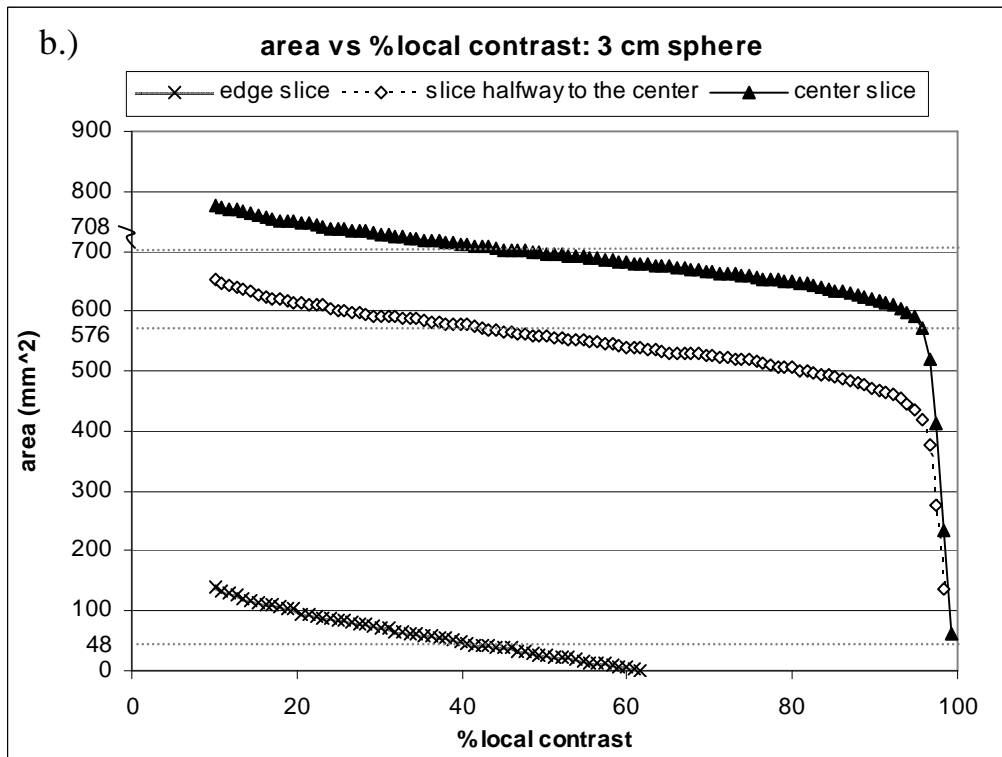
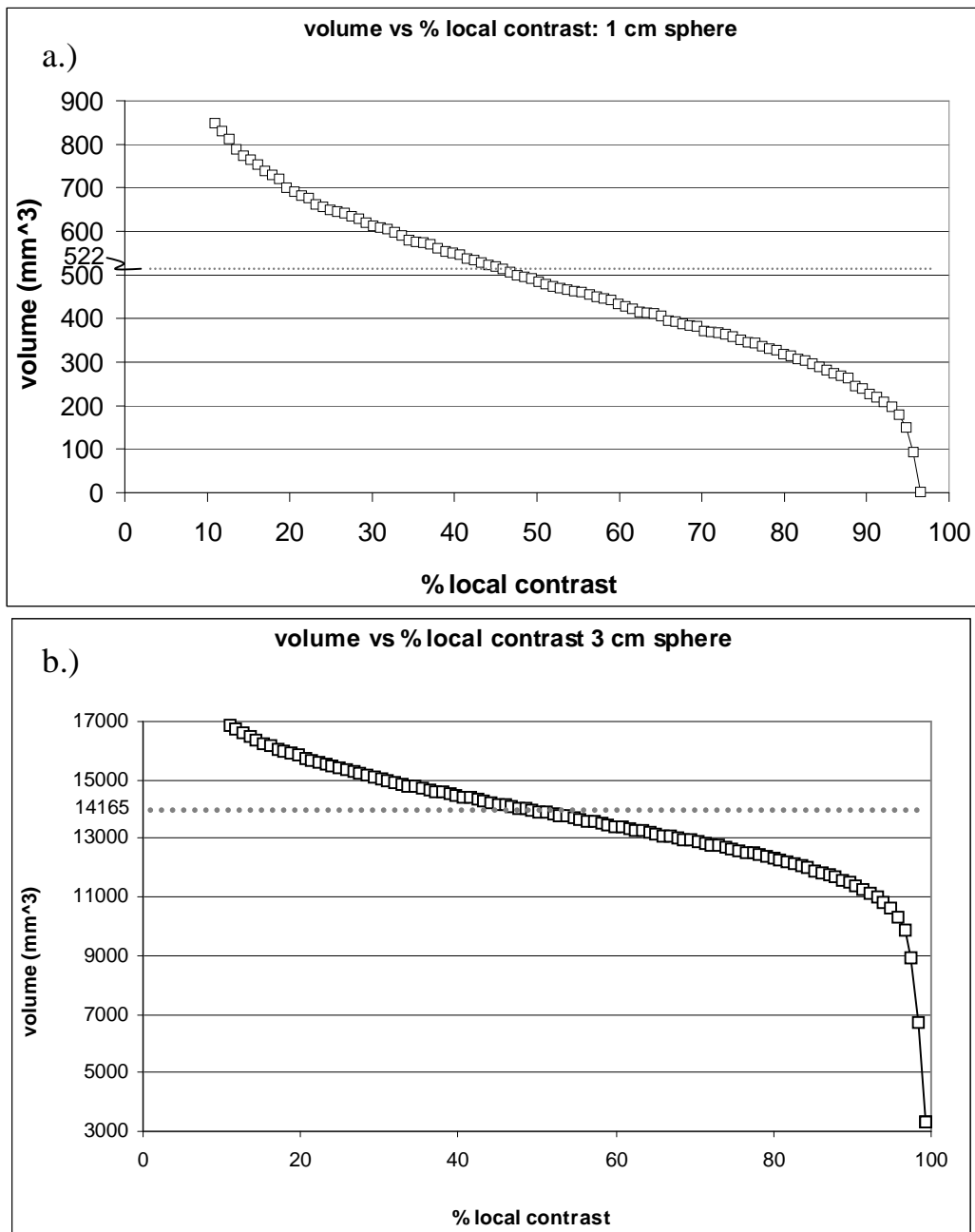


Figure caption: The area vs. % local contrast attribute maps for the spheres shown in Figures 3.34-3.36. a.) three slices from the 1 cm sphere, b.) three slices from the 3 cm sphere, and c.) three slices from the 5 cm sphere data. The attribute maps for all three spheres are fairly linear over a wide range of thresholds.

Figure 3.38: Volume vs. % local contrast attribute maps for the stationary 1, 3, and 5 cm spheres imaged with 3DCT.



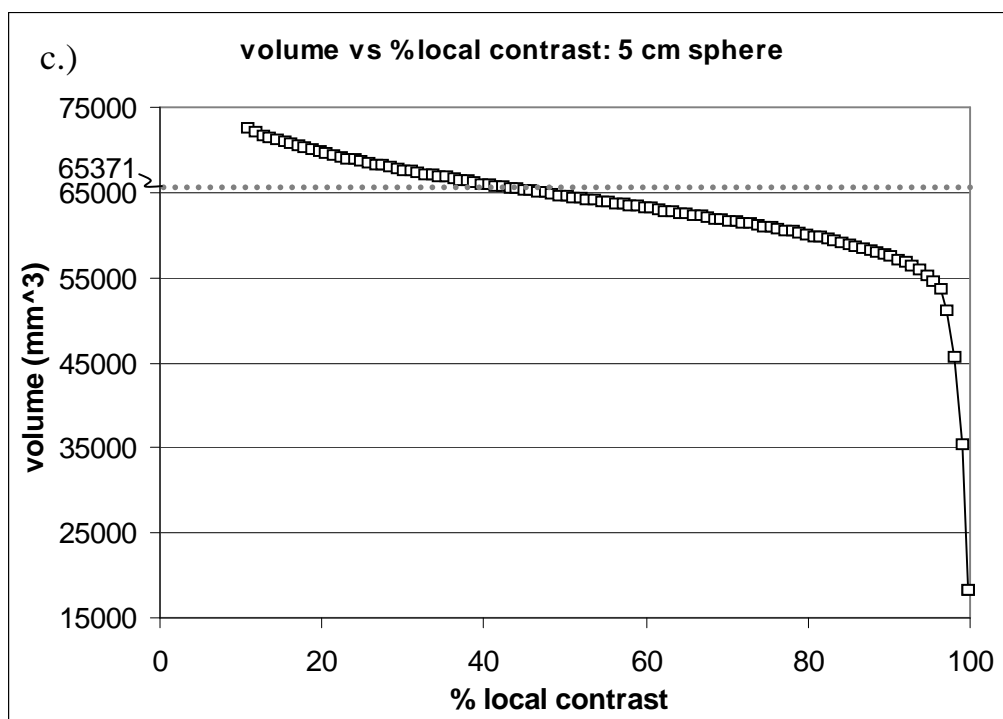
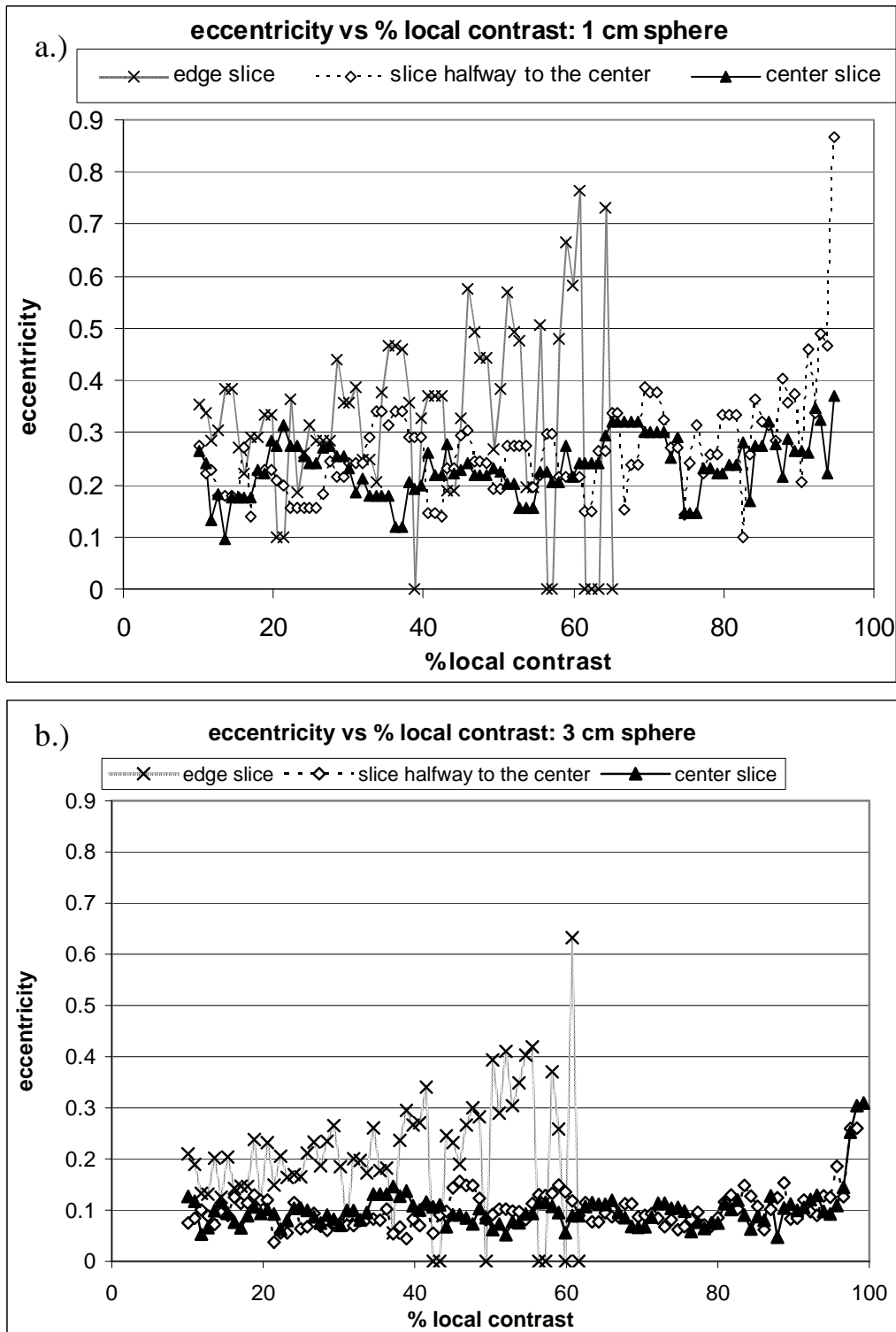


Figure caption: The volume vs. % local contrast attribute maps for the stationary spheres seen in Figures 3.34 - 3.36. a.) the 1 cm sphere, b.) the 3 cm sphere, and c.) the 5 cm sphere. The true volumes of the 1, 3, and 5 cm spheres are 522 mm^3 , 14165 mm^3 , and 65371 mm^3 , respectively.

Figure 4.39 shows the attribute maps of cross sectional eccentricity vs. % local contrast for the same three slices of each sphere appearing in Figures 3.34 - 3.36. In general, eccentricity fluctuates about a mean value over a wide range of threshold for all but the edge slices. For all sphere sizes, the fluctuations of eccentricity seen in the edge slices are about the same. Looking at the inner slices, the fluctuation is less for the larger sphere, since the inclusion/exclusion of only a few pixels has little effect on the overall shape of the imaged cross section. The sweep upward and increased fluctuation at higher thresholds is simply due to increased homogeneity of the selected pixels' values. As seen in the area attribute maps, at high % local contrast, a relatively small change in threshold now excludes a large number of pixels, more significantly altering the shape of the segmented area.

Figure 3.39: Eccentricity vs. % local contrast attribute maps for the static 1, 3, and 5 cm spheres imaged with 3DCT



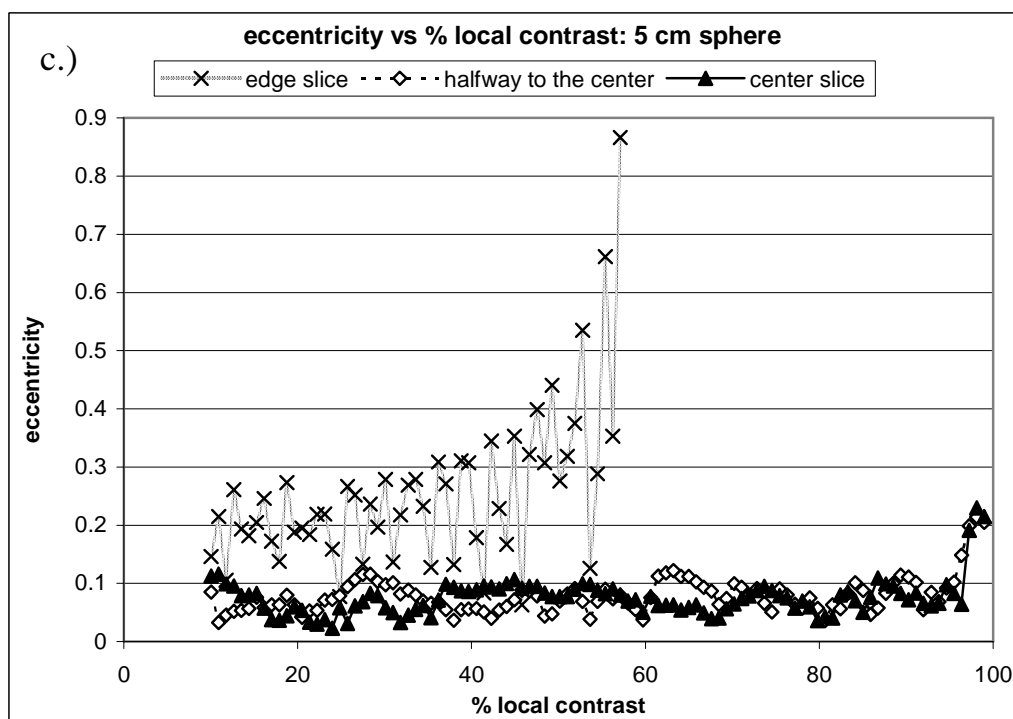
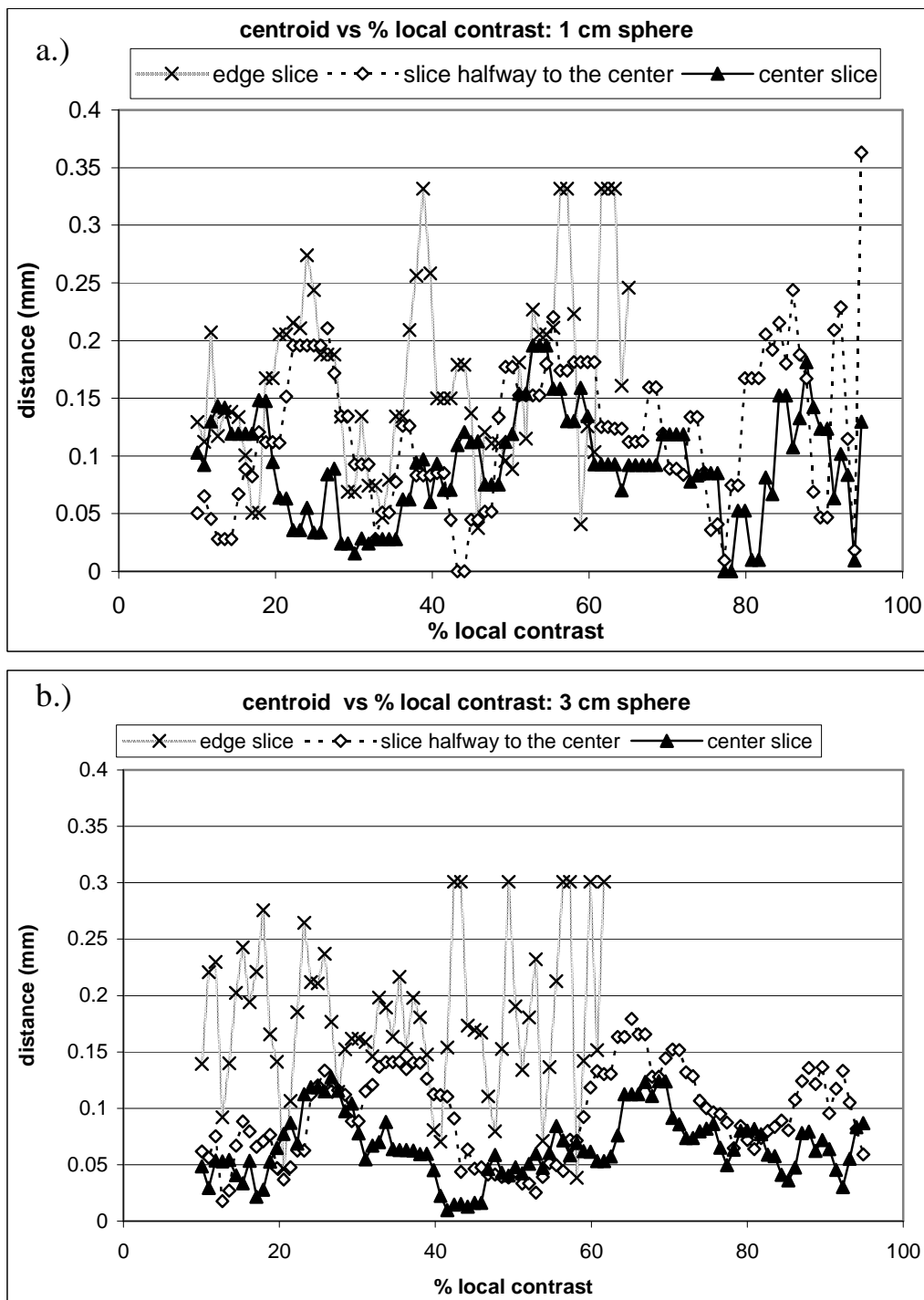


Figure caption: Eccentricity vs. % local contrast for the stationary spheres seen in Figures 3.34 - 3.36. a.) three slices from the 1 cm sphere, b.) three slices from the 3 cm sphere, and c.) three slices from the 5 cm sphere data. Regardless of their diameter, the edge slices of the spheres are dominated by partial volume effects. Thus, the response of the edge slices to thresholding for all the spheres is similar.

The centroid vs. % local contrast attribute maps for the cross sectional images of the three stationary spheres appearing in Figures 3.34 - 3.36 are shown in Figure 3.40. The centroid is expressed here by its distance from the (x,y) coordinates of the center of the sphere (as segmented for metric measurement). There is consistently less fluctuation in centroid position as the object gets bigger, essentially for the same reasons as with the eccentricity. The centroid attribute is calculated by 'center of mass'; the less the shape is affected, the less the centroid position is affected.

Figure 3.40: Centroid vs. % local contrast attribute maps for the static 1, 3, and 5 cm spheres imaged with 3DCT



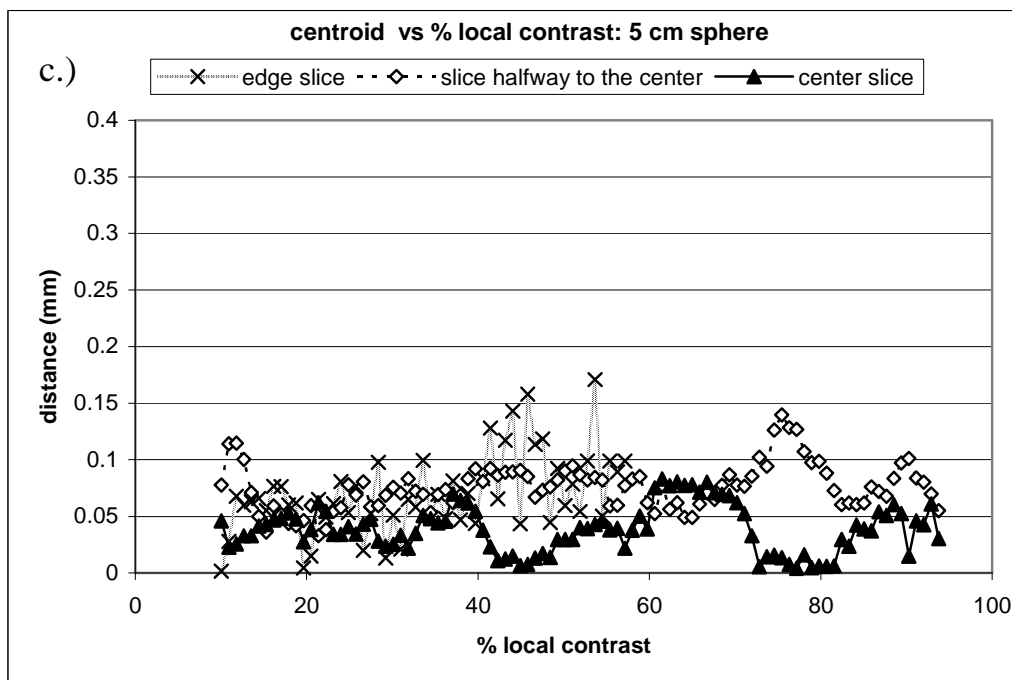


Figure caption: Centroid vs. % local contrast for the spheres shown in Figures 3.34 - 3.36. a.) three slices from the 1 cm sphere, b.) three slices from the 3 cm sphere, and c.) three slices from the 5 cm sphere data. As the sphere becomes larger the fluctuation in centroid position is lessened. The fluctuating values of distance are all well under the dimensions of a single pixel. That the center slice does not reach zero distance for the center slice at the threshold used to find the center of the sphere is simply a matter of rounding error.

It is from these graphs that the threshold errors are derived. These errors give an indication of the true threshold sensitivity of each phase image.

4DCT Residual Motion Artifacts

What follows are examples of the artifacts found in the 4DCT data sets along with their effects on the attribute maps of each sphere. In order to illustrate the effects of residual motion artifacts, only the fastest phases from the data collected with the 1.5 cm cams are shown.

1 cm Sphere

Figure 4.41 displays select slices of the 1 cm sphere as it undergoes motion in the SI direction, the AP-LR direction, and the SI-AP-LR direction. Again, the slices shown are the edge slice, the slice halfway to the middle of the sphere, and the center slice. These are presented with outlines indicating where the segmented boundary would lie at 20, 40, 60, and 80 % local contrast.

Figure 3.41: Three slices of the 1 cm sphere undergoing motion in the SI, AP-LR, and SI-AP-LR directions.

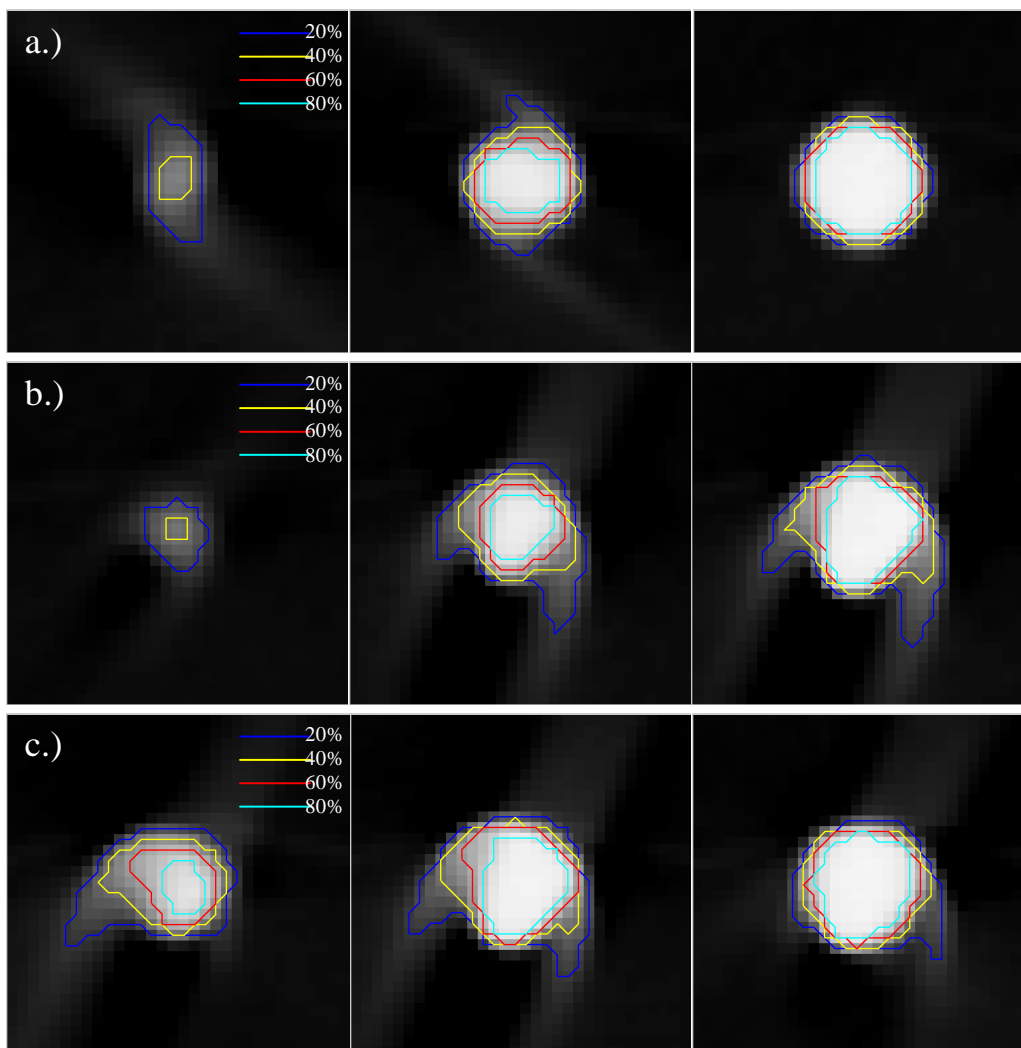
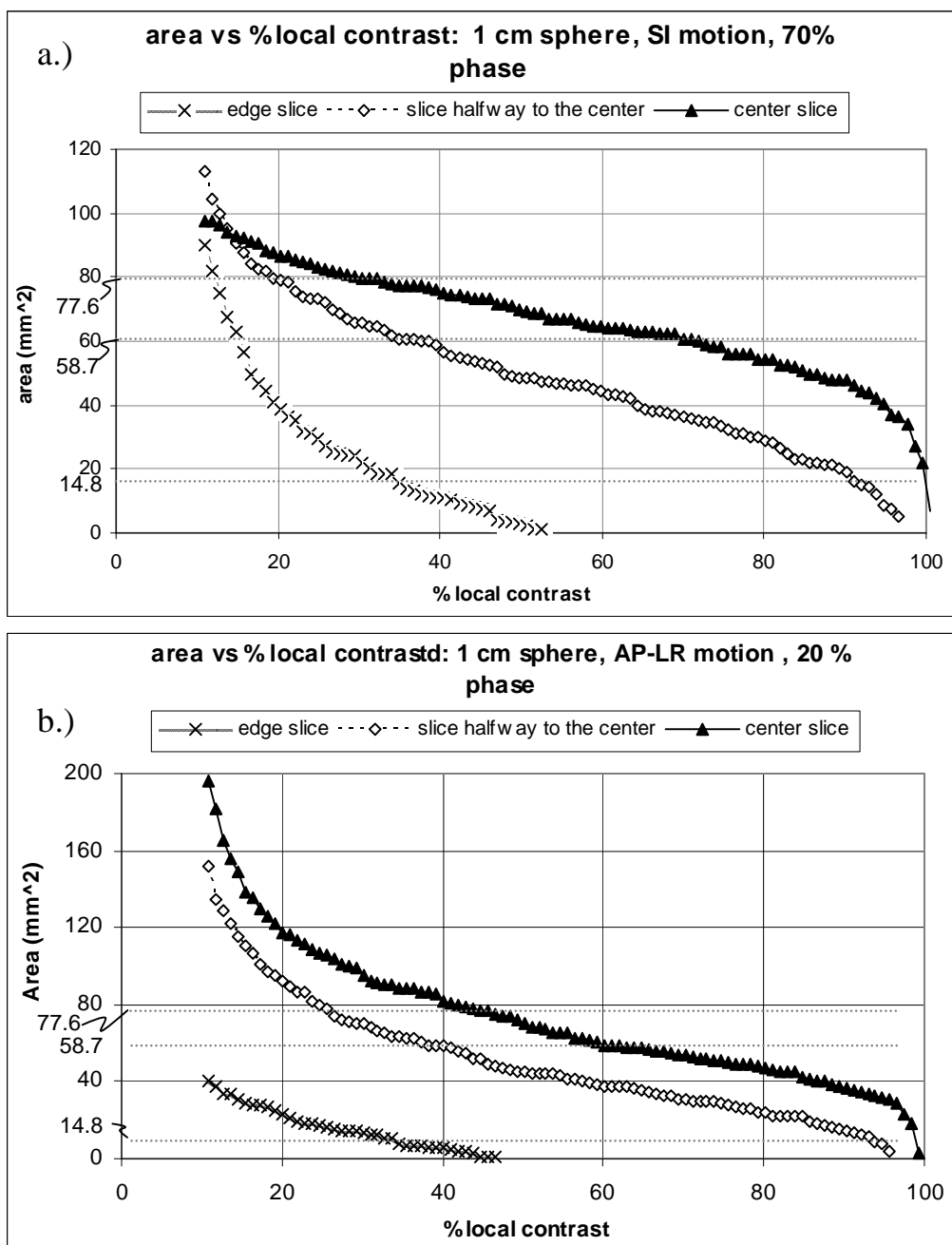


Figure caption: Three slices of the 4DCT acquisition of the moving 1 cm sphere. a.) 1 cm sphere SI motion, b.) 1 cm sphere AP-LR motion, c.) 1 cm sphere SI-AP-LR motion. From left to right, the edge slice, the halfway to the middle slice, and the center slice. The outlines of the sphere using 20, 40, 60, and 80 % local contrast thresholds are shown

Figure 3.42 gives the area vs. % local contrast attribute maps from the 1 cm sphere 4DCT data sets shown in Figure 3.41. The spiraling of densities generated from SI motion penetrates deep into the segmented cross sections of the sphere, affecting its overall response to threshold. That SI motion affects the area in the edge slices to a greater extent than more central slices can be seen by the steep descent and steeper overall slope of the area attribute map for that slice (see Figure 3.42a). This steep descent at low thresholds is due to the inclusion of low-density pinwheel artifacts. For AP-LR motion (Figure 3.42b), the artifacts impact the different cross sectional areas more equally. Again, the swoop at the low threshold end comes from the inclusion of low-density residual motion artifacts. The effect of the SI-AP-LR residual motion (Figure 3.42c), like the SI motion, has less impact on the center slice.

Figure 3.42: Area vs. % local contrast attribute maps for the 1 cm spheres imaged with 4DCT undergoing motion in the SI, AP-LR, SI-AP-LR directions



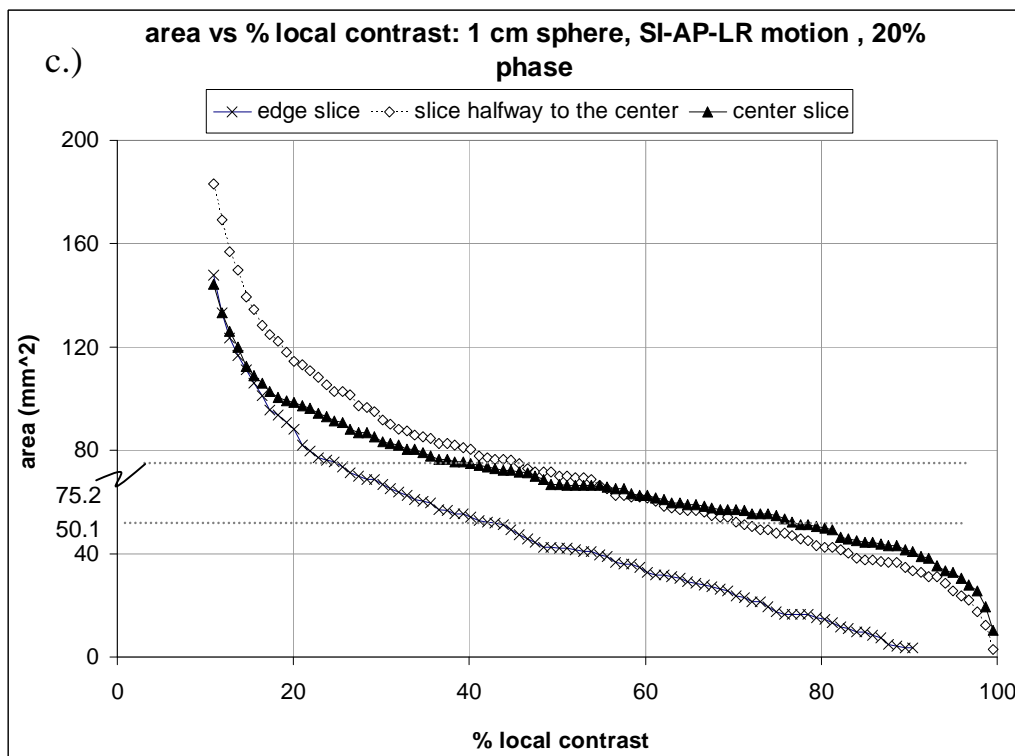
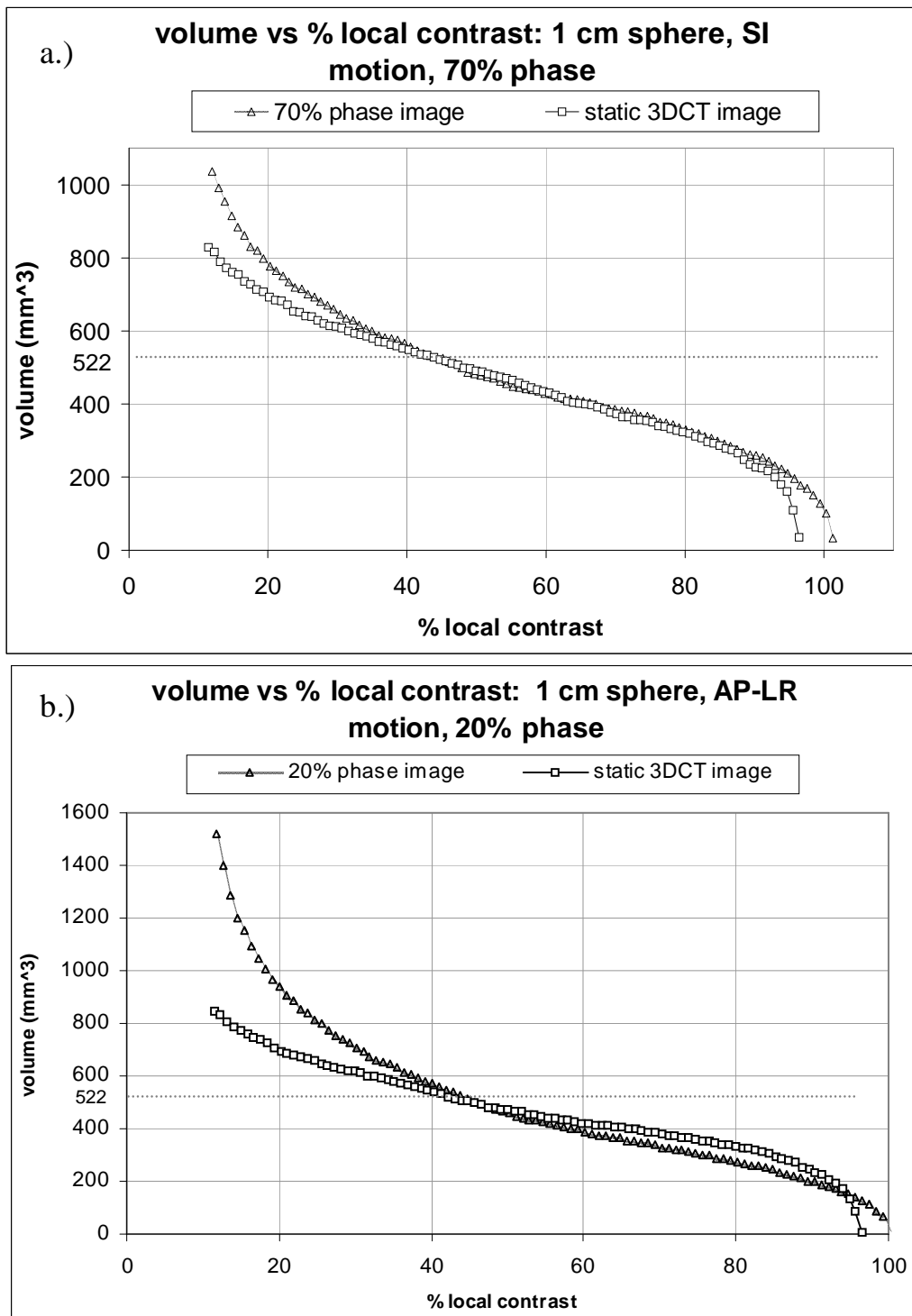


Figure caption: Area vs. % local contrast for three slices of the 1 cm sphere depicted in Figure 4.18 undergoing motion in the a.) SI direction, b.) AP-LR direction, and c.) SI-AP-LR direction. For the SI and SI-AP-LR motions, the center slice is the least affected by the artifacts, but for the AP-LR motion, the center slice is the most affected.

Figure 3.43 shows the corresponding volume vs. % local contrast attribute maps. Also shown are the volume attribute maps from the static reference images accompanying each 4DCT acquisition. The increase in volume at low thresholds for the 1 cm sphere undergoing SI motion is, again, due to inclusion of partial projection artifacts. The steeper overall slope and lack of a rapid decline in volume at the highest thresholds attests to the increased diversity of pixel values penetrating deep into the sphere's segmented image.

Figure 3.43: Volume vs. % local contrast attribute maps for the 1 cm spheres imaged with 4DCT undergoing motion in the SI, AP-LR, SI-AP-LR directions



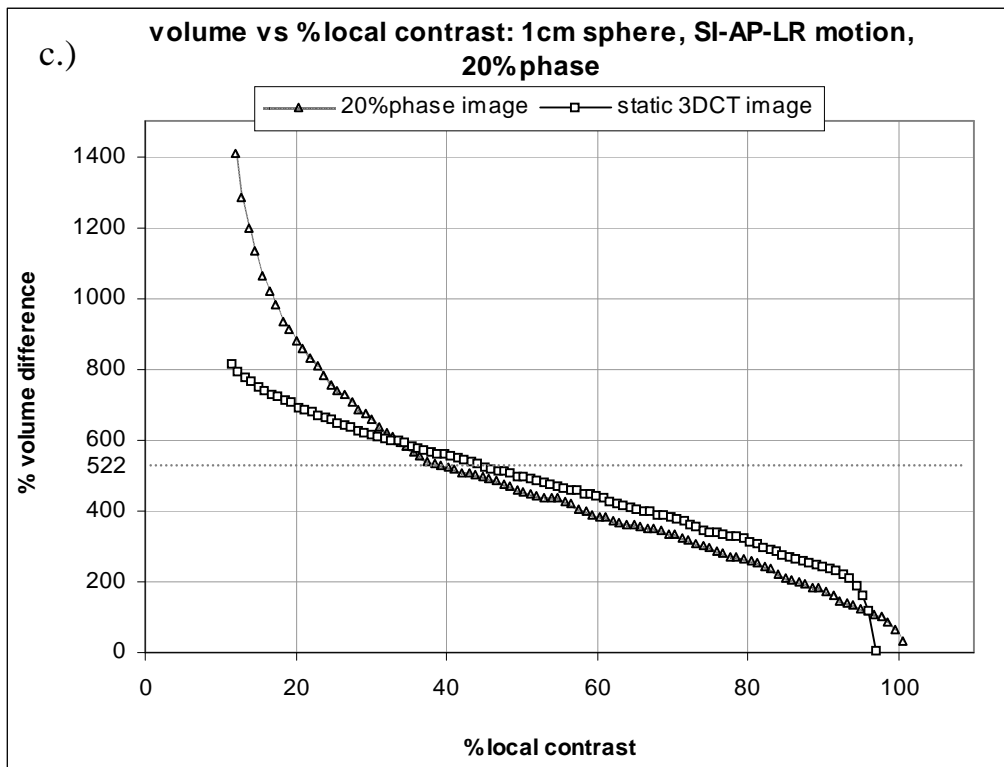
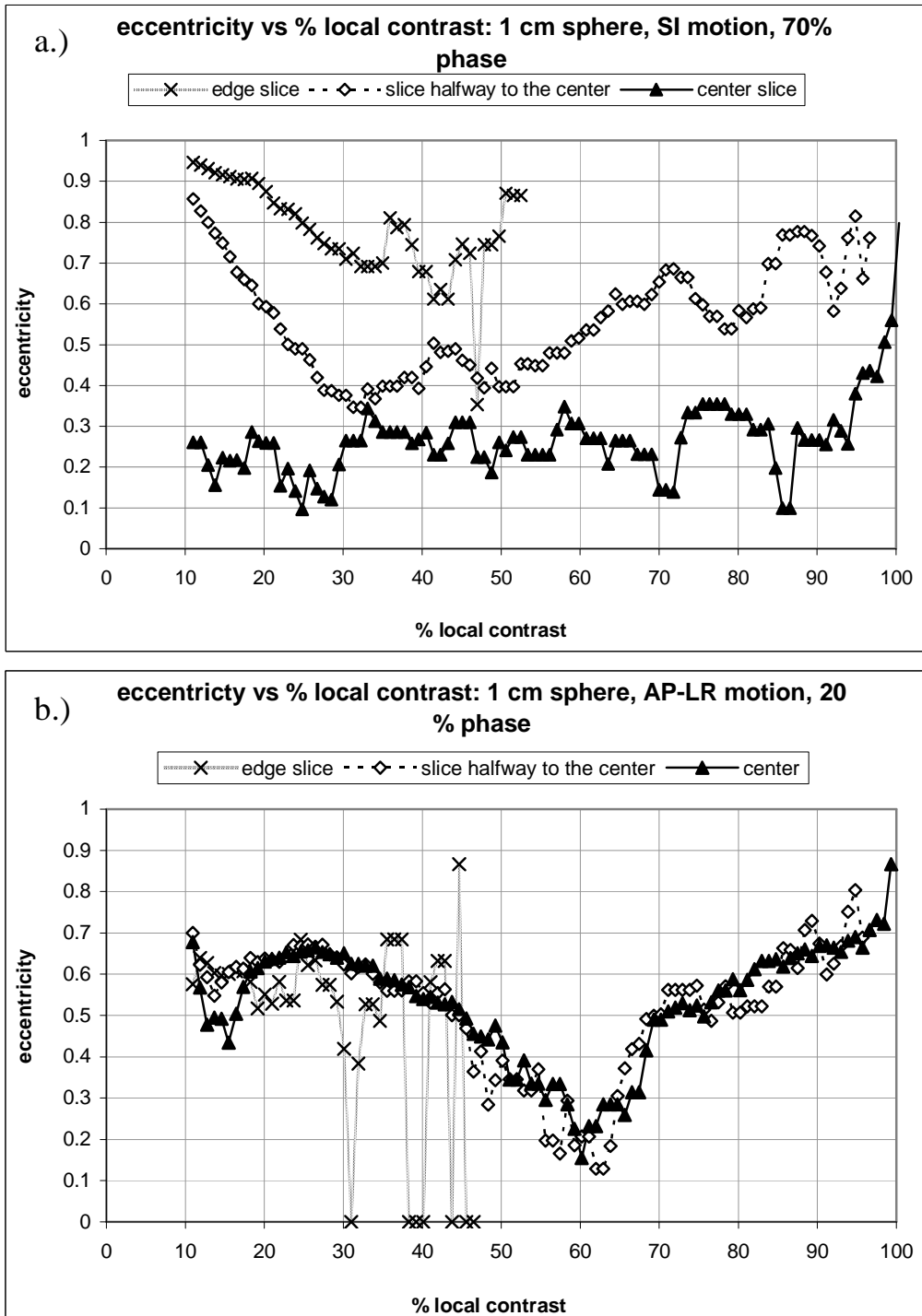


Figure caption: Volume vs. % local contrast for three slices of the 1 cm sphere depicted in Figure 3.41 undergoing motion in the a.) SI direction, b.) AP-LR direction, and c.) SI-AP-LR direction. For the 1 cm sphere, volume's response to thresholding is most affected by AP-LR and SI-AP-LR motions.

For AP-LR motion, the mis-assignment of densities also affects the overall density of the object, as its 4DCT volume attribute map shows a steeper slope than its 3DCT counterpart. Of all the inspected motions, the AP-LR 4DCT attribute map is the most different from the 3DCT map, indicating that the volume of the 1 cm sphere is most sensitive to in-plane motion artifacts. Both the SI and AP-LR attribute maps attain an accurate volume (i.e. 522 mm³) within the range of thresholds used to segment the sphere for metric measurement (i.e. ~ 40 – 45 % local contrast). Yet, for the SI-AP-LR motion, the 4DCT graph dips below the static volume attribute map at around 35% local contrast, and is, thus, imaged smaller than actual size.

Figure 3.44 shows the eccentricity vs % local contrast graphs for these same 1 cm cross sectional images depicted in Figure 3.41. Again, only the attribute maps from the edge slice, the halfway to the middle slice, and the center slice are shown.

Figure 3.44: Eccentricity vs. % local contrast attribute maps for the 1cm spheres imaged with 4DCT undergoing motion in the SI, AP-LR, and SI-AP-LR directions



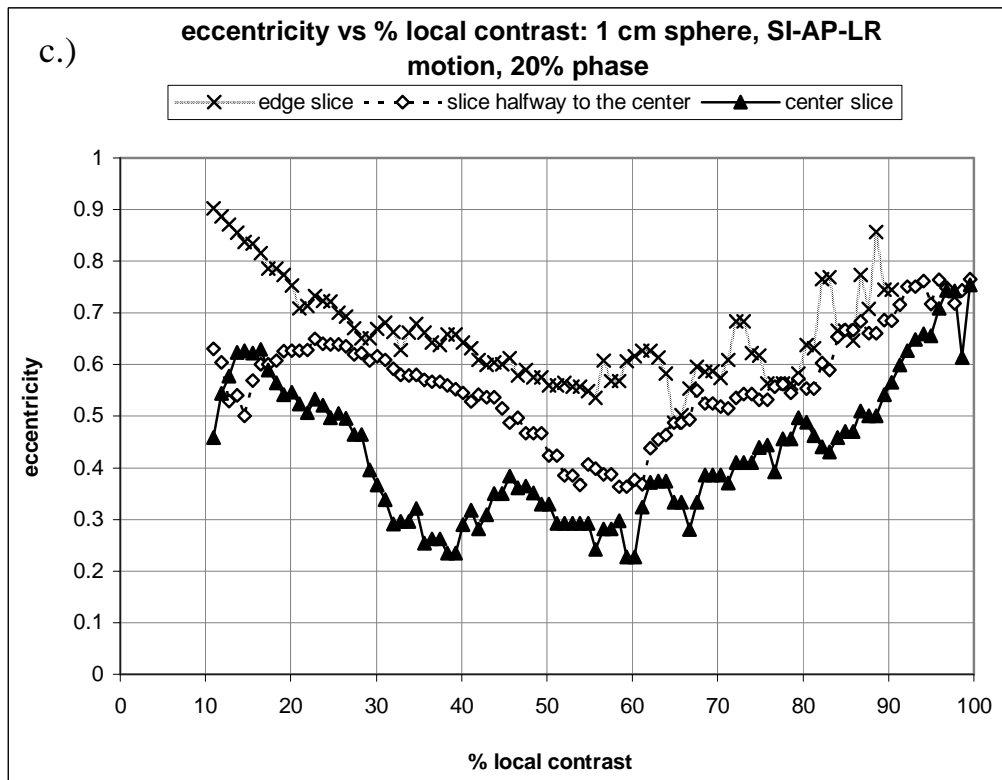
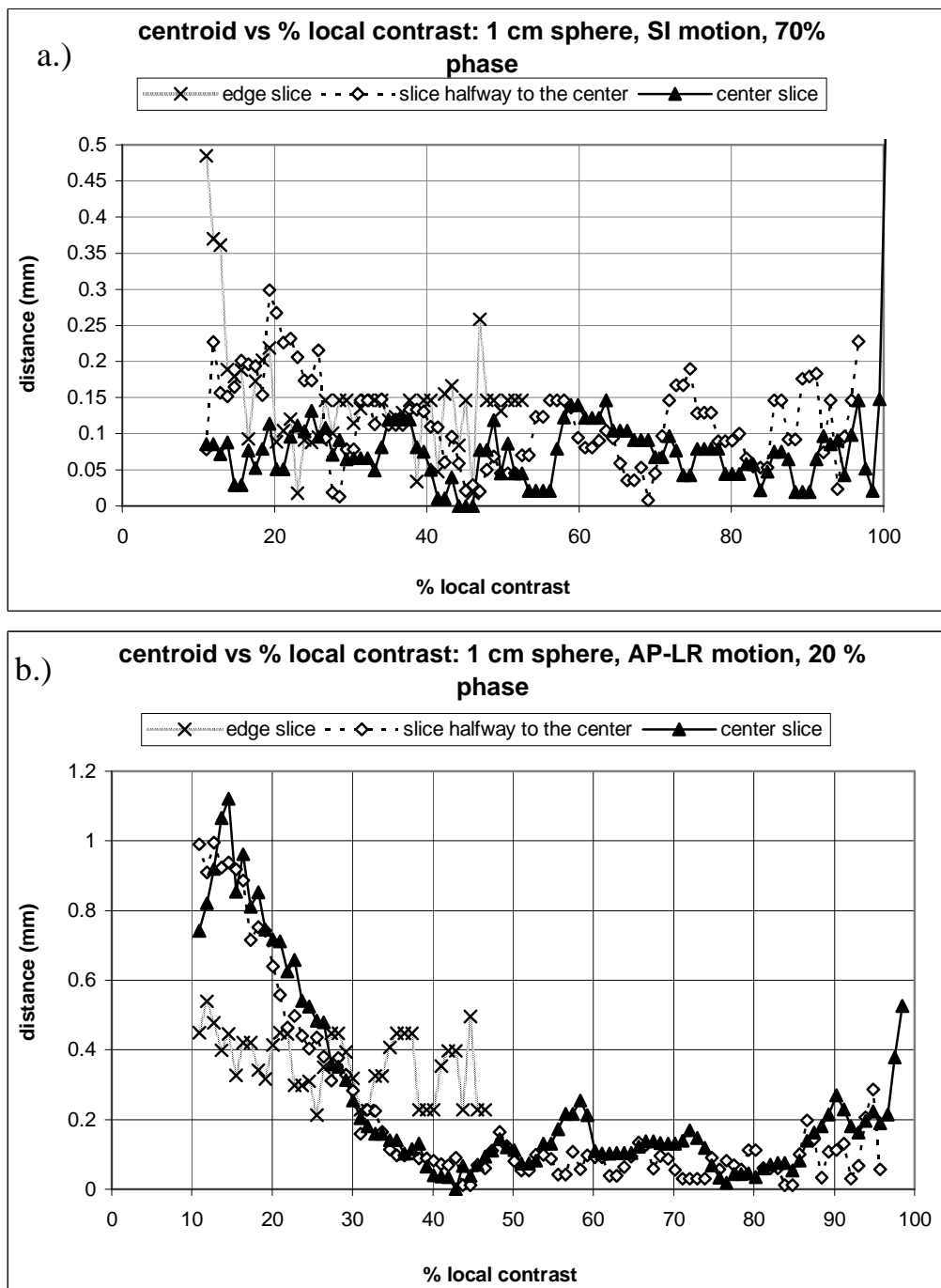


Figure caption: Eccentricity vs. % local contrast for three slices of the 1 cm sphere undergoing motion. a.) SI motion affects the edge and halfway slices the most. b.) AP-LR motion causes strong deformation of the eccentricity maps for the more central slices. c.) For motion in the SI-AP-LR direction, all three slices are strongly affected by the residual motion artifacts.

Like the eccentricities seen in the static 3DCT images (see Figure 3.39), the eccentricity of each cross section fluctuates with contrast, however, the overall shape of the attribute maps differs from the 3DCT acquisitions of the stationary spheres. At low thresholds, residual motion artifacts cause increased eccentricity for all types of motion. At high thresholds, the increased inhomogeneity of the pixel values throughout the entire cross sectional image causes the eccentricity of even the most central slices to respond strongly to increased threshold. There is typically a dip in the eccentricity between that caused by the inclusion of low density motion artifacts and that caused by overall pixel inhomogeneity, however, the location of this dip does not often coincide with the threshold yielding the sphere's true volume. For SI motion, the center slice's eccentricity map shows the most similarity to the static sphere, again revealing the 1 cm sphere's relative insensitivity to pinwheel artifact. Conversely, the heavily bowed eccentricity maps of the halfway and center slices of the AP-LR motion reveal again the small sphere's vulnerability to the in-plane motion artifacts. When undergoing SI-AP-LR motion, all the eccentricities of the 1 cm sphere's cross sectional are strongly affected by residual motion.

Lastly, the centroid vs. % local contrast attribute maps for the cross sectional images of Figure 3.41 are given in Figure 3.45. For SI motion, threshold has little impact on the object's centroid (2,163). Except where low density artifacts are included, the centroid under AP-LR motion is relatively insensitive to threshold as well. However, for all three motions at once, the center point begins to drift at high thresholds.

Figure 3.45: Centroid vs. % local contrast attribute maps for the 1 cm spheres imaged with 4DCT undergoing motion in the SI, AP-LR, SI-AP-LR directions



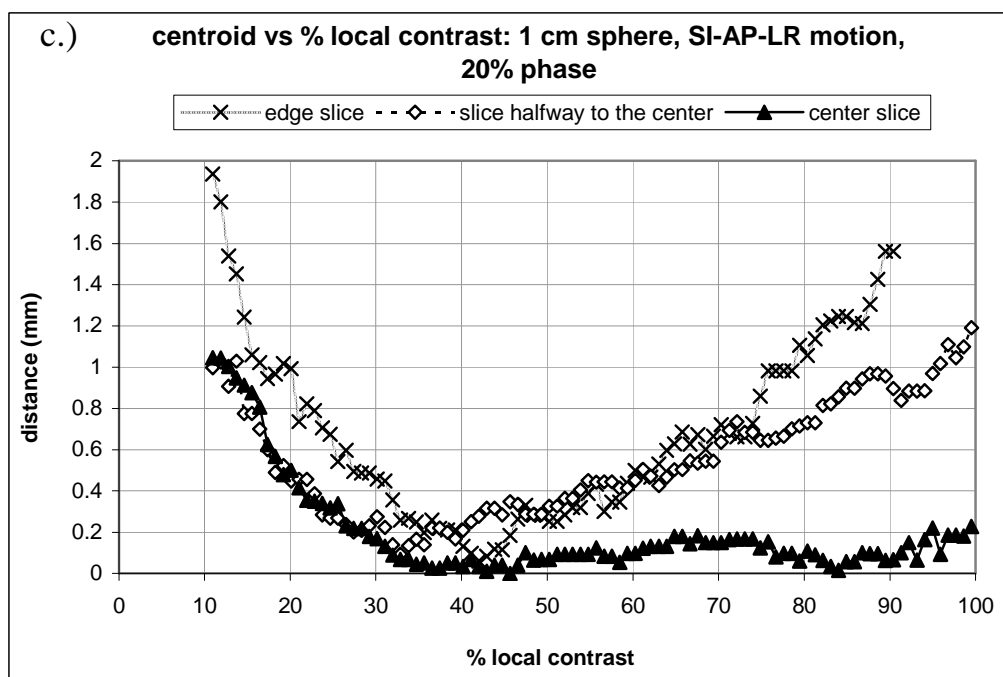


Figure caption: Centroid vs. % local contrast for three slices of the 1 cm sphere depicted in Figure 4.18 undergoing motion in the a.) SI direction, b.) AP-LR direction, and c.) SI-AP-LR direction. Centroid is represented by its distance from the transverse plane coordinates (i.e. x,y) of the center of the sphere. The SI motion looks the most like the static scan of the 1 cm sphere. The AP-LR and SI-AP-LR motions show a drift of centroid with threshold at low % local contrast. Under SI-AP-LR motion and for the edge and halfway slices, this drift occurs at high thresholds as well.

3 cm Sphere

Following along the same lines of discussion, Figure 3.46 shows select slices from the 4DCT acquisitions for the 3 cm sphere with motion in the SI direction, AP-LR direction, and SI-AP-LR direction. Again, these images are presented with the 20, 40, 60, and 80 % local contrast threshold outlines.

Figure 3.47 gives the area attribute maps for the cross sectional images of the 3 cm sphere appearing in Figure 3.46, and Figure 3.48 gives the corresponding volume attribute maps. For all types of motion, the differences between the slopes of the different slice locations is not as extreme as for the 1 cm sphere. This is because the relative sizes of the artifacts compared to the cross sectional areas of the 3 cm sphere are smaller. This is also the reason why the swoop at low thresholds is not as dramatic. For SI and SI-AP-LR motions, the area attribute map is steepest for the cross section of the edge slices, however, for the AP-LR motion, the slice half way between the edge and the center shows the most deviation from the static case. Since smaller cross sections are affected more by the mis-assignment of densities arising from AP-LR motion, it is reasonable that the halfway slice would show more sensitivity to thresholding. That this increased sensitivity does not extend to the cross sectional images on the edge slices (noting the edge slice of the 1 cm AP-LR area map, see Figure 3.42b), is due to the partial volume affect afflicting nearly every pixel; the overall lower density of the object means less disparity in density values between the sphere and its background, and so creates a less dramatic artifact.

Figure 3.46: Three slices of the 3 cm sphere undergoing motion in the SI, AP-LR, and SI-AP-LR directions.

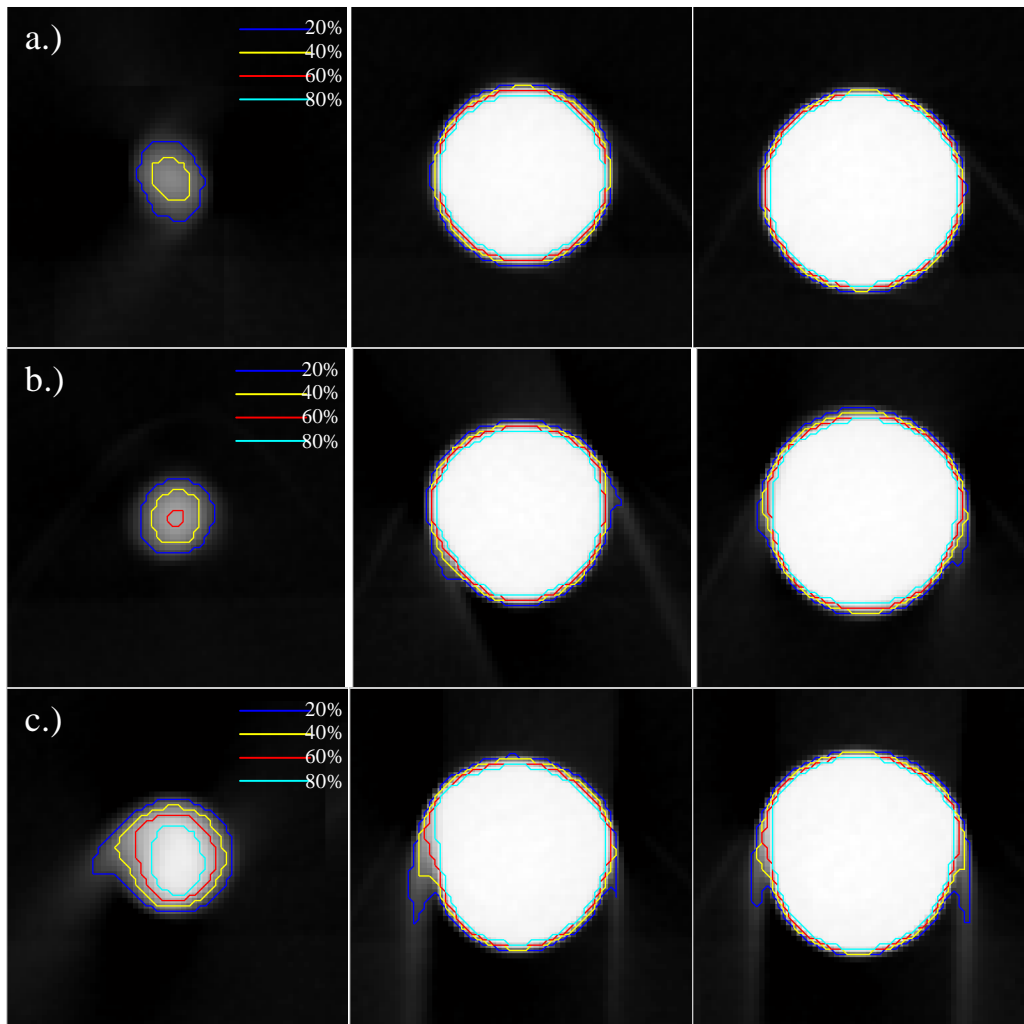
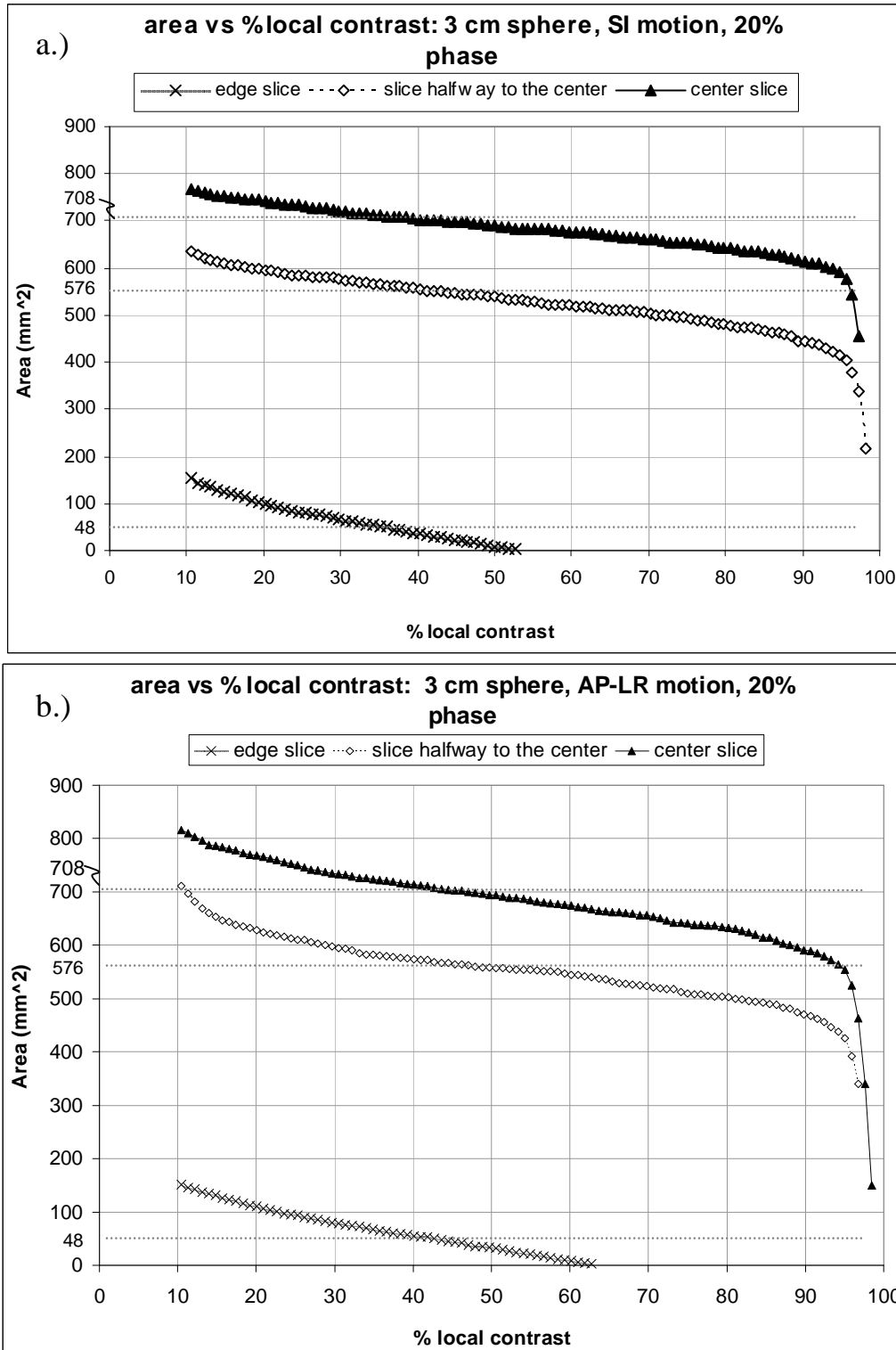


Figure caption: From left to right, the edge slice, the halfway to the middle slice, and the center slice. The outlines are where the boundary of the segmented cross sectional image would lie with 20, 40, 60, and 80 % local contrast thresholds. a.) 3 cm sphere SI motion, b.) 3 cm sphere AP-LR motion, c.) 3 cm sphere SI-AP-LR motion.

Figure 3.47: Area vs. % local contrast attribute maps for the 3 cm spheres imaged with 4DCT undergoing motion in the SI, AP-LR, SI-AP-LR directions



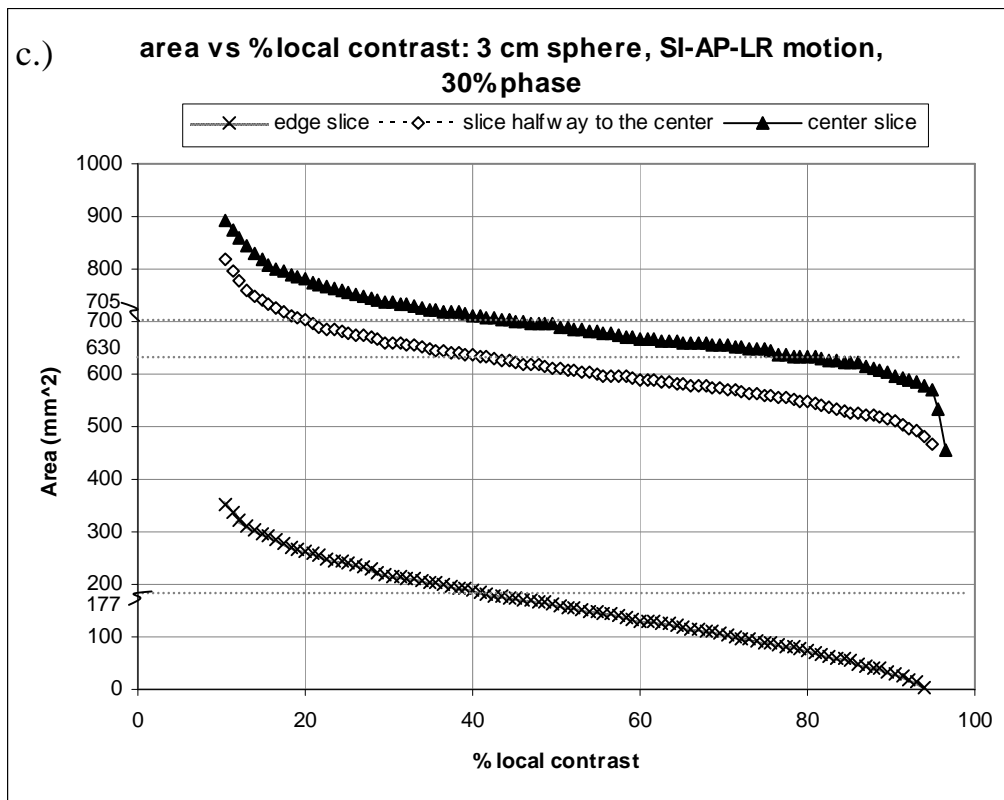
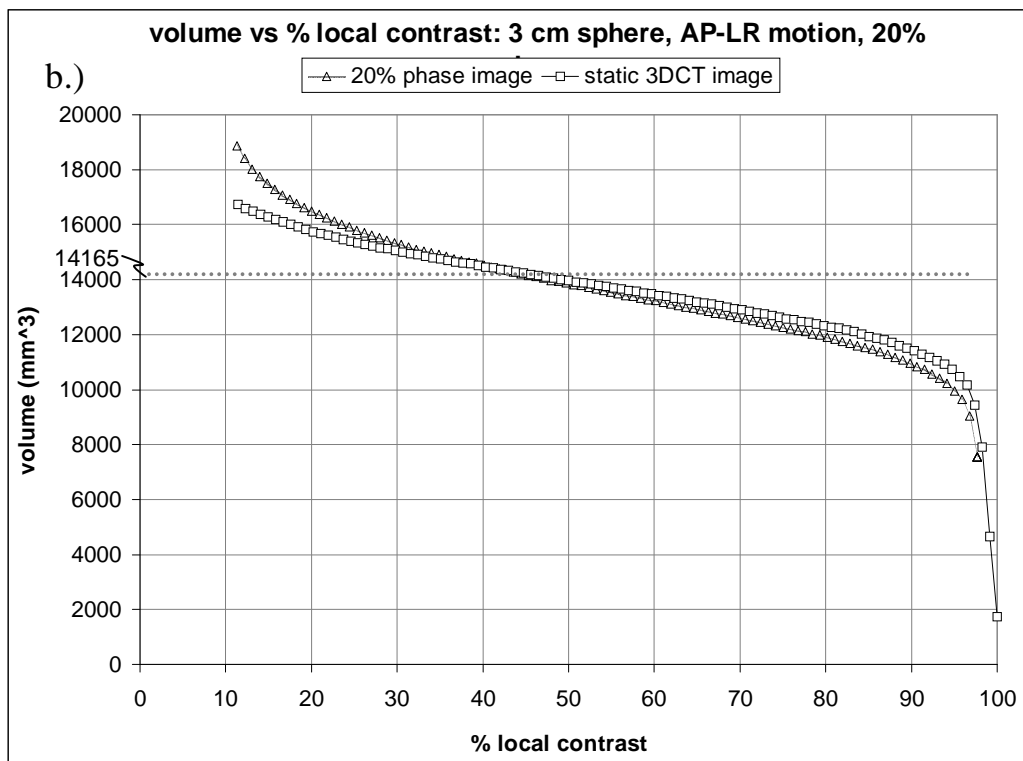
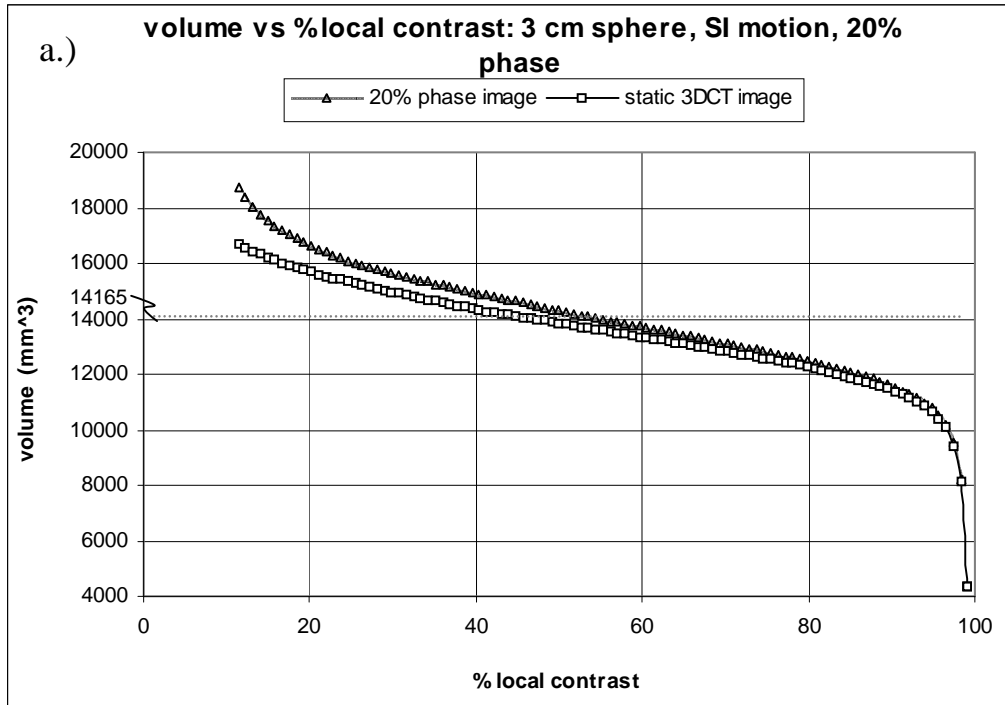


Figure caption: Area vs. % local contrast for three slices of the 3 cm sphere depicted in Figure 3.46 undergoing motion in the a.) SI direction, b.) AP-LR direction, and c.) SI-AP-LR direction. The consequences of residual motion on the cross sectional areas of the 3 cm sphere are not as dramatic as for the 1 cm sphere.

Figure 3.48: Volume vs. % local contrast attribute maps for the 3 cm spheres imaged with 4DCT undergoing motion in the SI, AP-LR, SI-AP-LR directions



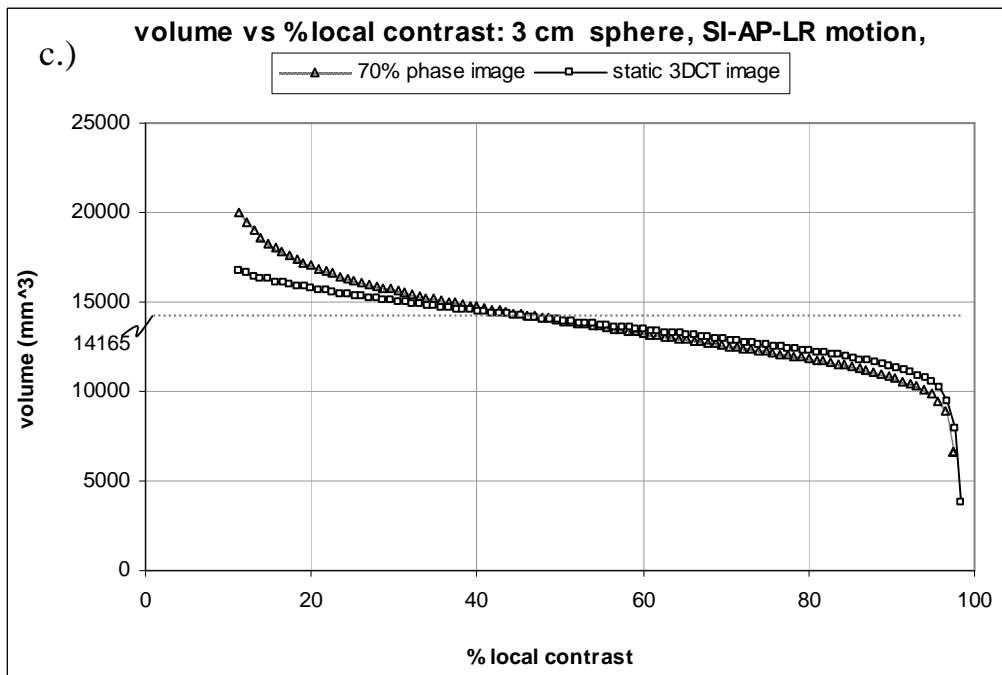


Figure caption: Volume vs. % local contrast for the 3 cm sphere depicted in Figure 3.46 undergoing motion in the a.) SI direction, b.) AP-LR direction, and c.) SI-AP-LR direction. Unlike for what was seen with the 1 cm sphere data, the 3 cm sphere AP-LR motion shows the least difference from the static scan.

Looking at the volume attribute maps in Figure 3.48, like the 1 cm sphere, the 3 cm sphere is also affected by the inclusion of low density artifacts and an overall decrease in density. Unlike what was seen in the 1 cm sphere data, the AP-LR motion seems to have the least impact on the 3 cm sphere volume's response to threshold.

The 3 cm sphere's eccentricity attribute maps for the cross sectional images appearing in Figure 3.46 are shown in Figure 3.49. The eccentricity of the center slices under SI motion shows essentially the same pattern as a function of threshold as does the static image of the 3 cm sphere (See Figure 3.39b). This is true also for the edge slice under the AP-LR motion. In the rest of the 3 cm data, the eccentricity's response to thresholding is similar to that seen in the 1 cm data.

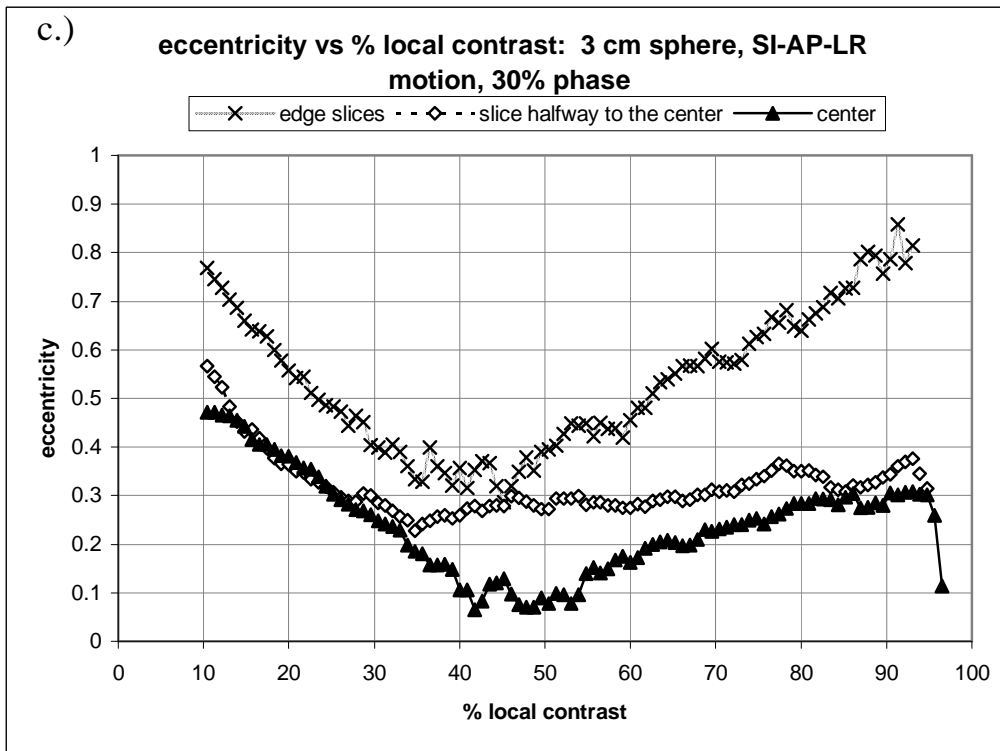
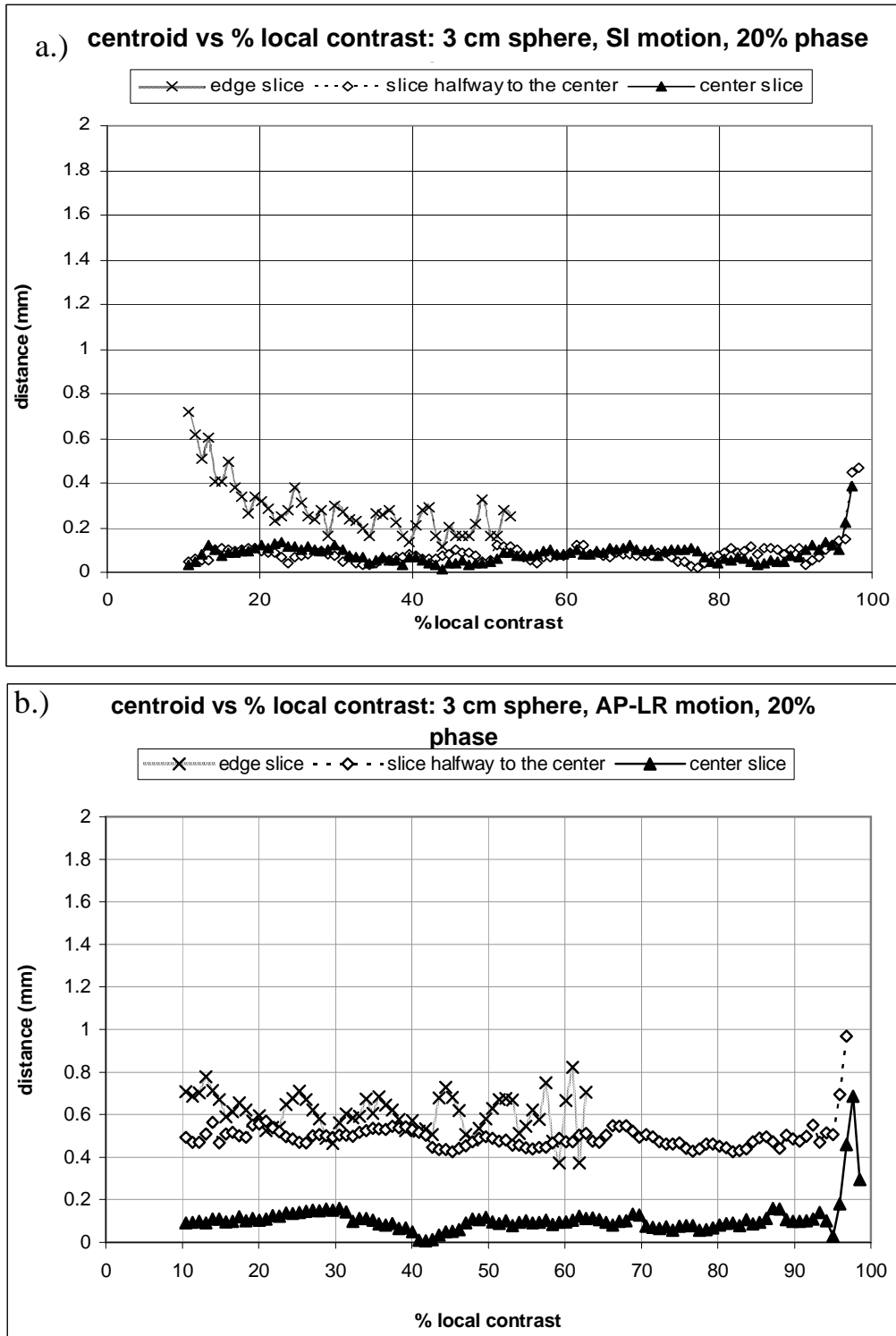


Figure caption: Eccentricity vs. % local contrast for three slices of the 3 cm sphere depicted in Figure 3.46 undergoing motion in the a.) SI direction, b.) AP-LR direction, and c.) SI-AP-LR direction. For the AP-LR motion, the edge slice cuts through a good chunk of the sphere (see Figure 3.36c) and so the map extends over a wide range of thresholds.

The centroid vs % local contrast attribute maps for the images of Figure 3.46 are shown in Figure 3.50. Like the 1 cm sphere, the 3 cm sphere's centroid is relatively insensitive to threshold under SI motion. For the AP-LR motion, the fluctuation is comparable to that seen in the static image, with no dramatic shifts with threshold. However, the minor offset in absolute position of each imaged center indicates some asymmetry in the cross sectional areas of the edge and halfway slices. With the SI-AP-LR motion, all slices are affected by the inclusion of low density artifacts (i.e. the drift in centroid at low thresholds), but only the edge slice suffers sufficient variation in pixel densities to dramatically alter the centroid calculation at high thresholds as well.

Figure 3.50: Centroid vs. % local contrast attribute maps for the 3 cm spheres imaged with 4DCT undergoing motion in the SI, AP-LR, and SI-AP-LR directions



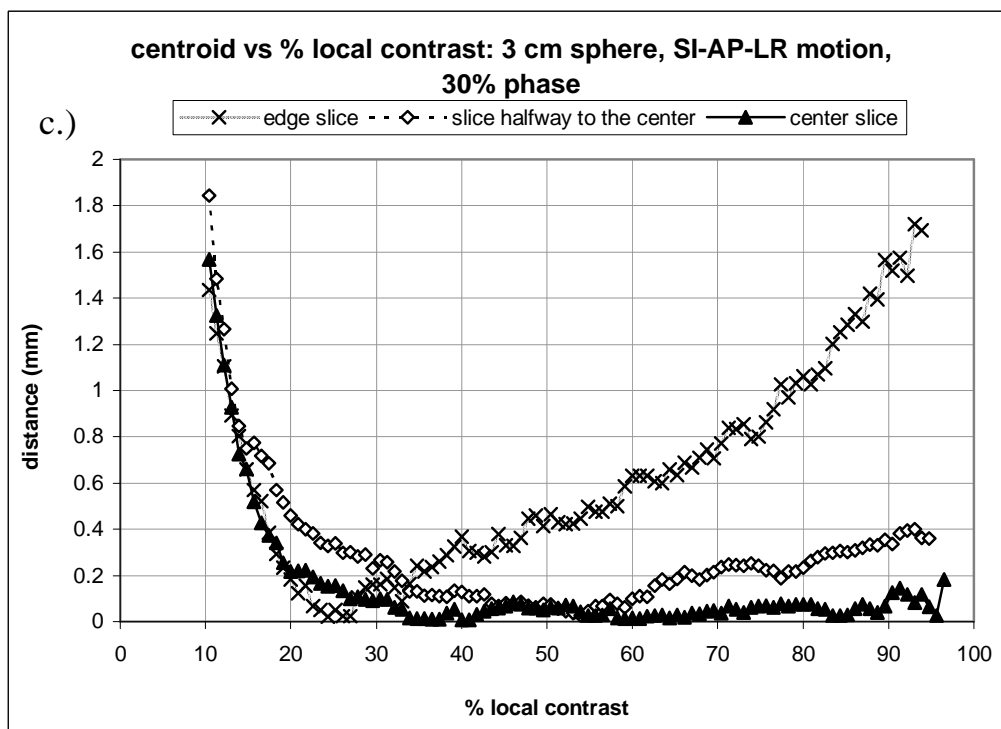


Figure caption: Centroid vs. % local contrast for three slices of the 3 cm sphere depicted in Figure 3.46 undergoing motion in the a.) SI direction, b.) AP-LR direction, and c.) SI-AP-LR direction. For all types of motion, the 3 cm sphere centroid in the center slice is stable over a wide range of thresholds. For the AP-LR and SI-AP-LR motions, the mis-assignment of densities causes an asymmetry that is noticeable in the centroid drift of the edge and halfway slices.

5 cm Sphere

For the 5 cm sphere, the images corresponding to the cross sectional area attribute maps are shown in Figure 3.51. The images are shown with the outlines of the segmented boundaries of the object at 20, 40, 60, and 80 % local contrast. Again, SI, AP-LR, and SI-AP-LR motions are investigated. The area vs. % local contrast attribute maps for these images are given in Figure 3.52.

As seen in the data from the smaller spheres, the threshold's effect on the area of the segmented cross section for the 5 cm sphere has the greatest impact on the edge slice when undergoing SI and SI-AP-LR motions, and for the AP-LR motion, the largest impact is on the halfway slice. For the SI and SI-AP-LR graphs, the slopes of the area vs % local contrast maps become less steep as you move towards the center of the sphere because the strength of the pinwheel artifact diminishes. Looking at the volume attribute maps for these images (Figure 3.53), the volume of the 5 cm sphere appears more impacted by SI motion than the 3 cm sphere. This may be expected due to the dramatic changes in its cross sectional diameter towards the edges, resulting in larger pinwheel artifacts. Even so, the relative impact of the SI motion on the 5 cm sphere's volume is still less than what is seen with the 1 cm sphere due to its much larger volume. Of all the motions, the SI-AP-LR motion appears to have the most effect on the largest sphere's imaged volume.

Figure 3.51: Three slices of the 5 cm sphere undergoing motion in the SI, AP-LR, and SI-AP-LR directions.

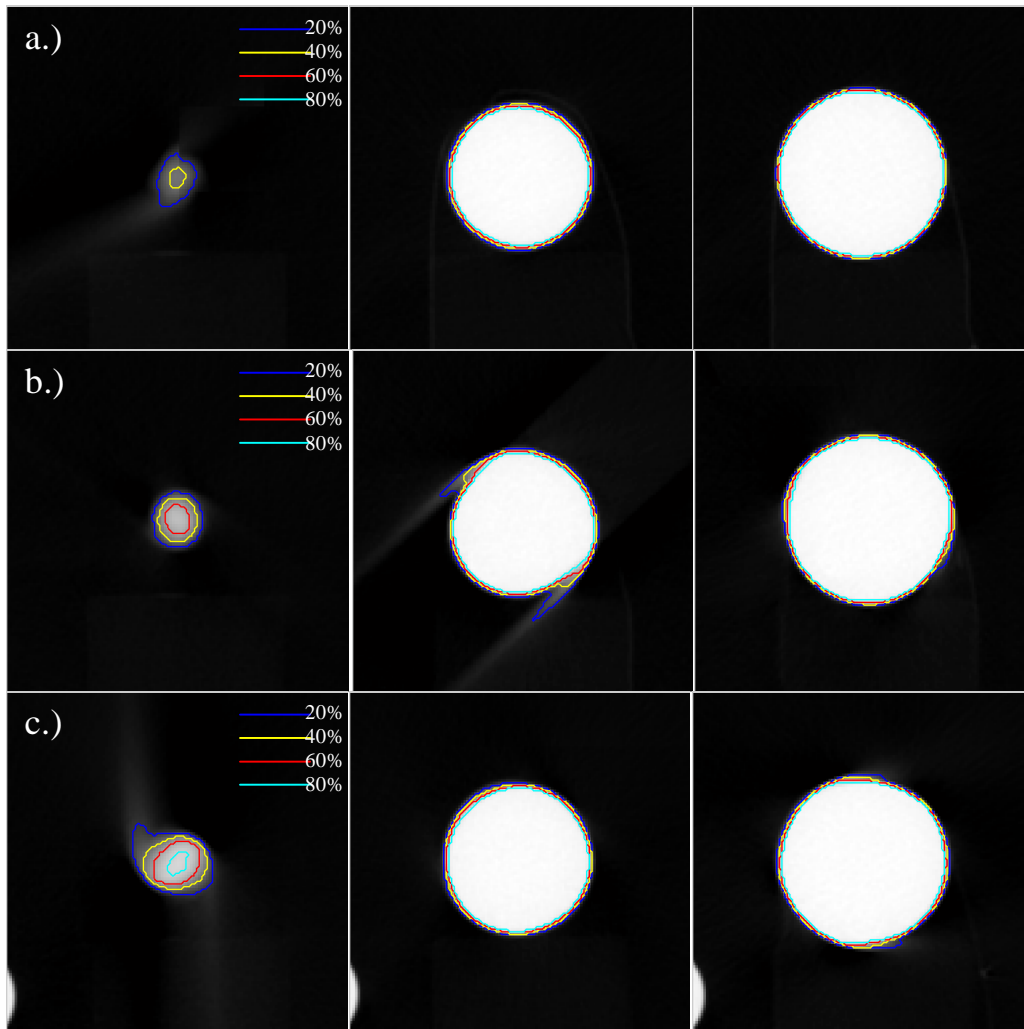
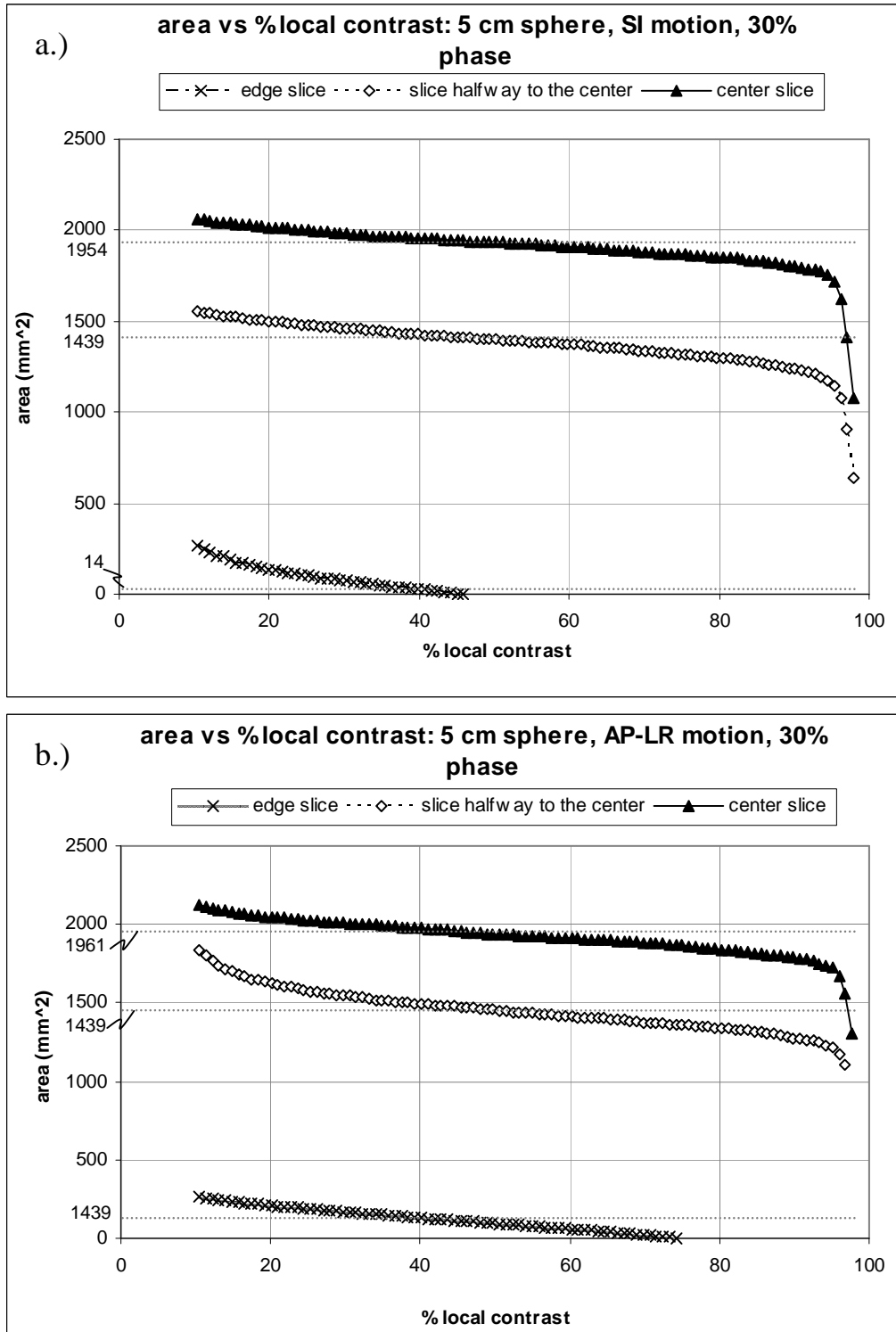


Figure caption: From left to right, the edge slice, the halfway to the middle slice, and the center slice. The outlines are 20, 40, 60, and 80 % local contrast thresholds. a.) 5 cm sphere SI motion, b.) 5 cm sphere AP-LR motion, c.) 5 cm sphere SI-AP-LR motion—a little piece of the stationary reference object is visible.

Figure 3.52: Area vs. % local contrast attribute maps for the 5 cm spheres imaged with 4DCT undergoing motion in the SI, AP-LR, and SI-AP-LR directions



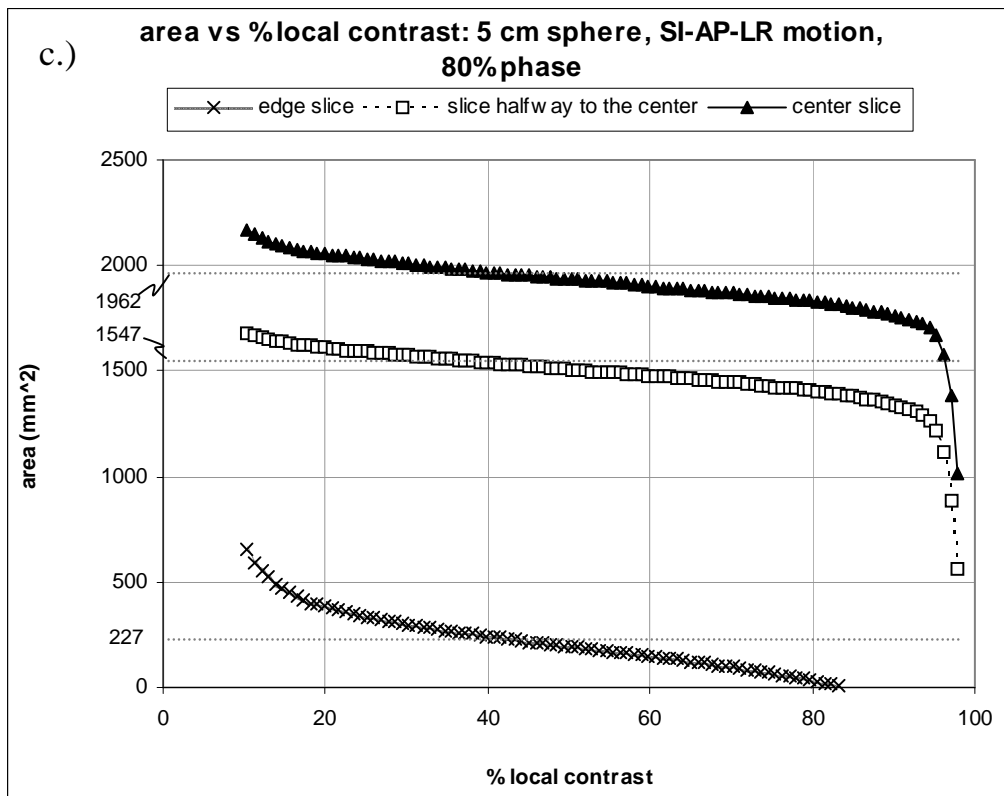
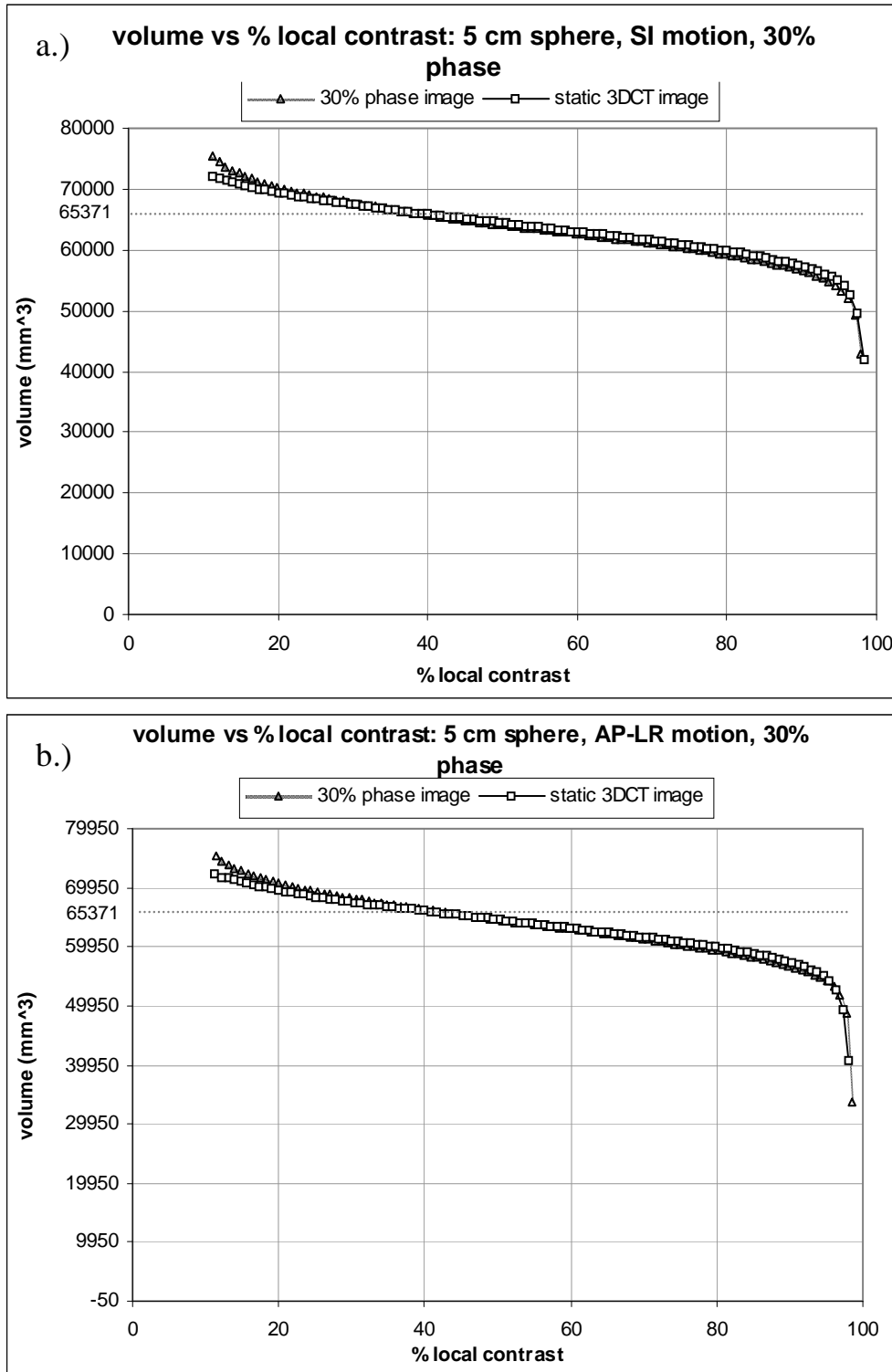


Figure caption: Area vs. % local contrast for three slices of the 5 cm sphere undergoing motion. a.) For SI motion, the edge slice is the most affected due to the large pinwheel artifacts. b.) For AP-LR motion, the halfway slice shows the most effect from the residual motion artifacts, the edge slice being very low density and the center slice being very large. c.) Motion in the SI-AP-LR direction affects the edge slice the most.

Figure 3.53: Volume vs. % local contrast attribute maps for the 5 cm spheres imaged with 4DCT undergoing motion in the SI, AP-LR, SI-AP-LR directions



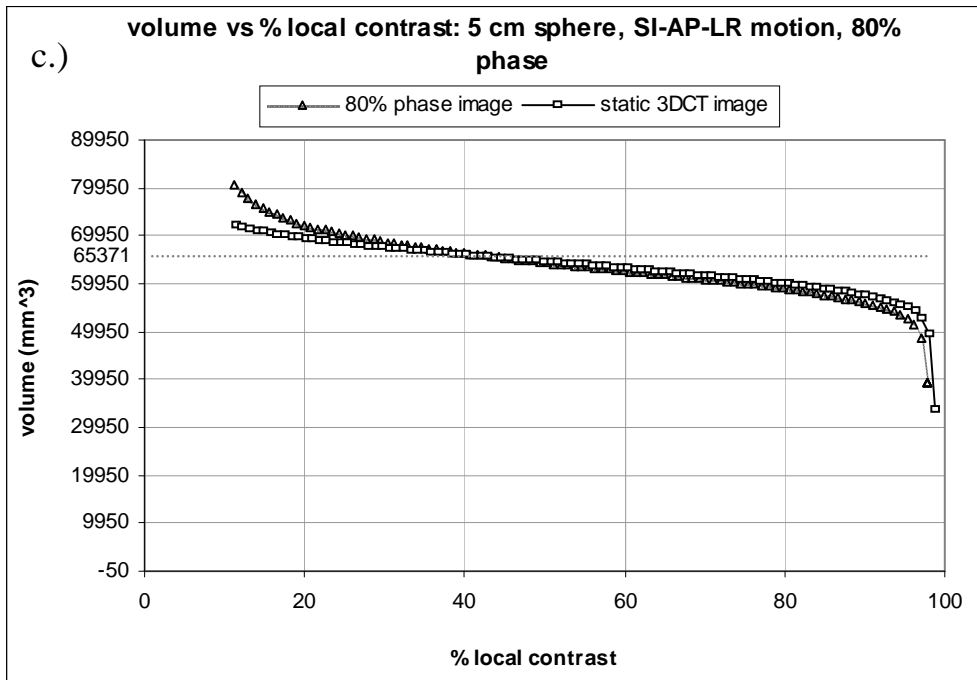
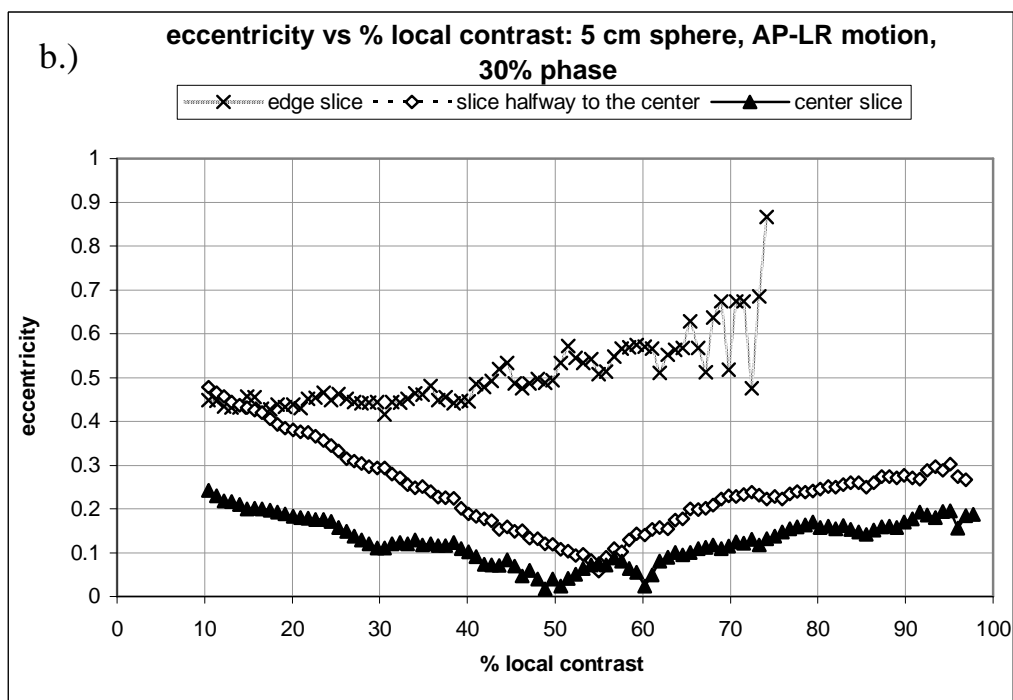
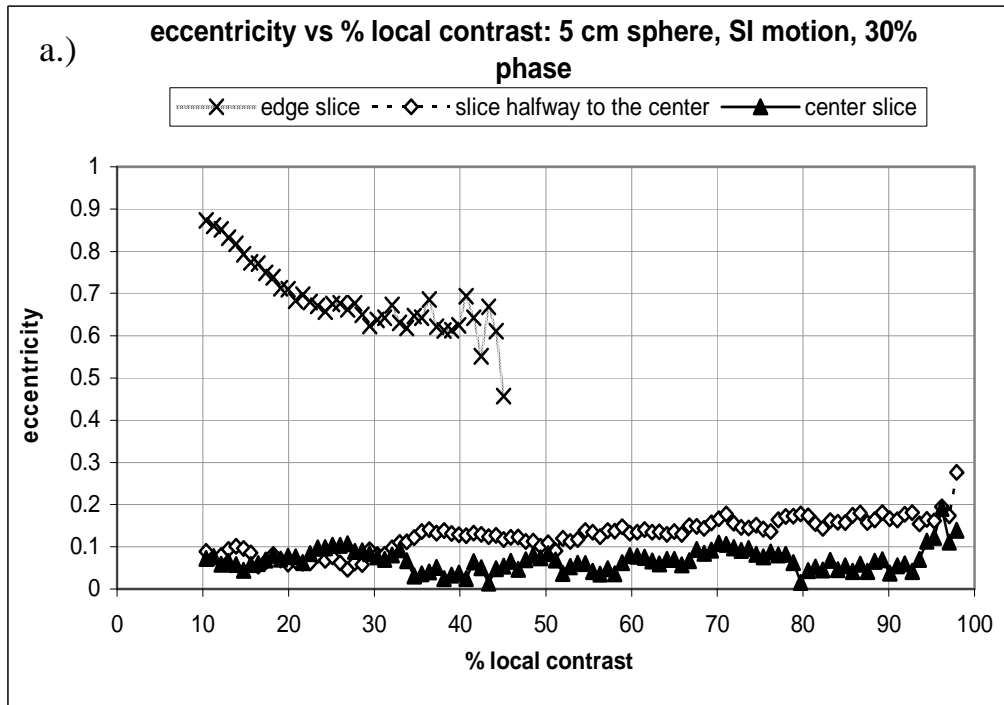


Figure caption: Volume vs. % local contrast of the 5 cm sphere undergoing motion in the a.) SI direction, b.) AP-LR direction, and c.) SI-AP-LR direction. Because of the 5 cm sphere's large size, the volume is not as affected by residual motion artifacts. For all types of motion, however, evidence of low density artifacts and an overall increased sensitivity to threshold are still evident.

The eccentricity and centroid attribute maps for the 5 cm sphere cross sectional images shown in Figure 3.51 are found in Figures 3.54 and 3.55, respectively.

Figure 3.54: Eccentricity vs. % local contrast attribute maps for the 5 cm spheres imaged with 4DCT undergoing motion in the SI, AP-LR, SI-AP-LR directions



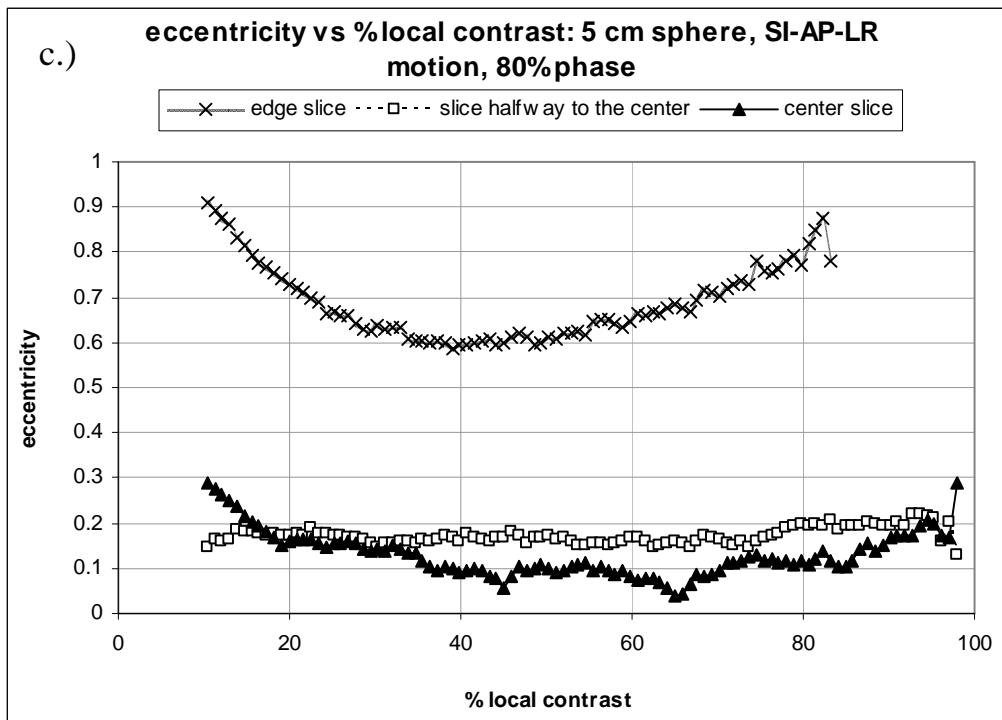
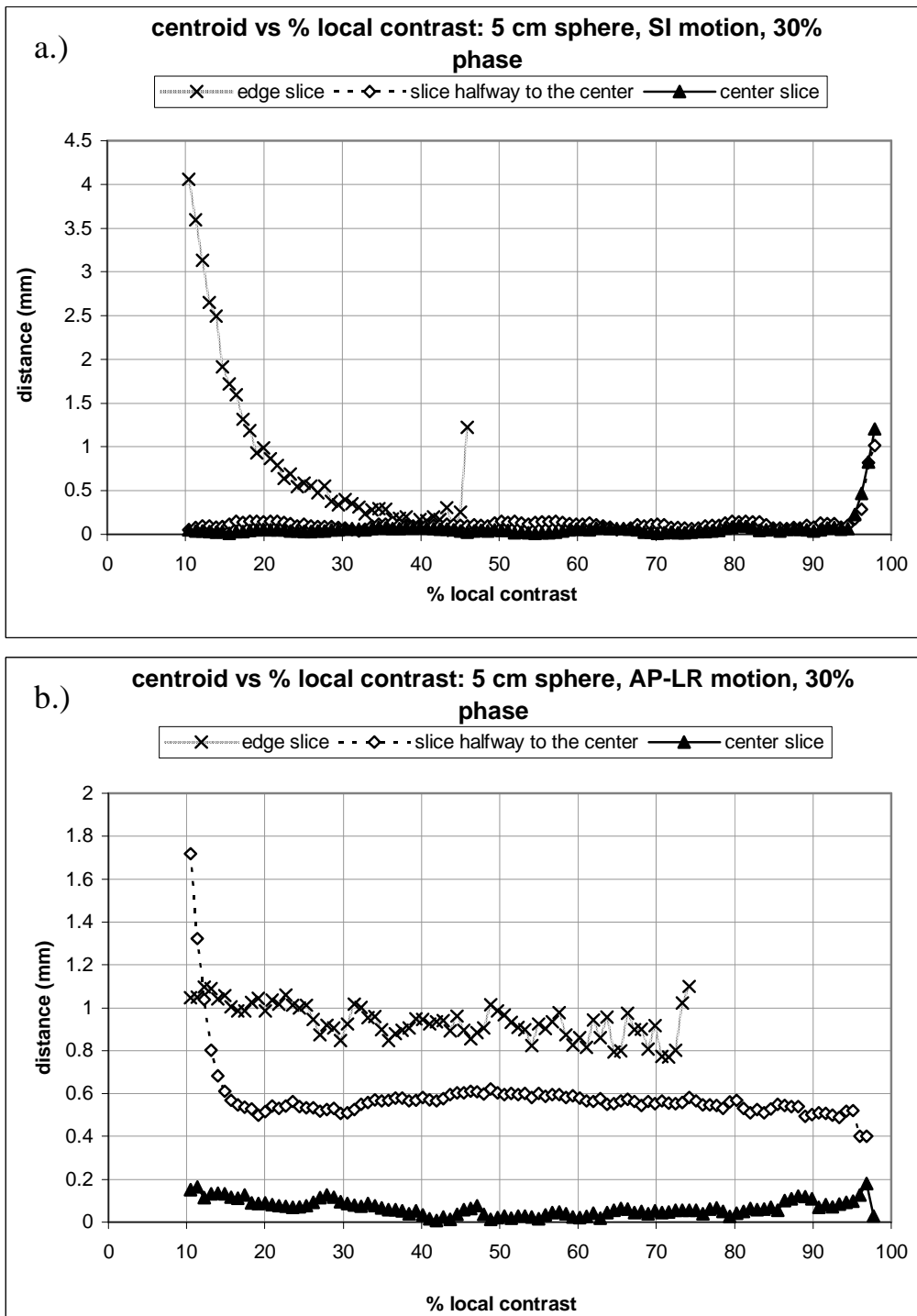


Figure caption: Eccentricity vs. % local contrast for three slices of the 5 cm sphere undergoing motion in the a.) SI direction, b.) AP-LR direction, and c.) the SI-AP-LR direction. As with the smaller sphere sizes, eccentricity of the edge slice is high due to partial volume effects and accentuated residual motion artifacts. For motion with an AP-LR component, the inner slices bow, dipping down to stationary sphere levels near the threshold range specified by the reference object.

The eccentricity attribute map for the 5 cm sphere undergoing SI motion is similar to that of the static sphere (see Figure 3.39c), especially for the center slice, which appears impervious to threshold. Since such a small cross sectional area of the sphere was captured by the edge slice (see Figure 3.51a), partial volume effects dominate, and all that is seen in the eccentricity attribute map for this slice are residual motion artifacts which dwindle quickly with threshold. The eccentricity of the AP-LR and SI-AP-LR motions respond in a similar fashion as the 1 and 3 cm spheres, exhibiting a pattern of increased eccentricity at low thresholds due to inclusion of residual motion artifacts, as well as an increase at high thresholds from the greater inhomogeneity of pixel values. For the halfway slice of the SI-AP-LR motion, however, the eccentricity is much like the static image, although higher in value.

Since in the SI motion phase image, the edge slice captured only a small sliver of the sphere, consisting primarily of low density artifacts, the centroid consistently migrates with increasing threshold (see Figure 3.55). The centroid on the other two slices, however, is quite stable over a wide range of thresholds. Like the 3 cm sphere, when under AP-LR motion, the centroid just shows an offset in position, but is consistent with threshold. For the SI-AP-LR motion, the centroid of the area imaged on the middle slice is impervious to threshold, but that on the edge slice reveals the presence of a large artifact (see Figure 3.51c). On the halfway to center slice, the centroid drifts slightly with increased threshold like the 3 cm sphere.

Figure 3.55: Centroid vs. % local contrast attribute maps for the 5 cm spheres imaged with 4DCT undergoing motion in the SI, AP-LR, SI-AP-LR directions



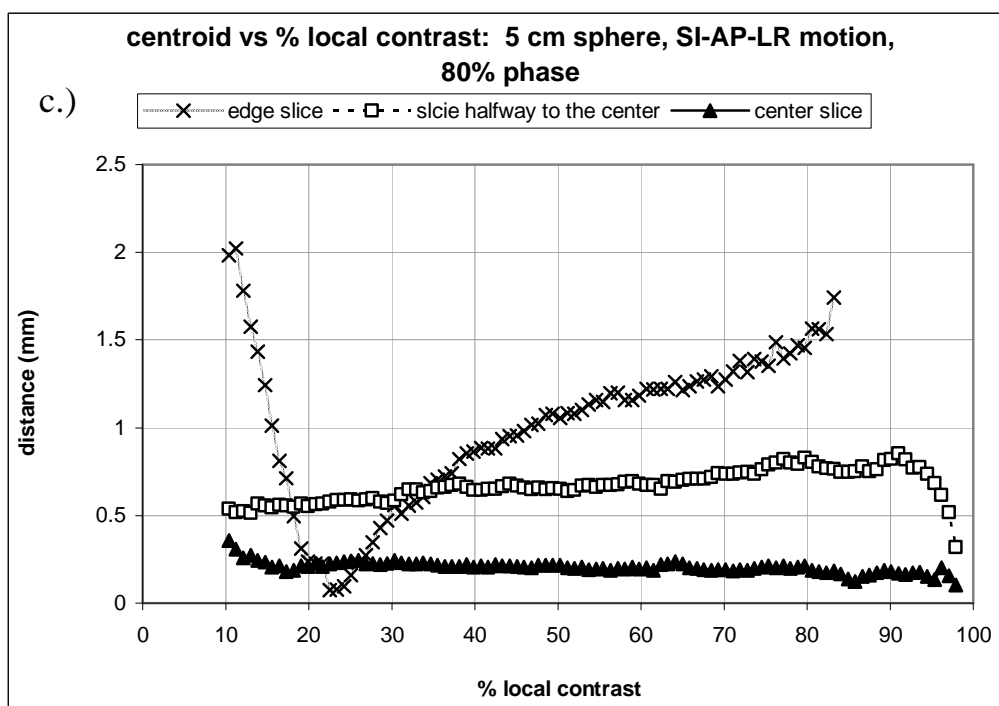


Figure caption: Centroid vs. % local contrast for three slices of the 5 cm sphere undergoing motion in the a.) SI direction, b.) AP-LR direction, and c.) SI-AP-LR direction. For the SI motion, the edge slice appears to consist of nothing but partial volume effects and residual motion artifacts. The centroids of the inner two slices, however, are virtually impervious to the effects of SI motion. AP-LR motion creates an offset in centroid location, but is still consistent over a wide range of thresholds. In the SI-AP-LR maps, the presence of a large artifact in the edge slice is evident, as well as some offset in centroid position in the halfway slice.

Summary of Residual Motion Artifacts

Although motion in the SI direction produces the largest pinwheel artifacts for the 5 cm sphere, the impact of the artifact on the overall imaged shape of the sphere is greatest for the 1 cm sphere due to its relatively small size. For all sphere sizes, the pinwheel artifact is reduced at the center, where the cross section seen by the imaging plane changes the least during image acquisition. The horseshoe crab artifact generated by AP-LR motion has a greater impact on the smaller sphere because the motion caught during image acquisition is still large compared to the diameter of the object. Thus, for the smaller cross sectional images of the 3 and 5 cm spheres, the AP-LR motion can cause significant artifacts as well. Cross sectional images of the edge slices of all the spheres, however, have reduced contrast with their backgrounds due to partial volume effects, and thus, the mis-assignment of densities arising from AP-LR motion is not as severe. The combined artifacts arising from AP-LR and SI motions together have a significant effect on all sphere sizes. Yet, overall, the 5 cm sphere is the most impervious to residual motion artifacts given its many central slices with large cross sectional areas.

Only the fastest phases have been presented here in order to highlight the effects of residual motion on the attributes of the 4DCT phase images. However, it should not be assumed that these artifacts plague all 4DCT images. The slower phases are virtually artifact free, as seen in Figure 3.56. Each of these examples is from the 50 % phase (i.e. peak exhale) from one of the 4DCT data sets shown earlier.

Figure 3.56: Three slices from each sphere size at the 50% phase

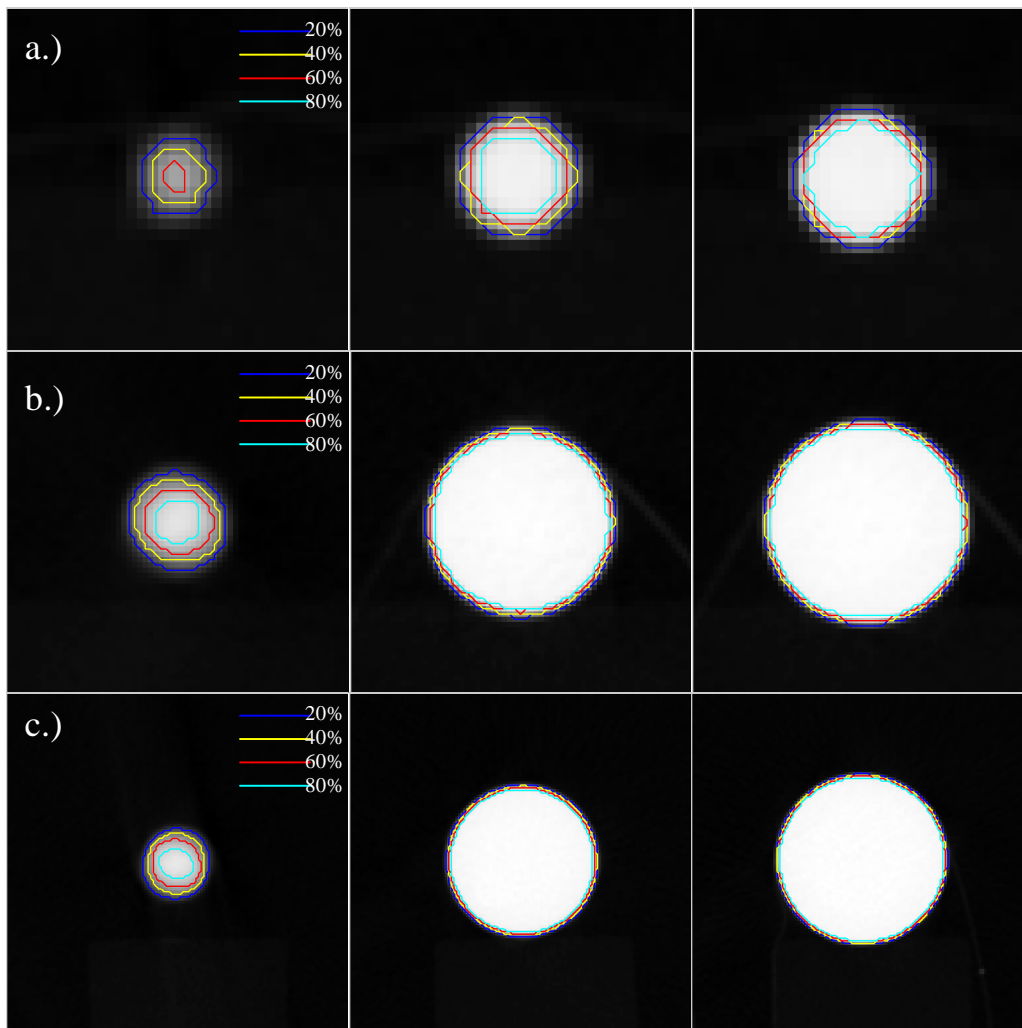


Figure caption: Select slices of the 50% phase from the same 4DCT acquisition shown earlier. From right to left: the edge slice, the slice halfway to the center, and the middle slice of a.) the 1 cm sphere undergoing AP-LR motion, b.) the 3 cm sphere undergoing SI motion, and c.) the 5 cm sphere undergoing SI-AP-LR motion. Being turn around points in the spheres' trajectories, the 50% and 00% phases are the "slow" phases, virtually devoid of motion artifacts. (The 5 cm sphere is not shown at the same magnification, and so appears smaller than the 3 cm sphere.)

Functional Dependencies of the Metrics

There are three variables in the quantitative measurement experiment. These are type of motion, amplitude of motion, and sphere size. As well, for each 4DCT acquisition, the 10 reconstructed phases of motion image the sphere at different velocities. Peak inhale (00%) and peak exhale (50%), being the turn-around points in the sphere's trajectory, are the slowest phases, and the sphere should be virtually stationary. The 20% and 70% phases occur just before the sphere attains its maximum velocity, and the 30% and 80% phases, just after. Due to the symmetry of the circular cams, the speeds of all 4 phases should be identical. Due to the linear nature of CT acquisition, the advancement of the scanning plane is in a fixed relationship with the mechanical motion of the phantom. During the sphere's path from peak inhale to peak exhale, the scanning

plane is moving against the motion of the phantom, and for the return trip to peak inhale, it is moving with the scanning plane (please see Figure 3.57). Along with the various velocities of the sphere throughout its journey, this fixed relationship to the advancing scanning plane means that no two phases are equivalent, giving each metric some degree of phase dependency. The following discussion highlights the functional dependencies of each metric on the type of motion, amplitude of motion, sphere size, as well as the phase of motion.

Figure 3.57: Sphere moving with or against the motion of the scanning plane.

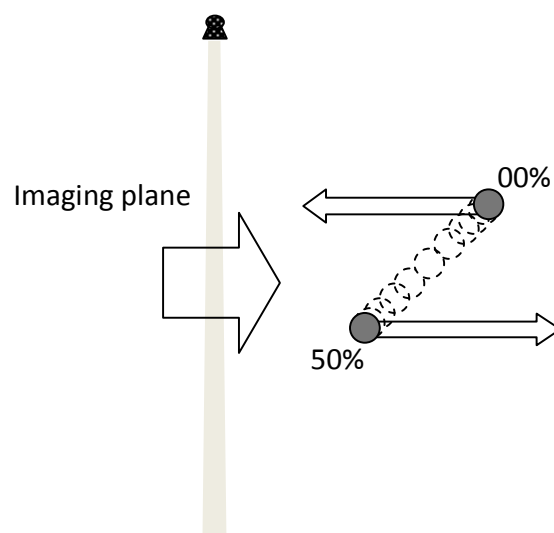


Figure caption : Even though the tube images the same slice location for a duration longer than the period of motion, it is slowly advancing the entire time.

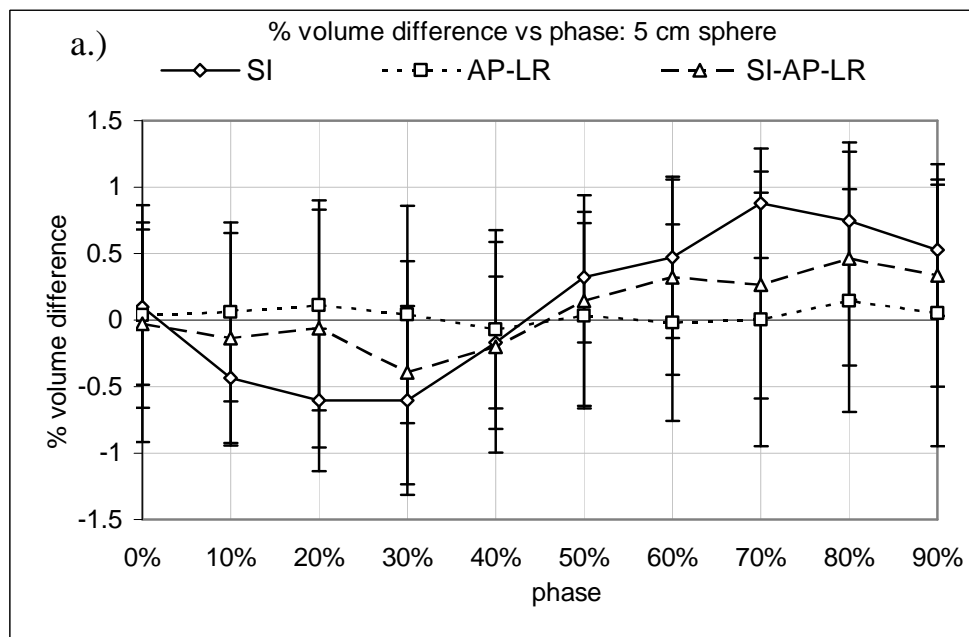
Here, Bellows and RPM data have been grouped together, and although each 4DCT acquisition is labeled with the respiratory monitoring system used, there is no distinction made between the two. In the context of these quantitative measurements, they are equivalent.

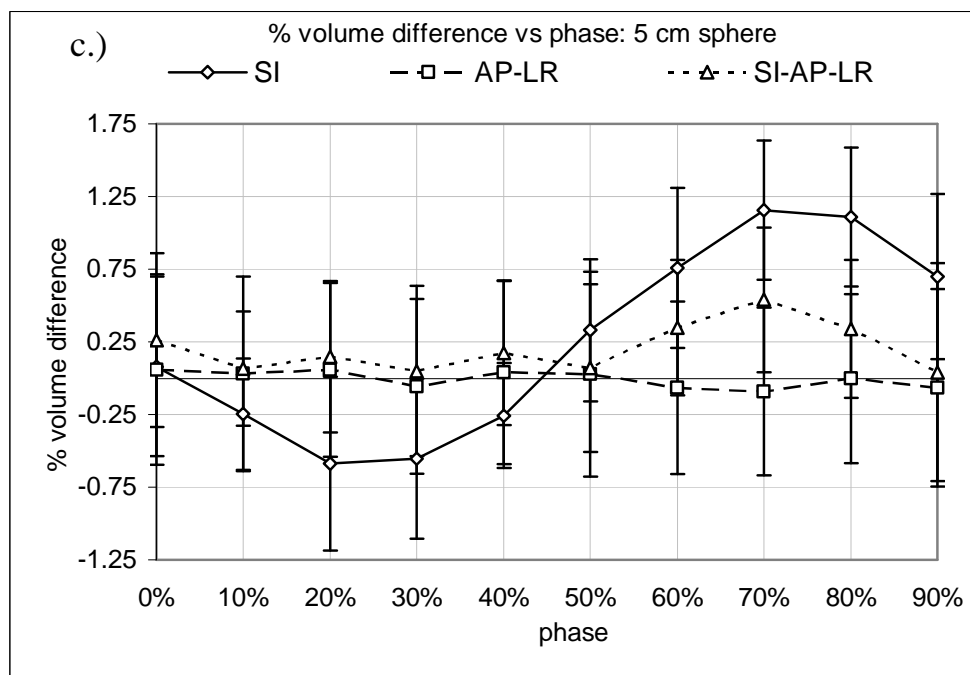
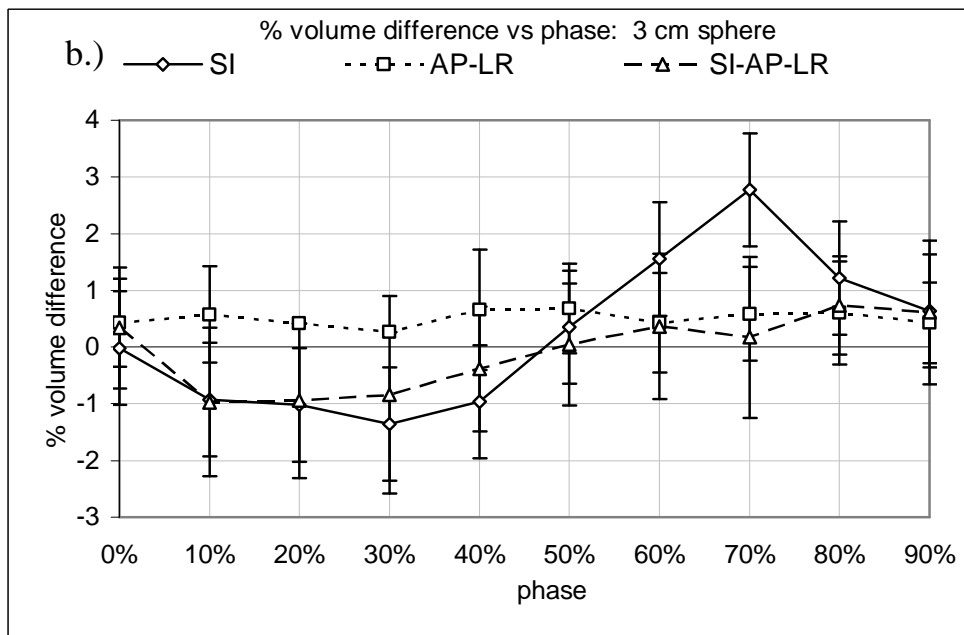
% Volume Difference

A phase dependency is clearly visible in the *% volume difference* data. Figure 3.58 shows the metric of *% volume difference* graphed against the phases of motion for the three types of motion, SI, AP-LR, and SI-AP-LR. In each example, the *% volume difference* is negative when the sphere moves against the advancement of the scanning plane from the 00% to the 50% phase, indicating that the sphere is imaged smaller than its true volume. From the scanning plane's perspective, the z-extent of the sphere shrinks throughout the acquisition. Then, on the sphere's return journey to the 00% phase, it moves with the scanning plan, causing the sphere to appear elongated in the z-direction, and thus, these *% volume differences* are positive (3). The resulting sinusoidal shape appears in all *% volume difference* data where an SI component of motion exists. The maximum volumetric differences appear in the faster phases (e.g. 30 or 70 %), where the cross section of the sphere caught by the scanning plane is changing most rapidly. This pattern of volumetric discrepancy has been noted by other investigators (2,44). The AP-LR motion, being perpendicular to the scanning plane, shows no phase dependency, but rather, just hovers around some mean value. One might expect that the *% volume*

difference would also be greatest for the faster phases due to the possible inclusion of low density residual motion artifacts, but this effect is not seen. Notice that the % *volume difference* vs phase for SI-AP-LR motion, while producing the distinctive sinusoidal shape, shows smaller amplitudes than the SI motion despite the fact that the component of motion causing the phase dependency is identical for both. Thus, the convolution of AP-LR artifacts with SI artifacts diminishes the severity of the directional dependency with respect to the scanning plane. For all types of motion, the % *volume differences* are lowest at or near the 00% and 50% phases. At these phases the sphere is essentially stationary and the residual motion artifacts are minimal.

Figure 3.58: % volume difference vs. phase for different types of motion





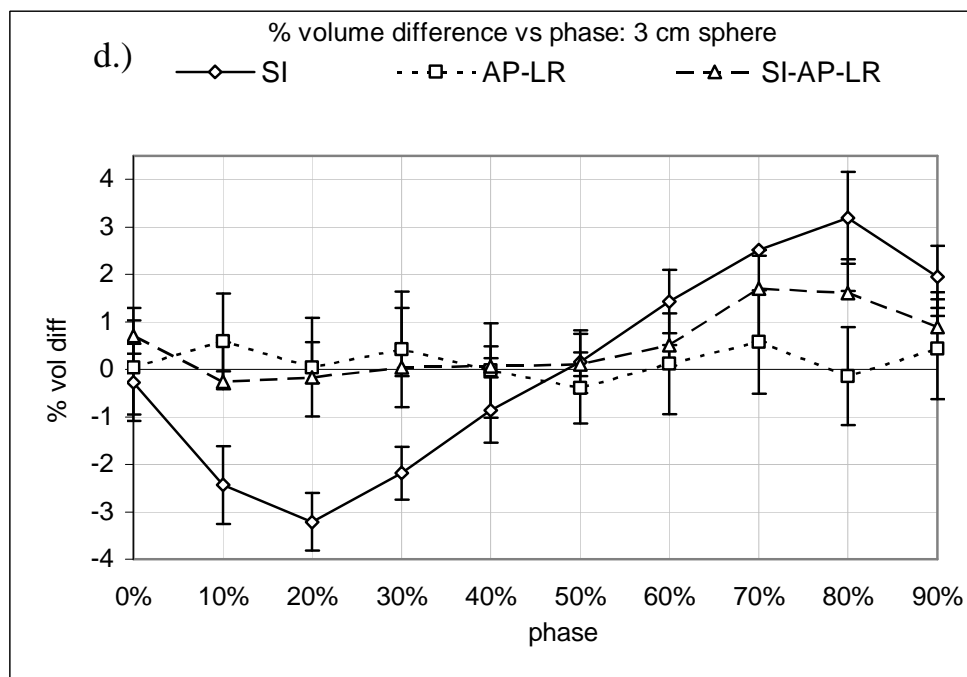
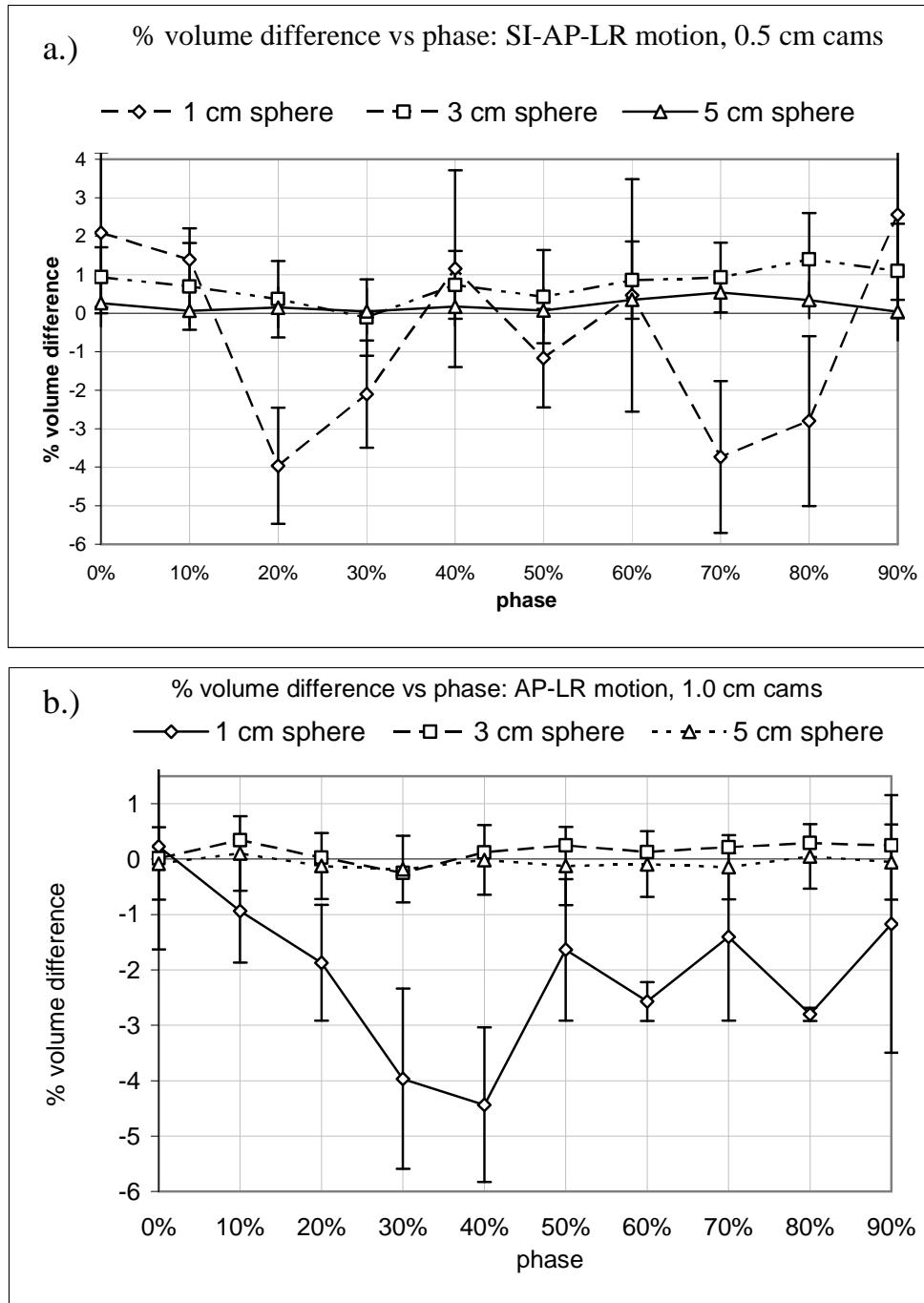


Figure caption: % volume difference vs. phase for different types of motion. Graphs for the 1 cm sphere are not shown since this data is too noisy to show any phase dependence. a.) 5 cm sphere, Bellows, 1.5 cm cams, b.) 3 cm sphere, Bellows 1.5 cm cams, c.) 5 cm sphere, Bellows 0.5 cm cams, d.) 3 cm sphere, Bellows 1.5 cm cams. The characteristic sinusoidal shape appears in all volume data with an SI component of motion. Convolution of AP-LR with SI artifacts, however, diminishes the phase discrepancy arising from motion with and against the scanning plane.

Figure 3.59 shows the % volume difference vs. phase for the different sizes of spheres. In each example, regardless of the type of motion, the larger the sphere the smaller the absolute value of the % volume difference (2,32). This is due to: the larger number of voxels in the reconstructed image, the smaller surface to volume ratio which minimizes the influence of partial volume effects, and the fact that the extent of any residual motion artifacts are smaller compared to the extent of the sphere. The error bars for the 1 cm sphere are large since its high surface area and the relative size of its artifacts make it much more susceptible to threshold uncertainties. It is common for the 1 cm sphere to image smaller than its true volume regardless of the phase of motion, predominately due to partial volume effects. Since the mean % volume difference for the 1 cm sphere in the static reference images is 1.09% too small, the thresholds prescribed by the 3 cm diameter reference object may be slightly high for the 1 cm diameter sphere. With a standard deviation of 1.65 %, reconstructing a small spherical volume with $0.78 \times 0.78 \times 2.00 \text{ mm}^3$ voxels is noisy. The 3 cm sphere data has error bars smaller than the 1 cm sphere data, but larger than the 5 cm sphere data; as the spheres get larger the % volume difference is more resistant to variations in threshold.

Figure 3.59: % volume difference vs. phase for different sphere sizes



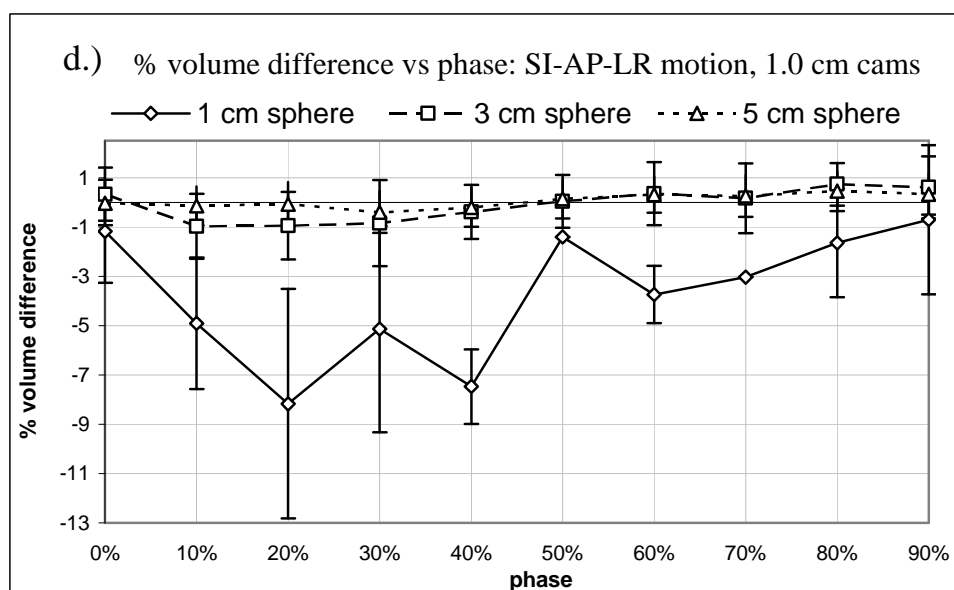
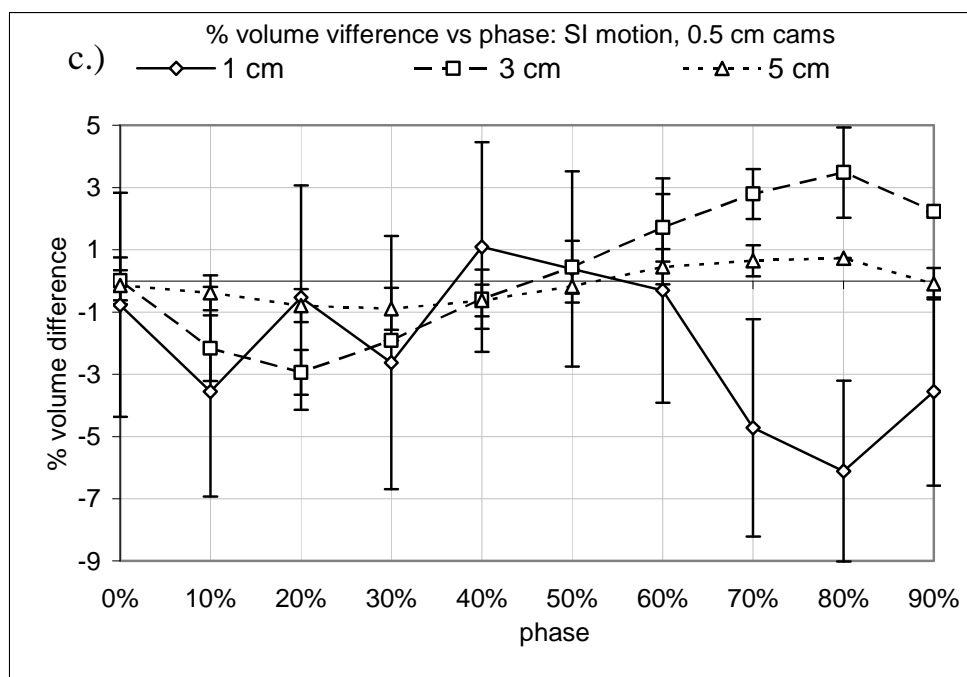


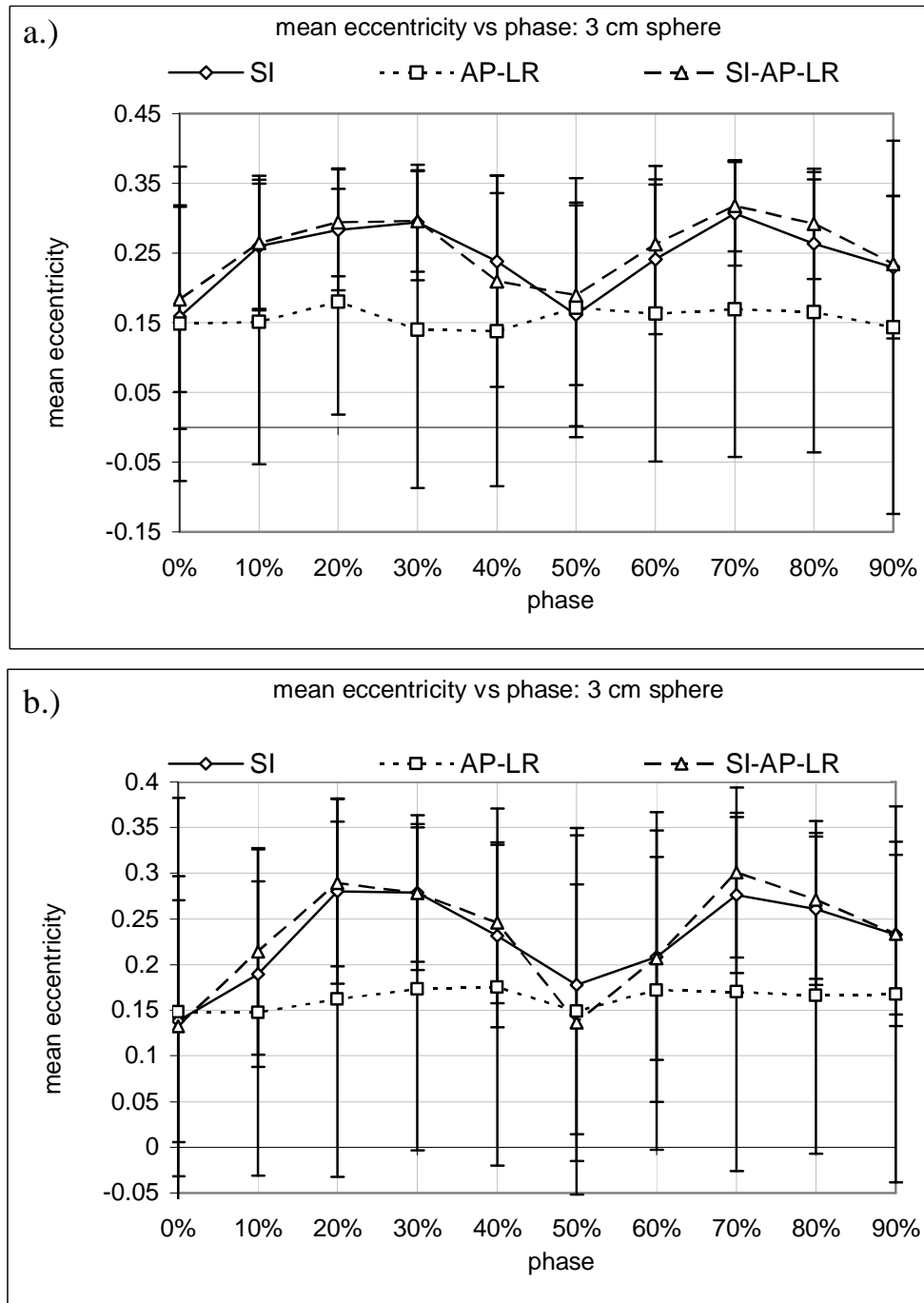
Figure caption: % volume difference vs. phase comparing the different sizes of spheres. a.) SI-AP-LR motion, Bellows 0.5 cm cams, b.) AP-LR motion, RPM 1.0 cm cams, c.) SI motion, Bellows 0.5 cm cams, d.) SI-AP-LR motion, Bellows 1.0 cm cams. The 1 cm data is noisy, with larger error bars than the 3 & 5 cm spheres, indicating a greater sensitivity to thresholding. The 3 cm data consistently has a larger % volume difference than the 5 cm sphere data, as well as larger error bars. Thus, the larger the sphere, the smaller the volume discrepancy and the more resistant it is to threshold sensitivity.

Mean Eccentricity

Figure 3.60 shows *mean eccentricity* versus phase for the different types of motion. The spiraling of electron densities created from SI motion has a greater impact on the object's segmented shape than the mis-assignment of densities found with AP-LR

motion. The AP-LR motions show much less phase dependency; all that can be said is that, typically, the 00% and 50% phases have among the lowest mean eccentricities. For the SI-AP-LR motion, convolution of the AP-LR horseshoe artifact with the SI pinwheel artifact has no mitigating effect on the eccentricity metric. Since the nature of SI and AP-LR artifacts are different, it is reasonable to assume that they have different responses to thresholding—notice that the AP-LR motion has larger error bars.

Figure 3.60: Mean eccentricity vs. phase for different types of motion



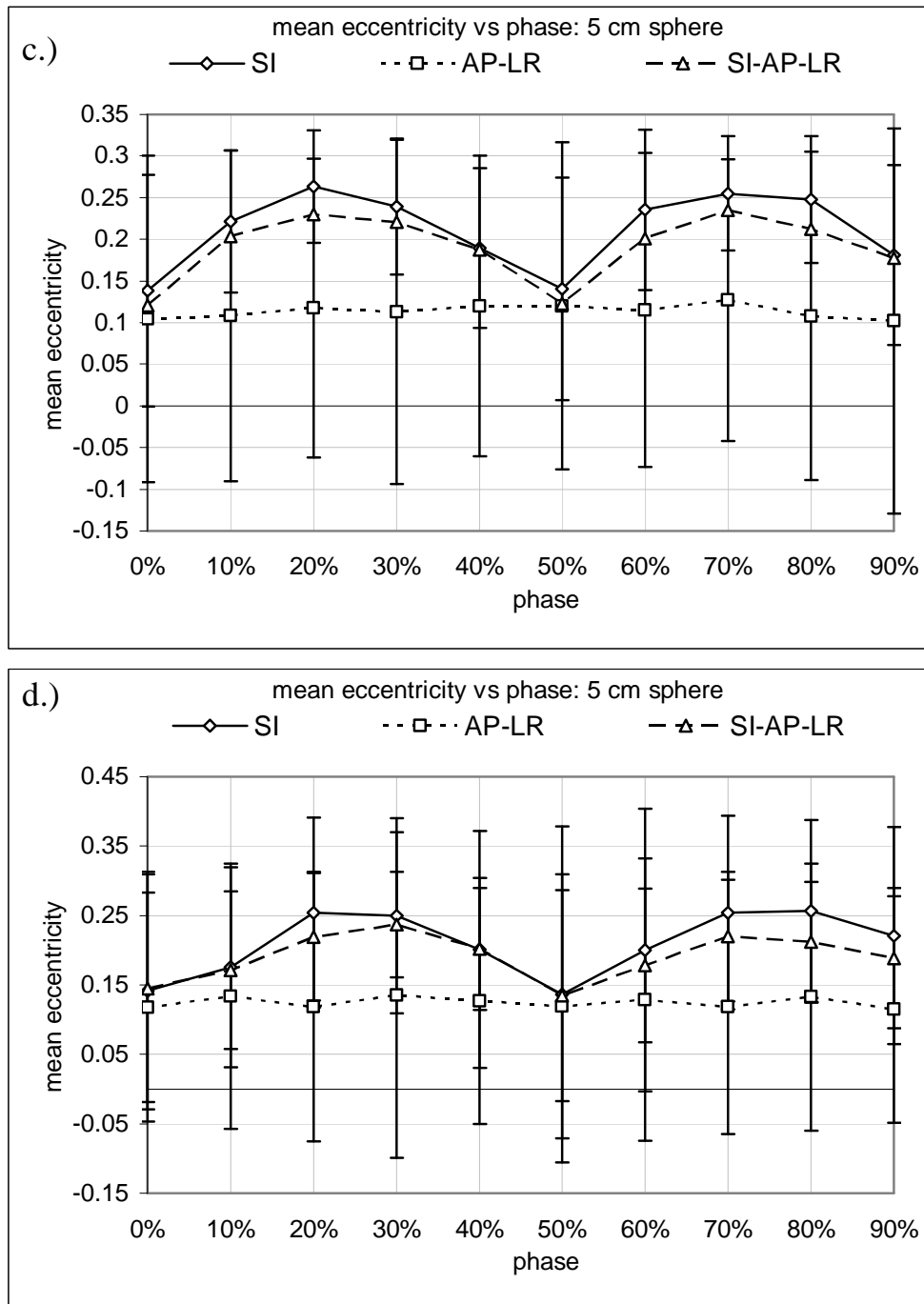
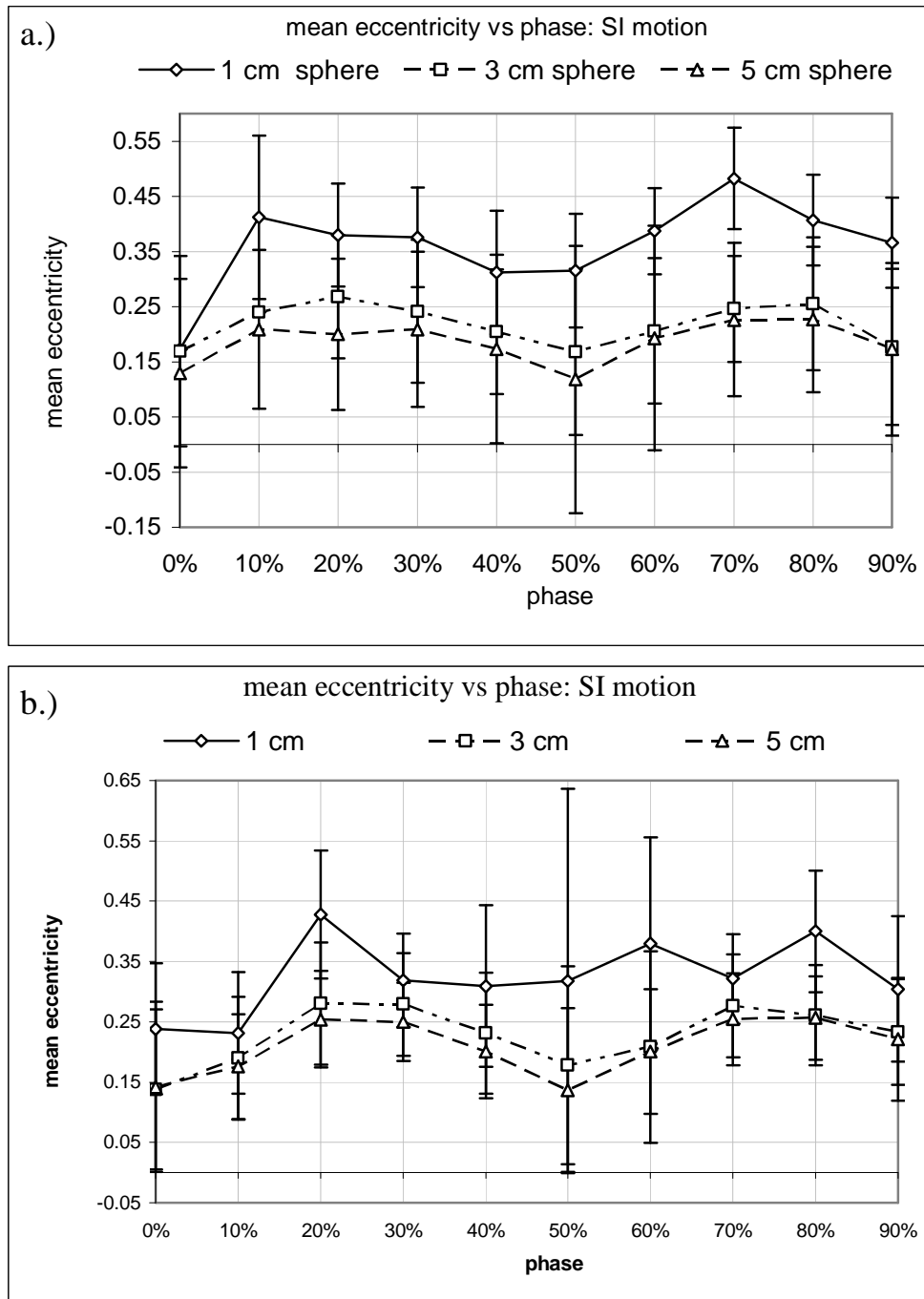


Figure caption: *Mean eccentricity vs. phase for different types of motion. a.) 3 cm sphere, RPM 1.0 cm cams, b.) 3 cm sphere, Bellows 1.0 cm cams, c.) 5 cm sphere, RPM 1.0 cm cams, d.) 5 cm sphere, Bellows 1.0 cm cams. Note the phase dependency where an SI component of motion is present. Unlike with the % volume difference metric's phase dependency, the convolution of the AP-LR motion artifact does not appear to mitigate the mean eccentricity's response to phase of motion.*

Sphere size should have the same impact on *mean eccentricity* as on *% volume difference*, and for the same reasons. Figure 3.61 shows the mean eccentricity vs phase

plots for the different sphere sizes. Since both pinwheel and horseshoe crab artifacts are geometrically non-isotropic, alterations in volume due to residual motion artifacts will reduce the circular symmetry of the segmented sphere in each slice. Thus, the smaller the sphere the larger *mean eccentricity*. Again, the 1 cm sphere data is more irregular and shows the greatest variation with phase.

Figure 3.61: Mean eccentricity vs. phase for different sizes of spheres



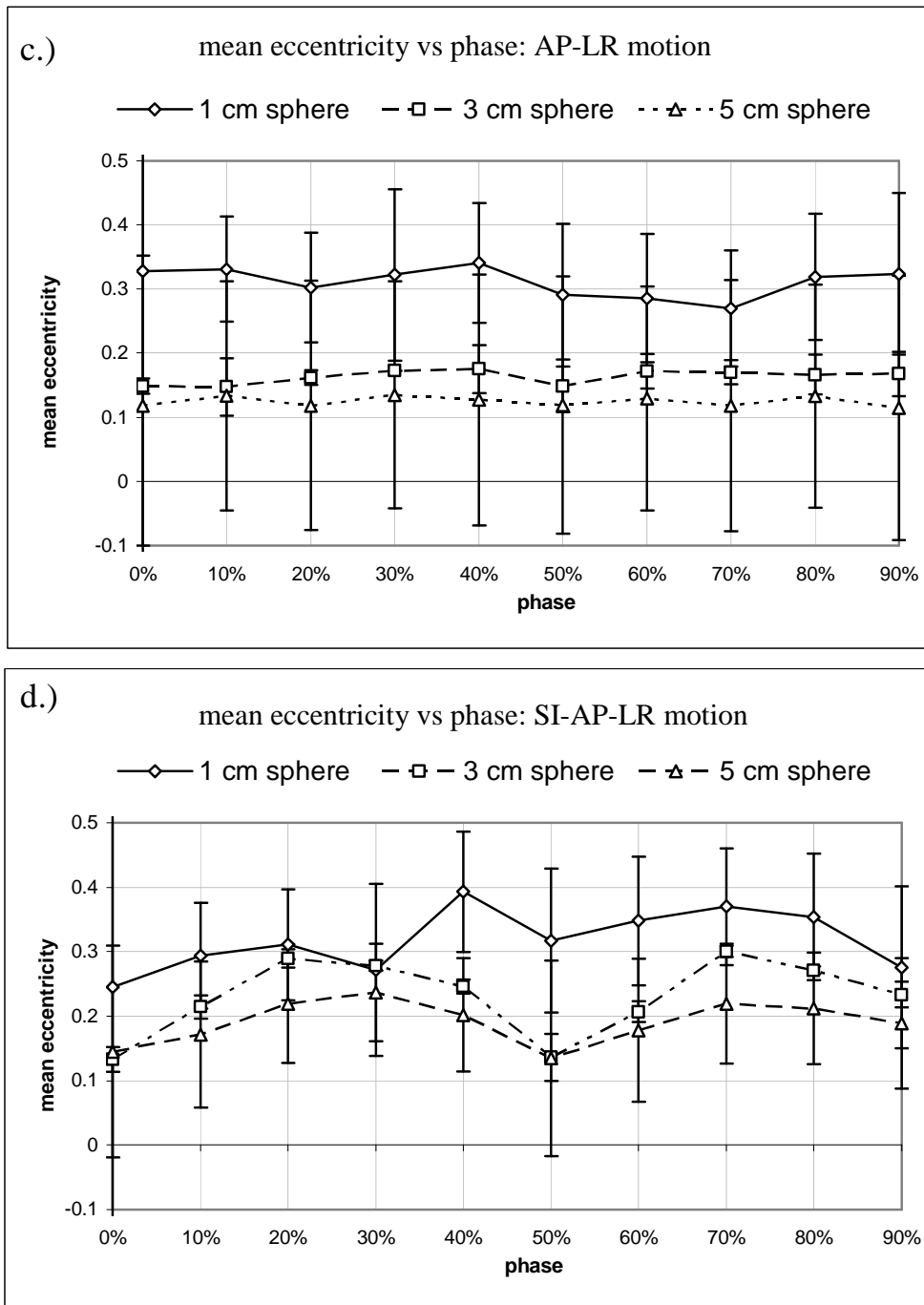
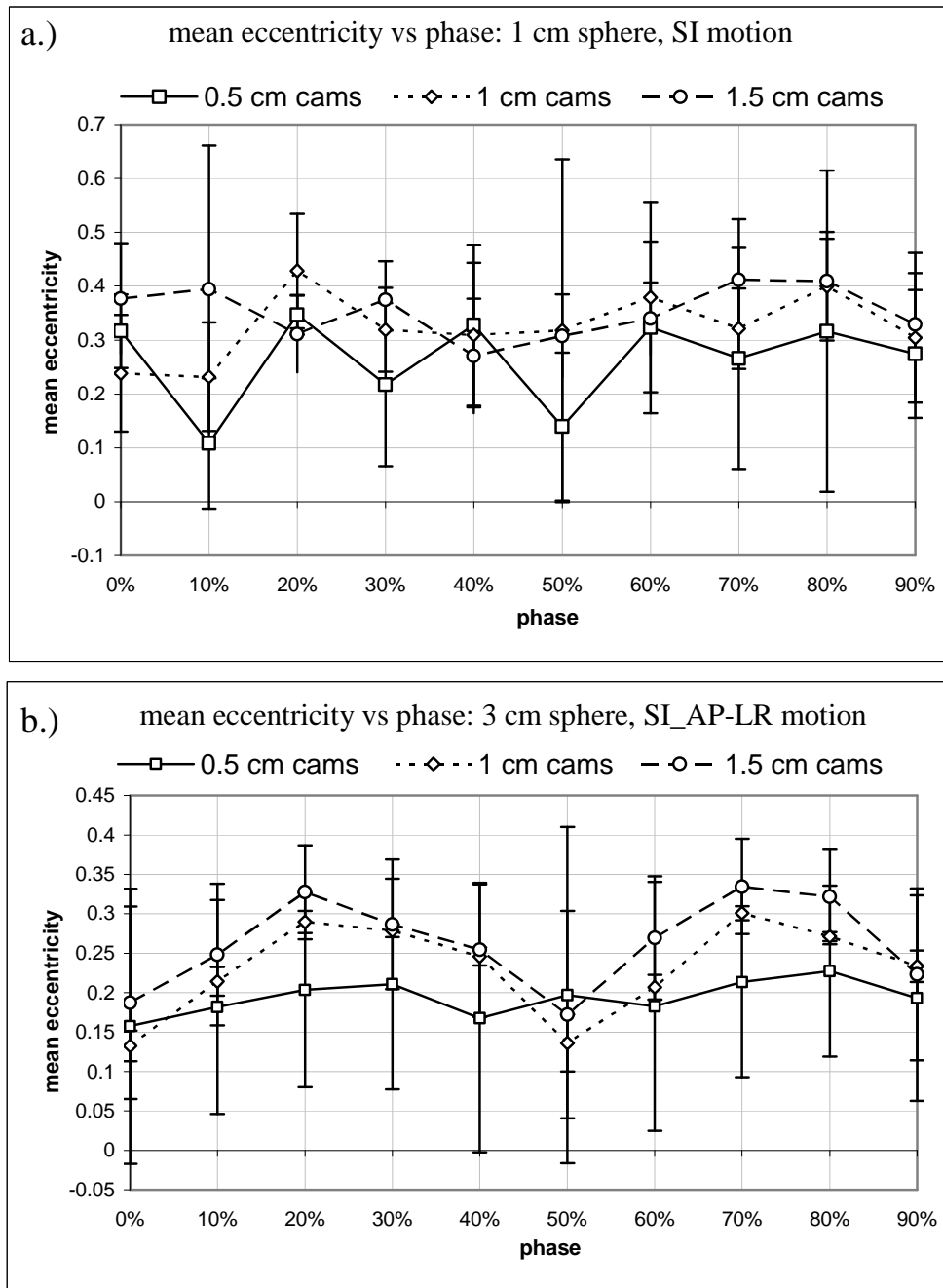


Figure caption: Mean eccentricity vs. phase comparing different sizes of spheres. a.) SI motion, RPM 1.5 cm cams, b.) SI motion, Bellows 1.0 cm cams, c.) AP-LR motion, Bellows 1.0 cm cams, d.) SI-AP-LR motion, Bellows 1 cm cams. Again the 1 cm data is more erratic than that of the 3 & 5 cm spheres.

Since *mean eccentricity* is closely linked to residual motion artifacts, it is reasonable to expect that the amplitude of motion should have an impact on the metric: the faster the motion, the more motion captured by the image acquisition, the more extreme the artifact (67). Indeed this is the case. Figure 3.62 shows *mean eccentricity* vs

phase plots for different amplitudes of motion, where the effect is even noticeable in the noisy 1 cm sphere data (i.e. Figure 3.62a; predominately, the 0.5 cm cam data has the lowest *mean eccentricities*). The dependency appears clearest for motions with an SI component, but can be seen in AP-LR motion as well (see Figure 3.62c and d). As evident in nearly all the *mean eccentricity* graphs of Figures 3.60-3.62, variation in the sphere's speed as it traverses its path from peak inhale to peak exhale also gives *mean eccentricity* phase dependence.

Figure 3.62: Mean eccentricity vs. phase for different amplitudes of motion



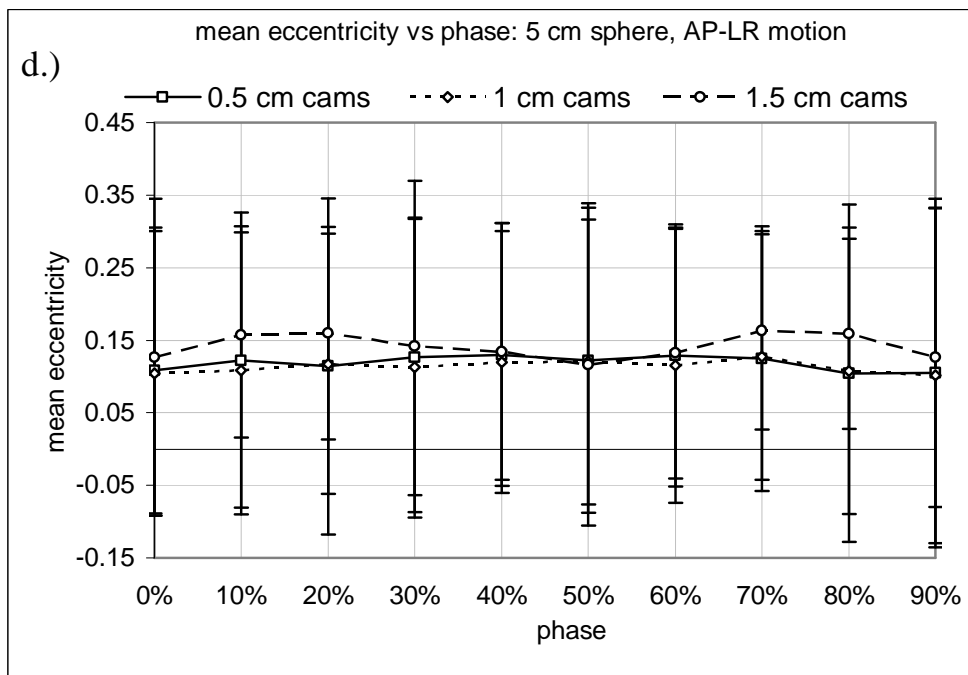
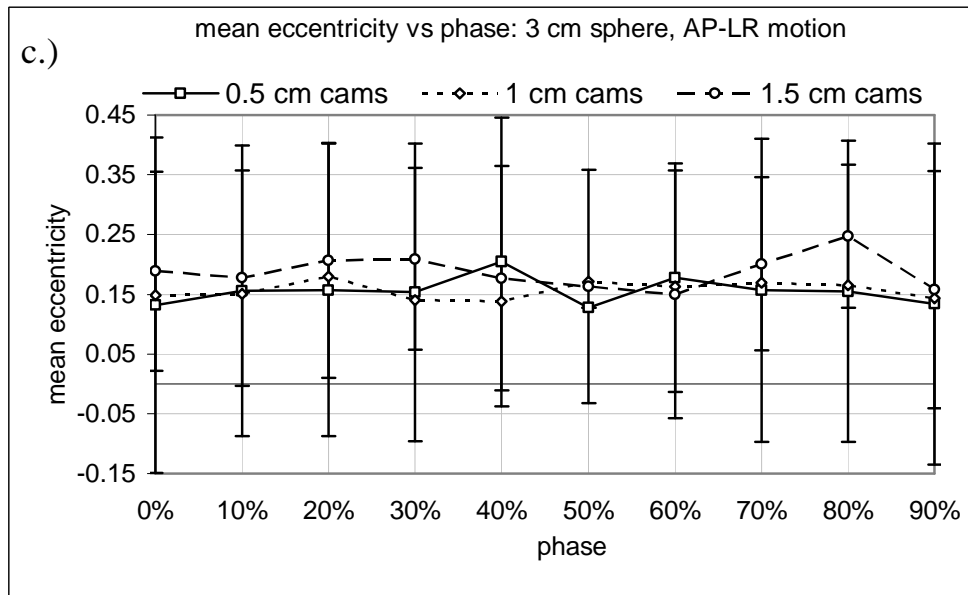
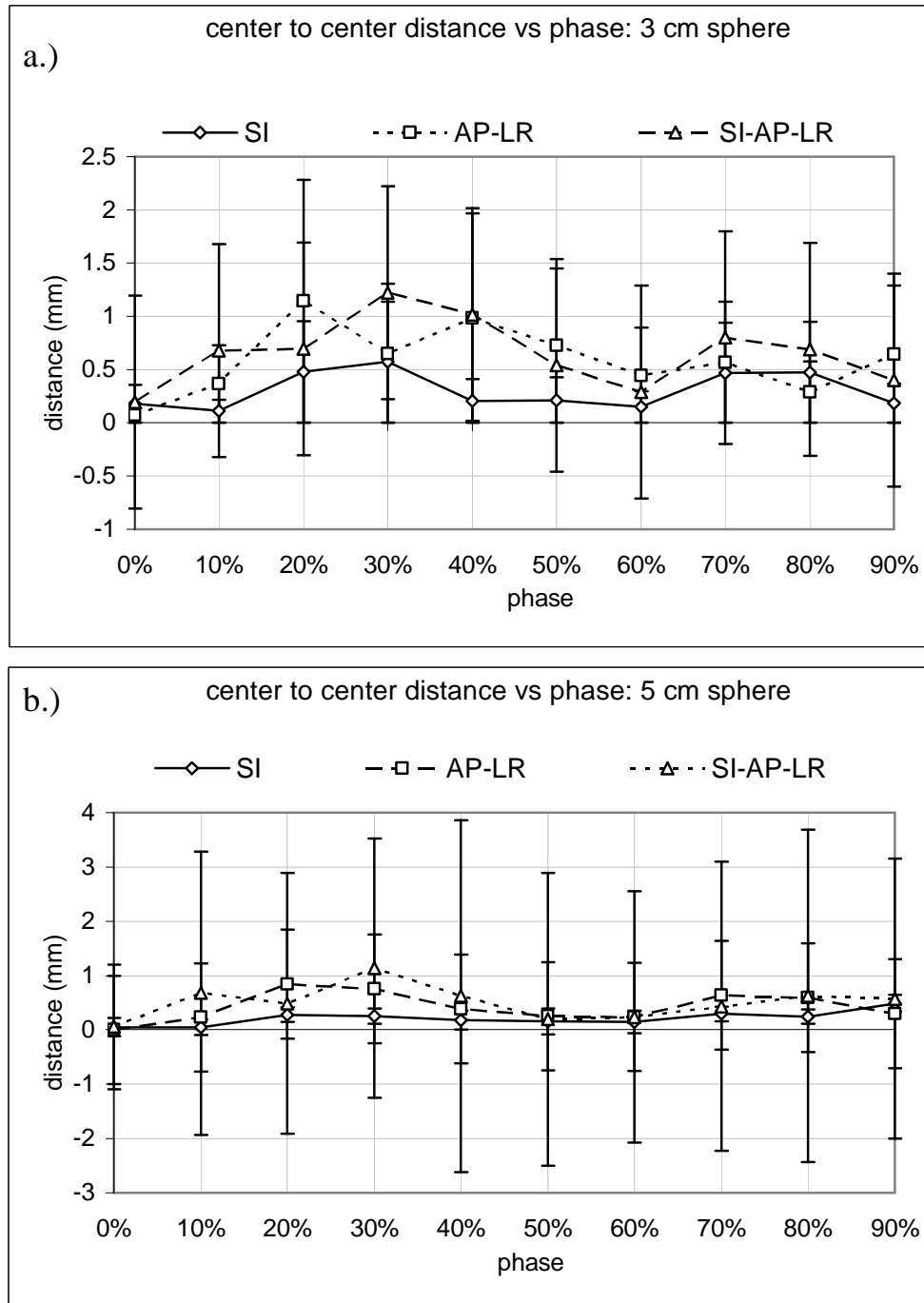


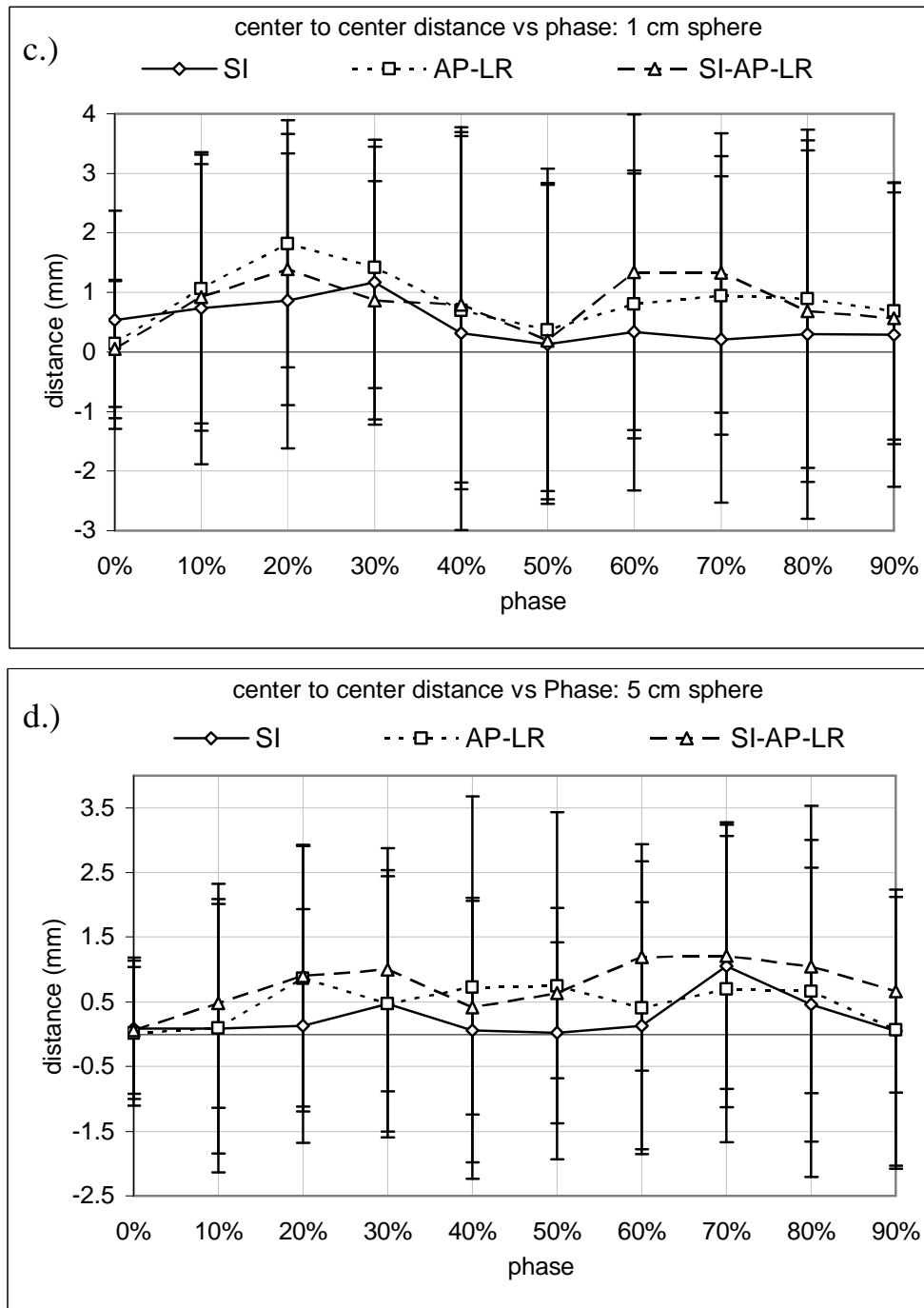
Figure caption: *Mean eccentricity vs. phase for different cam sizes. a.) 1 cm sphere, SI-motion, Bellows, b.) 3 cm sphere, SI-AP-LR motion, Bellows, c.) 3 cm sphere, AP-LR motion, RPM, d.) 5 cm sphere, AP-LR motion, RPM.* The trend of greater *mean eccentricity* with larger cam sizes is only clearly seen with the SI-AP-LR motions, but even with the noisy 1 cm data, the 0.5 cm cams have a tendency to yield the lowest values of the metric, and 1.5 cm cams the highest. The only clear trend with AP-LR motion data is that the 1.5 cm cams attain the highest mean eccentricity.

Center to Center Difference

Figure 3.63 shows the *center to center distance* vs phase for the different types of motion. In general, the SI motion exhibits better location agreement than motions with an AP-LR component.

Figure 3.63: Center to center distance vs. phase for different types of motion

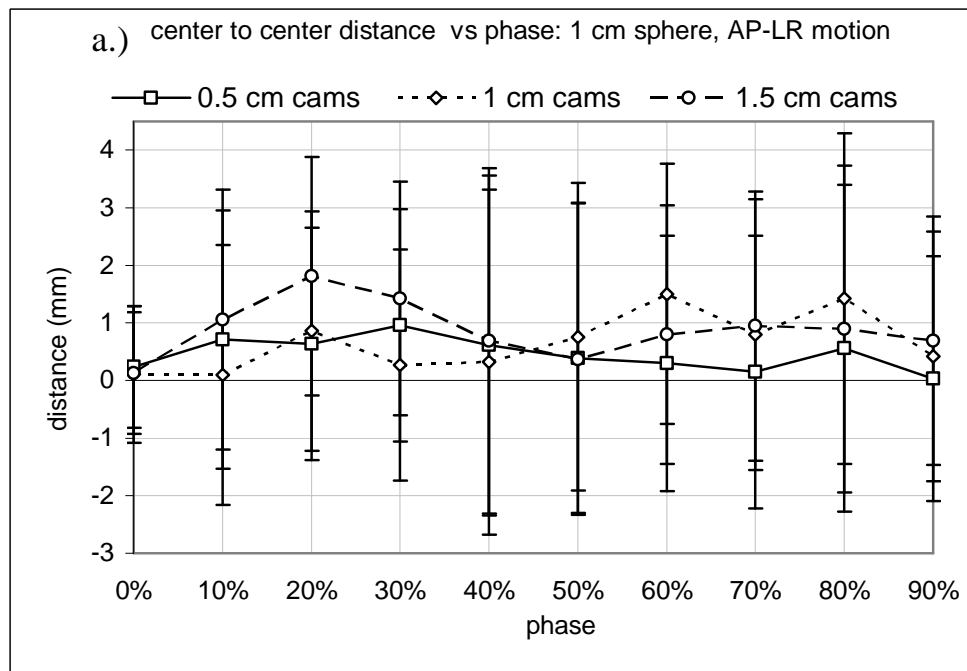


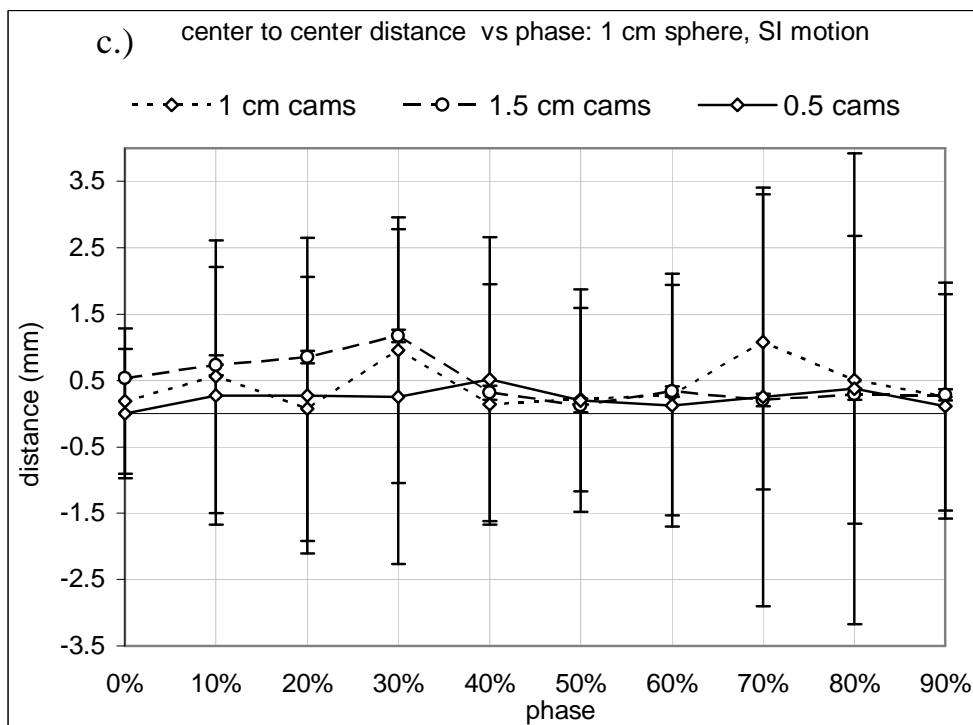
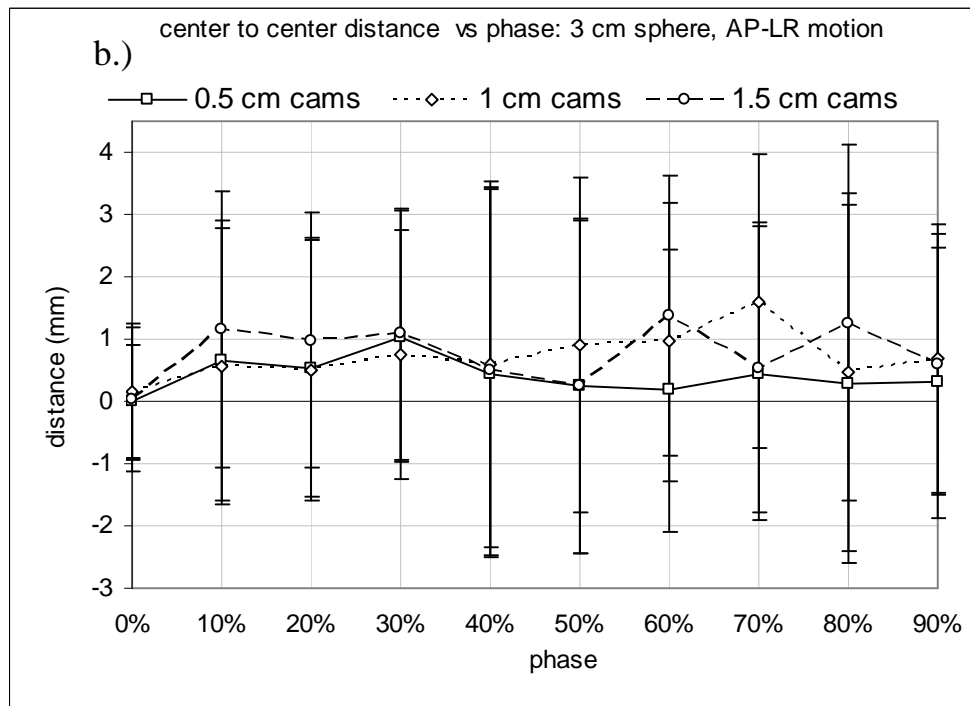


A phase dependency is also evident in Figures 3.63 - 3.65. There are some deviations, however, particularly at the 50% phase, perhaps due to phantom error. The *center to center distance* vs phase graphs for the 1 cm sphere in Figure 3.64b and d are typical of phantom error. Indeed, a center to center agreement within a millimeter for the 50% phase is one of the criteria for acceptance of data. In general, the slower phases give better center to center agreement for all types of motion.

Under the basic assumption that motion is causing any discrepancies seen in each sphere's size, shape, and volume, amplitude of motion dependency for the *center to center distance* seems plausible. Figure 3.64 shows the *center to center distance* vs phase for different cam sizes, giving the clearest examples of an amplitude dependency, yet the only thing that can be said with any certainty is that, in general, the 0.5 cm amplitude gives the smallest *center to center distances*. Other errors in centroid location could be obscuring the metric's dependency, however. In addition to thresholding and resolution errors, phantom error and the respiratory monitoring system's ability to accurately detect peak exhale are possible (39), and in the former case, probable.

Figure 3.64: Center to center distance vs. phase for different amplitudes of motion





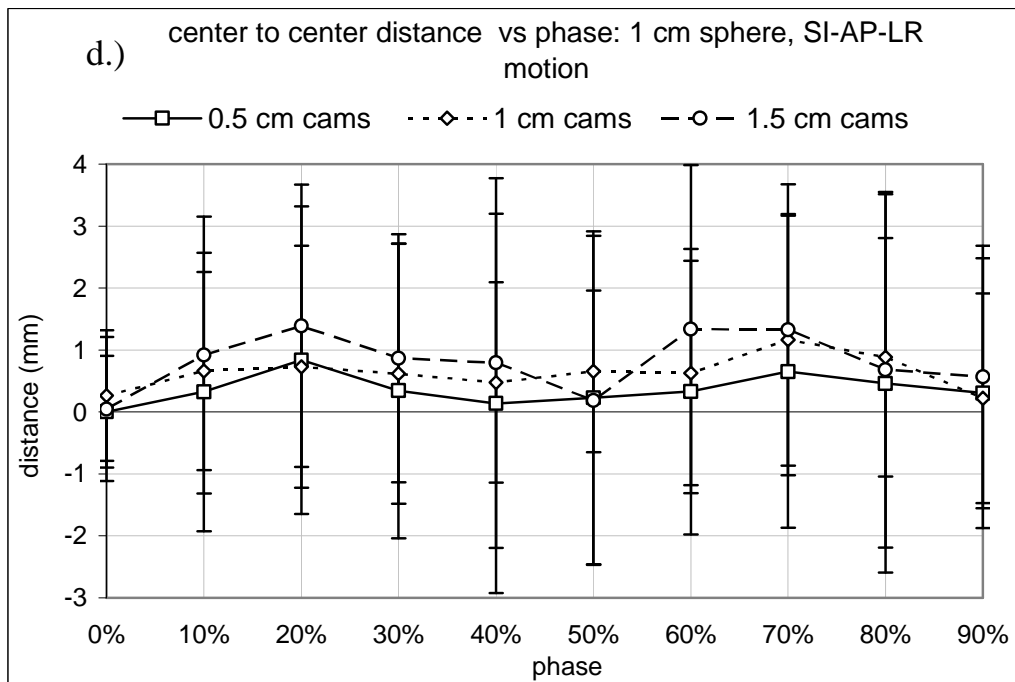


Figure caption: Center to center distance vs. phase comparing different amplitudes of motion. a.) 1 cm sphere, AP-LR motion, RPM, b.) 3 cm sphere, AP-LR motion, RPM, c.) 1 cm sphere, SI motion, RPM (the 0.5 cm cams are Bellows since the RPM system is unable to detect 0.5 cm amplitude SI motion), d.) 1 cm cams, SI-AP-LR motion, RPM. In each case, the 0.5 cm cams seem to have the smallest *center to center distances*.

For all the *center to center distance* data investigated, no sphere size dependency was evident. Figure 3.65 gives the *center to center distance* vs phase for the different sphere sizes. Since Matlab finds the centroid of a segmented area using a center of mass calculation, symmetry dictates the centroid position, thus, it is reasonable that the centroid position shows no dependency on object size. This argument, however, can only be accepted for symmetric objects.

Figure 3.65: Center to center distance vs. phase for different sizes of spheres

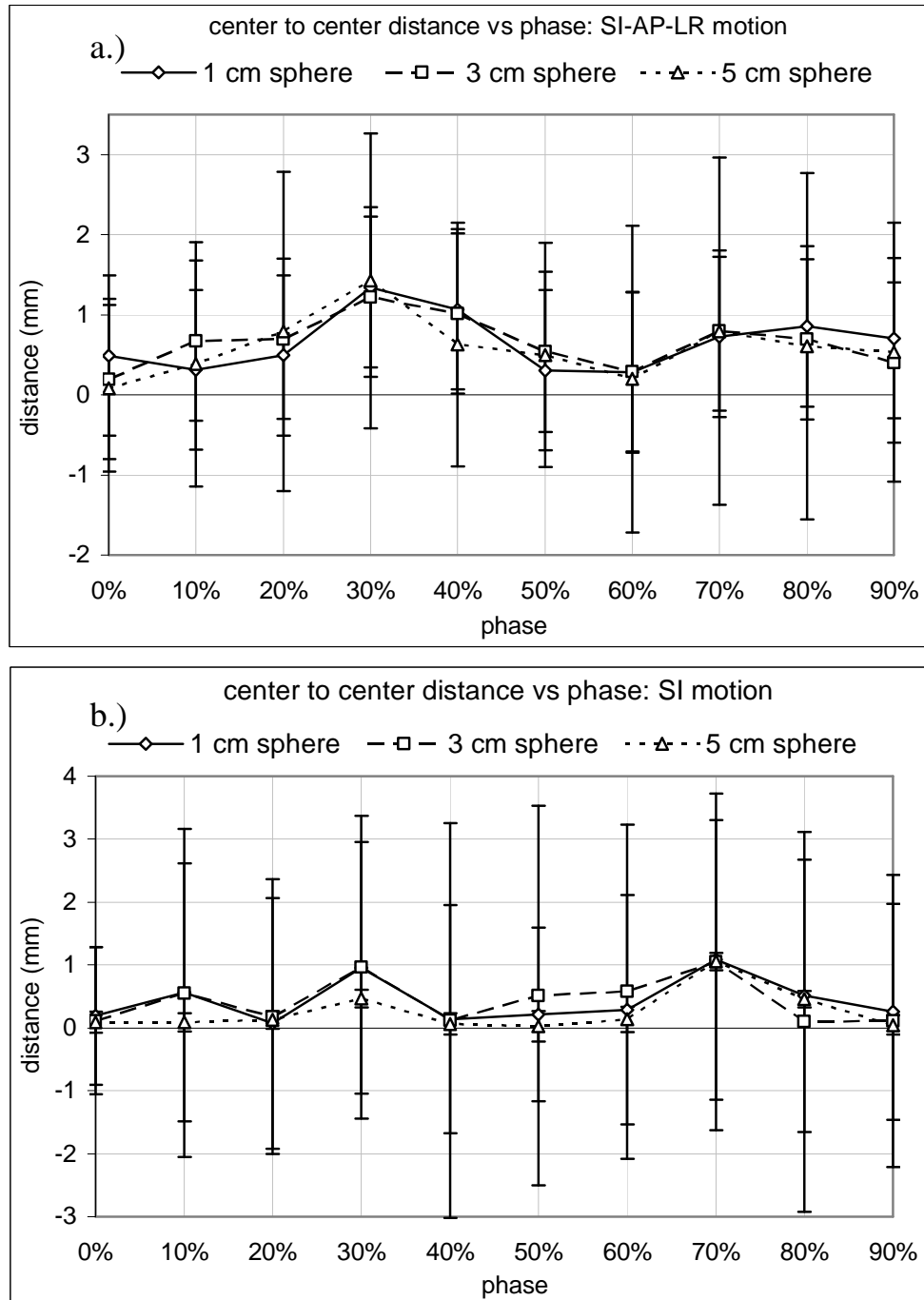


Figure caption: *Center to center distance vs. phase for different sizes of spheres. a.) SI-AP-LR motion, Bellows 1.0 cm cams, b.) SI motion, RPM 1.0 cm cams. No discernable size dependency was found in any of the center to center distance data.*

Maximum Distance to Agreement

Of all the functional dependencies, only the phase of motion shows any impact on the *maximum distance to agreement*. This is surprising since the metric should be affected by in-plane (i.e. eccentricity) and axial artifacts (i.e. see Figure 3.57). Figure 3.66 shows data in favor of an amplitude of motion dependency, and although phase dependencies such as those seen in Figure 3.65 are far more common than not, the trend is not universally evident. In general, slower phases exhibit better surface to surface agreement.

With sphere size, some of the *maximum distance to agreement* data shows a slight dependency while other graphs have all three spheres right on top of each other (see Figure 3.67). However, the phase of motion dependency is evident here as well.

Figure 3.68 shows the *maximum distance to agreement* vs. phase for different types of motion. In all the data, no discernable pattern with type of motion is evident. Although it is possible that the dependencies of mean eccentricity and % volume difference do have an impact on this metric, they cannot be seen through the experimental noise.

Figure 3.66: Maximum distance to agreement vs. phase for different amplitudes of motion

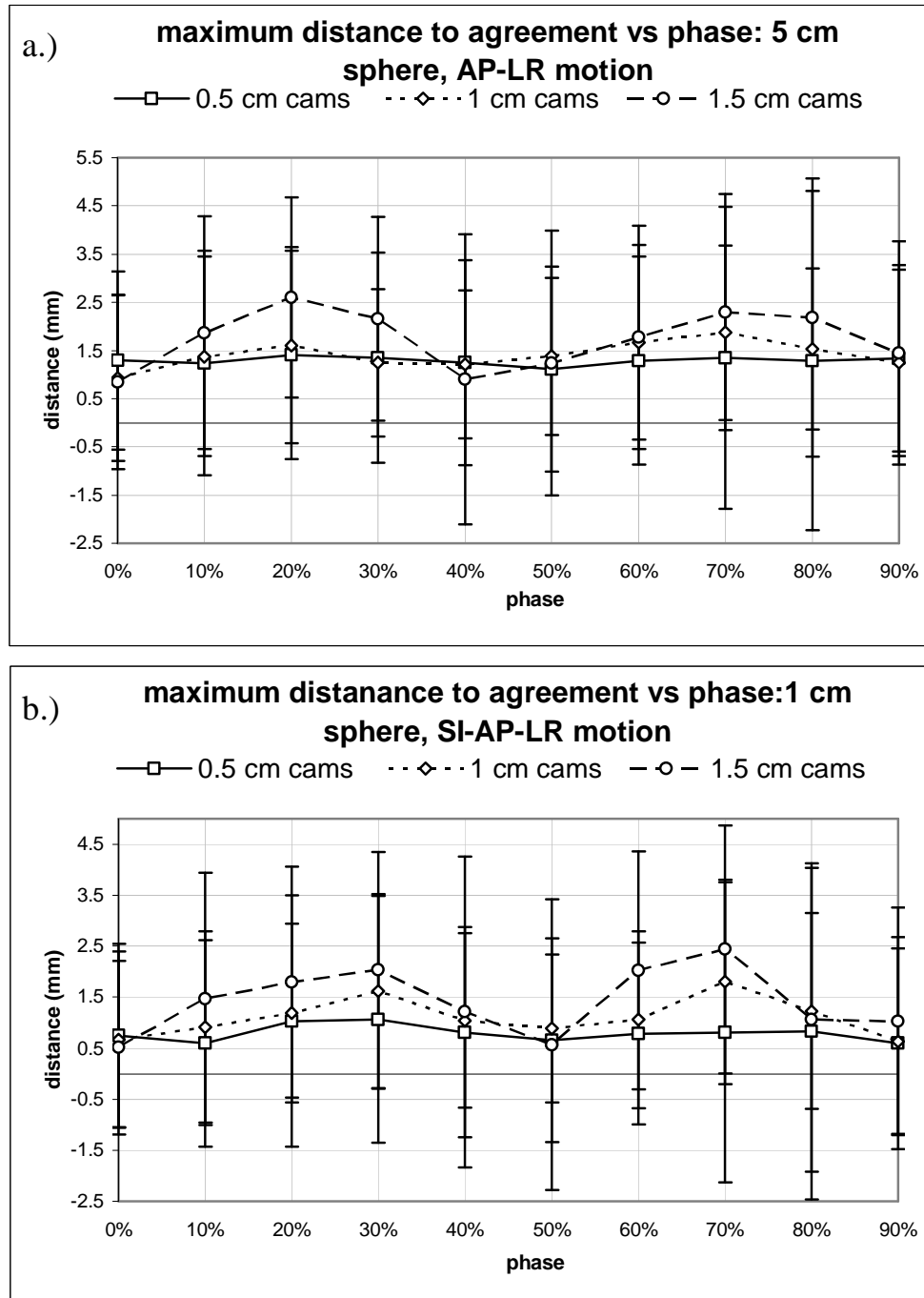


Figure caption: *Maximum distance to agreement vs. phase of motion for different displacement amplitudes. a.) 5 cm sphere, AP-LR motion, RPM, b.) 1 cm sphere, SI-AP-LR motion, RPM. Although there seems to be a trend with cam size, it is not present in all the maximum distance to agreement data, and all the data are well within the estimated errors of one another.*

Figure 3.67: Maximum distance to agreement vs. phase for different sphere sizes

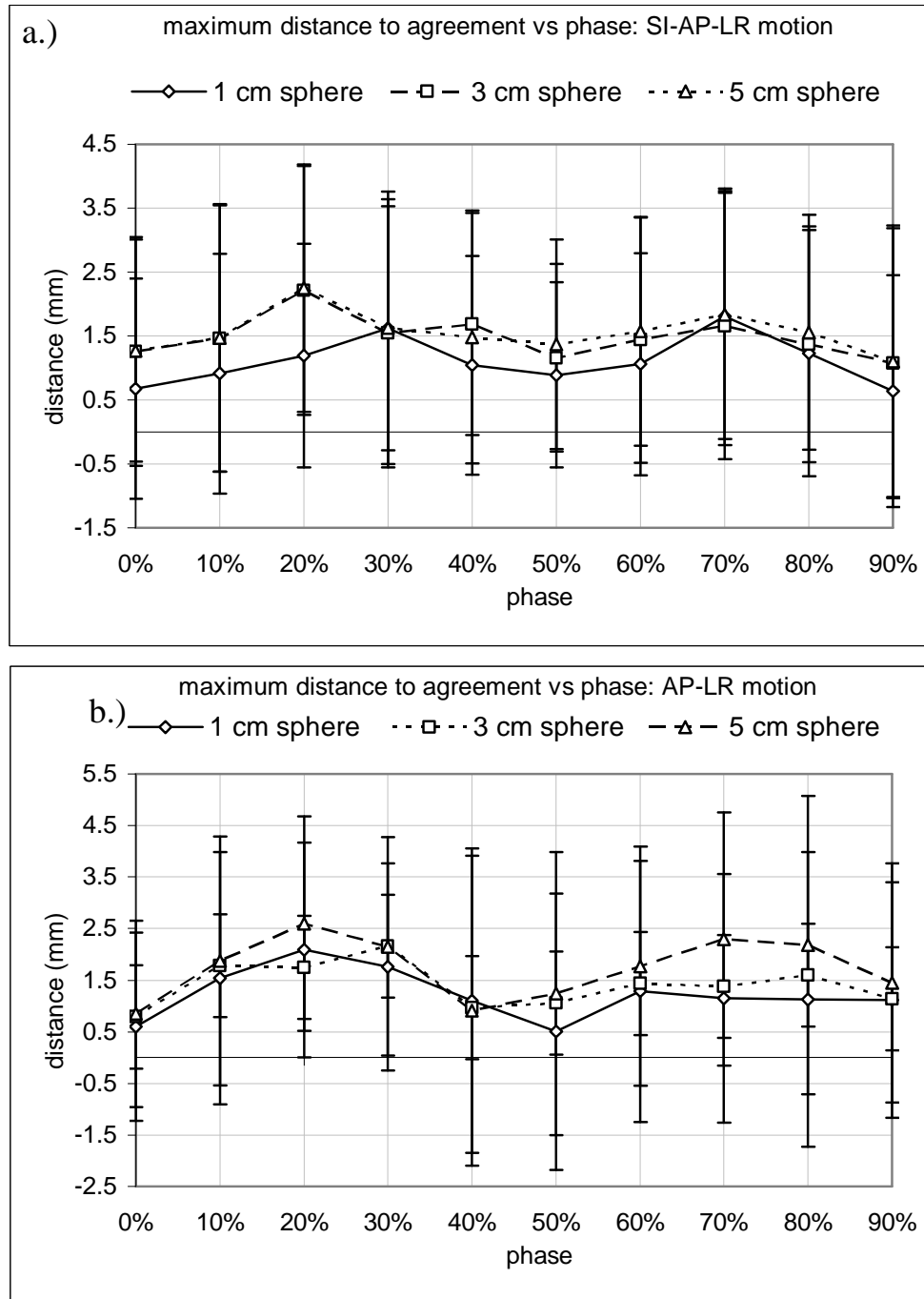


Figure caption: *Maximum distance to agreement vs phase for the different sphere sizes. a.) SI-AP-LR motion, RPM 1.0 cm cams, b.) AP-LR motion, RPM 1.5 cm cams. Some graphs show a larger surface to surface discrepancy with increased sphere size. However, all the data for any given sphere size is well within the estimated error of that from any other sphere size.*

Figure 3.68: Maximum distance to agreement vs. phase for different types of motion

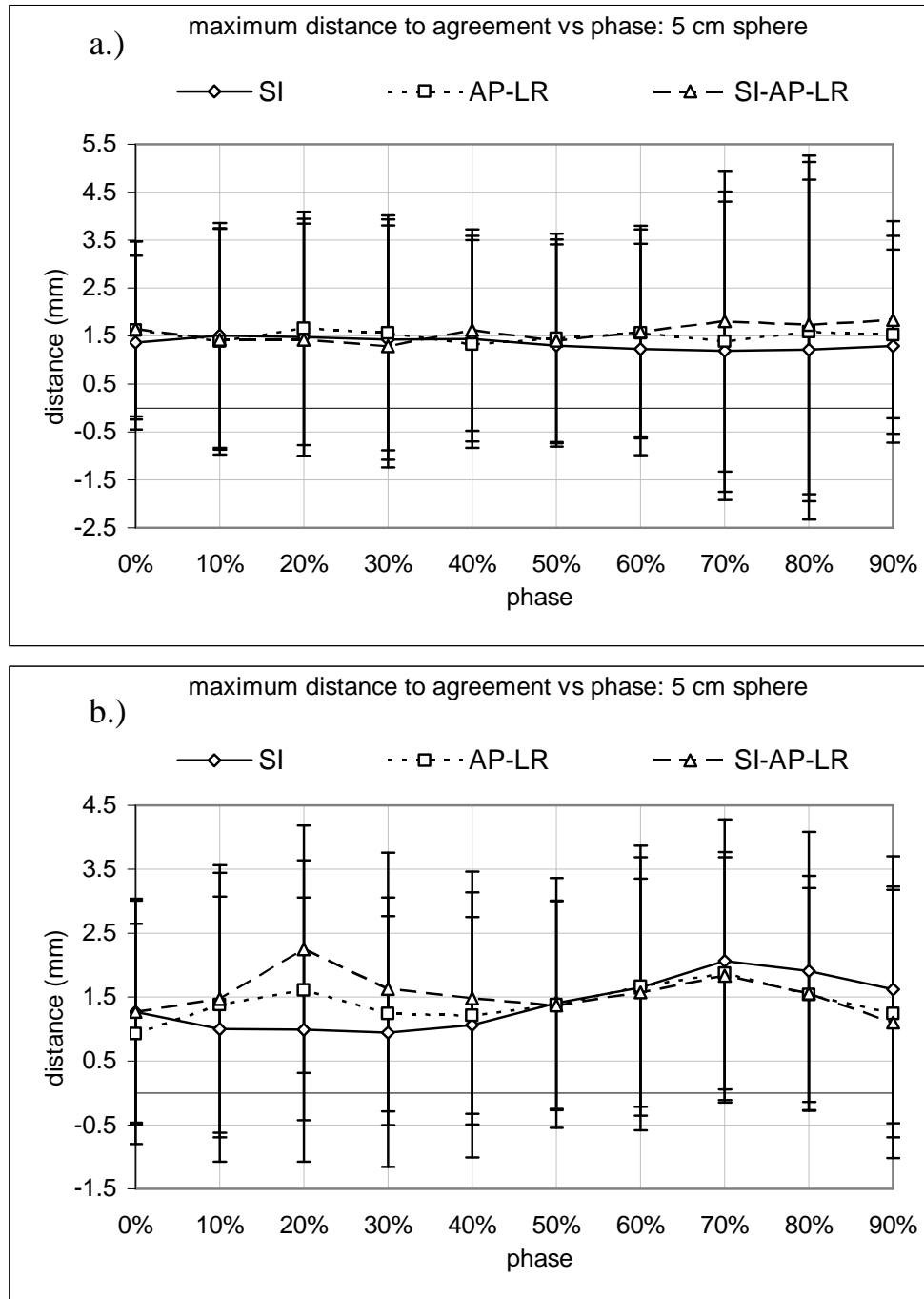
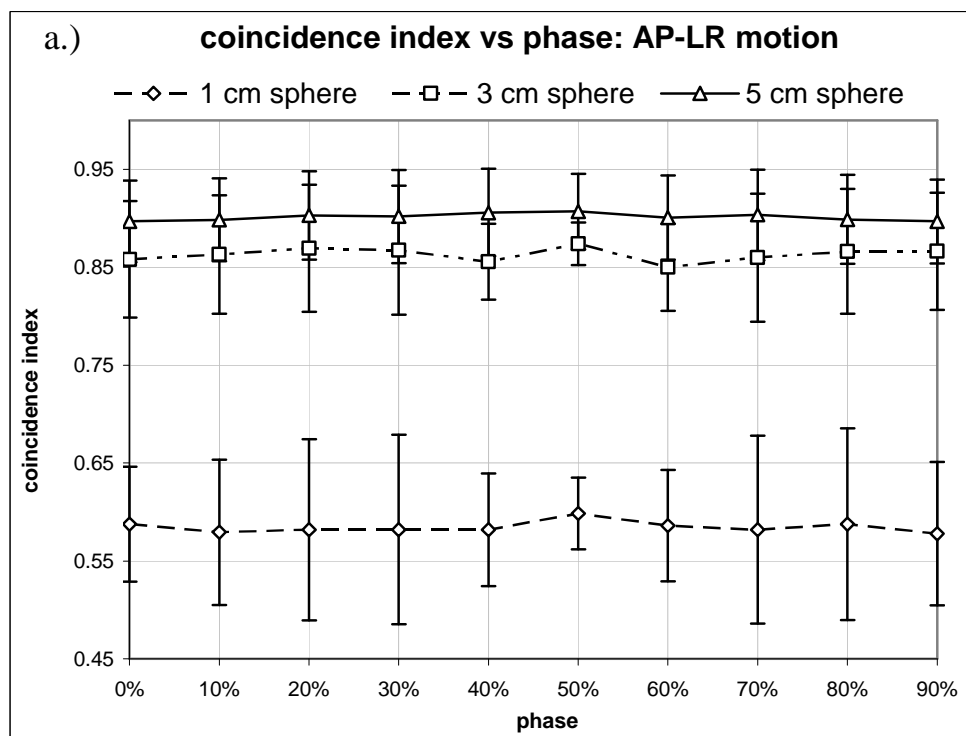


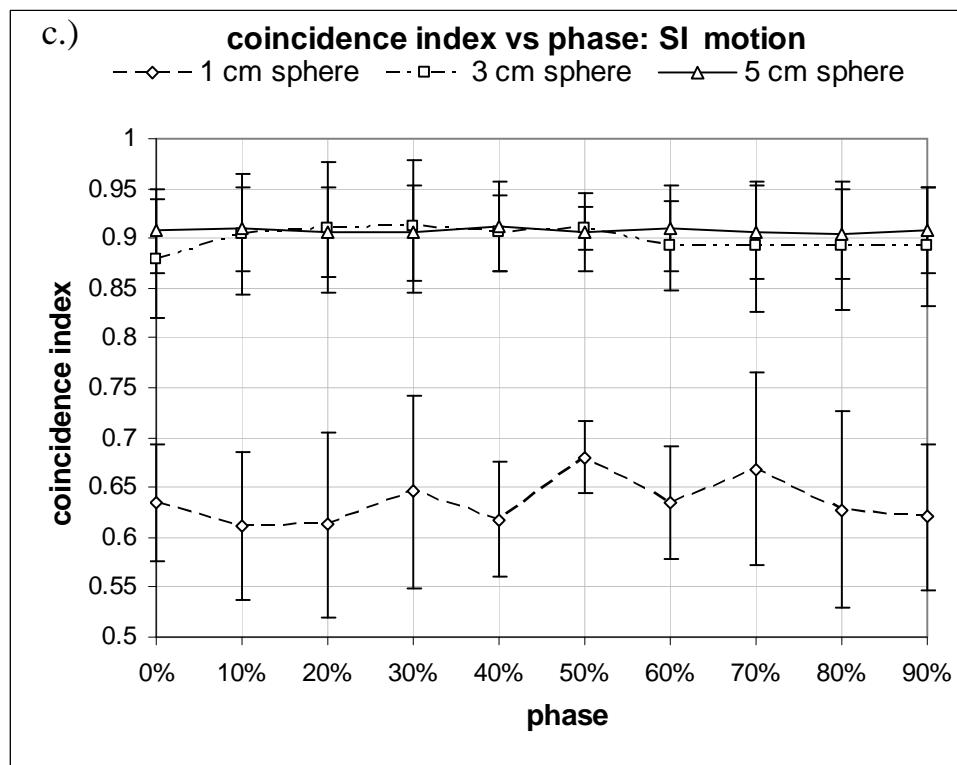
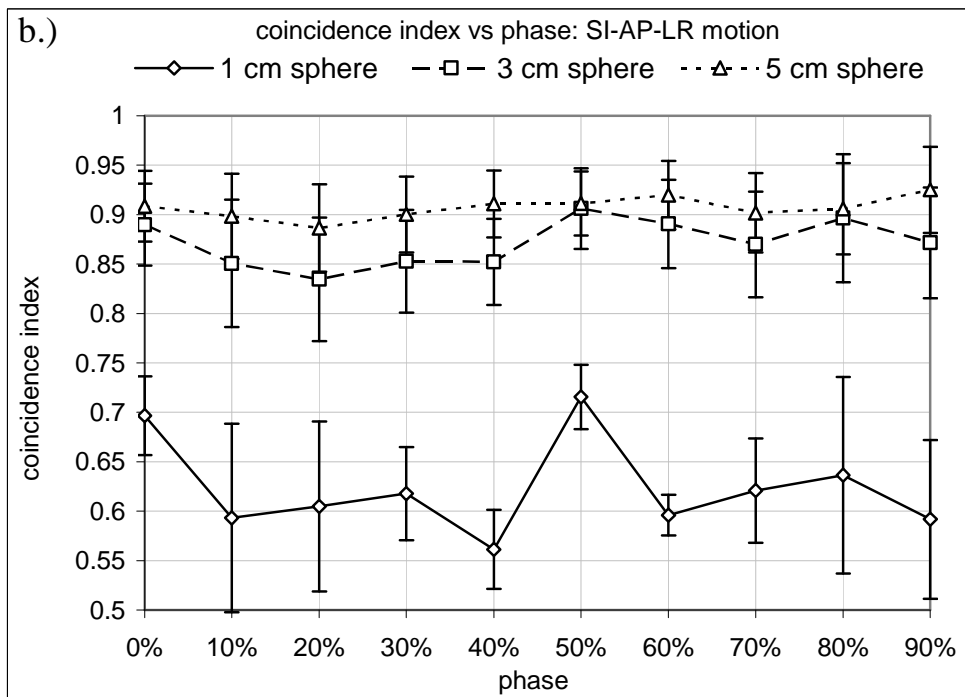
Figure caption: *Maximum distance to agreement vs. phase for different types of motion. a.) 5 cm sphere, Bellows 0.5 cm cams, b.) 5 cm sphere, RPM 0.5 cm cams. The surface to surface distance shows no discernable functional dependency with the type of motion.*

Coincidence Index

With the *coincidence index*, the objective is to represent the overall geometric accuracy of the system with a single number. Like the *maximum distance to agreement* metric, the *coincidence index* should show dependencies similar to *mean eccentricity*, *% volume difference*, as well as the position metrics. Yet, the index only shows a clear dependence on sphere size, and to a lesser extent, phase of motion. (see Figure 3.69). Indeed, all that can be said about a phase dependency is that the thresholding error tends to be less for the slower phases, possibly indicating reduced threshold sensitivity for these phases.

Figure 3.69: Coincidence index vs. phase for different sphere sizes





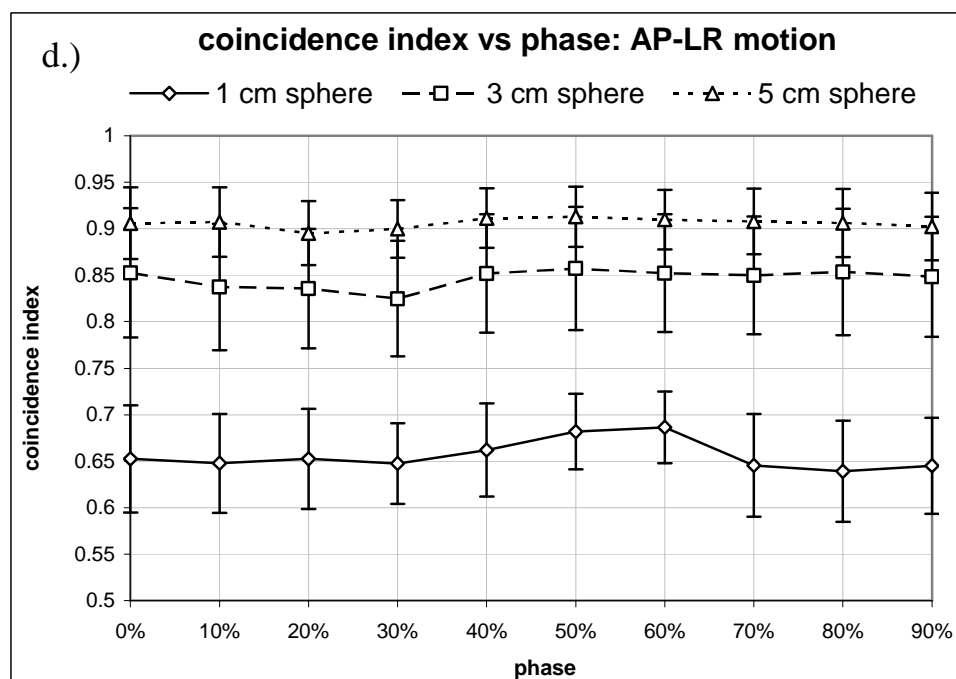


Figure caption: Coincidence index vs. phase for the different sphere sizes. a.) AP-LR motion, Bellows 0.5 cm cams, b.) SI-AP-LR motion, RPM 1.0 cm cams, c.) SI motion, Bellows 0.5 cm cams, d.) AP-LR motion, RPM 0.5 cm cams. The coincidence index improves with the larger spheres, owing to, at least in part, the larger number of pixels available to reconstruct the shape of the spheres. There also seems to be a phase dependency of the error bars, showing a phase dependency on threshold sensitivity.

Summary of Functional Dependencies

A summary of all the functional dependencies are given in Table 3.6. The *% volume difference* is sensitive to sphere size; the larger the sphere the lower the *% volume difference* simply due to measurement error: more voxels used to reconstruct the volume enables a more accurate rendering, as well, the impact of residual motion artifacts is lessened by the relative size of the object. Type of motion and phase of motion also affect the *% volume difference* by the type and extent of the motion specific artifacts. *Mean eccentricity* is also affected by size, phase, and type of motion, and for the same reasons as *% volume difference*. It is even more sensitive to motion, however, as it also shows a clear dependency on amplitude (i.e. the speed at which the sphere was moving). The *center to center distance* is relatively insensitive to sphere size and type of motion, however, the speed of the sphere affects the location measurement as evidenced by both its amplitude and phase dependency. The *maximum distance to agreement* shows a clear dependence on phase. It could be expected that it would have the same dependencies as *mean eccentricity* or *% volume difference*, since the shape of the imaged sphere would impact the metric. That such dependencies are not observed could be attributed to the sensitivity of the experiment or the method of calculation which specifically targets the protruding arms/horns of the residual motion artifacts. The *coincidence index* exhibits a clear dependence on sphere size and the phase of motion. Again, all the dependencies of *% volume difference* and *mean eccentricity* could be expected for this metric as well, and a more sensitive experiment may possibly reveal such dependencies.

Table 3.6: The functional dependencies of the five metrics of geometric evaluation

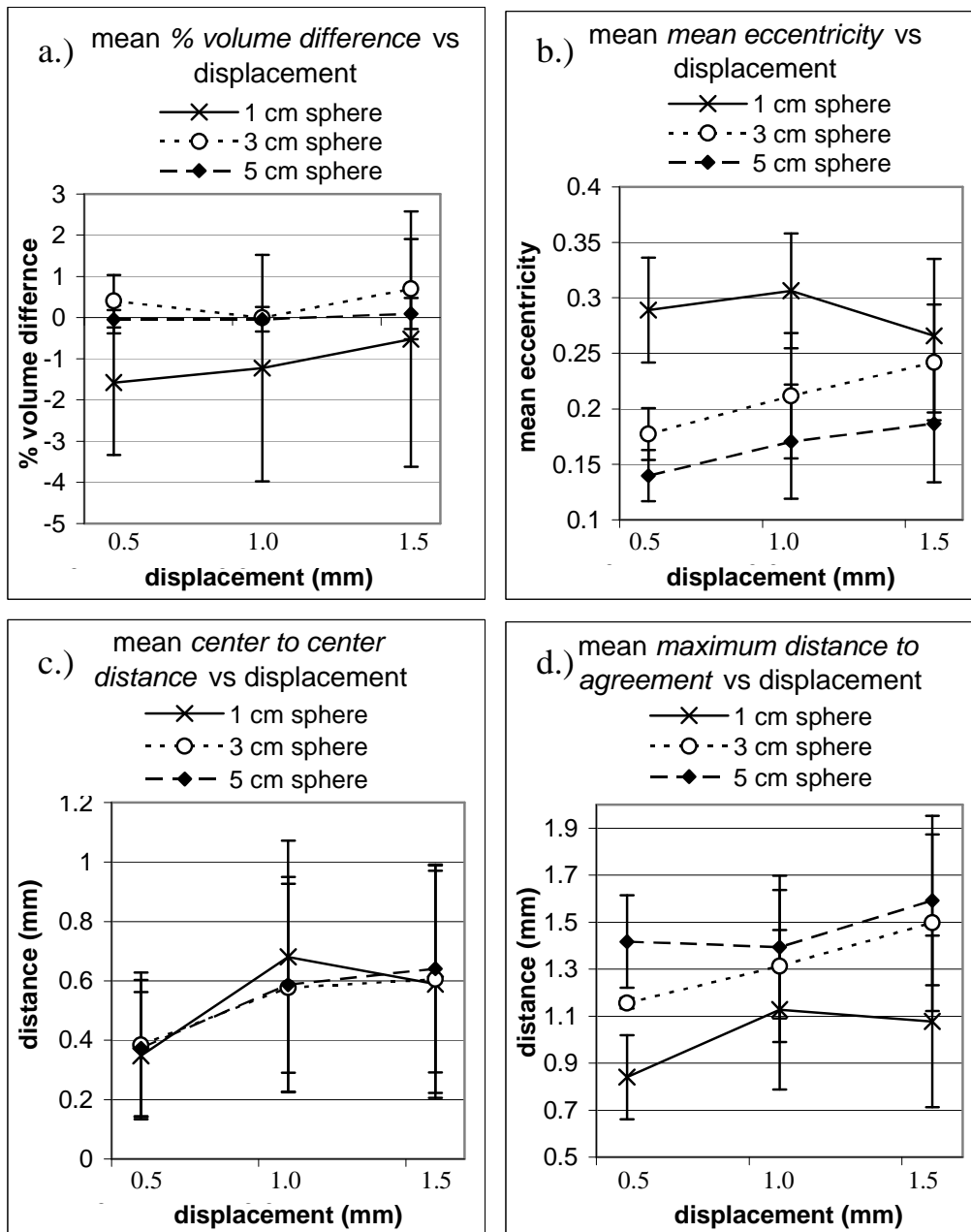
Metric	Functional dependence			
	sphere size	amplitude of motion	type of motion	phase of motion
% volume difference	X		X	X
Mean eccentricity	X	X	X	X
Center to centre distance		X		X
Max distance to agreement				X
Coincidence index	X			X

Figure caption: The functional dependencies of the five metrics used to evaluate the geometric accuracy of the 4DCT imaging system.

Consolidation of Quantitative Data

Moulding this data into a usable form requires some consolidation. The only dependency shared by all five metrics is phase. Unfortunately, the large number of phases is not conducive to consolidation. The other obvious choice is sphere size –the majority of metrics show strong size dependencies, and it is a clinically relevant question to ask, “Given a tumor of size such ‘n such, what sort of accuracy can I expect?” Amplitude of motion is also a relevant concern, and the fact that it reveals the imaging system’s response to speed can be directly related to the phase dependency (i.e. fast and slow phases of motion). Thus, as a preliminary step, the data is grouped by sphere size and graphed against the amplitude of motion (see Figure 3.70). Each data point in the graphs represents the mean value of that metric, and the error bars are one standard deviation of the measured values. With a complete data set, each data point would be the average of that metric over all types of motion and phases of motion, for a total of 60 images. However, there are fewer images for the 0.5 cm and 1.5 cm cam data points. Recall that the RPM system was unable to detect SI motion with the smallest cams, thus only 50 images are represented in each data point at 0.5 cm displacement. In addition, mechanical failure of the phantom forced an abandonment of attempts to acquire the SI-AP-LR motion for the 3 and 5 cm spheres using the RPM system with the 1.5 cm cams. This means that for those sphere sizes, only 50 images are included at the 1.5 cm displacement. Since the Bellows and RPM systems exhibit otherwise equivalent functioning, the omission of the redundant data sets should not affect the result.

Figure 3.70: Consolidation of the 5 metrics



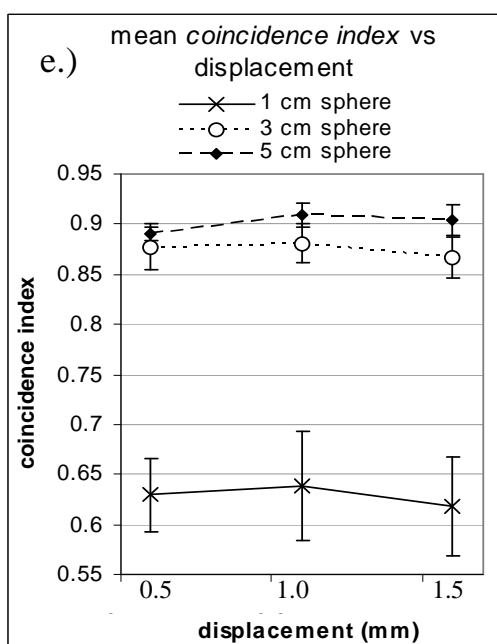


Figure caption: Consolidation of the quantitative data. a.) the mean *maximum distance to agreement* vs. cam size, b.) mean *center to center distance* vs cam size, c.) mean *coincidence indexes* vs cam size, d.) the *mean eccentricity* vs cam size, and e.) the % *volume difference* vs cam size. For only the mean *center to center distance* and mean *maximum distance to agreement* graphs are the data points sufficiently grouped to merge the data from all 490 phase images into a single number, yielding, respectively, the quantitative accuracy of the 4DCT imaging system to trace and localize a moving object. For the other metrics, the data is divided into two groups: 1 cm sphere data and 3 & 5 cm sphere data combined.

For the mean *center to center distance*, the data points are closely grouped for all cam sizes, plus there does not appear to be any significant trend with amplitude of motion. Thus for this metric, the data from all 490 images are grouped into a single number representing the 4DCT system's ability to track moving objects. The mean *maximum distance to agreement* data is also grouped fairly tightly, and so is also consolidated into a single number representing the 4DCT system's ability to localize moving objects. For the mean of the *coincidence index* and *mean eccentricity* metrics, however, the 1 cm sphere data is distinctly separate from the other data points. Again, there is no obvious trend with amplitude, so for these two metrics, all the data for the 3 and 5 cm spheres are grouped together, and the 1 cm data is kept separate. Although the mean % *volume difference* data is tightly grouped, the large error bars on the 1 cm data suggests that grouping all the data together may occult the precision of the 3 and 5 cm data. Thus, like the means of the *coincidence indexes* and *mean eccentricities*, the mean % *volume difference* data is separated in two groups by sphere size.

The final results are found in Table 3.7. For all metrics, the performance of the 4DCT imaging system is worse for the 1 cm sphere compared to the 3 and 5 cm spheres. The average % *volume difference* for the 1 cm sphere is -1.3% with a standard deviation of 2.3% , indicating that the 1 cm sphere was typically imaged smaller than its true volume. The largest deviation of the 1 cm sphere from its true volume is $-8 \pm 5\%$ too small (there is also an outlier of $8 \pm 5\%$ too large). The best performance of the 4DCT system in capturing the true volume of the 1 cm sphere is $0 \pm 2\%$ volume difference. The 3 and 5 cm spheres not only image much closer to their true volumes with a mean % *volume difference* of 0.22% too large, these measurements are also more consistent with a standard deviation of only 0.55% . For the 3 and 5 cm sphere group, the worst measurement of % *volume difference* is for the 3 cm sphere at $3 \pm 1\%$ too large, and the best measurement is for the 5 cm sphere at $0.1 \pm 0.6\%$ too large. The average *mean eccentricity* measured for the 1 cm sphere is 0.31 with a standard deviation of 0.06 . The largest *mean eccentricity* is 0.48 ± 0.09 , and the best performance in measuring the shape of the 1 cm sphere yields a *mean eccentricity* of 0.1 ± 0.1 . Recall that this metric is an average of eccentricities over all cross sectional images of the sphere, and so includes

edge slices which contribute high eccentricities due to increased partial volume effects as well as heightened residual motion artifacts. For the 3 and 5 cm spheres, the average *mean eccentricity* is 0.18 with a standard deviation of 0.5. Thus, for all sphere sizes, the measured *mean eccentricities* are fairly consistent. The worst measured *mean eccentricity* for the 3 and 5 cm spheres is 0.3 ± 0.6 from the 3 cm sphere data, and the best is 0.1 ± 0.2 from the 5 cm sphere data. Looking at the *coincidence index* for these spheres, the 1 cm sphere scores 0.62 out of a perfect 1, with a standard deviation of 0.06. The 3 and 5 cm spheres averaged 0.89 with a standard deviation of 0.02. The best score achieved with the 1 cm sphere is 0.74 ± 0.03 , and the worst is 0.50 ± 0.09 . The best score from the 3 and 5 cm grouped data is 0.93 ± 0.06 achieved with the 5 cm sphere, and the worst is 0.82 ± 0.06 , which comes from the 3 cm sphere data.

Table 3.7: Results summary table for the metrics of quantitative analysis

Metric		mean	stdev	max	min
% volume difference	1 cm	-1.3 %	2.3 %	$-8 \pm 5 \%$ ^A	$0 \pm 2 \%$ ^B
	3 & 5 cm	0.22 %	0.55 %	$3 \pm 1 \%$ ^C	$0.1 \pm 0.6 \%$ ^D
Mean eccentricity	1 cm	0.31	0.06	0.48 ± 0.09 ^E	0.1 ± 0.1 ^F
	3 & 5 cm	0.18	0.05	0.3 ± 0.6 ^G	0.1 ± 0.2 ^H
Center to center distance (mm)		0.6	0.4	2.6 ± 2.1 ^I	0.03 ± 2.13 ^J
Max distance to agreement (mm)		1.2	0.4	2.6 ± 2.1 ^K	0.5 ± 2.7 ^L
Coincidence index	1 cm	0.62	0.06	0.74 ± 0.03 ^M	0.50 ± 0.09 ^N
	3 & 5 cm	0.89	0.02	0.93 ± 0.06 ^O	0.82 ± 0.06 ^P

Table caption: For each metric, the mean gives the 4DCT imaging system's average performance in accurately imaging the spheres. The letters appearing in the upper right indicate the acquisition: A) 20% phase of SI-AP-LR motion, Bellows 1.0 cm cams; B) 10% phase of SI-AP-LR motion, RPM 1.0 cm cams C) 3 cm sphere, 20% phase of SI-motion, Bellows 1.5 cm cams; D) 5 cm sphere, 90% phase, SI-AP-LR motion, RPM 0.5 cm cams; E) 70% phase, SI-motion, RPM 1.5 cm cams; F) 10% phase of SI-motion, Bellows 0.5 cm cams; G) 3 cm sphere, 70% phase of SI-motion, Bellows 1.5 cm cams; H) 5 cm sphere, 50% phase of SI-motion, Bellows 0.5 cm cams; I) 5 cm sphere, 20% phase, AP-LR direction, RPM 1.5 cm cams; J) 3 cm sphere, SI-motion, Bellows 1.0 cm cams; K) 5 cm sphere, 20% phase, AP-LR direction, RPM 1.5 cm cams; L) 1 cm sphere, 90% phase of SI motion, Bellows 0.5 cm cams; M) 50% phase of AP-LR motion, Bellows 1 cm cams; N) 20% phase of AP-LR motion, RPM 1.5 cm cams; O) 5 cm sphere, 40% phase of AP-LR motion, Bellows 1.5 cm cams; P) 3 cm sphere, 30% phase of AP-LR motion, RPM 0.5 cm cams.

Discussion of 4DCT Geometric Accuracy

Threshold sensitivity

Other authors have remarked on the increased sensitivity to thresholding in 4DCT phase images (2,163). In this study, threshold sensitivity is imbedded in each metric's error. Only two of the metrics have a direct static 3DCT equivalent for comparison of thresholding sensitivity between 3DCT and 4DCT acquisitions: *% volume difference* and *mean eccentricity*.

Table 3.8 gives an apples-to-apples comparison of the average threshold error in 3DCT and 4DCT measurement of *% volume difference* for all three sphere sizes. The average threshold error for the 1 cm sphere when stationary is $1.94 \pm 0.62 \%$ (where the error is one standard deviation of all measurement errors.) For the 4DCT images of the 1 cm dynamic sphere, the mean and standard deviation of error due to thresholding is $2.28 \pm 1.13 \%$. For both the static 3DCT and the dynamic 4DCT images, as the size of the sphere increases, the average thresholding error decreases, and so does the variability in

the error; the larger the imaged object, the less sensitive its volume is to thresholding. For all sphere sizes, the thresholding error is larger for the 4DCT acquisitions. This is to be expected from the volume attribute maps. For both the static and 4DCT images, the volume vs. % local threshold is roughly linear over a wide range of thresholds (see Figures 3.43, 3.48, and 3.53). The slopes for the moving spheres imaged with 4DCT tend to be steeper than for their static counterparts imaged with 3DCT.

Table 3.8: Average thresholding error in % *volume difference* measurements

	1 cm sphere	3 cm sphere	5 cm sphere
Static 3DCT	1.94 ± 0.62 % (17)	0.58 ± 0.23 % (16)	0.43 ± 0.18 % (16)
dynamic 4DCT	2.28 ± 1.13 % (170)	0.79 ± 0.35 % (160)	0.63 ± 0.31 % (160)

Table caption: Thresholding errors in the % *volume difference* metric. The numbers in parentheses indicate the number of images examined. There are ten times more phase images because every 10 phase 4DCT acquisition is accompanied by a single static 3DCT image. The 3 & 5 cm sphere data combined yield average errors of: Static 3DCT = 0.58 ± 0.23 %, and dynamic 4DCT = 0.71 ± 0.35 %.

Looking at the thresholding errors of the *mean eccentricity* for both the static 3DCT and dynamic 4DCT images given in Table 3.9, again, as the sphere becomes larger the thresholding error reduces. However, when the static errors are compared to the 4DCT errors, it appears as though the 1 cm sphere imaged with 4DCT shows a greater threshold dependency while the 3 cm sphere shows less. The thresholding errors for the 5 cm sphere are about the same whether the object is imaged while stationary with 3DCT or while in motion with 4DCT. Recall that the eccentricity attribute maps for the static spheres (see Figure 3.39), although fluctuating, hover around some mean value over a wide range of thresholds. In the 4DCT eccentricity maps, the eccentricity is bowed, dipping down to levels comparable to the static scans only over a constricted range of thresholds –with a window of only about 5 - 10 % local contrast (see Figures 3.44, 3.49, and 3.54). This range of low eccentricity values coincides roughly with the “optimal” range of thresholds specified by the stationary reference object, however, not in all instances (i.e. see Figure 3.44). In a clinical situation where there is no reference object, if the chosen threshold(s) fall outside this narrow range, the eccentricity would not only increase, it would also be subject to much greater variability with threshold (i.e. be on a steep portion of the attribute map).

Table 3.9: Average thresholding error in the mean eccentricity measurements

	1 cm sphere	3 cm sphere	5 cm sphere
Static 3DCT	0.023 ± 0.015 % (17)	0.028 ± 0.018 % (16)	0.018 ± 0.009 % (16)
Dynamic 4DCT	0.045 ± 0.031 % (170)	0.019 ± 0.011 % (160)	0.018 ± 0.015 % (160)

Table caption: Combining the 3 & 5 cm data : Static = 0.023 ± 0.015 % and Dynamic = 0.019 ± 0.013 %. The thresholding error depends on the shape of the eccentricity attribute map for each cross sectional image of the object and on what portion the segmented sphere lies. Also, note the reduced fluctuation with threshold for the maps of the dynamic 1 and 3 cm sphere (i.e. Figures 3.44 and 3.49, respectively) compared to the maps from the static images (i.e. Figure 3.39).

Thresholding sensitivity of the *center to center distance* metric cannot be compared to any center to center distances with the static scans because this measurement is relative to the phantom movement. However, if we look at the centroid attribute maps for the static 3DCT (Figure 3.40) and dynamic 4DCT images (Figures 3.45, 3.50, 3.55),

both are fairly stable over a wide range of thresholds. The relative insensitivity of the centroid to thresholding in 4DCT images has been noted previously (2,163).

Imaged Volume

When the 1 cm sphere is stationary and imaged with a non-temporally correlated CT (i.e. 3DCT), the average % *volume difference* is -1.09 % with standard deviation of 1.65 % (please see Table 3.5). When the sphere is moving and imaged using 4DCT, the average % volume difference is -1.3 % with a standard deviation of 2.6 % (see Table 3.7). The larger variation in volumes with 4DCT is to be expected since all the phases of motion have been included, yet in terms of the absolute volumetric differences, the mean for dynamic 4DCT is only slightly higher than that achieved with the standard 3DCT clinical protocols and a stationary sphere. Grouping the 3 and 5 cm spheres together, the mean % *volume difference* between the 3DCT imaged static spheres and their true volumes was 0.10 % with a standard deviation of 0.36 %, compared to the 4DCT data sets of 0.22 % with a standard deviation of 0.55 %. These results are in keeping with those of Shih et al. who noted that spheres larger than 1.8 cm maintained volume discrepancies below 7 % (115).

Other authors have commented on the high degree of accuracy of 4DCT in producing representative volumes (121,88,115). Reitzel considers a GTV volume within 5 % sufficiently accurate (118). The 1 cm sphere data fits this criterion within one standard deviation, although there are a couple of extreme outliers: 8% too small and 8 % too larger, both in the 20 % phase of SI-AP-LR motion. As seen in Figures 3.58 and 3.59, the % *volume differences* are closest to zero in the 00% and 50% phase. The largest discrepancies are observed in the fastest phases (i.e. 20, 30, 70, 80% phases) 83 % of the time, coinciding with the maximum speed captured in the 4DCT acquisitions (88). This is also in keeping with published results (44).

Imaged Shape

Mechanical measurement reveals maximum eccentricities of 0.133, 0.086, and 0.057 for the 1, 3, and 5 cm spheres, respectively. Under dynamic conditions, 4DCT yields *mean eccentricities* of 0.31 for the 1 cm sphere and 0.18 for the 3 and 5 cm spheres. Recall that only planes passing through the center of each sphere were investigated with physical measurements whereas the *mean eccentricity* metric evaluates each cross sectional image to give the average eccentricity of all segmented areas constituting the imaged volume of the sphere. In all 4DCT images of the spheres, the cross sectional images on edge slices exhibit considerably more shape deformity than those on interior slices but are weighted equally by the metric. As well, an eccentricity of 0.3 translates to a difference of only 5% between the major and minor axes of an ellipse, and for the 1 cm sphere, the addition or subtraction of the smallest dimension of an individual voxel (i.e. 0.78 mm) to a single axis alters its length by about 8 %. Under static conditions, standard clinical 3DCT yields corresponding *mean eccentricities* of 0.27 for the 1 cm sphere, and 0.103 for the 3 and 5 cm spheres.

Comparing the 4DCT acquisitions of moving spheres to the 3DCT acquisitions while stationary, the *mean eccentricity* is larger in the 4DCT images for every sphere size (See Table 3.7). For both the 3DCT and 4DCT images, the mean eccentricity decreases with increasing sphere size due to the low surface area to volume ratio minimizing partial volume effects as well as the impact of any residual motion artifacts. The increase in shape conformity with increasing sphere size has also been documented (2). Yet, in the static images, the standard deviation in mean eccentricity also drops as the spheres get larger (with the larger number of pixels, the shape depiction is more reliable), but in the 4DCT images, the standard deviation remains relatively constant regardless of size. This

is most likely due to how the data has been grouped. Each type of motion has its own distinct eccentricity pattern (See Figure 3.49); when grouped together, the disparity of these patterns overwhelms the size advantage for consistency.

As with the volume differences, motion artifacts are least at the 00% and 50% phases where motion is the least (32,39), and fast phases show the worst artifacts (39). In patient data, the targets will be irregularly shaped and susceptible to deformation which could cause additional shape distortions beyond what is seen in this report, however, in a ten patient study by Wu et. al, these deformations were not considered significant (153). Also, motion artifacts should not be as severe in patient data, since less dramatic difference in density between the objects of interest and the background will mollify both in plane and transverse plane motion artifacts (2).

Table 3.10: Mean eccentricities for each sphere size imaged with static 3DCT and dynamic 4DCT

Sphere sizes	Mean eccentricity			
	Static 3DCT images		Dynamic 4DCT images	
	Mean	Standard deviation	Mean	Standard deviation
1 cm	0.27	0.05	0.31	0.06
3 cm	0.12	0.01	0.20	0.06
5 cm	0.083	0.008	0.16	0.06
3 & 5 cm	0.10	0.02	0.18	0.05

Table caption: *Mean eccentricity* measurements for the static 3DCT and dynamic 4DCT images. For both types of imaging, the standard deviation in *mean eccentricity* get smaller as the spheres get larger. However, in the 4DCT images, the standard deviation remains relatively constant regardless of size due to the grouping of distinct eccentricity patterns (see Figure 3.26).

Tracking Ability

Rietzel considers the ability to track an object adequate if the discrepancy is less than 1 mm (118). The mean *center to center distance* of all phase images meets this criterion to within one standard deviation (i.e. from Table 4.3: 0.6 ± 0.4 mm). The largest center to center distance measured is 2.6 mm, and is the only data set with a center discrepancy over 2 mm (i.e. RPM, 5 cm sphere 1.5 cm cams, AP-LR motion). The next closest discrepancy is only 1.58 mm, from a different phase of the same 4DCT acquisition. Yet, with all error accounted for, even this outlier is acceptable. The high contrast produced by acrylic spheres surrounded by air corresponds well to the clinical situation in which mobile tumors are fully circumscribed by lung. Departure from this high contrast scenario, however, could prove problematic.

Given the stability of the centroid in the center slice for even the fastest phases (see Figures 3.45, 3.50, and 3.55) and that, in patient data, SI motion is the most prominent motion while affecting the *center to center distance* the least (see Figure 3.63), the most important factor in accurately tracking an object with 4DCT is temporal resolution. Even with very small slice thickness and very fast tube speed, it is possible to still miss the full extent of motion if an insufficient number of phases are reconstructed (121,122). This is particularly true when a phase shift exists between the external marker and the internal anatomy, which is common in patient data (21,162,129,88,24). Since the retrospective method allows for unlimited reconstruction without additional dose to the patient, the maximum default number of phases should be chosen for all patients (e.g. ten phases) and additional phases reconstructed off-line if a phase shift between the marker and target is suspected.

Localization

Rietzel considered a surface to surface agreement of 0.5 ± 2 mm adequate (140). The *maximum distance to agreement* did not exceed 2.6 mm for all 490 examined images, with a mean value of 1.2 ± 0.4 mm. For slow phases, the surface to surface distances are typically sub-millimeter, and any resulting delineation errors may easily be accounted for by typical clinical margins (e.g. here at The Cross Cancer Institute, 5 - 15 mm). Thus, 4DCT produces acceptable localization for gating. When contouring all phases of motion, such as for an ITV, discrepancies of several millimeters are still possible. Table 4.7 gives the largest measured *maximum distances to agreement* for each sphere size and displacement.

Table 3.11: The Largest measured *maximum distance to agreement* for each sphere size and amplitude of motion

Amplitude	1 cm Sphere	3 cm Sphere	5 cm Sphere
0.5 cm cams	1.2 mm	1.8 mm	1.9 mm
1.0 cm cams	1.8 mm	2.2 mm	2.2 mm
1.5 cm cams	2.0 mm	2.3 mm	2.6 mm

Table caption: The largest surface to surface distances show a trend of increasing with sphere size as well as with increasing displacement.

Although the data points for the mean *maximum distance to agreement* are grouped fairly closely in Figure 3.70b, the largest measured *maximum distance to agreement* follows a trend of increasing with increasing sphere size and displacement amplitude.

Coincidence index

With its small number of voxels and increased sensitivity to threshold, one would expect that the *coincidence index* for the 1 cm sphere should be low, and with an average value of 0.62, it is (see Table 4.6). For the 5 cm sphere, the index hovers around 0.90, on average, a mere 0.03 point improvement over the 3 cm sphere. Thus, the index clearly shows some diminishing returns on geometrical accuracy with increased size. This can be attributed to the presence of residual motion artifacts which, although they can be minimized by a fast tube rotation speed, cannot be completely eliminated. In clinical use, 90 % of patient 4DCT scans show some artifact other than blurring (164). An extensive survey of 4DCT by Rietzel et al. indicates a conservative estimate of these artifacts would be about 2.5 mm for typical respiratory patterns (2).

There are no stepladder artifacts in this data set, testifying to both the periodicity of the phantom and the high performance accuracy of the Bellows and RPM respiratory monitoring systems. The problem is certainly still common in patient data, however, particularly near the diaphragm where the motion is the greatest, or near the heart, where the cardiac beat, being on a different timescale than respiratory motion, is unaccounted for with the 4DCT technique. In addition, as discussed earlier, irregularities in patient breathing patterns or not allowing sufficient time for the respirator monitoring system to learn the patient's breathing pattern can also lead to stepladder artifacts (157).

It should be expected that all in-slice artifacts would be less severe in patient data than what is seen here. Human physiology has less abrupt changes in electron density than an acrylic sphere surrounded by air. The reconstruction algorithm will see less inconsistency between projection angles and therefore, it is more likely to attribute densities to the various structures appropriately (2). Of course, there will always be a

propensity for partial projection artifacts involving the diaphragm and other nearby structures simply due to the magnitude and direction of motion in that region (157).

Figure 3.33 gives an example of some mysterious reconstruction choices of the Philips algorithm. Although it is not known exactly what the algorithm is doing, it is obvious that it is attempting to improve the consistency of the image by blocking out residual motion artifacts. It is not known where the replacement data comes from nor what impact replacing data at the location of the target has on its delineation. This is just one example why each 4DCT system should be individually evaluated (47).

Summary and Conclusion of Quantitative Measurements

The geometric accuracy of a Philips Brilliance CT scanner's 4DCT capabilities is quantitatively evaluated. Both the Philips Bellows and Varian Real-Time Position Management (RPM) Respiratory Gating System are utilized. A mechanical phantom imparts clinically relevant motion to acrylic spheres of various diameters, and the size, shape, and position of these spheres, as measured with 4DCT, are compared to their true size, shape, and position.

The accuracy in the volume of the imaged spheres is sensitive to sphere size; the larger the sphere the lower the *% volume difference* due to measurement error as well as the relative size of the object compared to the amplitude of its motion. Type and phase of motion also affect the *% volume difference* by the type and extent of the motion specific artifacts. Differences between true and segmented volumes for the 1cm sphere did not exceed 8 %, (mean 1.3%, standard deviation = 2.3%). For the 3 and 5 cm spheres, the combined average volumetric difference is 0.22% with a standard deviation of 0.55%. *Mean eccentricity* is also affected by size, phase, and type of motion and also shows a clear dependency on the speed at which the sphere is moving. The average *mean eccentricity* is 0.31 for the 1 cm sphere, and 0.18 for the 3 and 5 cm sphere data combined. The tracking ability of the 4DCT system, measured by the *center to center distance*, is relatively insensitive to sphere size and type of motion, however, the speed of the sphere affects the location measurement as evidenced by both its amplitude and phase dependency. For all sphere sizes, types of motion and amplitudes of motion, the average performance of the 4DCT system yields a *center to center distance* of 0.6 ± 0.4 mm. Localization, as expressed in the *maximum distance to agreement* metric is accurate on average to 1.2 ± 0.4 mm. The *coincidence index*, a single number that represents the 4DCT system's ability to image the true size, shape, and location of the spheres, exhibits a clear dependence on sphere size and the phase of motion. The highest score attained by the 1 cm sphere is 0.74 out of a perfect 1.0. On average, the system produced a coincidence index of only 0.62 ± 0.06 for the 1 cm sphere. However, for the 3 and 5 cm sphere data combined, the average index was 0.89 ± 0.02 .

From the data presented in this thesis, it is evident that the Philips big bore CT, with either the Philips Bellows or Varian RPM respiratory monitoring systems, is capable of imaging mobile acrylic spheres in air to a high degree of accuracy. This high contrast scenario corresponds well to the clinical situation in which mobile tumors are fully circumscribed by lung.

Chapter 4: Analysis of Image Quality

Methods of Image Quality Analysis

In order to evaluate the image quality of 4DCT acquisitions, measurements of image noise, CT#, and modulation transfer function (MTF), as well as a qualitative

analysis of high and low contrast resolution are compared with those of a standard clinical non-temporally correlated CT scan (3DCT).

Imaging Protocols

The 4DCT image acquisitions differ from 3DCT in pitch, tube current, and tube rotation speed. Two protocols for each type of scan are investigated: a *clinical* protocol which uses standard clinical CT settings for both 3DCT and 4DCT thoracic acquisitions (detailed in Table 4.1) and an *optimized* protocol with increased exposure and reduced field of view (FOV). The optimized protocols are given in Table 4.2 (all else being the same as for the clinical scans).

There has been some confusion as to the definition of exposure. In the DICOM header for both clinical protocols, an Exposure (often referred to by its units mAs) of 400 mAs is given. This is, in fact, the *effective exposure* (mAs_{eff}), defined as

$$mAs_{\text{eff}} = mAs/\text{pitch}, \quad 4.1$$

which is distinct from the more common definition of (tube current) x (acquisition time)²⁶. The concept of exposure was originally defined for axial acquisitions, a situation in which each slice location would not normally be exposed to more than a single rotation of the tube. With the advent of helical acquisitions, however, the pitch drastically affects the amount of radiation a single slice location receives, thus the quantity of *effective exposure* is the more relevant metric for helical scan techniques, particularly when estimating dose to a patient. In 4DCT, where as many as ten or more images may be reconstructed for each slice location, the mAs_{eff} does not necessarily represent the exposure contributing to a single cross sectional image. Thus, for discussions on image quality, the common definition of mAs must be used. Inspection of Table 4.1 reveals that the mAs of the clinical 3DCT protocol is 275 mAs, and for the clinical 4DCT it is only 32.5 mAs. The difference is a factor of 8.5.

Table 4.1: Clinical protocols

protocol	3DCT	Pulmo 4DCT
<i>Filter type</i>	B	B
<i>Scan type</i>	Helical	Helical
<i>FOV</i>	400 mm	400 mm
<i>Slice thickness</i>	2 mm	2 mm
<i>Tube potential</i>	120 kVp	120 kVp
<i>Reconstruction</i>	180°	180°
<i>Detector collimation</i>	16 x 1.5 mm	16 x 1.5 mm
<i>Voxel size</i>	0.78 x 0.78 x 2.00 mm ³	0.78 x 0.78 x 2.00 mm ³
<i>Effective Exposure</i>	400 mAs	401 mAs
<i>Pitch</i>	0.688	0.081
<i>Tube current</i>	275 mA	65 mA
<i>Rotation speed</i>	1 s	0.5 s

Table caption: Filter type B is typical for body imaging. In the DICOM header, “Effective Exposure” is referred to simply as “Exposure”.

²⁶ Where *acquisition time* is the time required for the tube to complete one full rotation.

Table 4.2: Optimized protocols

protocol	3DCT	4DCT
<i>FOV</i>	350 mm	350 mm
<i>Effective exposure</i>	600 mAs	1198 mAs
<i>Tube current</i>	413 mA	194 mA

Table caption: In the optimized scans, the FOV is reduced (essentially “zooming-in”, but still clinically relevant) and the effective exposure and tube current are increased from that used in the clinical scans. All other imaging protocols are the same as for the clinical scans.

The Phantoms

A Catphan 600 series CT quality assurance phantom is used in conjunction with the in-house conebeam quality assurance software *ConebeamQA* to measure the noise, mean CT#,s, and MTF for each protocol. As well, the high and low contrast segments of the Catphan are qualitatively evaluated. In addition to the Catphan CT# data, a small Lexan (i.e. low density plastic) cylinder (diameter 2.5 cm and length 4.5 cm) is used to evaluate the CT#s of moving objects. A lightweight high contrast phantom consisting of an acrylic cylinder (diameter of 5 cm and length of 4.4. cm) with holes drilled through it of various sizes and separation distances is used to investigate the high contrast resolution of moving objects. Images of all three phantoms are shown in Figure 4.1.

Figure 4.1: Image Quality Phantoms

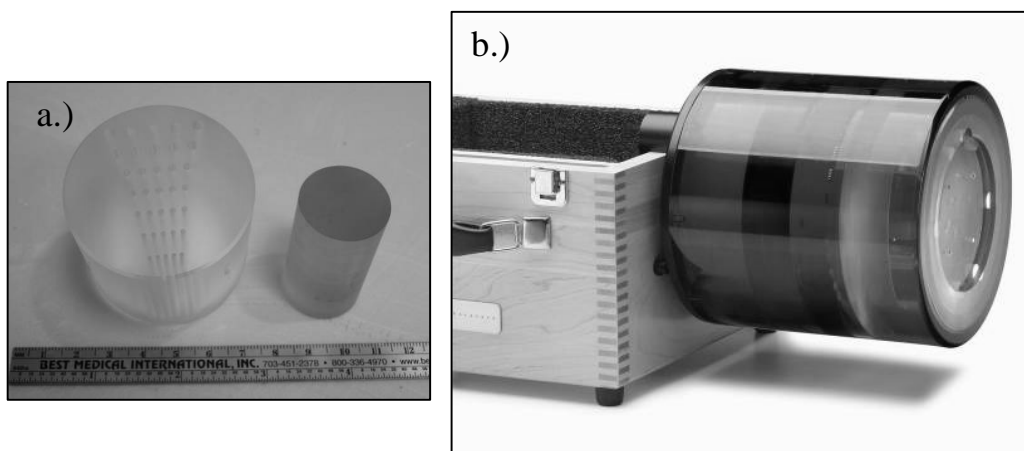


Figure caption: a.) The two mobile phantoms: a lightweight acrylic high contrast phantom and a Lexan cylinder. b.) the Catphan 600 series CT quality assurance phantom.

The Catphan, being too large to set into motion with any mechanical device available for this study, is imaged while stationary with both 4DCT and 3DCT acquisitions. Ten reconstructed 4DCT phase images of the Catphan are compared with ten 3DCT images of the phantom. The smaller high contrast phantom and uniform Lexan cylinder are also imaged while stationary using a ten phase 4DCT acquisition and ten 3DCT scans. Since these phantoms are lightweight enough to be set into motion, they are also imaged with 4DCT while undergoing motion in the SI-AP-LR direction at an amplitude of 1 cm in each orthogonal direction. Imaging of all phantoms is performed using both clinical and optimized protocols.

CT# Evaluation

To evaluate the equivalence of the 10 reconstructed phases of a stationary object, the mean and standard deviation of CT#s from a large number of pixels (i.e. ~10,000) are collected from the specified slice of the uniform solid water module of the Catphan (CT 486, see Figure 4.2).

Using the specified slice of the Catphan CT# module (CTP 404, depicted in Figure 4.3) and our in-house *ConebeamQA* software, the mean CT#s of seven different materials are averaged over all ten 4DCT phase images. Likewise, the mean CT#s from all ten 3DCT images of the phantom are also averaged and the percent difference between the 4DCT and 3DCT measurements calculated for each material.

Figure 4.2: Catphan Uniform Solid Water Module (CTP 486)

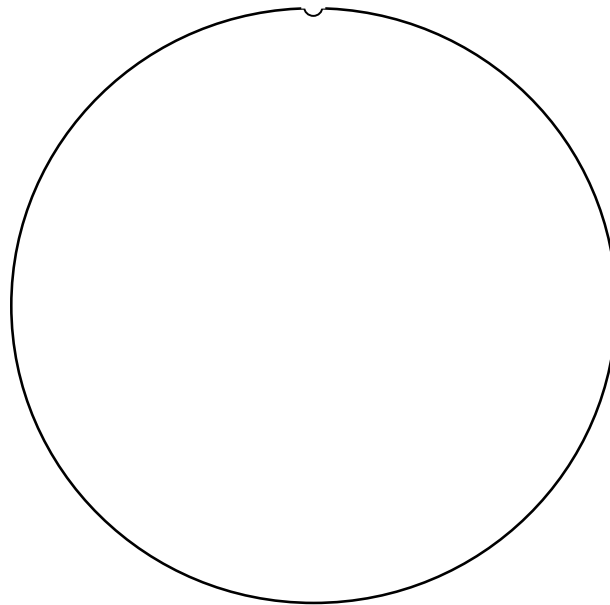


Figure caption: The uniform solid water module is a featureless slab with the same radiological properties as water. The correct (or optimal) slice of each Catphan module is identified by a tick at the top center of the specified slice.

Figure 4.3: Catphan CT# Module CTP 404

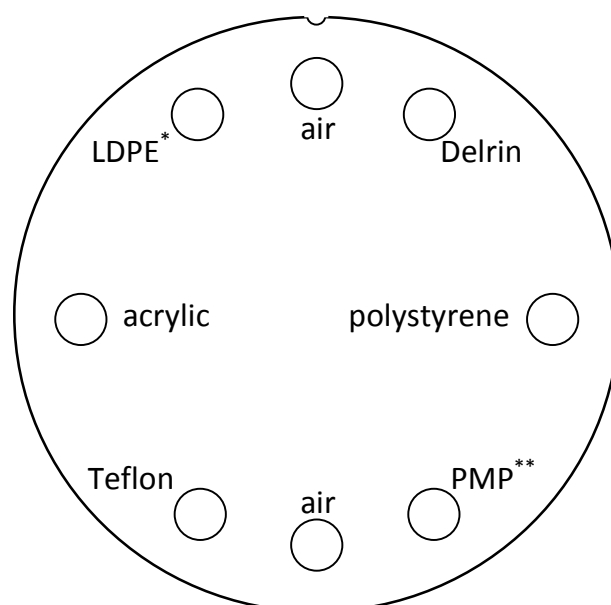


Figure caption: The 8 plugs (7 materials, since two are air only) in the Catphan CT# module. * Low density polystyrene, ** Propylene Glycol Monomethyl Ether Propionate

A quantitative analysis of CT#s in moving objects is performed using the 3DCT and 4DCT images of the Lexan cylinder. In ImageJ, histograms of the object's CT#s are extracted from the center of the cylinder (i.e. the center of the center slice) with an ROI set more than 5 pixels in from the edge of the object (to avoid partial volume affects). The ten histograms from the ten 3DCT images acquired while the cylinder is stationary are summed and compared with the summation of ten histograms extracted from the ten 4DCT phase images of the stationary object as well as the summed histograms from the ten 4DCT phase images acquired while the object is in motion.

Noise Measurement

Noise, expressed as the standard deviation of pixel values in a uniform region, is calculated from the Catphan uniform solid water module (CTP 486) using the *ConebeamQA* software. Pixel values are collected from 5 ROIs on a specific slice of each 4DCT phase image and the noise is calculated for each ROI (see Figure 4.4). For each phase image, the noise is averaged over the five ROIs. The results are then averaged over all ten 4DCT phase images, yielding a single noise value for the entire 4DCT acquisition. The result is compared to the average of similarly collected noise values from the ten 3DCT images of the Catphan.

Low contrast Resolution

Low contrast resolution is the imaging system's ability to represent an object as distinct from its background when the attenuation properties of the object and its background are very similar (156p18). Using the specified slice of the Catphan low contrast module (CTP 515, depicted in Figure 4.5); window and level are chosen for optimal low contrast visibility. The smallest discernable low contrast plug is identified for each type of acquisition.

Figure 4.4: The placing of 5 ROIs on the Catphan Uniform Solid Water Module

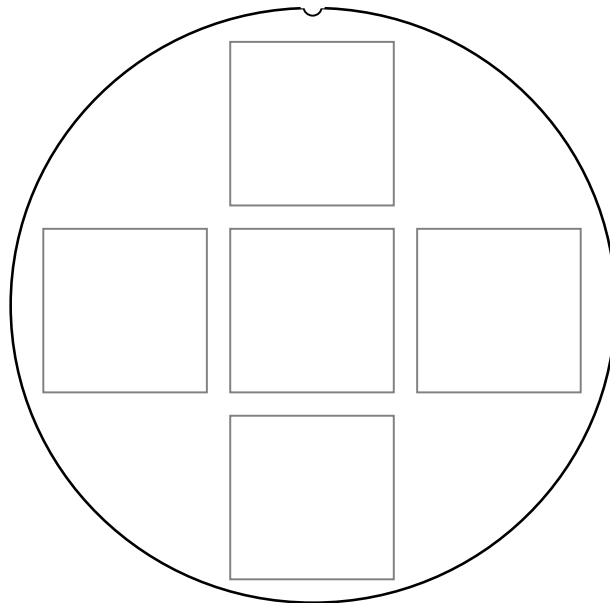


Figure caption: Using the ConebeamQA software, the noise measurements are collected from 5 ROIs: center, top, right, bottom, and left.

Figure 4.5: Catphan Low Contrast Module CTP 515

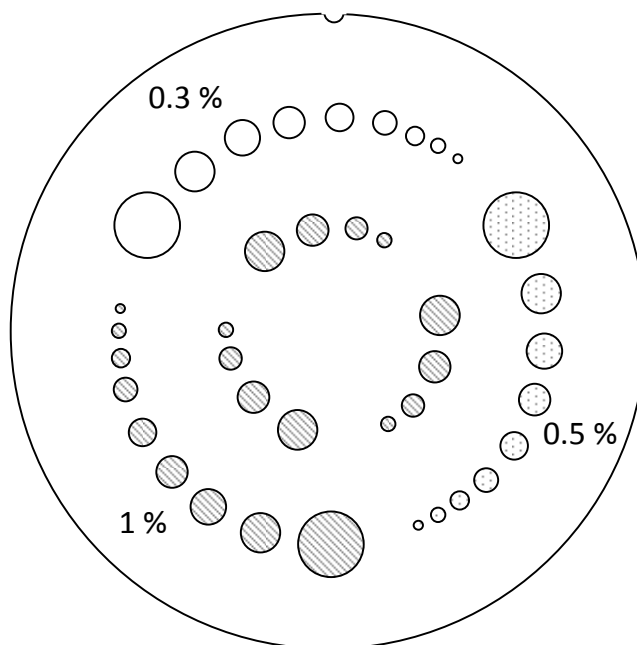


Figure caption: Outer ring: supra-slice-- indicates a cylindrical plug that spans many slices of the Catphan module. Inner ring: sub-slice-- plugs are very short cylinders intended to span less than a single slice. The nominal contrast values are expressed as a % difference between the plug and its background. All the inner ring sub-slice plugs are 1% contrast.

High contrast Resolution

High contrast resolution is the imaging system's ability to differentiate objects of very dissimilar densities when they are within close proximity to one another. Using the specified slice of the Catphan 21 line pair high resolution module (CTP 528, depicted in Figure 4.6), window and level are chosen for optimal visualization of the line pair patterns. The smallest discernable pattern is identified for each type of acquisition.

Since the Catphan is too heavy to move, the small acrylic high contrast phantom is imaged while mounted on the moving platform of the mechanical phantom used in the Quantitative Measurements section. Line profiles (i.e. the CT#s collected along a straight line) are taken through selected patterns (e.g. the smallest pattern consisting of 1 mm holes spaced 1 mm apart, see Figure 4.1a), and the contrast calculated as

$$CT\#_{\max} - CT\#_{\min} . \quad 4.2$$

The contrast between the dynamic 4DCT acquisition and the stationary 3DCT acquisitions are compared.

Figure 4.6: Catphan High Contrast Module CTP 528

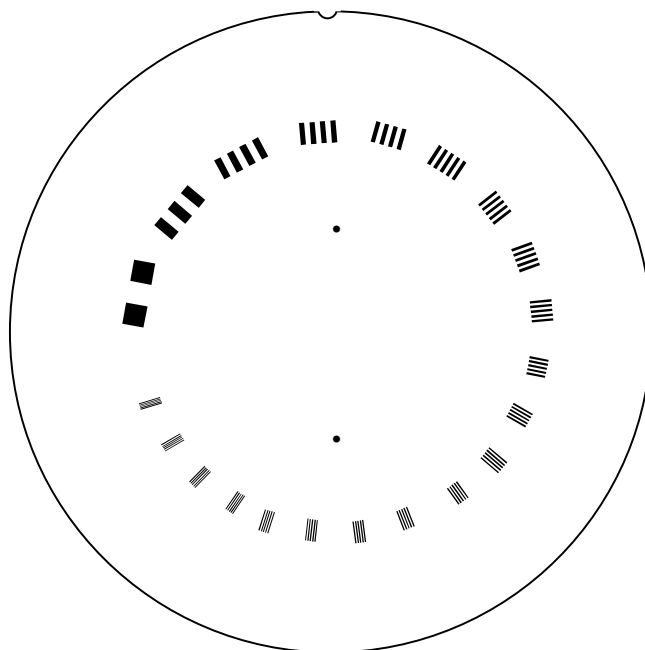


Figure caption: The high contrast module contains 21 line pair gauges, ranging from 1 - 21 line pairs per centimeter (lp/cm). This slice also contains two small tungsten beads. These beads represent point objects used in the measurement of an MTF.

Modulation Transfer Function

Since it is not possible to separate an imaging system's resolution from its contrast, the MTF is measured as an expression of both (165). The MTF is the Fourier transform of the system's line spread function. Here, the point spread function (psf) is imaged as the 2D spatial distribution of pixel values in the immediate vicinity of a small tungsten bead. The specified slice of the Catphan point source module (CTP 528) is used. The *ConebeamQA* software code calculates the MTF from a 2D discrete Fourier transform of the psf

$$Y_{k_1 k_2} = \sum_{n_1=0}^{N_1-1} \left(e^{-2\pi i k_1 n_1 / N_1} \sum_{n_2}^{N_2-1} e^{-2\pi i k_2 n_2 / N_2} y_{n_1 n_2} \right), \quad 4.3$$

where $y_{n_1 n_2}$ is the 2D matrix of the psf, and n_1 and n_2 are vectors of indices of lengths N_1 and N_2 , respectively. Likewise, k_1 and k_2 are vectors of indices of length N_1 and N_2 . The nested summation essentially calculates the discrete Fourier transform of all the rows, then all the columns, by matrix multiplication of the psf by a transform of complex exponentials²⁷ (166). The values in the resulting transformed 2D matrix $Y_{k_1 k_2}$ are then radially binned to create a 1D MTF. The ten MTFs of the ten 4DCT phase images are averaged and graphed along with the average MTFs of the ten 3DCT images. Error bars are one standard deviation of the measured values.

Results of Image Quality Analysis

CT#

There is an intrinsic ambiguity to evaluating 4DCT scans due to the number of images volume reconstructed from a single acquisition. Which image volume do you use? How legitimate would it be to combine the data collected from the various phase images? Table 4.3 gives the mean and standard deviation of CT#s (in true HU) in a large region of uniform solid water (i.e. the Catphan uniform solid water module) from the 10 4DCT phase images acquired while the phantom is stationary.

Table 4.3: Mean and standard deviation of pixel values in a large uniform density region imaged while stationary with clinical 4DCT

4DCT phase image	mean (HU)	stdev (HU)
00%	15.222	22.152
10%	15.657	22.652
20%	15.330	19.299
30%	15.834	19.001
40%	16.004	18.769
50%	15.493	18.053
60%	15.806	18.134
70%	16.102	22.104
80%	15.497	22.002
90%	15.444	21.871

Table caption: The 10 4DCT phase images of the Catphan's uniform solid water module yields an average CT# of 15.64 ± 0.29 , where the error is one standard deviation of the presented values. The average standard deviation in CT#s is 20.40 ± 1.89 . Again, the error is one standard deviation of presented values. The area from which these statistics are collected is 6475.22 mm^2 (i.e. 103×103 pixels).

²⁷ The fast Fourier transform is a discrete Fourier transform that computes quickly. There are many different types of fast Fourier transforms, differing from one another and the discrete Fourier transform only in processing algorithms, not in any mathematical sense (166).

The average mean and standard deviation of CT#s for the clinical 4DCT images are 15.64 ± 0.29 and 20.40 ± 1.89 , respectively, where the error is one standard deviation in the presented values. For comparison, Table 4.4 shows the mean and standard deviation of CT#s in the same region of uniform solid water from the 10 static clinical 3DCT images. The standard deviation in reported values for the mean CT#s is only 0.07, and for the standard deviation of CT#s it is 0.05.

Table 4.4: Mean and standard deviation of pixel values in a large uniform density region imaged while stationary with clinical 3DCT

3DCT image	mean (HU)	stdev (HU)
1	14.326	5.195
2	14.322	5.180
3	14.202	5.220
4	14.446	5.297
5	14.239	5.155
6	14.259	5.246
7	14.254	5.235
8	14.228	5.194
9	14.246	5.309
10	14.228	5.267

Table caption: The 10 3DCT images of the Catphan's uniform solid water module yield an average CT# 14.28 ± 0.07 , where the error is one standard deviation of the presented values. The average standard deviation in CT#s is 5.23 ± 0.05 . Again, the error is one standard deviation of presented values. The area from which these statistics are collected is 6475.22 mm^2 .

Table 4.6 gives the CT#s measured from the stationary Catphan imaged with clinical 3DCT and 4DCT scans.

Table 4.6: Mean CT#s for 7 materials measured with 3DCT and 4DCT

	Mean CT # (HU)		
	mean 3DCT static	mean 4DCT static	% diff
Air(top)	-954.0 ± 0.9	-955 ± 3	0.07 %
Teflon	911.1 ± 0.5	912 ± 3	0.07 %
Acrylic	122.4 ± 0.6	123 ± 3	0.46 %
LDPE	-86.7 ± 0.7	-84 ± 4	2.66 %
Air(bottom)	962.7 ± 0.8	-963 ± 3	0.04 %
Delrin	340.1 ± 0.7	341 ± 4	0.22 %
Polystyrene	-31.0 ± 0.6	-29 ± 2	6.61 %
PMP	-173.3 ± 0.9	-173 ± 3	0.32 %

Figure caption: The average CT#s of the 3DCT scans compared against the average of all ten 4DCT phase images. Nominal values: Air -1000 HU, Teflon 990 HU, Acrylic 120 HU, LDPE -100 HU, Delrin 340 HU, Polystyrene -35 HU, and PMP -200 HU (167).

The materials range from very high to very low densities. Although the low density materials (i.e. LDPE and Polystyrene) show the most discrepancy between the 3DCT and 4DCT acquisitions, all the 4DCT mean values are within one standard deviation of those measured with 3DCT. The percent differences between the 3DCT and 4DCT CT#s,

while not exceeding 7 %, are more often below 1 %. Even for polystyrene with the greatest percent difference, the absolute mean CT#s differ by only 2 HU.

Figure 4.7: Cumulative histograms of CT#s in a uniform low density plastic cylinder imaged while stationary with clinical 3DCT

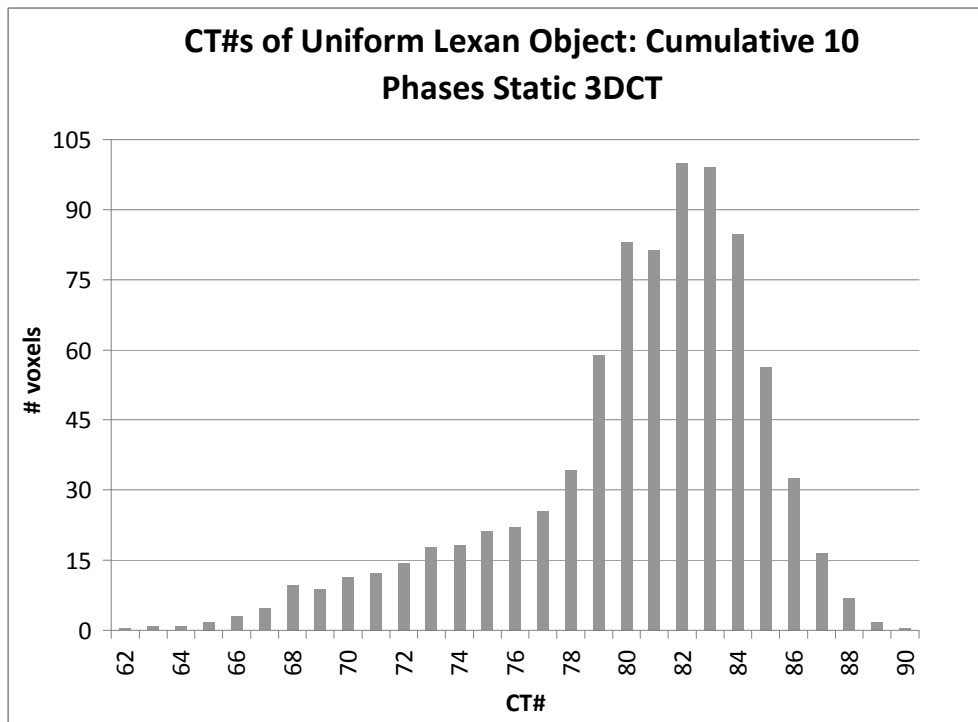


Figure caption: The sum of 10 histograms collected from 10 different 3DCT scans of the stationary uniform Lexan cylinder imaged using clinical protocols. The ROI from which the pixel samples are collected is set more than 5 pixels in from the perimeter of the object to avoid partial volume effect. The cumulative histogram has been normalized to 100 counts.

The cumulative histogram of CT# for the ten static 3DCT images acquired using clinical protocols is found in Figure 4.7. In Figure 4.8, the envelope of this cumulative histogram is presented along with the envelopes of similar cumulative histograms from the 10 phase images of two 4DCT acquisitions: one acquired while the object is stationary and the other acquired with the cylinder undergoing SI-AP-LR motion with an amplitude of 1 cm in each orthogonal direction. All histograms are constructed from pixels well within the boundary of the object, and such, are not affected by partial volume effects.

Figure 4.8: Cumulative histograms of CT#s in a uniform low density plastic cylinder imaged while stationary with clinical 3DCT and 4DCT, and while in motion with clinical 4DCT

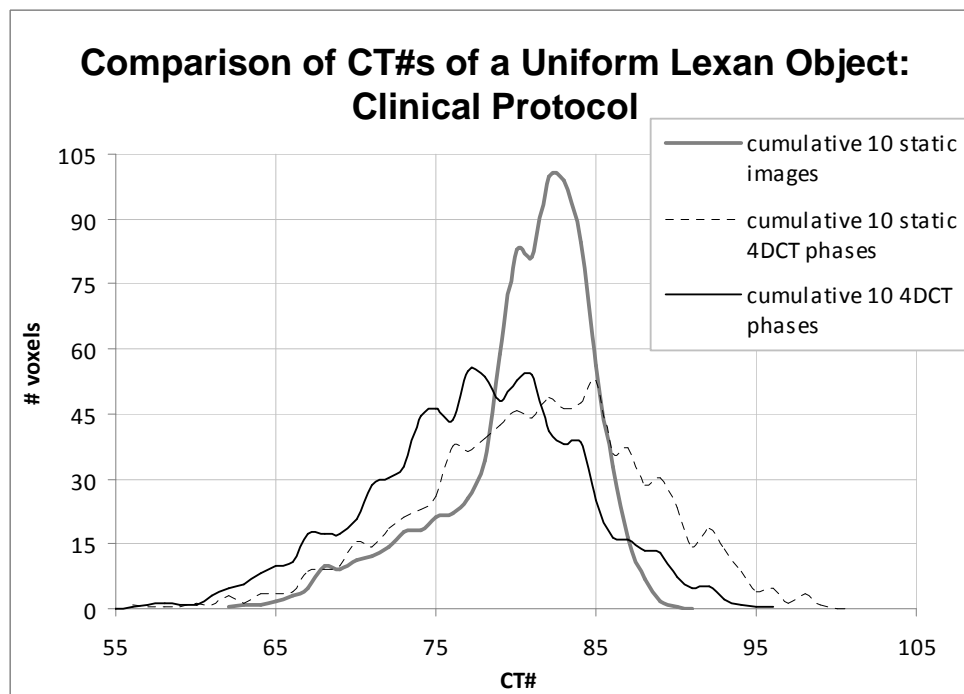


Figure caption: The envelope of the cumulative histogram from three different clinical acquisitions of the uniform Lexan cylinder: 3DCT images acquired while the object is stationary, 4DCT acquired while the object is stationary, and 4DCT acquired while the object is undergoing motion in the SI-AP-LR direction with an amplitude of 1 cm in each of the three orthogonal directions. An ROI $10.92 \times 10.92 \text{ mm}^2$ is used for all 30 histograms.

The mean and median pixel values of the ten static 3DCT scans are 80.3 HU and 81.8 HU, respectively. For the 4DCT acquisition of the same static object, both the mean and median CT#s increase to 81.2 HU and 82.1 HU, respectively. This increase is very slight –the most dramatic difference between the 3DCT and 4DCT acquisitions of the stationary object being the shape of the cumulative CT# histogram. The broadening of the distribution with the 4DCT acquisition (even though the object is imaged while stationary and so void of residual motion artifacts) could be expected from the increase in standard deviation of pixel values (i.e. seen in Table 4.3 compared to Table 4.4). That the mean pixel values of the 3DCT and 4DCT acquisitions are within 1 HU of one another is consistent with the Catphan CT# data. The cumulative histogram from the ten 4DCT phases acquired while the object is in motion shows a similar broadening of CT# distribution, with the mean and median CT#s slightly shifted down to 79.5 HU and 80.3 HU, respectively. This shift is to be expected due to the penetrating low density artifacts associated with both SI and AP-LR motion. Figure 4.9 shows the same histograms constructed from images of the low density plastic cylinder acquired using the optimized 3DCT and 4DCT protocols (i.e. increased mAs_{eff} and reduced FOV).

Figure 4.9: Cumulative histograms of CT#s in a uniform low density plastic cylinder imaged while stationary with optimized 3DCT and 4DCT, and while in motion with clinical 4DCT

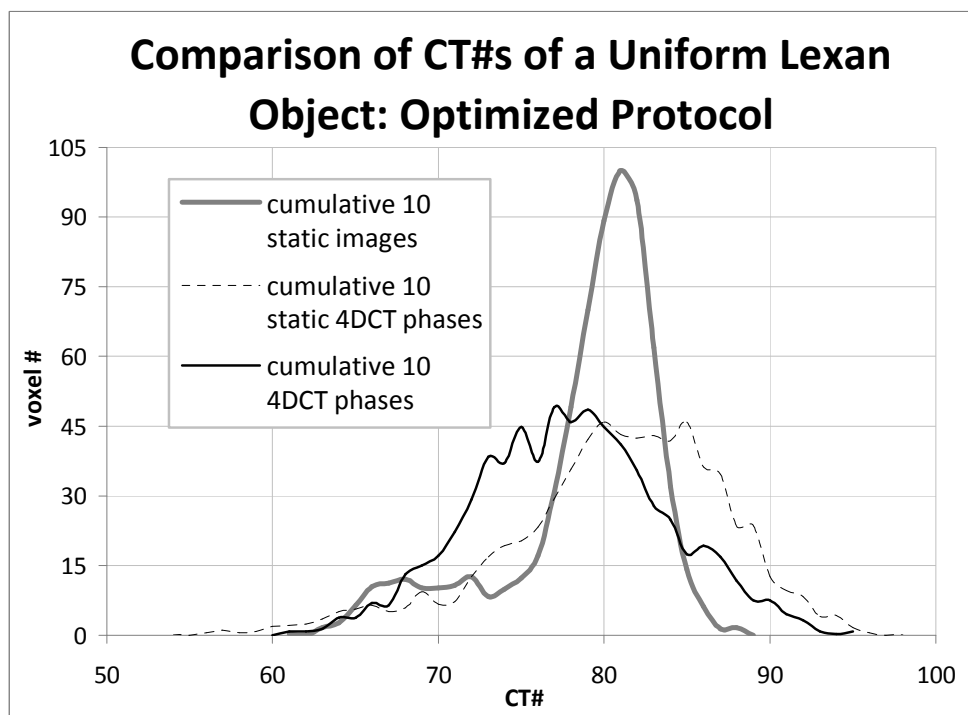


Figure caption: The envelope of the cumulative histogram from three different optimized acquisitions of the uniform Lexan cylinder: 3DCT images acquired while the object is stationary, 4DCT acquired while the object is stationary, and 4DCT acquired while the object is undergoing motion in the SI-AP-LR direction with an amplitude of 1 cm in each of the three orthogonal directions. An ROI 12.48 x 12.48 mm² is used for all 30 histograms.

Table 4.7: Summary of measured CT# distributions for clinical & optimized 3DCT and 4DCT acquisitions of a uniform low density plastic cylinder

	Clinical CT#s (HU)				Optimized CT#s (HU)			
	mean	median	range	FWHM	mean	median	range	FWHM
Static 3DCT	80.3	81.8	29	6	78.8	79.8	28	5
Static 4DCT	81.2	82.1	45	14	81.2	80.9	44	13
Dynamic 4DCT	79.5	80.3	44	11	80.0	79.9	37	12

Table caption: The mean, median, full range of CT# values, and FWHM for each acquisition. With the increased mA_{eff} of the optimized scans, the distributions of all 3 types of acquisitions become slightly narrower, presumably due to noise reduction.

In the optimized 3DCT scans, the mean CT# of the low density plastic cylinder is 78.8 HU with a median of 79.8 HU, 1.5 HU and 2 HU lower, respectively, than what was measured with the clinical protocols. For the 4DCT acquisition of the stationary object, the mean and median are 81.2 and 80.9 HU, respectively, only 0.2 HU and 1.2 HU different from their clinical counterparts, respectively. From the 4DCT acquisition of the moving object, the mean is 80.0 HU and the median is 79.9 HU, 0.5 and 0.4 HU different from the clinical scans, respectively. In going from the clinical to the optimized

protocols, the mean and median CT#s of the 4DCT distributions change less than the 3DCT distributions. The relative pattern of the distributions, however, are the same for both protocols: the distributions are broadened for 4DCT acquisitions and shifted to higher CT# when the object remains stationary, but to lower CT#s when motion is present. These results are summarized in Table 4.7.

Noise

The noise data collected from the Catphan solid water module is shown in Tables 4.8, 4.9, and 4.10, giving the standard deviation in pixel values from the clinical 3DCT, clinical 4DCT, and optimized 4DCT scans, respectively. Looking solely at a stationary object, the noise increased by 328 % in the clinical 4DCT images compared to the standard clinical 3DCT scans. Optimized 4DCT images exhibited a noise increase of 200% compared to clinical 3DCT images.

Table 4.8: Noise values collected from ten clinical 3DCT scans

Image	Noise				
	center	top	right	bottom	left
1	5.437	5.239	5.609	6.204	6.571
2	5.503	5.712	6.749	6.653	7.367
3	5.542	5.536	5.854	5.638	6.258
4	5.59	5.724	6.481	6.294	6.614
5	5.4	5.819	5.619	6.272	5.863
6	5.436	5.564	6.077	5.393	6.475
7	5.337	5.332	5.942	6.298	6.283
8	5.357	5.475	5.783	6.555	6.09
9	5.465	6.184	5.747	6.42	6.591
10	5.524	5.548	6.017	6.1	6.242

Table caption: The standard deviations in pixel values for the five ROIs in ten clinical 3DCT images of the specified slice of the Catphan solid water module (CTP 486). The mean (error is one standard deviation) of measured noise values in all ten images is 5.94 ± 0.48 .

Table 4.9: Noise values collected from ten clinical 4DCT scans

phase	Noise				
	center	top	right	bottom	left
00%	22.949	20.463	20.596	19.609	20.521
10%	23.759	21.987	20.362	19.013	20.113
20%	20.495	18.173	17.012	19.13	19.158
30%	19.504	16.735	18.086	17.885	18.005
40%	20.261	18.99	17.814	18.137	15.845
50%	19.244	17.388	16.957	15.471	18.679
60%	19.169	18.156	16.048	18.694	16.865
70%	22.1	19.907	20.362	21.926	20.242
80%	21.716	21.23	20.704	20.816	19.444
90%	22.844	20.529	19.424	19.827	19.896

Table caption: The standard deviations in pixel values for the five ROIs in the ten clinical 4DCT phase images of the specified slice of the Catphan solid water module (CTP 486). The mean of measured noise values in all ten images is 19.44 ± 1.86 (error is one standard deviation).

Table 4.10: Noise values collected from ten optimized 4DCT scans

phase	Noise				
	center	top	right	bottom	left
00%	11.958	10.569	11.26	9.978	10.362
10%	11.959	11.379	9.789	10.105	9.877
20%	11.941	10.438	10.396	10.236	10.616
30%	12.26	10.934	11.439	11.137	10.541
40%	14.307	12.827	13.161	12.021	12.051
50%	13.938	13.312	12.474	11.387	12.797
60%	14.421	12.987	12.523	12.858	12.82
70%	14.184	12.579	12.803	12.474	12.221
80%	14.688	13.17	11.662	12.518	13.407
90%	13.233	12.444	12.066	13.334	13.291

Table caption: The standard deviations in pixel values for the five ROIs in the ten optimized 4DCT phase images of the specified slice of the Catphan solid water module (CTP 486). The mean of measured noise values in all ten images is 12.10 ± 1.25 (again, error is one standard deviation).

Low Contrast Resolution

The effect of increased noise on low contrast resolution can be seen in Figure 4.10. When the contrast in an image is low, statistical variation in fluence collected by the detectors (i.e. from the x-ray's formation and interaction with the absorbing medium) can overwhelm subtle differences in fluence due to the attenuation properties of the object and its background. With the 3DCT imaging technique (Figure 4.10a), typically 4 or more of the 0.3 % nominal contrast plugs are distinguishable from the background. For the majority of slices in the clinical 4DCT phase images, however, only two or three of the largest 1 % nominal contrast inserts are discernable, and in some images, only the largest one. Going to the optimized 4DCT scan (Figure 4.10c), the low contrast resolution improves to a degree; the largest of the 0.3 % nominal contrast inserts is visible, yet, at the cost of tripling the delivered dose.

Figure 4.10: Low Contrast images acquired with clinical 3DCT, clinical 4DCT, and optimized 4DCT

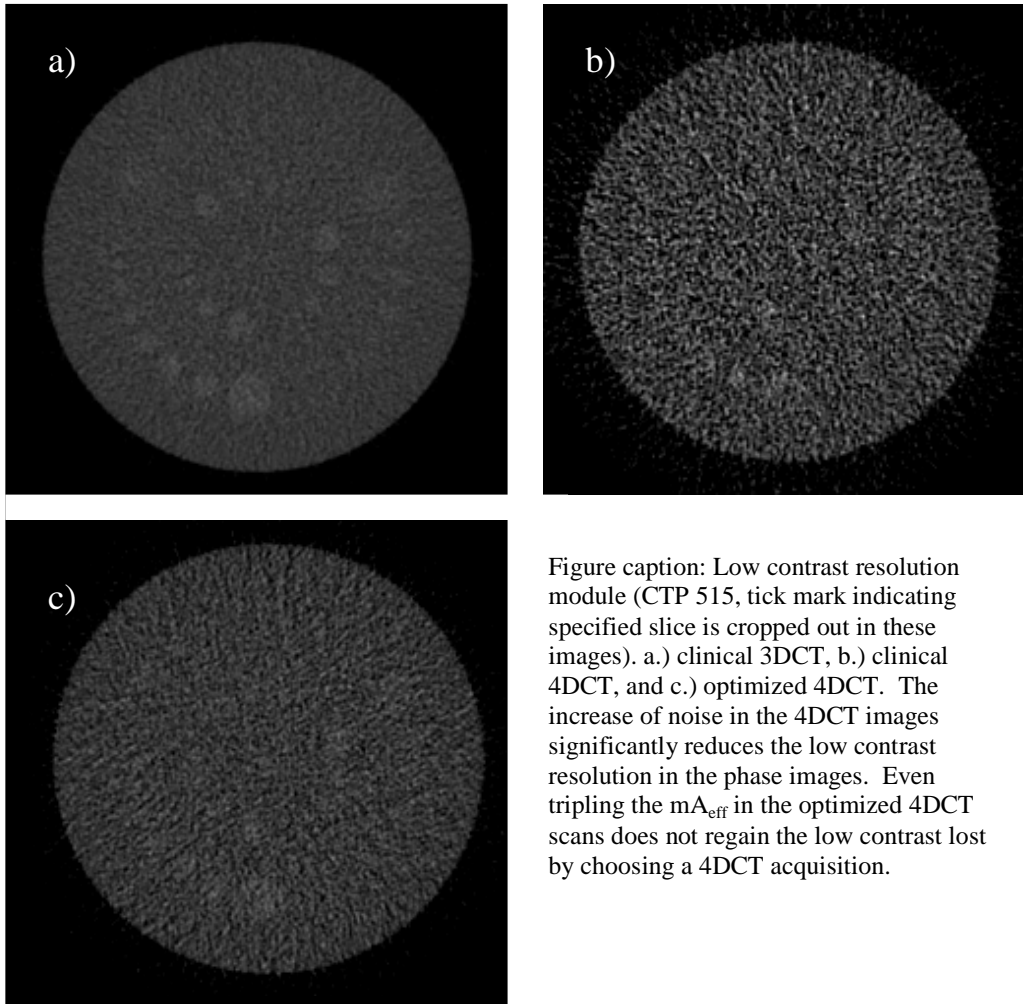


Figure caption: Low contrast resolution module (CTP 515, tick mark indicating specified slice is cropped out in these images). a.) clinical 3DCT, b.) clinical 4DCT, and c.) optimized 4DCT. The increase of noise in the 4DCT images significantly reduces the low contrast resolution in the phase images. Even tripling the mA_{eff} in the optimized 4DCT scans does not regain the low contrast lost by choosing a 4DCT acquisition.

High Contrast Resolution

The high contrast resolution Catphan inserts for the clinical 3DCT scan, clinical 4DCT scan, and optimized 4DCT scan are shown in Figure 4.11. The 6 lp/cm bar pattern is distinguishable in both the 3DCT and 4DCT clinical protocol scans. This is not surprising since high contrast resolution is determined by the system's MTF, not image noise_(156p2). Reducing the FOV with the optimized 4DCT scan allows the 7 lp/cm pattern to be resolved.

Figure 4.11: High Contrast images acquired with clinical 3DCT, clinical 4DCT, and optimized 4DCT

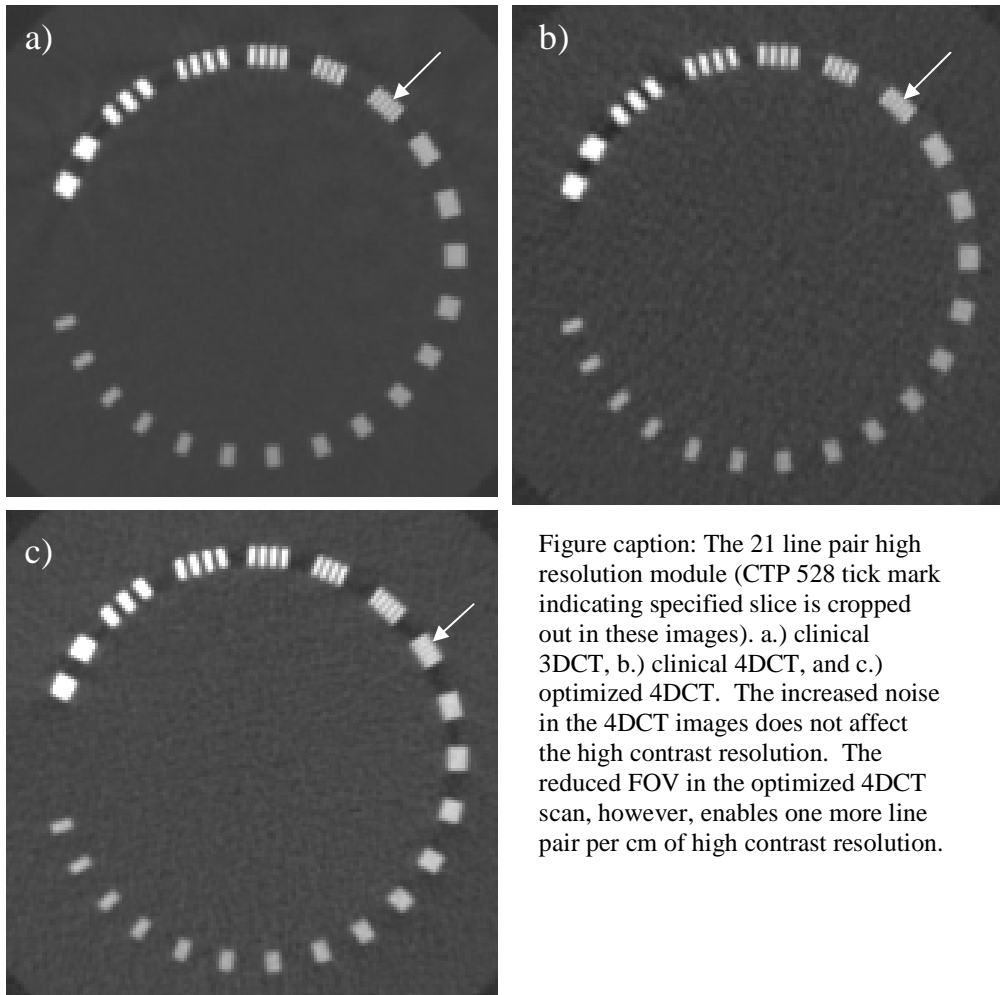


Figure caption: The 21 line pair high resolution module (CTP 528 tick mark indicating specified slice is cropped out in these images). a.) clinical 3DCT, b.) clinical 4DCT, and c.) optimized 4DCT. The increased noise in the 4DCT images does not affect the high contrast resolution. The reduced FOV in the optimized 4DCT scan, however, enables one more line pair per cm of high contrast resolution.

To investigate the high contrast resolution of a moving object, the small acrylic high contrast phantom is imaged with 4DCT while moving in the SI-AP-LR direction and line profiles through the hole patterns are compared to those from 3DCT images taken while the phantom is stationary. Figure 4.12 shows the static 3DCT image of the phantom as well as the line profiles through select high contrast hole patterns: the top row (3 mm holes with a 3 mm gap between them), the middle row (2 mm holes with a 2 mm gap), and the bottom row (1 mm holes with a 1 mm gap). For the 3DCT acquisition of the stationary phantom, the contrast calculated (Equation 4.4) from the 1mm hole pattern is 95 HU.

Figure 4.12: Line profiles through a small acrylic high contrast phantom imaged with 3DCT while stationary

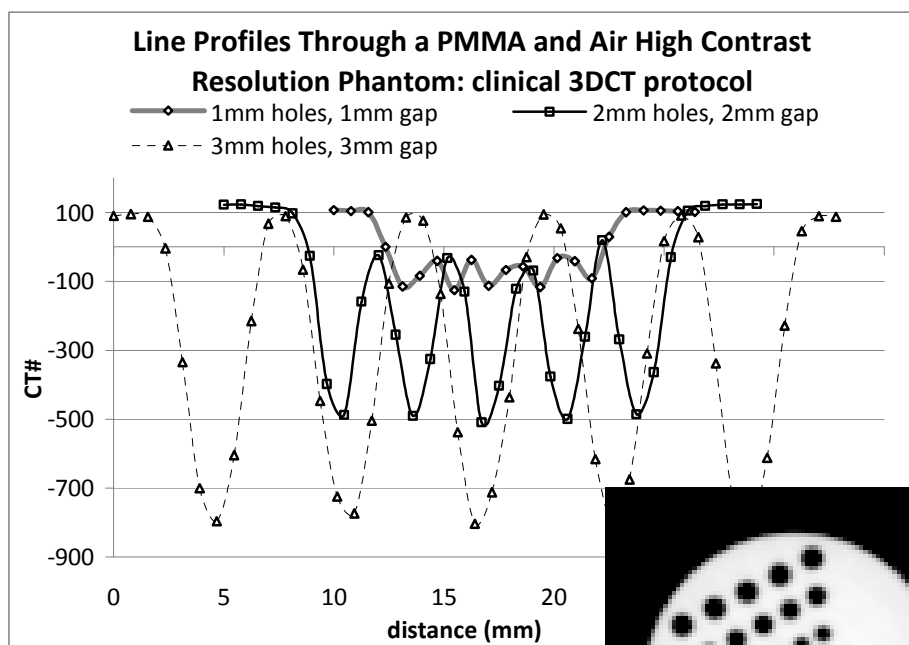


Figure caption: Line profiles through select high contrast test patterns, i.e. the top row (3 mm holes with a 3 mm gap between them), the middle row (2 mm holes with a 2 mm gap), and the bottom row (1 mm holes with a 1 mm gap). Also shown is the image from which these profiles were acquired

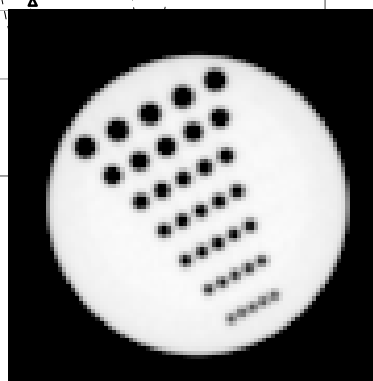


Figure 4.13 shows the equivalent graph from the same slice in the 80 % phase image of the dynamic 4DCT acquisition. The contrast calculated from the smallest hole pattern of this 4DCT phase image is 130 HU, 35 HU higher than for the static 3DCT image. The direction of the residual motion artifacts is different in each slice of the phase image, since this depends on the initial acquisition angle of the tube Φ_0 . In these experiments, Φ_0 is a random variable. Figure 4.14 shows three slices from the same 80% phase image (slice 2 is the same cross sectional image shown in Figure 4.14b.) Figure 4.15 gives the line profiles through the smallest hole pattern in each image shown in Figure 4.14. The measured contrasts in the smallest hole pattern for slices 1, 2, and 3 are 55 HU, 130 HU, and 136 HU, respectively. The residual motion artifacts in Slice 1 cut through the line patterns, and the measured contrast for this image is lower than what is seen in the static 3DCT image. Slices 2 and 3 are contiguous and their artifacts are nearly antiparallel. Notice in Figure 4.15 that the contrasts for slices 2 and 3 are similar but offset 50 HU from each other. Thus, not only can the high contrast be affected by residual motion artifacts, and so may be different for each slice of the phase image, it can be both higher and lower than what would be seen in a static 3DCT image.

Figure 4.13: Line profiles through a small acrylic high contrast phantom imaged with 4DCT while moving in the SI-AP-LR direction

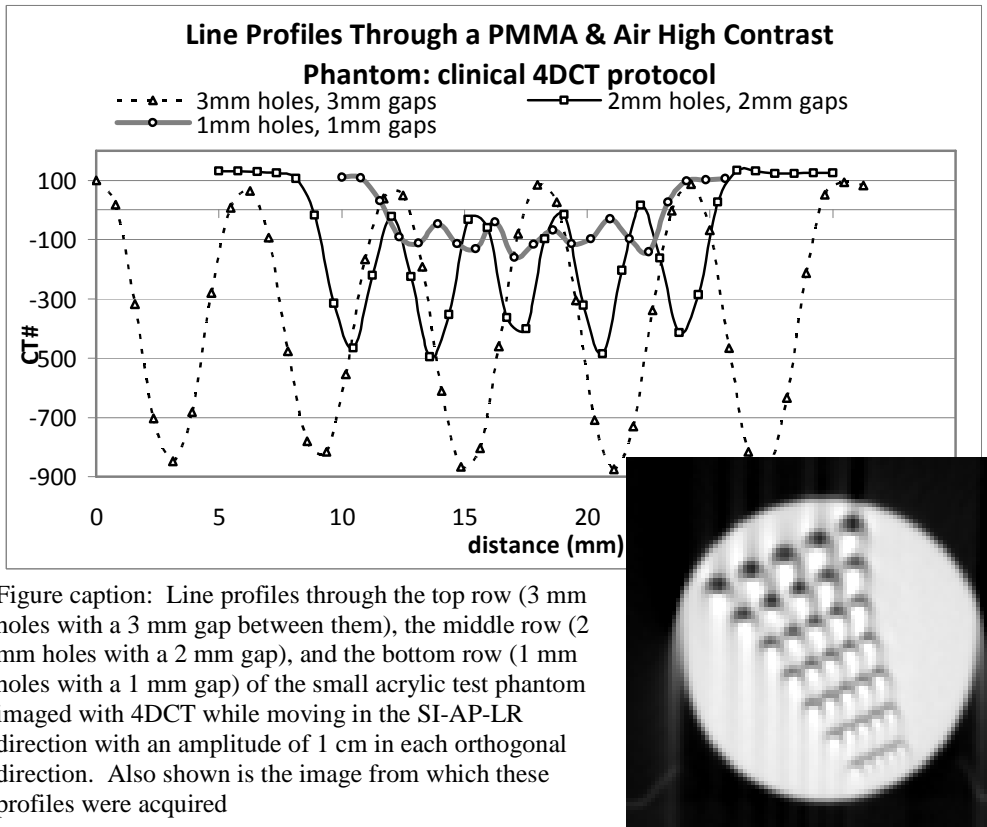


Figure 4.14: Three slices of a small acrylic high contrast phantom moving in the SI-AP-LR direction, imaged with 4DCT, 80% phase

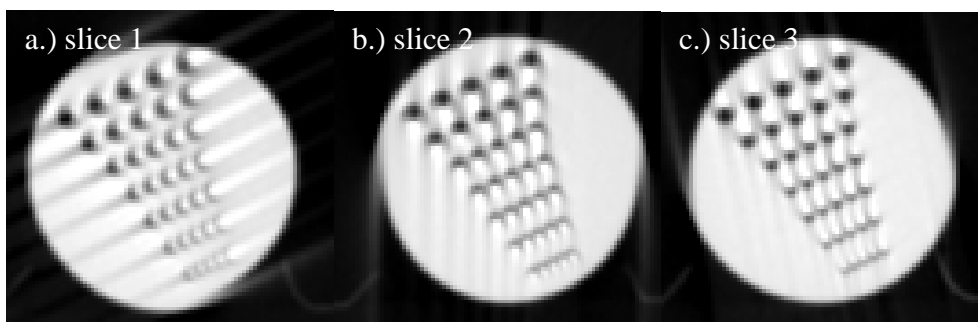


Figure 4.15: Line profiles through the smallest hole pattern of acrylic high contrast phantom undergoing motion in the SI-AP-LR direction, imaged with 4DCT: 3 slices from the same 4DCT phase image

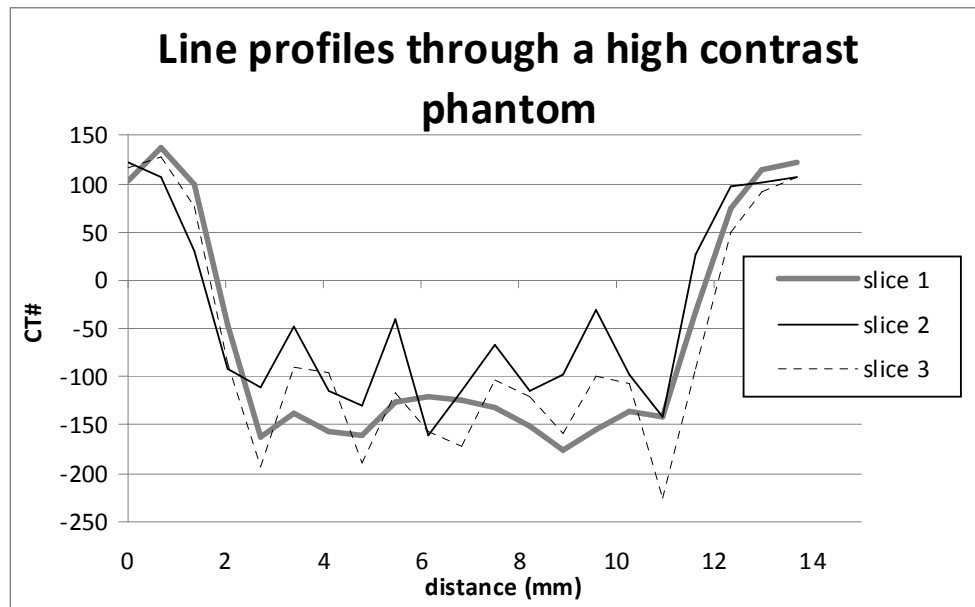


Figure caption: Line profiles through the smallest high contrast pattern of the small acrylic high contrast phantom imaged while moving in the SI-AP-LR direction with an amplitude of 1 cm in each orthogonal direction. All three cross sectional images are from different slices of the same 80% phase image of the 4DCT acquisition.

MTF

The MTFs of the clinical and optimized scans are shown in Figure 4.16. Both clinical scans are within acceptable tolerances (31p18-30). The clinical 4DCT MTF is slightly higher than that of the clinical 3DCT acquisition, but they are still within error of one another up until about 4 lp/cm. The optimized 3DCT and 4DCT scans are also within error of one another, and appear to give an advantage over both clinical scans at lower spatial frequencies, presumably due to the reduced FOV. The error bars on the 4DCT scans are slightly larger than on the clinical 3DCT.

Figure 4.16: The MTFs of the clinical 3DCT and 4DCT protocols, and the optimized 3DCT and 4DCT protocols.

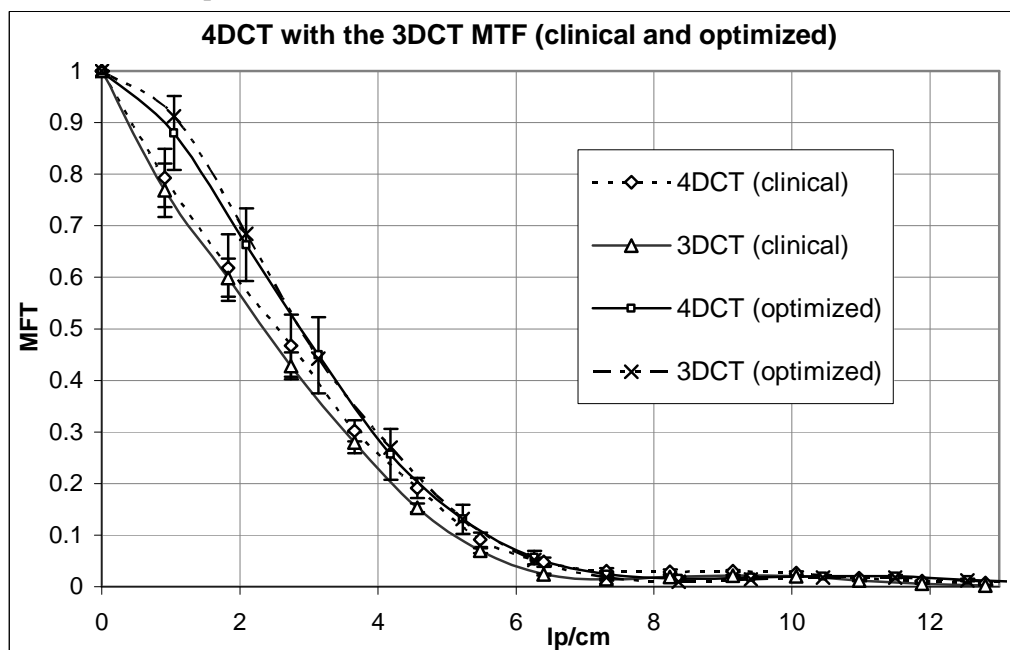


Figure caption: The MTFs of the clinical 3DCT and 4DCT scans are each averaged from 10 images. So is the optimized 4DCT MTF, however the optimized 3DCT MTF was taken from a single image, and thus has no error bars. (Acceptable is within 15 % of (1,0.9), (2,0.64), (3,0.34), (4,0.15), (5,0.05), (6,0.02), and (7,0) (31p18-30).)

Discussion of 4DCT Image Quality

To use 4DCT in treatment planning, the images must have sufficient high and low contrast resolution for delineation of targets and organs at risk as well as accurate electron densities for calculation of the delivered dose.

The accuracy and consistency of mean CT#s indicates that 4DCT phase images are appropriate for treatment planning. In a study by Goharian et al., a Catphan was placed on a moving platform, and the measured CT#s were found to be within $\pm 5\%$ of the those from static images (including polystyrene) (201). While most of the materials examined here are well within 5% of the static image values, the polystyrene is 6.6% off. With a nominal CT# of around -35 HU, differences of only a few HU are sufficient to exceed a 5% criteria. With the small Lexan cylinder (i.e. low density plastic, nominal CT# of ~ 120 HU) the differences in both the mean and median CT# for the clinical protocols, under all imaging conditions, are less than 2 HU, about 2.5%.

For CT, the predominant source of noise is statistical variation in the fluence of x-rays arising from their formation and subsequent interactions with the phantom and detectors (168)). To a much lesser extent, electronic noise in the projection data, which is relatively constant, also affects the image noise (157,147). Looking solely at a stationary object, the noise increased by 328% in the clinical 4DCT images compared to the standard clinical 3DCT scans. This increase can be explained by the decrease in exposure (i.e. mAs – the tube current times the rotation speed). The signal to noise ratio (SNR) squared is proportional to the dose, which is proportional to the exposure

$$\text{SNR}^2 \sim \text{dose} \sim \text{mAs}. \quad 4.4$$

(151p19). Since noise is the standard deviation of the signal σ , SNR is inversely proportional to σ , thus

$$\sigma^2 \sim 1/\text{dose}. \quad 4.5$$

The standard deviation of the 3DCT acquisitions signal σ_1 can be expressed as

$$\sigma_1 = k/\sqrt{(275 \text{ mA} * 1 \text{ s})} \quad 4.6$$

(where k is a constant of proportionality concerning spatial resolution (168p17)), and that of the 4DCT signal σ_2 as

$$\sigma_2 = k/\sqrt{(65 \text{ mA} * 0.5 \text{ s})}. \quad 4.7$$

The ratio of these predicts an increase in noise by a factor of 2.9 (i.e. $\sigma_2/\sigma_1 = \sqrt{(275/32.5)} = 2.9$. The constants, being equal, cancel). The measured increase of 3.3 ± 0.6 (the error derived using 1 standard deviation of collected values) is within error of the value predicted by the drop in exposure alone. Thus, even though both 3DCT and 4DCT scans show the same mAs_{eff} in the DICOM header, 4DCT images will, in general, be much noisier due to the reduced exposure. Since the mAs_{eff} is tripled in the optimized 4DCT acquisition, the expected increase in noise over the clinical 3DCT images is a factor of only 1.7 (i.e. $\sigma_2/\sigma_1 = \sqrt{(275/97)}$; the measured noise increase is 2.0 ± 0.4 . The increased noise of 4DCT is the primary cause of the broadening in the CT# distributions for the 4DCT acquisitions seen in Figures 4.7 and 4.8, as well as the slight shift in mean and median CT#s to higher values for the stationary 4DCT acquisitions. However, the reconstruction algorithm's effect on the images CT#s cannot be discounted entirely.²⁸

Although the increase in noise going from a 3DCT to a 4DCT acquisition can be attributed to exposure differences between the 3DCT and 4DCT images (i.e. 4DCT utilizes fewer x-rays per image), the reconstruction algorithm can also affect the noise (157), and the exact nature of both algorithms is unknown. Goldman claims that pitch does not affect noise in helical multislice CT (147), however, Flohr shows that noise increases ever so slightly as pitch is decreased (169). Neither paper addresses the n-PI method specifically—thus, without undertaking a specific experiment, it is difficult to say whether the extremely low pitch of the 4DCT protocol contributes to either the noise itself or the observed variation in noise from phase image to phase image.

The exposure in 4DCT images is reduced in order for the tube to withstand extended scan times and to prevent an exorbitant dose to the patient (32,63). Although

²⁸ From Table 5.6, the CT# distributions for the dynamic 4DCT acquisitions span a smaller range of values and have a smaller FWHM than the 4DCT acquisitions taken while the object is at rest. If you recall Figure 4.10 and the patchwork-like reconstruction choices of the Philips 4DCT reconstruction algorithm, you will notice that not all slices are treated equally; only some cross sectional images appear to have data patched in from other slices. It is clear that the algorithm is making some complex choices as to when (and possibly how) to alter the data in a given cross sectional image. Most likely, these decisions are based on the significance of residual motion artifacts found in that slice. Thus, since the 4DCT acquisition of the stationary object contains no residual motion artifacts, the algorithm is not altering the data to the extent that it is for the 4DCT acquisition of the moving cylinder. When the algorithm includes data from other slices, it increases the SNR of the cross sectional image; thus we see dynamic 4DCT images have a tighter CT# distributions.

the tube rotates around the same slice location for approximately 4 s, not all the exposure to that slice location (i.e. mA_{eff}) goes into the formation of that cross sectional image. In a study by Vedam et al., the tube current was reduced to 100 mA without any noticeable effect on noise, although the author admits that no noise evaluation was performed (32). However, this problem of increased noise due to decreased tube current is known. A study by Dinkle et al. reports no pattern of increased noise in any particular phase of the 4DCT image sets (157).

Low contrast resolution is dominated by image noise (168), and although the loss of low contrast with 4DCT is dramatic, the aeration of lung tissues even at end exhale gives CT high contrast in that region. When the tumor is not surrounded by low density tissue but attached or adjacent to other structures of similar density, such as the chest wall or the mediastinum, delineation is difficult. Even with the low contrast resolution provided by clinical 3DCT, either PET information or an additional CT with contrast is often required to improve delineation. Registration of 4DCT with PET images (4DPET (63,170)) using intensity-based methods has been shown to improve low contrast resolution and increase SNR of the resulting images (171).

High contrast resolution in CT is not particularly sensitive to noise, nor is the system's MTF. Both are primarily influenced by CT resolution. Thus, it is not surprising that high contrast resolution and MTFs for both 3DCT and 4DCT image acquisitions are nearly identical—the focal spot size, detected aperture, the number of radial detectors, filter function, pixel size, and number of projections (156p2) are the same for both acquisitions. With the reduced FOV of the optimized 4DCT scans, an additional line pair per millimeter is resolved, exceeding the high contrast resolution of the clinical 3DCT scan. Yet, despite minor improvements in low contrast resolution attained by tripling effective exposure, it is difficult to justify the likewise increase in patient dose which would result clinically, particularly as low kV radiation is becoming recognized as a significant source of radiation to the public (172). The effect of residual motion artifacts on high contrast resolution may be problematic, especially for intensity based deformable registration methods which are sensitive to image quality (173).

Summary and Conclusion of 4DCT Image Quality

Each CT manufacturer supporting 4DCT provides its own proprietary software, and multiple options exist for acquiring the respiratory signal (31,45,46). Thus, each 4DCT system must be individually assessed for accuracy before it may be used in RT treatment planning (47). An evaluation of image quality for the 4DCT capabilities of the Philips' Brilliance Big Bore imaging system are performed with the Varian Real-Time Position Management (RPM) Respiratory Gating System. Measurements of image noise, CT#, and modulation transfer function (MTF), as well as a qualitative analysis of high and low contrast in 4DCT images, are compared with those of standard clinical non-temporally correlated CT scans (i.e. 3DCT images).

The accuracy and consistency of mean CT#s in 4DCT phase images indicate that 4DCT is an appropriate technique for treatment planning. For stationary objects, the mean CT#s did not differ from those in 3DCT acquisitions by more than 6.61%. For an object with similar density to tissue, moving in the SI-AP-LR direction with an amplitude of 1 cm in each orthogonal direction, the mean CT# of all ten phases of the 4DCT acquisition is only 0.8 HU lower than the average of ten 3DCT images acquired while the object is stationary.

An increase in noise of 328 % due to decreased tube current significantly affects the low contrast resolution in the 4DCT phase images. However, the aeration of lung tissues even at end exhale enables sufficient contrast in the thoracic region. In the

absence of residual motion artifacts, the high contrast resolution and MTF of 3DCT and 4DCT acquisitions are nearly identical. Yet, residual motion artifacts can alter high contrast regions, causing the high contrast resolution to vary from slice to slice in 4DCT phase images.

Chapter 5: Summary and Conclusion

Summary of Results

Four dimensional computed tomography (4DCT) addresses many of the issues associated with respiratory motion in target delineation; it uses a fast tube rotation to minimize motion artifacts (32,33) and provides spatiotemporally resolved volumes to reveal the presence and extent of target motion. Yet, each 4DCT system must be individually assessed for accuracy prior to its use in RT treatment planning (47). Here, a Philips Brilliance 16 slice CT scanner and two respiratory monitoring systems (i.e. the Philips Bellows and Varian's Real-Time Position Management (RPM) Respiratory Gating System) are quantitatively evaluated for geometric accuracy. A mechanical phantom imparts clinically relevant motions to acrylic spheres of various diameters, and five metrics of evaluation are computed. The *% volume difference* indicates the accuracy of the 4DCT system in representing the true size of moving objects, *mean eccentricity* evaluates shape representation in 4DCT images, and *center to center distance* and *maximum distance to agreement* measure the system's ability to track and localize mobile volumes, respectively. The fifth metric, the *coincidence index*, is a single score representing the system's overall ability to capture the true size, shape, and position of mobile targets.

The *% volume difference* is sensitive to sphere size. In general, larger volumes are rendered more accurately due to the greater number of voxels involved. In general, the relative impact of residual motion artifacts diminishes as target sizes increase. Type of motion and phase of motion also affect the *% volume difference* according to the form and extent of motion specific artifacts. *Mean eccentricity* is also affected by size, phase, and type of motion in a similar manner to *% volume difference*; also, a clear dependency on amplitude is also observed. *Center to center distance* proves insensitive to sphere size and type of motion, however, the speed of the sphere affects this location measurement as evidenced by both its amplitude and phase dependency. *Maximum distance to agreement* shows a clear dependence on phase, and the *coincidence index* only exhibits a clear dependence on sphere size and the phase of motion.

Differences between true and segmented volumes for the 1cm sphere do not exceed 8 %, (mean 1.3 % too small with a standard deviation of 2.3 %). For the 3 and 5 cm spheres, the combined average volumetric difference is only 0.22 % with a standard deviation of 0.55 %. The average *mean eccentricity* for the 1 cm sphere is 0.31, and for the 3 and 5 cm sphere data combined it is 0.18. For all sphere sizes, types of motion, and amplitudes of motion, the average tracking performance of the 4DCT system yields a *center to center distance* of 0.6 ± 0.4 mm. Localization, as expressed in the *maximum distance to agreement* metric is accurate, on average, to 1.2 ± 0.4 mm. For the *coincidence index*, the highest score attained by the 1 cm sphere is 0.74 out of a perfect 1.0. On average, the 4DCT system produces a *coincidence index* of only 0.62 ± 0.06 for the 1 cm sphere. However, for the 3 and 5 cm sphere data combined, the average index is 0.89 ± 0.02 .

In order to evaluate the image quality of 4DCT acquisitions, measurements of image noise, CT#, and modulation transfer function (MTF), as well as a qualitative analysis of high and low contrast are compared with those of a standard clinical 3DCT scan. The 4DCT image acquisitions differ from 3DCT in pitch, tube current, and tube rotation speed. For stationary objects, the mean CT#s do not differ from those in 3DCT acquisitions by more than just a few HU; the largest measured discrepancy is 6.61 % for polystyrene (nominal CT# of -35 HU). For a roughly tissue equivalent density object moving in the SI-AP-LR directions with an amplitude of 1 cm in each orthogonal direction, the mean CT# of ten phase images acquired from a single 4DCT acquisition is only 0.8 HU lower than the average of ten 3DCT images acquired while the object is stationary. An increase in noise by 328 % due to decreased tube current significantly affects low contrast resolution in the 4DCT phase images. In the absence of residual motion artifacts, the high contrast resolution and MTF of 3DCT and 4DCT acquisitions are nearly identical. Yet, residual motion artifacts can alter high contrast regions, causing contrast in 4DCT phase images to vary from slice to slice.

Clinical Implications

The image quality of the Philips 4DCT thoracic imaging protocol is clinically acceptable, as one might hope from any Philips protocol. Mean CT#s in both stationary and mobile objects imaged with 4DCT are within a few Hounsfield units of those measured from the same objects imaged while stationary with 3DCT. As such, any quantitative CT# measurements from 4DCT images for treatment planning purposes will fall under the same calibrations parameters as for standard clinical 3DCT images. Modulation transfer function and high contrast resolution are nearly identical for both protocols. Noise in 4DCT images, however, is greatly increased due to the reduced tube current. As a result, low contrast resolution suffers serious deterioration from what is seen in clinical thoracic 3DCT images. Even so, aeration of lung tissues can still provide sufficient high contrast for delineation when tumors are completely surrounded by healthy lung; as well, contrast enhanced CT is routinely utilized for delineation when necessary. Residual motion artifacts can alter contrast in 4DCT images, and so, automatic segmentation algorithms which are sensitive to image quality and high contrast in particular, may require additional supervision. Here at the Cross Cancer Institute, automatic contouring with the Eclipse treatment planning system (version 8.6, Varian Medical Systems, Palo Alto, CA) reliably delineates only body contours and lung volumes (i.e. tissue/air interfaces)—its application to other structures, including bony anatomy, is problematic at best, often requiring considerable manual editing. At worst, this state of the art planning system completely fails to produce useful structure delineation. Thus, at the Cross Cancer Institute, all tumors are manually contoured by radiation oncologists based upon their personal medical expertise. The impracticality of manually delineating every organ in every phase, however, is a major hindrance to attaining full utilization of 4DCT's potential. The results of this investigation suggest that, in high contrast situations such as a tumor completely surrounded by aerated lung tissue, automatic threshold segmentation of 4DCT images using local contrast levels of 40 - 45 % may yield target volumes sufficiently accurate for radiotherapy treatment planning. Of course, this hypothesis must be tested using real patient data prior to clinical implementation of any such technique.

From the data presented in this thesis, it is evident that 4DCT, using the Philips big bore CT in conjunction with either the Philips Bellows or Varian RPM respiratory monitoring systems, is capable of tracking mobile acrylic spheres in air to a high degree

of accuracy. This high contrast scenario corresponds well to the clinical situation in which mobile tumors are fully circumscribed by lung. Any departure from high contrast geometry could prove problematic, however, particularly as uncertainties in differentiation between diseased and healthy tissue under low contrast conditions may be exacerbated by significant noise increases in 4DCT images.

Volume delineation of mobile targets imaged with 4DCT is less accurate than when the same objects are imaged while stationary with 3DCT, which can only be expected from motion artifacts in CT. Still, the 0.5 s tube rotation provides a temporal resolution of $\frac{1}{4}$ second, minimizing the extent of residual motion artifacts which lead to volume discrepancies. In moving from stationary 3DCT to dynamic 4DCT, the mean volumetric error increases 0.12 % for the 3 and 5 cm sphere combined data (i.e. % *volume difference* of 0.1 % with static 3DCT and 0.22 % with dynamic 4DCT). For the 1 cm sphere, the mean volumetric error increases by only about 0.24 % in going from 3D static to 4D dynamic scanning. Considering that a single voxel (i.e. $0.78 \times 0.78 \times 2.0 \text{ mm}^3 = 1.2 \text{ mm}^3$) constitutes 0.23 % of the entire 1cm sphere's volume, these differences are relatively insignificant. Greater disparity between dynamic 4DCT and static 3DCT imaging arises with regard to rendered shape. Under dynamic conditions, 4DCT images of the 1 cm sphere yield *mean eccentricity* values 0.04 higher than what is measured from static 3DCT images, and 0.08 larger for the 3 and 5 cm sphere combined data. With both volume and shape rendering, the larger spheres suffer less absolute deformation in dynamic 4DCT imaging but more relative deformation in moving from stationary 3DCT to dynamic 4DCT, indicating that resolution uncertainties, which are identical for both imaging modalities, dominate for smaller objects. If residual motion artifacts are still a concern, Philips also offers a 0.44 s tube rotation speed.

Perhaps a more clinically relevant measure of quantitative accuracy is provided by the *maximum distance to agreement* and *coincidence index* metrics. The *coincidence index* indicates the degree of overlap observed between the volume rendered by 4DCT and that expected based on the known shape, size, and motion of the objects in question. For the 1cm sphere, the *coincidence index* ranges from 0.5 to 0.74, translating into overlaps of 66.7 % and 85.1 %, respectively. These numbers result from surface to surface disagreements between the imaged and known spheres as indicated by the *maximum distance to agreement* metric (i.e. in this instance: between 0.5 and 2.0 mm). Here at The Cross Cancer Institute, standard clinical practice results in 5 - 15 mm margins around the GTV in order to produce a PTV for treatment planning. Such margins will readily compensate for errors in delineation resulting from residual motion artifacts in 4DCT images. Depending on the demands of a given treatment plan, however, a phase dependent GTV margin may be warranted in order to convert the segmented image of the tumor into a volume more certain to contain the physical GTV. For those phases corresponding to rapid tumor movement, a uniform GTV margin of 2.6 mm may be reasonably suggested by the results of this investigation. A perusal of Table 3.11 is recommended prior to selection of any such margin, however, as both size and amplitude of motion affect the maximum observed surface to surface discrepancies. Also, adding a uniform margin of 2.0 mm around the segmented image of a 1 cm sphere, for instance, may create a volume that circumscribes the actual object, but may not necessarily improve the *coincidence index* score, which ranks the amount of healthy tissue contained within the GTV equally with the amount of diseased tissue neglected. Analysis of how added margins affect the *coincidence index* would be a useful tool in evaluating margin schemes devised from 4DCT images. In general, delineation errors implied from the *maximum distances to agreement* metric are smaller for phases with little or no residual motion (e.g. at or near end inhale and end exhale). For the end inhale

and end exhale phases, the required GTV margin would be of such a diminutive size that it may be safely ignored.

Future Work

While the process of acquiring 4DCT images is nearing maturity, there may, however, be some room for development of motion optimized CT filter functions. Clinically, recommended 4DCT protocols should be further investigated for optimization. Breath coaching programs, with multiple modalities of communicating with patients require development and implementation. Given that any phase offset between target and external respiratory signal is problematic, attempts at novel methods of acquiring a reliable respiratory trace from the target itself are warranted.

In post processing, there is still much work to be done on noise in 4DCT images. The SNR can be increased by registering different phase images together (63) –no paltry task depending on the extent of motion and deformation in the different phase images. As well, registration of 4DCT images to other imaging modalities (e.g. 4DPET, 4DMRI) has the potential to significantly improve their therapeutic utility. A wealth of precious patient specific data rests within 4DCT images, yet, in order to make full utilization of this information clinically viable, reliable automated segmentation algorithms need development to efficiently and accurately delineated the target as well as critical organs in each phase image.

Application of 4DCT data to predictive algorithms could help facilitate the future of IGRT. Patient specific tracking algorithms to maintain target recognition and to compensate for mechanical lag time could be constructed from 4DCT data. In addition, for non-gated treatments utilizing IMRT, algorithms to interpolate anatomy between phase images are required. Depending on the selected treatment option and the performance of each 4DCT system, determination of 4DCT margins may be necessary. Undoubtedly, new and imaginative ways of utilizing the patient specific spatiotemporal resolution of 4DCT have yet to be discovered. The geometric accuracy of the Philips/Bellows and Philips/Varian RPM systems suggests the technique is appropriate for implementation in a variety of research projects, such as 4D Monte Carlo inverse treatment planning or the identification of appropriate margins to account for sorting errors and intra-fraction variability due to inconsistent patient breathing.

Conclusion

The geometric precision of the Philips Big Bore 4DCT imaging system with both Philips Bellows and Varian RPM respiratory monitoring systems, as well as the accuracy and consistency of mean CT#s in 4DCT phase images, indicate that 4DCT is an appropriate imaging technique for treatment planning. Having 4DCT capabilities at The Cross Cancer Institute will enable more patient appropriate margins and a wider selection of treatment options for patients, as well as open the door to advanced research in four dimensional radiation therapy techniques.

Bibliography

1. P. J. Keall, G. S. Mageras, J. M. Balter, R. S. Emery, K. M. Forster, S. B. Jiang, J. M. Kapatoes, K. A. Low, M. J. Murphy, B. R. Murray, C. R. Ramsey, M. B. van Herk, S. S. Vedam, J. W. Wong, and E. Yorke, "The management of respiratory motion in radiation oncology report: AAPM Task Group 76", Med. Phys. 33(10), October 2006
2. E. Rietzel, T. Pan, and G. Chen, "Four-dimensional computed tomography: Image formation and clinical protocol", Med. Phys. 32(4), 874-889 (2005)
3. G. T. Y. Chen, J. H. Kung, and K. P. Beaudette, "Artifacts in computed tomography scanning of moving objects", Seminars in Radiation Oncology 14(1), 19-26 (January 2004)
4. M. van Herk, "Errors and Margins, in Radiotherapy", Seminars in Radiation Oncology 14(1), 52-64 (January 2004)
5. M. Witte, J. van der Geer, C. Schneider, J. Lebesque, and M van Herk, "The effects of target size and tissue density on the minimum margin required for random errors", Med. Phys. 31(11), (November 2004)
6. J. van Meerbeeck, S. Meersschout, R. De Pauw, I. Madani, W. De Neve, "Modern radiotherapy as part of combined modality treatment in locally advanced non-small cell lung cancer: Present status and future prospects", The Oncologist 13, 700-708 (2008)
7. S. Senan, D. Ruyscher, P. Giraud, R. Mirimanoff, and V. Budach, "Literature-based recommendation for treatment planning execution in high-dose radiotherapy for lung cancer", Radiother. Oncol. 71(2), 139-146 (2004)
8. J. Wolthaus, J. Sonke, M. van Herk, S. Belderbos, M. Rossi, J. Lebesque, and E. Damen, "Comparison of different strategies to use four-dimensional computed tomography in treatment planning for lung cancer patients", Int. J. Radiat. Oncol. Biol. Phys. 70(4), 1229-1238 (2008)
9. S. Novello, and T. Le Chevalier, "Chemotherapy for non-small cell lung cancer: Part 1. Early Stage Disease", Oncology 17, 357-363 (2003)
10. G. Sibley, "Radiotherapy for patients with medically inoperable stage I non-small cell lung carcinoma", Cancer 82(3), 433-438 (1998)
11. A. Jemal, R. Siegal, E. Ward, Y. Hao, J. Xu, T. Murray, and M. J. Thun, "Cancer Statistics, 2008", CA: A Cancer Journal for Clinicians 58, 71-96 (2008)
12. Canadian Cancer Society/National Cancer Institute of Canada: "Canadian Cancer Statistics 2008", Toronto, Canada, 2008." April 2008, ISSN 0835-2976

13. T. Pan, T. Lee, E. Rietzel, and G. T. Y. Chen, "4D CT Imaging of a volume influenced by Respiratory Motion on Multi-slice CT", Med. Phys. 31 (2), (February 2004)
14. W. Smythe, "Treatment of Stage I and II Non-small-cell lung cancer: Surgery for stage I and II NSCLC as "Standard of Care", Cancer Control 8(4), 318-325 (2001)
15. I. Unlu, G. Diniz, B. Komurcuoglu, M. Gayaf, T. Gokce, I. Karadogan, C. Akcay, "Comparison of curative and palliative radiotherapy efficacy in unresectable advanced non-small cell lung cancer patients with or without metastasis", Saudi Medical Journal 27(6), (January 2006)
16. C. W. Stevens, R. F. Munden, K. M. Forster, J. F. Kelly, Z. Liao, G. Starkschall, S. Tucker, and R. Komaki, "Respiratory-driven lung tumor motion is independent of tumor size, tumor location, and pulmonary function", Int. J. Radiation Oncology Biol. Phys. 51(1), 62-68 (2001)
17. S. Kwa, J. Lebesque, J. Theuws, L. Marks, M. Munley, G. Bentel, K. Oetzel, U. Spahn, M. Graham, R. Drzymala, J. Purdy, Al Lichter, M. Martel, and R. Ten Haken, "Radiation pneumonitis as a function of mean lung dose: an analysis of pooled data of 540 patients", Int. J. Radiation Oncology Biol. Phys. 42(1), 1-9 (1998)
18. D. Oetzel, P. Schraube, F. Hensley, G. Sroka-Perez, M. Menke, and M. Flentje, "Estimation of pneumonitis risk in three-dimensional treatment planning using dose-volume histogram analysis", Int. J. Radiation Oncology Biol. Phys. 33(2), 455-460 (1995)
19. M. Graham, J. Purdy, B. Emami, W. Harms, W. Bosch, M. Lockett, and C. Perez, "Clinical dose-volume histogram analysis for pneumonitis after 3D treatment for non-small cell lung cancer (NSCLC)", Int. J. Radiation Oncology Biol. Phys. 45(2), 323-329 (1999)
20. S. Erridge, Y. Seppenwoolde, S. Muller, M. van Herk, K. De Jaeger, J. Belderbos, L. Boersma, J. Lebesque, "Portal imaging to assess set-up errors, tumor motion and tumor shrinkage during conformal radiotherapy of non-small cell lung cancer", Radiotherapy and oncology : Journal of the European Society for Therapeutic Radiology and Oncology 66(1), 75-85 (2003)
21. S. Vedam, P. Keall, V. Kini, and R. Mohan, "Determining parameters for respiration-gated radiotherapy", Med Phys 28(10), 2139-2146 (2001)
22. S. Vedam, V. Kini, P. Keall, V. Ramakrishnan, H. Mostafavi, and R. Mohan, "Quantifying the predictability of diaphragm motion during respiration with a noninvasive external marker", Med. Phys. 30(4), 505-513 (2003)
23. Y. Seppenwoolde, H. Shirato, K. Kitamura, S. Shimizu, M. van Herk, J. Lebesque, and K. Miyasaka, "Precise and real-time measurement for 3D tumor motion in lung due to Breathing and heartbeat, measured during radiotherapy", Int. J. Radiation Oncology Biol. Phys. 53(4), 882-834 (2002)

24. H. Liu, N. Koch, G. Starkschall, M. Jacobson, K. Forster, Z. Liao, R. Komaki, and C. Stevens, "Evaluation of internal lung motion for respiratory-gated radiotherapy using MRI: Part II – margin reduction on internal target volume", Int. J. Radiation Oncology Biol. Phys. 60(5), 1473-1483 (2004)
25. J.Cai, G. Miller, T. Altes, P. Read, S. Benedict, E. Lange, G. Cates, J. Brookeman, J. Mugler, and K. ShengK "Direct measurement of lung motion using hyperpolarized Helium-3 MR tagging", Int. J. Radiat. Oncol. Biol. Phys. 68(3), 650-653 (2007)
26. S. Shimizu, H. Shirato, S. Ogura, H. Akita-Dosaka, K.Kitamura, T. Nishioka, K. Kagei, M. Nishimura. K. Miyasaka, "Detection of lung tumor movement in real-time tumor-tracking radiotherapy", Int. J. Radiat. Oncol. Biol. Phys. 51(2), 304-310 (2001)
27. E. Weiss, K. Wijesooriya, V. Dill, and P. Keal. "Tumor and normal tissue motion in the thorax during respiration: analysis of volumetric and positional variation using 4D CT", Int. J. Radiat. Oncol. Biol. Phys. 67(1), 296-307 (2007)
28. C. Plathow, S. Ley, C. Fink, M. Puderbach, W. Hosch A. Schmahl, J. Debus, and H. Kauczor, "Analysis of intrathoracic tumor mobility during whole breathing cycle by dynamic MRI", Int. J. Radiat. Oncol. Biol. Phys. 59(4), 952-959 (2004)
29. C. Ross, D. Hussey, E. Pennington, W. Stanford, J. Doornbos, "Analysis of movement of intrathoracic neoplasms using ultrafast computerized tomography", Int. J. Radiat. Oncol. Biol. Phys. 18(3), 671-677 (1990)
30. R. George, S. Vedam, T. Chung, V. Ramakrishnan, and P. Keall, "The application of the sinusoidal model to lung cancer patient respiratory motion", Med. Phys. 32(9), 2139-2146 (2005)
31. Instructions for use--Brilliance CT, big bore configuration, Vol 1, Philips Medical Systems 4535 673 85451
32. S. S. Vedam, P. J. Keall, V. R. Kini, H. Mostafavi, H. P. Shukla, and R. Mohan, "Acquiring a Four-Dimensional Computed Tomography Dataset Using an External Respiratory Signal", Phys. Med. Biol. 48, 45- 62 (2003)
33. I. Gagné, and D. Robinson, "The impact of tumor motion upon CT imaged integrity and target delineation", Med. Phys. 31(2), 3378-3392 (2004)
34. L. Archambault, S. Vedam, G. Starkschall, R. Mohan, and S. Beddar, "Determination of Prospective Displacement Gate Threshold for Respiratory-Gated Radiation Delivery From Retrospective Phase-Based Gate Threshold Selected at 4D CT Simulation", Med. Phys. 34(6), 2546-2546 (2007)
35. L. Ekberg, O. Holmberg. L. Wittgren, G. Bjelkengren, and T. Landberg, "What margins should be added to the clinical target volume in radiotherapy treatment planning for lung cancer?", Radiotherapy and Oncology 48, 71-77 (1998)

36. C. Ramsey, I. Cordrey, and A. Oliver "A comparison of beam characteristics for gated and non-gated clinical x-ray beams", Med Phys 26(10), 2086-2091 (1999)
37. J. Hayman, M. Martel, R. Ten Haken, P. Normolle, R. Todd III, J. Littles, M. Sullivan, P. Possert, T. Turrisi, and A. Litcher, "Dose Escalation in Non-Small-Cell Lung Cancer Using Three-Dimensional Conformal Radiation Therapy: Update of a Phase I Trial", Journal of Clinical Oncology 19(1), 127-136 (2001)
38. www.medicaldosimetry.org/meetings/2008handouts/S-2keskemety.pdf
39. P. J. Keall, G. Starkschall, H. Shukla, K. M. Forster, V. Ortiz, C. W. Stevens, S. S. Vedam, R. George, T. Guerrero, and R. Mohan, "Acquiring 4D Thoracic CT Scans Using a Multislice Helical Method", Phys. Med. Biol. 49, 2053-2067 (2004)
40. M. Nakamura, Y. Narita, Y. Matsuo, M. Narabayashi, M Nakata, S. Yano, Y. Miyabe, K. Matsugi, A. Sawada, Y. Norihisa, T. Mizowaki, Y. Nagata, and M. Hiraoka "Geometrical differences in target volumes between slow CT and 4DCT imaging in stereotactic body radiotherapy for lung tumors in the upper and middle lobe", Med. Phys. 35(9), 4142-4148 (2008)
41. K. Wijesooriya, C. Bartee, J. Siebers, S. Vedam, and P. Keall, "Determination of maximum leaf velocity and acceleration of a dynamic multileaf collimator: Implications for 4D radiotherapy", Med. Phys. 32(4), 932-941
42. S. Vedam, A. Docef, D. Todor, and V. Kini, "Predicting respiratory motion for four-dimensional radiotherapy", Med. Phys. 31(8), 2274-2283 (2004)
43. D. Pokhrel, and M. Murphy, "Characterization of the Stability of Respiration for Patients Undergoing Motion Adaptive Lung Tumor Radiotherapy," Med. Phys. 34(6), 2368-2368 (2007)
44. X. A. Li and P. J. Keall, Moderator: C. G. Orton, "Respiratory Gating for Radiation Therapy is Not Ready for Prime Time", Med. Phys. 34(3), (March 2007)
45. Instructions for use--RPM Respiratory Gating System, Version 1.7, Varian Medical System P/N 100025304-01
46. G. Mageras and E. Yorke, "Deep inspiration breath hold and respiratory gating strategies for reducing organ motion in radiation treatment", Seminars in radiation oncology 14(1), 65-75 (January 2004)
47. R. Liu, K. Rado, R. Wu, D. Stevens, T. Pan, and D. Cody, "Optimal CT imaging Protocol Settings for CT Simulators", Med. Phys. 34(6), 2344-2344 (2007)
48. A. Myers, "Crash Course: Respiratory System", Elsevier-Mosby 2006, 1600 J.F.K. Blvd, Ste 1800, Philadelphia, PA 19103-2899, Editor: P. McGowan

49. H. Alasti, Y. B. Cho, A. D. Vandermeer, A. Abbas, B. Norrlinger, S. Shubbra, and A. Bezjak, "A Novel Four-Dimensional Radiotherapy Method For Lung Cancer: Imaging, Treatment Planning and Delivery", Phys. Med. Biol. 51, 3251-3267 (2006)
50. E. D. Brandner, D. Heron, A. Wu, M. S. Huq, N. J. Yue, and H. Chen, "Localizing Moving Targets and Organs Using Motion-Managed CTs", Medical Dosimetry 31(2), 134-140 (2006)
51. <http://www.cancer.gov/cancertopics/pdq/prevention/lung/HealthProfessional>
52. <http://www.cancer.gov/cancertopics/pdq/treatment/small-cell-lung/HealthProfessional/page2>
53. W. Anderson, J. McAleer, S. Stranex, and G. Prescott, "Radical radiotherapy for inoperable non-small cell lung cancer: What factors predict prognosis?", Clinical Oncology 12, 48-52 (2000)
54. A. Allen, K. Siracuse, J. Hyman, and J. Balter, "Evaluation of the influence of breathing on the movement and modeling of lung tumors", Int. J. Radiat. Oncol. Biol. Phys. 58(4), 1251-1257 (2004)
55. J. Laskin, S. Erridge, A. Coldman, Y. D'yachkova, C. Speers, V. Westeel, G. Hislop, I. Olivotto and N. Murray, "Population-based outcomes for small cell lung cancer: impact of standard management policies in British Columbia", Lung Cancer (Amsterdam, Netherlands) 01/02/200402/2004; 43(1), 7-16
56. S. Erridge, C. Thomson, J. Davidson, R. Jones, and A. Price, "Factors influencing the use of thoracic radiotherapy in lung cancer –an analysis of the 1995 Scottish lung cancer audit", Clinical Oncology (Royal College of Radiologists (Great Britain))14(3), 219-227 (2002)
57. M. Martel, T. Haken, B. Hazuka, M. Kessler, M. Strawderman, A. Turrisi, T. Lawrence. B. Fraass, and A. Lichter, "Estimation of tumor control probability model parameters from 3-D dose distributions of non-small cell lung cancer patients", Lung Cancer 24(1), 31-37 (1999)
58. R. McGarry, L. Papiez, M. Williams, T. Whitford, and R. Timmerman, "Stereotactic body radiation therapy of early-stage non-small-cell lung carcinoma: Phase 1 study," Int. J. Radiat. Oncol. Biol. Phys. 63(4), 1010-1015 (2005)
59. J. Wulf, K. Baier, G. Mueller, and M. Flentje, "Dose-response in stereotactic irradiation of lung tumors", Radiother. Oncol. 77(1), 83-87 (2005)
60. D. Oetzel, P. Schraube, F. Hensley, G. Sroka-Perez, M. Menke, and M. Flentje, "Estimation of pneumonitis risk in three-dimensional treatment planning using dose-volume histogram analysis", Int. J. Radiat. Oncol. Biol. Phys. 33(2), 455-460 (1995)
61. Q. Chen, M. Weinhaus, R. Deibel, J. Ciezki, R. Macklis, "Fluoroscopic study of tumor motion due to breathing: Facilitating precise radiation therapy for lung cancer patients", Med. Phys. 28(9), September 2001

62. A. Piet, F. Lagerwaard, P. Kunst, J. van Sörnsen de Koste, B. Slotman, and S. Senan, “Can Mediastinal Nodal Mobility Explain the Low Yield Rates for Transbronchial Needle Aspiration Without Real-Time Imaging?”, Chest 131, 1783-1787 (2007)
63. L. Xing, B. Thorndyke, E. Schreiber, Y. Yang, T. Li, G. Kim, G. Luxton, and A. Koong, “Overview of Image-Guided Radiation Therapy”, Medical Dosimetry, 31(2), 91-112 (2006)
64. J. M. Balter, R. K. T. Haken, T. S. Lawrence, K. L. Lam, and J. M. Robertson, “Uncertainties in CT-based radiation Therapy treatment planning associated with patient breathing”, Int. J. Radiat. Oncol. Biol. Phys. 36(1),167-174 (1996)
65. M. MacManus and R. Hicks, “Where do we draw the line? Contouring tumor on positron emission tomography/computed tomography”, Int. J. Radiat. Oncol Biol. Phys. 71(1), 2-4 (2008)
66. A. Klopp, J. Cheng, S. Tucker, E. Sulman, P. Balter, H. Liu, M. Bucci, H. Macapinlac, R. Komaki, J. Cox, “Intrathoracic patterns of failure for non-small-cell lung cancer with positron-emission tomography/computed tomography-defined target delineation”, Int. J. Radiat. Oncol Biol. Phys. 69(5), 1409-1416 (2007)
67. S. Senan, O. Chapet, F. Lagerwaard, and R. Ten Haken, “Defining Target Volumes for Non-small Cell Lung Carcinoma”, Semin. Radiat. Oncol. 14(4), 308-314 (2004)
68. K. Wijesooriya, W. Weiss, V. Dill, L. Dong, R. Mohan, S. Joshi, and P. J. Keall, “Quantifying the Accuracy of Automated Structure Segmentation in 4D CT Images Using a Deformable Image Registration Algorithm”, Med. Phys. 35 (4), April 2008
69. H. Wang, S. Krishnan, Z. Wang, S. Beddar, T. Briere, C. Crane, R. Mohan, L. Dong, “Improving soft-tissue contrast in four-dimensional computed tomography images of liver cancer patients using a deformable image registration method”, Int. J. Radiat. Oncol Biol. Phys. 72(1), 201-209 (2008)
70. M. Guckenberger, J. Wulf, G. Mueller, T. Krieger, K. Baier, M. Gabor, A. Richter, J. Wilbert, M. Flentje, “Dose-response relationship for image-guided stereotactic body radiotherapy of pulmonary tumors: relevance of 4D dose calculation”, Int. J. Radiat. Oncol Biol. Phys. 74(1) 47-54 (2009)
71. G. Stroiian, C. Martens, L. Souhami, D. Collins, and J. Seuntjens, “Local correlation between monte-carlo dose and radiation-induced fibrosis in lung cancer patients”, Int. J. Radiat. Oncol. Biol. Phys. 70(3), 921-930 (2008)
72. D. Rice, W. Smythe, Z. Liao, T. Guerrero, J. Chang, M. McAleer, M. Jeter, A. Correa, A. Vaporciyan, H. Liu, R. Komaki, K. Forster, and C. Stevens, “Dose-dependent pulmonary toxicity after postoperative intensity-modulated radiotherapy for malignant pleural mesothelioma”, Int. J. Radiat. Oncol. Biol. Phys. 69(2), 350-357 (2007)

73. E. Yorke, A Jackson, K. Rosenzweig, S. Merrick, D. Gabrys, E. Venkatraman, C. Burman, S. Leibel, and C. Ling, "Dose-volume factors contributing to the incidence of radiation pneumonitis in non-small-cell lung cancer patients treated with three-dimensional conformal radiation therapy", Int. J. Radiat. Oncol. Biol. Phys. 54(2), 329-339 (2002)

74. Y. Seppenwoolde, J. Lebesque, K. Jaeger, J. Belderbos, L. Beersma, C. Shcilstra, G. Henning, H. Hayman, M. Martel, and R. Ten Haken, "Comparing different NTCP models that predict the incidence of radiation pneumonitis", Int. J. Radiat. Oncol. Biol. Phys. 55(3) 724-735 (2003)

75. Å. Søvik, E. Malinen, and D. Olsen, "Strategies for biologic image-guided dose escalation: A review", Int. J. Radiat. Oncol Biol. Phys. 73(3), 650-658 (2009)

76. R. McCammon, T. Schiefteer, L. Gaspar, R. Zaemisch, D. Gravidahl, B. KIavanagh, "Observation of dose-control relationship for lung and liver tumors after stereotactic body radiation therapy", Int. J. Radiat. Oncol Biol. Phys. 73(1), 112-118 (2009)

77. J. Hayman, M. Martel, R. Ten Haken, P. Normolle, R. Todd III, J. Littles, M. Sullivan, P. Possert, T. Turrisi, and A. Litcher, "Dose Escalation in Non-Small-Cell Lung Cancer Using Three-Dimensional Conformal Radiation Therapy: Update of a Phase I Trial", Journal of Clinical Oncology 19(1), 127-136 (2001)

78. M. A. Admiraal, D. Schuring, and C. W. Hurkmans, "Dose Calculations Accounting for Breathing Motion in Stereotactic Lung Radiotherapy Based on 4D-CT and the Internal Target Volume", Radiotherapy and Oncology 86, 55-60 (2008)

79. C. Nelson, G. Starkschall, J. Chang, "The potential for dose escalation in lung cancer as a result of systematically reducing margins used to generate planning target volume", Int. J. Radiat. Oncol. Biol. Phys. 65(2), 573-586 (2006)

80. [www.onkol.kielce.pl/zfm/kursy/summer_2003/pliki/day2/ICRU/ICRU%2050%20 &%20ICRU%2062.ppt](http://www.onkol.kielce.pl/zfm/kursy/summer_2003/pliki/day2/ICRU/ICRU%2050%20&%20ICRU%2062.ppt)

81. http://www.nhlbi.nih.gov/health/dci/Diseases/brnchi/brnchi_what1s.

82. http://www.nhlbi.nih.gov/health/dci/Diseases/ipf/ipf_what1s.html

83. http://www.nhlbi.nih.gov/health/dci/Diseases/peri/peri_diagnosis.html

84. <http://lungcancer.about.com/od/glossary/g/Hypoxia.htm>

85. <http://lungcancer.about.com/od/glossary/g/esophagitis.htm>

86. P. Jenkins, R. Milliner, and P. Latimer, "Shrinkage of locally advanced non-small-cell lung caners in reponse to induction chemotherapy: implication for radiotherapy treatment planning", Int. J. Radiat. Oncol. Biol. Phys. 69(4) 993-1000 (2007)
87. ICRU 50. Prescribing, recording, and reporting photon beam therapy. Bethesda, MD: International Commission on Radiation Units and Measurements; 1993 ICRU Report 50.
88. E. Rietzel, A. Liu, K. Doppke, J. Wolfgang, A. Chen, G. Chen, and N. Choi, "Design of 4D treatment planning target volumes", Int. J. Radiat. Oncol. Biol. Phys. 66(1), 287-295 (2006)
89. X. Lu, L. Shanmugham, Al Mahadevan, E. Nedea, M. Stevenson, I. Kaplan, E. Wong, S. Rosa, F. Wang, S. Berman, "Organ deformation and dose coverage in robotic respiratory-tracking radiotherapy", Int. J. Radiat. Oncol. Biol. Phys. 71(1), 281-289 (2008)
90. A. Bel, M van Herk, and J. Lebesque, "Target maragins for arandom geometrical treatment uncertainties in conformal radiotherapy", Med. Phys. 23, 1537-1545 (1996)
91. J. Anatolak, and I. Rosen, "Planning target volumes for radiotherapy: Howe much margin is needed?" Int. J. Radiat. Oncol. Biol. Phys. 44, 1165-1179 (1999)
92. J. Stroom, H. de Boer, H. Huizinga (()) "Inclusion of geometrical uncertainties in radiotherapy treatment planning by means of coverage probability" Int. J. Radiat. Oncol. Biol. Phys. 43, 905-919 (1999)
93. M. van Herk, P. Remeijer, C. Rasch, et al "The probability of correct target dosage: Dose-population histograms for deriving treatment margins in radiotherapy", Int. J. Radiat. Oncol. Biol. Phys. 74, 1121-1135 (2000)
94. B. Parker, A. Shiu, M. Maor (()) "PTV margin determination in conformal SRT of intracranial leasions" J. Appl. Clin. Med. Phys. 3, 176-189 (2002)
95. M. van Herk, P. Rmeijer, J. Lebesque, "Inclusion of geometric uncertainties in treatment plan evaluation" Int. J. Radiat. Oncol. Biol. Phys. 52, 1407-1422 (2002)
96. M. van Herk, J. van der Geer et. al "Modeling the effect of treatment uncertainties in radiotherapy on tumor control probability for different tumor cell density configurations", Int. J. Radiat. Oncol. Biol. Phys. 55, 447 (2003)
97. A. McKenzie, "How should breathing motion be combined with other errors when drawing margins around clinical target volumes?" Br. J. Radiol. 73, 973-977 (2000)
98. M van Herk, M. Witte, J. Geer (()), "Biological and fractionation effects of random geometrical errors", Int. J. Radiat. Oncol. Biol. Phys. 57, 1460-1471(2003)

99. A. McKenzie, M. van Herk, B. Mijnheer, "Margins for geometric uncertainty around organs at risk in radiotherapy", Radiother. Oncol. 62, 299-307(2002)
100. Y. Mutaf, and D Brinkmann, "Optimization of internal margin to account for dosimetric effects of respiratory motion", Int. J. Radiat. Oncol Biol. Phys. 70(5), 1561-1570 (2008)
101. E. Weiss, K. Wijesooriya, V. Ramakrishanan, and P. Keall, "Comparison of intensity-modulated radiotherapy planning based on manual and automatically generated contours using deformable image registration in four-dimensional computed tomography of lung cancer patients", Int. J. Radiat. Oncol Biol. Phys. 70(2), 572-581 (2008)
102. M. Engelsman, E. Damen, K. De Jaeger, K van Ingen, and B. Mijnheer, "The effect of breathing and set-up errors on the cumulative dose to a lung tumor", Radiother Oncol. 60(1), 95-105 (July 2001)
103. A. McKenzie, "Defining the PTV and PRV—New ideas about old problems", Radiat. Oncol. 73, 203 (2004)
104. S. Shimizu, H. Shirato, K. Kagei, T. Nishioka, X. Bo, H. Dosaka-Akita, S. Hashimoto, H. Aoyama, K. Tsuchiya, and K. Miyasaka, "Impact of respiratory movement on the computed tomographic images of small lung tumors in three dimensional (3D) radiotherapy", Int. J. Radiat. Oncol. Biol. Phys. 46(5), 1127-1133 (2000)
105. M. Imura, K. Yamazaki, K. Kubota, T. Itoh, R. Onimaru, Y. Cho, Y. Hida, K Kaga, Y. Onodera, S Ogura, H. Dosaka-Akita, H. Shirato, and M. Nishimura, "Histopathologic consideration of fiducial gold markers inserted for real-time tumor-tracking radiotherapy against lung cancer", Int. J. Radiat. Oncol Biol. Phys. 70(2), 382-384 (2008)
106. P. Kupelian, A. Forbes, T. Willoughby, K. Wallace, R. Manon, S. Meeks, L. Herrera, A. Johnston, and J. Herran, "Implantation and stability of metallic fiducials within pulmonary lesions", Int. J. Radiat. Oncol Biol. Phys. 69(3), 777-785 (2007)
107. F. J. Lagerwaard, J. R. Van Sornsen de Koste, M R. J. Nijessen-Visser, R. H. Schuchhard-Schipper, S. S. Oei, A. Munne, and S. Senan, "Multiple "Slow" CT Scans for Incorporating Lung Tumor Mobility in Radiotherapy Planning", Int. J. Radiat. Oncol. Biol. Phys. 51(4), 932-937 (2001)
108. E. Barnes, B. Murry, D. Robinson, L. Underwood, J. Hanson, and W. Roa, "Dosimetric evaluation of lung tumor immobilization using breath hold at deep inspiration", Int. J. Radiat. Oncol Biol. Phys. 50(4), 1091-1098 (2001)
109. J. Hanley, M. Debois, D. Mah, G. Mageras, A. Raben, K. Rosenzweig, B. Mychalczak, L. Schwartz, R. Gloeggler, W. Lutz, C. Ling, S. Leibel, Z. Fuks, and G. Kutcher, "Deep inspiration breath-hold techniques for lung tumors: the potential value of target immobilization and reduced lung density in dose escalation", Int. J. Radiat. Oncol. Biol. Phys. 45(3), 603-611 (1999)

- 110.** S. Hunjan, G. Starkschall, I. Rosen, K. Prado, N. Tolani, and P. Balter, "Comparison of breath-hold and free-breathing positions of an external fiducial by analysis of respiratory traces", Journal of Applied Clinical Medical Physics, 9(3), (summer 2008)
- 111.** S. Nishioka, T. Nishioka, M. Kawahara, S. Tanaka, T. Hiromura, K. Tomita, and H. Shirato, "Exhale Fluctuation in Respiratory-Gated Radiotherapy of the Lung: A Pitfall of Respiratory Gating Shown in a Synchronized Internal/External Marker Recording Study", Radiotherapy and Oncology 86, 69-76 (2008)
- 112.** T. Pan, X. Sun, and D. Luo, "A new cost effective and workflow-efficient amplitude-binning 4DCT" Int. J. Radiat. Onc. Biol. Phys. 72(1), Supplement 2008
- 113.** W. D. D'Souza, D. P. Nazareth, B. Zhang, C. Deyoung, M. Suntharalingam, Y. Kwok, C. X. Yu, and W. F. Regine, "The Use of Gated and 4D CT Imaging in Planning for Stereotactic Body Radiation Therapy", Medical Dosimetry, 32(2), 92-101 (2007)
- 114.** ICRU 62. Prescribing, recording, and reporting photon beam therapy (supplement to ICRU Report 50). Bethesda, MD: International Commission on Radiation Units and Measurements; 1999 ICRU Report 62.
- 115.** H. Shih, S. Jiang, K. Aljarrah, K. Doppke, N. Choi, "Internal target volume determined with expansion margins beyond composite gross tumor volume in three-dimensional conformal radiotherapy for lung cancer", Int. J. Radiat. Oncol. Biol. Phys. 60(2), 613-622 (2004)
- 116.** Y. Mutaf, and D Brinkmann, "Optimization of internal margin to account for dosimetric effects of respiratory motion", Int. J. Radiat. Oncol Biol. Phys. 70(5), 1561-1570 (2008)
- 117.** S. Shen, J. Dun, R. Popple, J. Fiveash, S. Spencer, X. Wu, S. Ye, P. Pareek, and I. Brezovich, "3-D Target Localization at the End Expiration Prior to Respiration-Gated Radiotherapy Treatment", Med. Phys. 34(6), 2386-2386 (2007)
- 118.** E. Rietzel, A. Liu, G. Chen, and N. Choi, "Maximum-intensity volumes for fast contouring of lung tumors including respiratory motion in 4DCT planning", Int. J. Radiat. Oncol Biol. Phys. 71(4), 1245-1252 (2008)
- 119.** K. Britton, G. Starkschall, H. Liu, J. Chang, S. Bilton, M. Ezhil, S. John-Baptiste, M. Kantor, J. Cox, R. Komaki, and R. Mohan, "Consequences of anatomic changes and respiratory motion on radiation dose distributions in conformal radiotherapy for locally advanced non-small-cell lung cancer", Int. J. Radiat. Oncol Biol. Phys. 73(1), 94-102 (2009)
- 120.** K. Park, L. Huang, H. Gagne, and L. Rapiez, "Do maximum intensity projection images truly capture tumor motion?", Int. J. Radiat. Oncol Biol. Phys. 73(2), 618-625 (2009)
- 121.** J. Biederer, J. Dinkel, G. Remmert, S. Jetter, S. Nill, T. Moser, R. Bendl, C. Thierfelder, M. Favel, U. Oelfke, M. Bock, C. Plathow, H. Bolte, T. Welzel, B. Hoffmann, G. Hartmann, W.

- Schlegel, J. Debus, M. Heller, and H. Kauczor, "4D-imaging of the lung: reproducibility of lesion size and displacement on helical CT, MRI, and cone beam CT in a ventilated ex vivo system", Int. J. Radiat. Oncol. Biol. Phys. 73(3), 919-926 (2009)
122. J. Cai, P. Read, J. Baisden, J Larmer, S. Benedict, and K. Sheng, "Estimation of error in maximal intensity projection-based internal target volume of lung tumors: a simulation and comparison study using dynamic magnetic resonance imaging", Int. J. Radiat. Oncol. Biol. Phys. 69(3), 895-902 (2007)
123. T. Haken, J. Balter, L. Marsh, "Potential benefits of eliminating planning target volume expansions for patients breathing in the treatment of liver tumors", Int. J. Radiat. Oncol. Biol. Phys. 38, 613-617 (1997)
124. M. Engelsmann, P. Remeijer, M. Van Herk (), "Field size reduction enables iso-NTCP escalation of tumor control probability for irradiation of lung tumors", Int. J. Radiat. Oncol. Biol. Phys. 51, 1290-1298 (2001)
125. H. Kubo and B. Hill, "Respiration gated radiotherapy treatment: A technical study" Phys. Med. Biol. 41, 83-91 (1996)
126. J. Sonke, J. Lebesque, and M. Herk, "Variability of Four-Dimensional Computed Tomography Patient Models", Int. J. Radiat. Oncol. Biol. Phys. 70(2), 590-598 (2008)
127. N. Wink, M. Chao, J. Antony, and L. Xing, "Individualized gating windows based on four-dimensional CT information for respiration-gated radiotherapy", Phys. Med. Biol. 53, 165-175 (2008)
128. G. Li, K. Camphausen, B. Mueller, C. Burman, B. Mychalczak, R. Miller, Y. Song, "Advance in 4D medical imaging and 4D radiation therapy", Techol. Cancer Res. Treat. 7(1), 67-81 (February 2008)
129. Y. Tsunashima, T. Sakae, Y. Shioyama, K. Kagei, T. Terunuma, A. Nohtomi, and Y. Akine, "Correlation between the respiratory waveform measured using a respiratory sensor and 3D tumor motion in gated radiotherapy", Int. J. Radiat. Oncol. Biol. Phys. 60(3), 951-958 (2004)
130. M. Hoogeman, J. Prevost, J. Nuyttens, J Poll, P. Levendag, and B Heijmen, "Clinical accuracy of the respiratory tumor tracking system of the cyberknife: assessment by analysis of log files", Int. J. Radiat. Oncol. Biol. Phys. 74(1), 297-303 (2009)
131. D. Yang, W. Lu, D. Low, J. Deasy, J. Hope, and I. El Naqa, "4d-CT motion estimation using deformable image registration and 4D respiratory motion modeling", Med. Phys. 35(10), 4577-4590 (2008)

132. L. Lin, C. Shi, Y. Lui, G. Swanson, and N. Papanikolaou, "Development of a novel post processing treatment planning platform for 4D radiotherapy", Technology in Cancer Research and Treatment, 7(2), 125-132 (April 2008)
133. E. Schreibmann, B. Thorndyke, T. Li, J. Wang, and L. Xing, "Four-Dimensional Image Registration For Image-Guided Radiotherapy", In. J. Radiat. Oncol. Biol. Phys. 71(2), 578-586 (2008)
134. J. Seco, G. Sharp, Z. Wu, D. Gierga, F. Buettner, H. Paganetti, "Dosimetric impact of motion in free-breathing and gated lung radiotherapy: a 4DCT Monte Carlo interfraction effects", Med. Phys. 35(1), 356-366 (2008)
135. K. Britton, G. Starkschall, S. Tucker, T. Pan, C. Nelson, J. Chang, J. Cox, R. Mohan, and R. Komaki, "Assessment of gross tumor volume regression and motion changes during radiotherapy for non-small-cell lung cancer as measured by four-dimensional computed tomography", Int. J. Radiat. Oncol Biol. Phys. 68(4), 1036-1046 (2007)
136. D. Sarrut, B. Delhay, P. Villard, V. Boldea, M. Beuve, and P. Clarysse, "A Comparison Framework for Breathing Motion Estimation Methods From 4-D Imaging", IEEE Transactions on Medical Imaging, 26(12), (December 2007)
137. C. Yu, D. Jaffray, J. Wong, "The effects of intra-fraction organ motion on the delivery of dynamic intensity modulation", Phys. Med. Biol. 43, 91-1004 (1998)
138. Y. Liang, H. Xu, J. Yao, Z. Li, and W. Chen, "Four-dimensional intensity-modulated radiotherapy planning for dynamic multileaf collimator tracking radiotherapy", Int. J. Radiat. Oncol Biol. Phys. 74(1), 266-274 (2009)
139. Y. Suh, E. Weiss, H. Zhong, M. Fatyga, J. Siebers, and P. Keal, "A deliverable four-dimensional intensity-modulated radiation therapy-planning method for dynamic multileaf collimator tumor tracking delivery", Int. J. Radiat. Oncol. Biol. Phys. 71(5), 1526-1536 (2008)
140. Y. Suh, E. Wiess, H. Zhong, M. Fatyga, J. Siebers, and P. Keall, "A deliverable four-dimensional intensity-modulated radiation therapy-planning method for dynamic multileaf collimator tumor tracking delivery", Int. J. Radiat. Oncol Biol. Phys. 71(5), 1526-1536 (2008)
141. S. Vedam, A. Docef, D. Todor, and V. Kini, "Predicting respiratory motion for four-dimensional radiotherapy", Med. Phys. 31(8), 2274-2283 (2004)
142. S. Vedam, A. Docef, M. Fix, M. Murphy, P. Keal, "Dosimetric impact of geometric errors due to respiratory motion prediction on dynamic multileaf collimator-based four-dimensional radiation delivery", Med. Phys. 32(6), 1607-1620 (June 2005)
143. S. Rathee, "Oncology 568: Introduction to computed tomography", Cross Cancer Institute, Winter Term, 2007

144. S. Rathee, "Oncology 568: Image reconstruction: Parallel beam", Cross Cancer Institute, Winter Term, 2007
- 145 G. Herman, "Computer Reconstruction from Projections: The Fundamentals of Computed Tomography", Academic Press Inc. 111 Fifth Avenue, NY NY 10003, 1980
146. S. Rathee, "Oncology 568: Image reconstruction: Fourier Methods and Fan Beam", Cross Cancer Institute, Winter Term, 2007
147. L. Goldman, "Principles of CT: Multislice CT-*", Journal of Nuclear Medicine Technology, 26(2), 57-68 (2008)
148. R. Bruening, A. Kuettner, Th. Flohr, "Protocols for Multislice CT" Second Edition, Springer-Verlag Berlin Keidelberg, 2003, 2006, Editor: Dr. Ute Heilmann, Heidelberg.
149. www.impactscan.org/rsna2001.htm
150. R. Proksa, Th. Kohlr, M. Grass, and J. Timmer, "The n -PI-Method for Helical Cone-Beam CT", IEEE Transactions on Medical Imaging, 19(9), (September 2000)
151. S. Rathee, "Oncology 568: Computed tomography—Digital modality", Cross Cancer Institute, Winter Term, 2007
152. D. Robinson, "On the Origin and Nature of Motion Induced CT Image Artifacts" In preparation, 2009
153. J. Wu, and W. D'Souza "Do mobile Tumors in the Lung Deform During Normal Respiration – An image registration Investigation", Med. Phys. 34(6), 2573-2573 (2007)
154. T. Pan, "Comparison of Helical and Cine Acquisitions for 4D-CT Imaging with Multislice CT", Med. Phys. 32 (2), (February 2005)
155. N. M. Wink, C. Panknin, and T. D. Solberg, "Phase Versus Amplitude Sorting of 4D-CT Data", Journal of Applied Clinical medical Physics, 7(1), (Winter 2006)
156. S. Rathee, "Oncology 568:Quality control issues", Cross Cancer Institute, Winter Term, 2007
157. J. Dinkel, T. Welzel, H. Bolte, B. Hoffmann, C. Thierfelder, U. Mende, H. Debus, M. Heller, H. Kauczor, and H. Biederer, "Four-Dimensional Multislice Helical CT of the Lung: Qualitative Comparison of Retrospectively Gated and Static Images in an Ex-vivo System", Radiotherapy and Oncology 85, 215-222 (2007)

- 158.** V. Kini, S. Vedam, P. Keall, S. Patil, C. Chen, and R. Mohan, "Patient training in respiratory-gated radiotherapy", Med. Dosim. 28(1), 7-11 (2003)
- 159.** B. White, R. Werner, W Lu, D Low, "Feasibility of unitizing pneumonic abdominal bellows for quantitative 4DCT", Med. Phys. 36(6), 2500 (June 2009)
- 160.** J. Killoran, A. Allen, B. Kann, and Y. Lyatskaya, "Inter fractional variability of breathing phase definition as determined by fiducial location", Med. Phys. 35(2), 753-763 (2008)
- 161.** S. Hunjan, G. Starkschall, I. Rosen, K. Prado, N. Tolani, and P. Balter, "Comparison of breath-hold and free-breathing positions of an external fiducial by analysis of respiratory traces", Journal of Applied Clinical Medical Physics, 9(3), (summer 2008)
- 162.** J. Hoisak, K. Sixel, R. Tirona, P. Cheung, and J. Pignol, "Correlation of lung tumor motion with external surrogate indicators of respiration", Int. J. Radiat. Oncol. Biol. Phys. 60(4), 1298-1306 (2004)
- 163.** M. Nakamura, Y. Narita, Y. Miyabe, Y. Matsuo, T. Mizowaki, Y. Norihisa, K. Takayama, Y. Nagata, and M. Hiraoka, "Physical evaluation of four dimensional computed tomography", Journal of JASTRO 19(4), 263-271 (2007)
- 164.** T. Yamamoto, U. Langner, B. Loo, J. Shen, and P. Keal, "Retrospective analysis of artifacts in four-dimensional CT images of 50 abdominal and thoracic radiotherapy patients", Int. J. Radiat. Oncol Biol. Phys. 72(4), 1250-1258 (2008)
- 165.** S. Rathee, "Oncology 568: Statistics, Contrast, Resolution, and Films", Cross Cancer Institute, Jan 28, 2007
- 166.** M. Frigo and S. Johnson, "The Design and Implementation of FFTW3", Proc. IEEE, 93(2), (February 2005)
- 167.** Instructions for use –Catphan 500 and 600 Manual, Copyright 2006
- 168.** T. Riauka "Oncology 568: Screen film systems", Cross Cancer Institute, Jan 23, 2007
- 169.** T. Flohr, K. Stierstorfer, H. Bruder, J. Simon, A Polacin, S Schaller, "Image reconstruction and image quality evaluation for a 16 slice CT scanner", Med. Phys. 30 (5), (May 2003)
- 170.** S. Nehmeh, T. Pan, A. Pevsner, K. Rosenzweig, E. Yorke, G. Megras, H. Schoder, P. Vernon, O. Squire, H. Mostafavi, S. Larson, J. Humm, "Four-dimensional (4D) PET/CT imaging of the thorax", Med. Phys. 31(12), (December 2004)
- 171.** H. Wang, S. Krishnan, Z. Wang, S. Beddar, T. Briere, C. Crane, R. Mohan, L Dong, "Improving soft-tissue contrast in four-dimensional computed tomography images of liver cancer

- patients using a deformable image registration method”, Int. J. Radiat. Oncol Biol. Phys. 72(1), 201-209 (2008)
- 172.** R. Fazel, H. Krumholz, Y. Wang, J. Ross, J. Chen, H. Ting, N. Shah, K. Nasir, A. Einstein, and B. Nallamothu, “Exposure to Low-Dose Ionizing Radiation from Medical Imaging Procedures”, The New England Journal of Medicine 361, 849-857 (August 2009)
- 173.** V. Boldea, B. C. Sharp, S. B. Jiang, and D. Sarrut, “4D-CT Lung Motion Estimation with Deformable Registration: Quantification of Motion Nonlinearity and Hysteresis”, Med. Phys. 35(3), (March 2008)
- 174.** S. Vedam, L. Archambault, G. Starkschall, R. Mohan, and S. Beddar, “Determination of prospective displacement-based gate threshold for respiratory-gated radiation delivery form retrospective phase-based gate threshold selected at 4DCT simulation”, Med. Phys. 34(11) 4247-4255 (November 2007)
- 175.** T. Tada, K. Minakuchi, T. Fujioka, M. Sakurai, M. Koda, I Kawase, T. Nakajima, M. Nishioka, T. Tonai, and T. Kozuka ”Lung cancer: intermittent irradiation synchronized with respiratory motion-results of pilot study” Radiology 207, 779-783 (1998)
- 176.** R. Berbeco, S. Nishioka, H. Shirato, S. Jiang, “ Residual motion of lung tumors in end-of-inhale respiratory gated radiotherapy based on external surrogates”, Med. Phys. 33(11), (November 2006)
- 177.** T. Neicu, R. Berbeco, J. Wolfgang, and S. Jiang, “Synchronized moving aperture radiation therapy (SMART): improvement of breathing pattern reproducibility using respiratory coaching”, Phys. Med. Biol. 51(3), 617-636 (2006)
- 178.** C. Haasbeek, R. Spoelstra, F. Lagerwaard, J van Sornsens de Koste, J. Cuijpers, B. Slotman, and S. Senan, “Impact of audio-coaching on the position of lung tumors”, Int. J. Radiat. Oncol Biol. Phys. 71(4),1118-1123 (2008)
- 179.** P. Keall, M. Chang, S. Benedict, H. Thames, S. Vedam, and P. Lin, “Investigating the temporal Effects of Respiratory Gated IMRT Treatment Delivery on in Vitro Survival: A Theoretical and Experimental Study”, Med. Phys. 34(6), 2463-2463 (2007)
- 180.** N. Wink, M. Chao, J. Antony, and L. Xing, “Individualized gating windows based on four-dimensional CT information for respiration-gated radiotherapy”, Phys. Med. Biol. 53, 165-175 (2008)
- 181.** C. Nelson, P. Balter, P. Lindsay, T. Briere, S. Vedam, R. Morice, R. Komaki, and G. Starkschall, “Uncertainties in Respiratory Gating for Lung Tumors”, Med. Phys. 34(6), 2368-2368 (2007)

- 182.** S. Ahn, B. Yi, Y. Suh, J. Kim, S. Lee, S. Shin, S. Shin, and E. Choi, “ A feasibility study on the prediction of tumor location in the lung from skin motion”, Br. J. Radiol. 77(9191), 588-596 (2004)
- 183.** N. Koch, H. Liu, G. Starkschall, M. Jacobson, K Forster, Z. Liao, R. Komaki, and C. Stevens, “Evaluation of internal lung motion for reapiatory-gated radiotherapy using MRI: Part 1 – Correlating internal lung motion with skin fiducial motion”, Int. J. Radiat. Oncol. Biol. Phys. 60(5), 1459-1472 (2004)
- 184.** G. Persson, D. Nygaard, M. Olson, T. Juhler-Nottrup, A. Pendersen, L. Specht, and S. Korreman, ”Can audio coached 4DCT emulate free breathing during treatment course?” Acta Oncologica 47, 1397-1405 (2008)
- 185.** P. Kupelian, C. Ramsey, S. Meeks, T. Willoughby, A. Forbes, T. Wagner, and K. Langen, “Serial megavoltage CT imaging during external beam radiotherapy for non-small-cell lung cancer: observations on tumor regression during treatment “Int. J. Radiat. Oncol. Biol. Phys. 63(4), 1024-1028 (2005)
- 186.** L. McDermott, M. Wendling, J. Sonke, M. van Herk, and B. Mihnheer, ”Anatomy changes in radiotherapy detected using portal imaging”, Radiotherpay and Oncloolgy 79, 211-217 (2006)
- 187.** M. Ezhil, C. Starkschall, R. Mohan, J. Cox, and R. Komaki, “Validation of a Model-Based Segmentation Approach to Propagating Normal Anatomic Regions of Interest Through the 10 Phases of Respiration”, Int. J. Radiat. Oncol. Biol. Phys. 71(3), 900-906 (2008)
- 188.** H. Johns and J. Cunningham, The Physics of Radiology: Fourth Edition, H. Johns and J. Cunningham, Charles C. Thomas, 2600 South First Street, Springfield, IL 62717, USA (1983)
- 189.** E. Podgoršak, Radiation Physics for Medical Physicists, Springer-Verlag Berlin Heidelberg, springeronline.com (2006)
- 190.** J. Wiegert, “Scattered radiation in cone-beam computed tomography: analysis. Quantification and compensation”, Dissertation: RWTH Aachen, 06 Fakultät für Elektrotechnik und Informationstechnik, 2007 RWTH Aachen University, 06 Faculty of Electrical Engineering and Information Technology, 2007
- 191.** <http://www4.nau.edu/microanalysis/Microprobe/>
- 192.** D. Griffiths, Introduction to Electrodynamics: Third Edition, Prentice-Hall Inc., Upper Saddle River, NJ 07458, USA (2004)
- 193.** B. Rothenstein, S. Popescu, and G. Spix, “Relativistic derivations of the electric and magnetic fields generated by an electric point charge moving with constant velocity”, ArXiv:physics [physics.gen-ph], [arXiv:physics/0601028v1](https://arxiv.org/abs/physics/0601028v1), 5, (January 2006)

- 194.** PHYWE LEP 5.5.03, “Duane-Hunt displacement law and Planck’s “quantum of action””, PHYWE series, Laboratory Experiments, Physic, PHYWE Systeme GMBH, 37070 Goettingen, Germany
- 195.** T. Riauka “Oncology 568:Exponential attenuation”, Cross Cancer Institute, Jan 9, 2007
- 196.** J. Cunningham “Oncology 550: Coherent Scattering; Photoelectric affect; Pair production”, Cross Cancer Institute, September 19, 2007
- 197.** J. Hubble, W. Veigele, E. Briggs, R. Brown, D. Cromer, and R. Howerson, “ Atomic Form Factors, Incoherent Scattering Functions, and Photon Scattering Cross Sections”, J. Phys. Chem. Ref. Data, 4(3), (1975)
- 198.** <http://physics.nist.gov/PhysRefData/Xcom/Text/intro.html>
- 199.** T. Riauka “Oncology 568:Imaging system and image formation”, Cross Cancer Institute, Jan 16, 2007
- 200.** S. Rathee, “Oncology 568:Computed tomography components”, Cross Cancer Institute, Winter Term, 2007
- 201.** M. Goharian, and R. Khan, “ Investigation of the Image Quality in Phase-Sorted 4DCT Data”, Med. Phys. 35(6): 2705-2705 (June 2008)

Appendix A: Additional Comments on 4DCT in RT

What gate?

It is widely accepted that satisfactory gating parameters are reliably achieved using 4DCT (174,153,129), partially because explicit knowledge of the displacement correlation between the target and the surrogate is not needed (1). All that is required is the identification of a reproducible phase and an adequate duty cycle (38).

To keep residual motion artifacts to a minimum, gating windows are often chosen around end inhale or end exhale phase. End exhale is a popular choice because it is the most reproducible (23,176,175). However, other authors have reported end inhale as the more stable phase (46) and, with the inflated lung, the dose coverage of the lung and heart can be reduced (89). The choice of which phase to use depends on the patient's ability to reliably reproduce it and the relative importance of minimizing the involvement of normal tissues and organs at risk (38,127). Berbeco et. al measured the residual target motion at end exhale to be 1.2 mm when using a phase-based gate and 1.0 mm with an amplitude gate. End inhale fluctuations were measured as 2.7 mm for phase-based and 2.2 mm for amplitude-based gating. These discrepancies between phase- and amplitude-based gating methods were eliminated when breath coaching was used (176). Thus, there may well be differences in the simulated gate and the actual delivered gate, especially if the simulation is derived from phase-based sorting and the actual RT gating is amplitude-based (174). Any such discrepancy should be verified and accounted for at the time of delivery (174). Although breath coaching has been shown to increase the reproducibility of the chosen gate, and thus improve the gating duty cycle (177,176), the amplitudes achieved under coached conditions are typically higher than for free breathing (46); therefore, the patient's ability to respond to coaching should be evaluated prior to treatment planning (178) so that he/she may either be coached for both planning and treatment or not at all.

The extended delivery time accompanying gated RT increases patient discomfort as well as elevates the risk of inter-fraction motion (49,21) –any patient motion during the treatment essentially negates the benefits of gating (21). A study by Keall et al. found that the dosimetric consequences of periodic irradiation and partial tumor irradiation in gated IMRT had less of an impact on RT than the extended delivery time, again, highlighting the importance of an appropriate duty cycle (179). Thus, as many phases as possible should be included in the gated ITV to keep treatment times short (50) without nullifying the benefit of the reduced margin size (180). The gating window will be much larger than the acquisition time of a single 4DCT phase image, thus, even if a turnaround point in the target's path is chosen, significant tumor motion will be included in the gating PTV, and so motion uncertainties in the IM cannot be avoided (181). One method of incorporating breathing uncertainty suggested by Tsunashima et. al involves utilizing the standard deviation of the respiratory trace at the chosen phase (129).

Inter-fraction baseline drift can range from 0.4 - 12.7 mm, and can be in any direction (111). This is a random error, with non-negligible dosimetric consequences. Inter-fraction baseline drift cannot be assessed prior to treatment, and so the necessary margins to account for this uncertainty remain population-based. Frequent gated portal images are necessary to not only verify the position of the target (or a surrogate) during the gate throughout the entire RT course, but also to measure the inter-fraction variations (46).

IMRT

In IMRT, isodose lines conform tightly to the target volume (119), yet it is the localization that results in the largest uncertainties with 4DCT. Gated IMRT is a viable option. Even though a fair amount of reproducibility in amplitude and extent of hysteresis over the course of RT has been reported (23, 173), use of a surrogate signal, such as the RPM system, to guide IMRT is dubious and could easily result in geometric misses if additional margins are not added to account for the uncertainty in reproducibility, base-line drift, anatomical consistency, and phase relation (162).

External markers

The Bellows system is not quantitative and, at the present, can only be used during imaging. The RPM waveform however, can be calibrated to provide quantitative measurement of surface motion (45). Many studies have shown a strong correlation between surface skin motion and tumor motion (182,129,183), yet this relationship is complex, affected by the location of the target, the location of the surface marker, and the patient's breathing pattern (183). Not only have phase offsets between reported between surrogate signal and the target (129,162,88), but this relationship is variable. Statistically distinct phase relationships can be measured at different times, appearing in phase then out of phase on different days or even during the same session (61,24). Since the phase and relative amplitude of the respiratory signal depend on the location of the marker block (160), it is imperative that the phase relationship between target and surrogate signal be defined at the time of imaging, that the marker block be placed in the same location during the entire planning and treatment process, and that the defined phase relationship is verified prior to each RT treatment.

Breath coaching

Breath coaching has been shown to greatly improve the reproducibility of patient breathing patterns. With audio coaching alone, the stability of frequency improves, but the amplitude variability can increase (111,158,184), and with visual coaching alone, amplitude reproducibility improves but frequency control can suffer (111,158). Audio-visual coaching shows the least variation in both amplitude and frequency (30), and the patient's performance improves with practice (158). Since the method of coaching can affect the target's motion, it should not be altered during the entire planning and treatment process (89).

With coaching, variations in the placement of the diaphragm at end exhale can be reduced by 21 % (46), lung volumes at end inspiration can increase by 43 %, and mean displacement of the ITV can be reduced by as much as 9.6 mm (89). Yet, not all patients are capable of following coaching instructions. Out of 33 patients in a study by Stevens et. al, half could not follow audio-visual instruction and 13 could only be coached with audio (16). It should be noted that dramatic changes in the anatomy due to RT, such as tumor shrinkage or increased aeration of the lung due to reduced atelectasis, may affect the patient's breathing pattern even with coaching.

Physiological variations

During the course of RT, the GTV defined by the planning 4DCT may not coincide with the position of the tumor during treatment (20), and the PTV can lose its

geographical relevance since planning margins are static while the patient's anatomy can be significantly altered by common physiological changes, such as weight loss or tumor shrinkage (185,119,135). In a study of eighty one lung cancer patients by McDermott et. al (186), 57% of these patients showed progressive anatomical changes and 37 % random anatomical changes. Another recent study by Maxim et. al (135) observed clinically significant changes in both tumor size and mobility throughout the course of RT. Interestingly, the end inhale and end exhale volumes in weekly 4DCT scans differed, showing a mean reduction of 41.7% and 37.1 %, respectively. This reduction did not follow any weekly trend (135). A study of ten patients by Kupelian et. al (185), using serial MVCT images from daily tomotherapy treatments, recorded tumor shrinkage at a rate of 1.2 % per day. From these images, new treatment plans were developed and compared to the original plan. As the tumor volumes dwindled, there was a small increase in deposited dose (i.e. D_{95}) ranging from 0.02 - 0.1% per day, presumably from the subsequent decrease in attenuation with reduced tumor volume (185). In the Maxim study, dose calculations from the EPI concluded that the reduction in tumor size resulted from high doses to the PTV; again, no weekly pattern presented itself, rather, the reduction in tumor volumes appeared to fluctuate (135). A recent study by Britton et. al (119), involving ten lung patients undergoing 3DCRT²⁹ and IMRT, looked at variation in the surrounding normal tissues as well as the target volumes during the course of RT. Fresh treatment plans were constructed from weekly 4DCT scans and compared to the original. Britton recorded a reduction in both the ITV and PTV for all patients along with reductions in dose coverage (e.g. D_{99} to the ITV down 5.7 %, and D_{95} to PTV down 20.5 %). With the receding tumor boundaries, the mean lung dose increased 2.2 %, and V_{20} went up 3.1 %. In general, the volumes of the other normal tissues in the vicinity (i.e. the esophagus, heart, and spinal cord) did not change significantly during RT the course, and the mean dose variation depended on that organ's position relative to the tumor (119).

All the authors agree that fast tumor shrinkage can lead to inter-fraction dose delivery errors, and that it is worse for larger tumors, which appear to shrivel more and in an irregular fashion (106). However, the worst dosimetric compromises involve positional uncertainties (119) exacerbated by physiological changes and small systematic margins (135). Use of daily onboard imaging such as CBCT is obviously necessary to verify target position (117), but these scans are also subject to motion artifacts, and 4DCBCT techniques should be implemented. Daily 4DMVCT treatment planning as in the Kupelian study is impractical even for centers with tomotherapy units, but a second 4DCT scan may be useful. Maxim notes the largest variations in tumor volumes typically occur on the second week of RT treatment, and suggests this may be a good time to reevaluate the treatment plan using an additional 4DCT scan (27). In terms of patient outcome, however, the threshold at which these dosimetric discrepancies become clinical relevant is still under assessment (119).

Threshold and Segmentation

To take full advantage of 4DCT, an efficient and reliable manner of contouring the multiple phase images must be adopted. Dose discrepancies as much as 9.3 Gy have been reported between the end inhale phase and free breathing RT, presumably due to the deformation of soft tissues and the motion of the ribs in and out of the beam (134). Thus, complete images must be taken of all the involved organs and each organ contoured in

²⁹ 3-dimensional conformal radiation therapy: a static external beam therapy planned in 3D to conform closely to tumor volumes.

every phase (187,7,64). Manual evaluation of every organ in every phase, however, is time consuming (78). Automated segmentation algorithms can offer clinically plausible contours with considerable time savings and minimal user interaction (187,101,65,68,39), but careful human assessment is still necessary due to the inevitable presence of residual motion artifacts (68,65). The effects of residual motion artifacts on high contrast resolution may be problematic as well, especially for intensity based deformable registration methods which are sensitive to image quality (173). Also, 4DCT does not account for motion induced from the heart beat, and variations in automated contouring of GTVs in the vicinity of the heart can vary as much as 5 mm (187).

Appendix B: X-ray Formation and Interactions with Matter

X-rays

X-rays are electromagnetic radiation in the range of approximately 0.01 to 10 nm (188p23). For medical applications, this range is broken into groups by the energy of the x-rays produced: *soft* x-rays range from 0.1 - 20 keV, *diagnostic* x-rays appropriate for radiographic imaging of the human body are 20 -140 keV, *orthovoltage*, used to treat superficial lesions, are about 80-300 kV, *intermediate* x-rays range from approximately 300 keV to 1 MeV, and final, anything over 1 MeV is referred to as *megavoltage*. X-rays can be generated by the change in momentum of a charged particle and by the removal of an orbital electron from an atom (189p87). Both events may result when an electron beam is stopped by an absorbing material, as in an x-ray tube.

An x-ray tube generates photons by liberating electrons from a heated filament and accelerating them into a high Z target (See Figure B.1)

Figure B.1: A simple x-ray tube

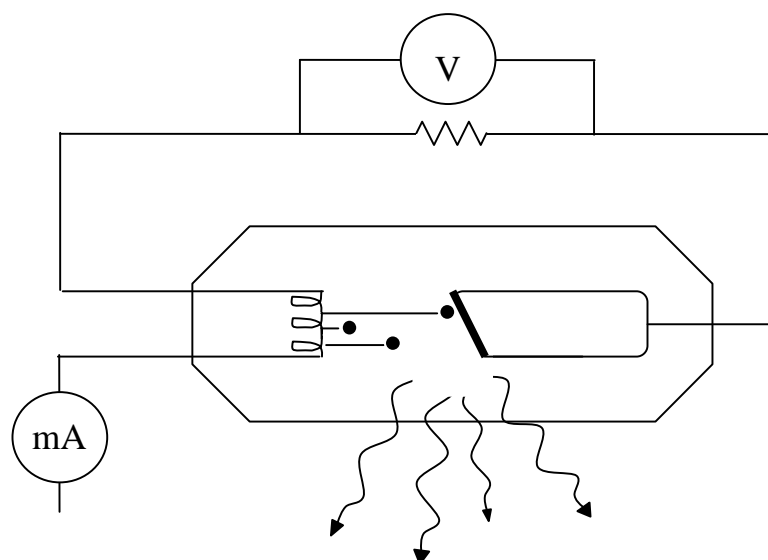


Figure caption (after (190)) A current is passed through the filament, heating it to the point where electrons are emitted from its surface. A voltage is applied between the filament and the target, drawing the free electrons towards the anode. The interactions of the electrons with the target generate x-rays.

When the electrons meet the target, their rapid deceleration results in *bremstrahlung*, while other electrons may collide with atoms of the anode to cause orbital vacancies, resulting in so called *characteristic radiation* as this radiation is characteristic of the anode's material (189p87). The spectrum of radiation emitted from an x-ray tube contains both *bremstrahlung* and characteristic radiation. Figure B.2 shows a generic x-ray spectrum of a tungsten target.

Figure B.2: The radiation spectrum of an x-ray tube with a tungsten anode

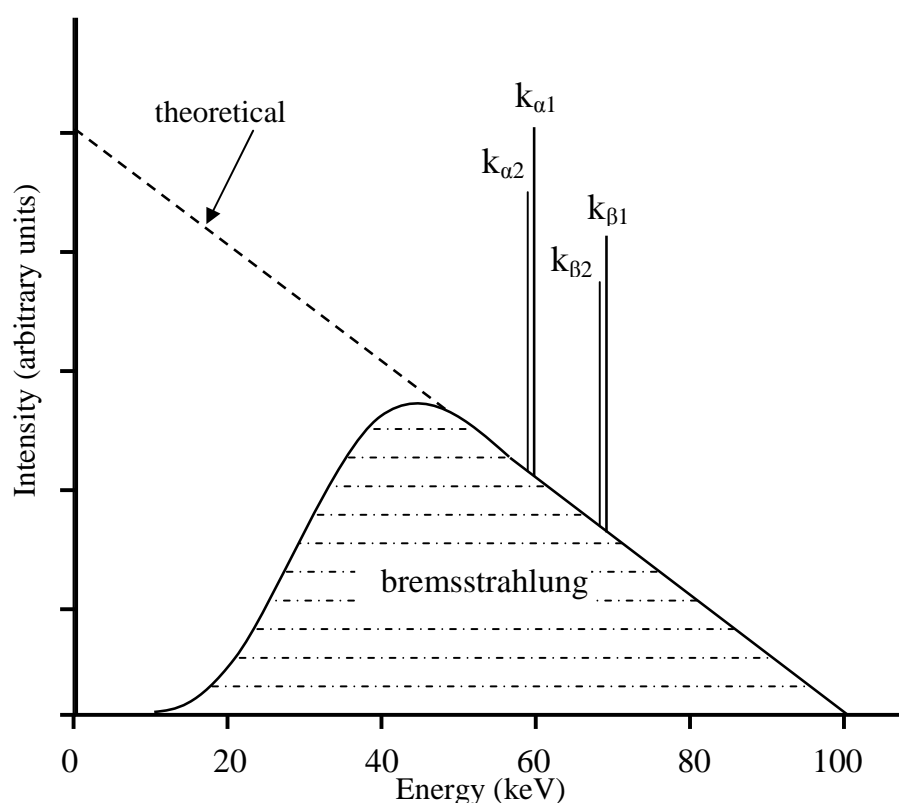


Figure caption (after (190)) Bremsstrahlung, resulting from the innumerable inelastic interactions of the impinging electrons with the atoms of the target, constitutes the bulk of the x-rays produced. The theoretical line shows the spectrum of bremsstrahlung if absorption by the target and other components of the x-ray tube is neglected. Characteristic radiation is named by the shells involved with the emission: 'k' indicates a transition from a higher shell to the K shell, 'α' means that the transition e^- originated from a shell one energy level up from the K shell (i.e. the L shell) and 'β' means two shells up (i.e. the M shell). The subscripts '1' and '2' distinguish the slight energy difference between the two electrons inhabiting each of the α and β shells.

Characteristic radiation

Characteristic radiation is produced when an orbital electron is removed from an atom and a more energetic orbital electron drops down to fill the vacancy (191). The excess energy of the replacement electron is released as a photon of energy

$$h\nu = E_K - E_L,$$

B.1

where E_K is the binding energy of the vacant orbital and E_L is the binding energy of the replacement electron's orbital (188p89) (See Figure B.4). Vacancies in an atom's orbital structure occur under a variety of circumstances, including, but not limited to, Coulombic interactions, nuclear decay, and the Auger effect (189p98). At medical x-ray energies, however, only the Coulombic forces between the electron beam and the atoms of the cathode cause orbital vacancies (188p87).

Figure B.3: Formation of a characteristic x-ray

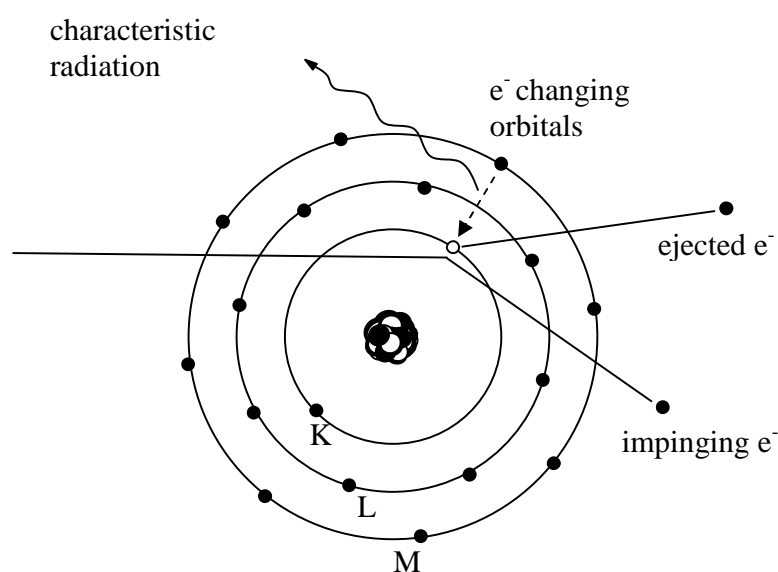


Figure caption (after (190))Characteristic x-rays are formed when an impinging e^- ejects an orbital electron, and an electron from a higher energy orbital drops down to take its place. The excess energy of the replacement electron is emitted as a photon.

As seen from Equation A.1, the energy of the characteristic photon is dictated by the energy of atomic orbitals, which are, in turn, determined by the atomic number of the cathode's material and the quantum numbers of the shells involved (189p98). Figure B.4 is the energy level diagram of a tungsten atom. The transition from the L shell to the K shell results in the emission of a 59 keV photon designated by k_α . A transition from the M to K shells, referred to as k_β , releases 67 keV. The fact that two k_α and two k_β peaks appear in Figure B.2 arises from the Pauli exclusion principle. Two electrons sharing the same orbital differ only in their spin quantum number s , and the slight difference in energies (e.g. between $k_{\alpha 1}$ & $k_{\alpha 2}$ seen in Figure B.2) arises from their respective spin-orbital coupling (191). In general, inner shell transitions result in characteristic x-rays with energies between 10 keV and 100 keV, while outer shell transitions emit radiation at energies on the order of just a few electron volts (189p90). However, not just any transition between energy levels results in the emission of a photon. Radiative transitions follow a selection rule based on quantum numbers l (defining the orbital cloud shape) and j (the total angular momentum of the electron)(191); Δl must equal ± 1 , and $\Delta j = \pm 1$ or 0, with the exemption that transitions from $j = 0$ to $j = 0$ are forbidden (189p90). Transitions which violate this rule result in the expulsion of an orbital electron (i.e. an Auger electron) rather than a photon. The electron carries away energy E_A equal to

$$E_A = (E_K - E_L) - E_M,$$

B.2

where E_M is the binding energy of the ejected electron's orbital (188p89). See Figure A.3. Yet, even if a radiative transition is allowed, it may still be accompanied by an Auger electron rather than a characteristic photon (189p90). The probability of a radiative emission is represented for each orbital by its *fluorescent yield* ω_K , where ω_K = the number of photons emitted per vacancy, and increases with atomic number (189p91).

Figure B.4: Energy level diagram of a tungsten atom showing the emission of characteristic radiation

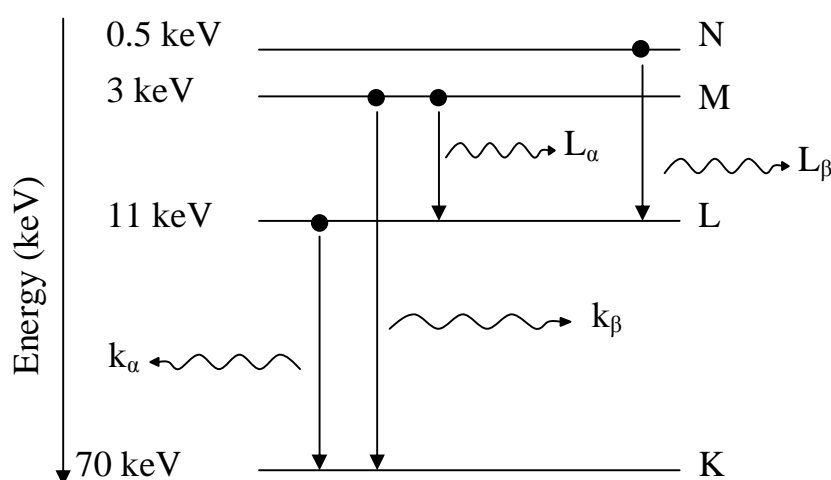


Figure caption (after (190)) The energy levels of the N, M, L, and K shells of a tungsten atom are labeled with their binding energy. Electrons dropping down from higher energy orbitals (i.e. those having a lower binding energy) emit photons with energy equal to the difference in energy between the two orbitals. See Figure B.2. (Figure not to scale)

Bremsstrahlung

When a charged particle is stationary, its energy is stored in an isotropic electric field around the particle

$$E(r) = \frac{1}{4\pi\epsilon_0} \frac{q}{r^2},$$

B.3

where q is the charge of the particle, and ϵ_0 is the dielectric constant of the vacuum ($\epsilon_0 = 8.85 \times 10^{-12} \text{ As/Vm}$) (189p93). The electric field of a moving charge is

$$E = \frac{1}{4\pi\epsilon_0} \frac{q}{r^2(c-v)^3} [(c-v)(c^2 - v^2) + r(c-v)a \sin \theta]$$

B.4

where r is the distance from the charge to the field point (192p460, 189p95) see Figure B.5, v and a are the charge's velocity and acceleration, respectively, and θ is the angle between a and r , and c is the speed of light (192p438).

Figure B.5: Vector diagram of a moving charge in a Coulombic field

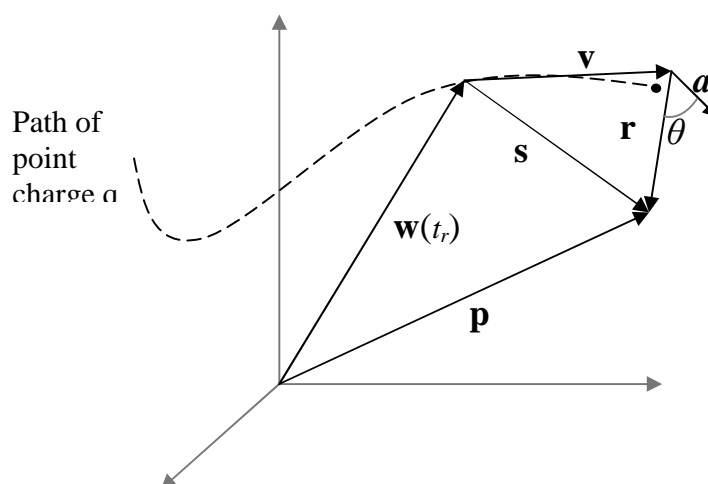


Figure caption (adapted from (192p430)) The calculation of the electric field for an arbitrarily moving point charge q . The vector $\mathbf{r} = c\hat{\mathbf{s}} - \mathbf{v}$ (where c is the speed of light) represents the distance from charge q to the observation point \mathbf{p} at the time of observation t . However, the information about q at \mathbf{p} originates from an earlier time t_r when the charge was at location $\mathbf{w}(t_r)$. Thus, integrating over the charge density to find the electric field at t_r entails doing so for two different moments in time since $t_r = t - (s/c)$. This is the origin of the two terms in the electric field of Equation B.4 (192p430).

The first term in brackets depends only on velocity and falls off with $1/r^2$. This is the energy field that is carried along with the particle (192p460), and is referred to as the *velocity field* or *near field*. The second term in brackets contains an acceleration term and falls with $1/r$ (192p438). This is the field that constitutes the radiated energy, and is known as the *acceleration field* (192p460), *far field*, or *radiation field*. When $v \ll c$, the radiation field becomes

$$E = \frac{1}{4\pi\epsilon_0} \frac{q}{rc^2} a \sin \theta \quad \text{B.5}$$

and the corresponding magnetic field is

$$B = E/c = \frac{\mu_0}{4\pi} \frac{q}{rc} a \sin \theta, \quad \text{B.6}$$

where μ_0 is the permeability of the vacuum ($\mu_0 = 4\pi \times 10^{-7} \text{ Vs/Am}$) (189p95). Thus, when a charged particle undergoes a change in momentum, part of its kinetic energy is emanated away as the electric and magnetic fields which propagate outwards from the particle at the speed of light. This is bremsstrahlung (189p94).

In an x-ray tube, Coulombic interactions between energetic electrons and the anode's nuclei cause the impinging electrons to accelerate, creating bremsstrahlung. See Figure B.6.

Figure B.6: Impinging electrons interacting inelastically with an atom

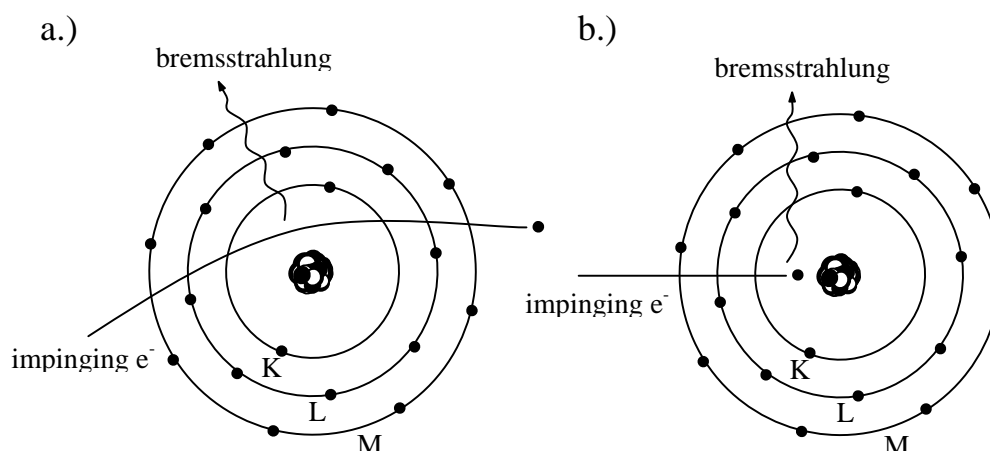


Figure caption (after (190)) An electron entering the Coulombic field of an atom emits radiation due to a.) a small change in momentum, b.) a rapid deceleration, and everything in between.

The acceleration of the electrons can be found by applying Newton's second law to Coulomb's force

$$ma = \frac{1}{4\pi\epsilon_0} \frac{eZe}{r^2} \quad \text{B.7}$$

$$a = \frac{1}{4\pi\epsilon_0} \frac{eZe}{mr^2}, \quad \text{B.8}$$

where m is the mass of the charged particle, e is the charge on an electron ($e = 1.602 \times 10^{-19}$ J), Z is the atomic number of the nucleus, and r is the distance between the two charges (189p97). The intensity of the radiation produced $I(r, \theta)$ is given by the Poynting vector (i.e. the cross product of the electric and magnetic field vectors divided by μ_0 (192p460)). In scalar terms, this is

$$I(r, \theta) = (\vec{E} \times \vec{B}) / \mu_0 = \epsilon_0 c E^2 = \frac{1}{16\pi\epsilon_0} \frac{e^2}{r^2 c^3} a^2 \sin^2 \theta \quad \text{B.9}$$

(since $B = E/c$ (G438) and $c^2 = 1/\epsilon_0\mu_0$ (192p376), and here, $q = e$) (189p96). Equation B.9 reveals bremsstrahlung's intensity dependence on a^2 and $\sin^2\theta$; thus, the maximum bremsstrahlung intensity is in the transverse plane to the charge's velocity at $\theta = \pi/2$, and zero in the direction of motion, when $\theta = 0$ or π . See Figure B.7. Also, since $I(r, \theta)$ is proportional to a^2 , it is insensitive to whether the impinging electron is accelerating or decelerating (192p464).

As seen in Equation B.4, E is affected by the speed of the charged particle (193); as $\beta = v/c$ increases, E is increased by a factor of $(1 - \beta \cos \theta)^{-5/2}$ (189p98). In this way the speed of the electrons also affects the intensity;

$$I(r, \theta) = \frac{1}{16\pi\epsilon_0} \frac{e^2}{r^2 c^3} \frac{a^2 \sin^2 \theta}{(1 - \beta \cos \theta)^5} \quad \text{B.10}$$

The inclusion of θ in this new factor alters the angular dependency of the emitted electric field, causing it to tip forward as the speed of the charge increases (189p98) (shown in Figure B.7). As the velocity of the electrons increases, the more forward peaked the radiation, and for each velocity, there is a characteristic angle θ_{\max} at which the bremsstrahlung radiation is the most intense. This angle may be found by integrating the intensity with respect to θ , and setting $\theta = \theta_{\max}$ to zero, resulting in

$$\theta_{\max} = \cos^{-1} \left[\frac{\sqrt{1 + 15\beta^2} - 1}{3\beta} \right]. \quad \text{B.11}$$

As β goes to 0, θ_{\max} approaches $\pi/2$, and as β goes to 1, θ_{\max} approaches 0. The decent is rapid; at only 100 keV, $\theta_{\max} = 35^\circ$ (189p100).

Figure B.7: Cross section view of the radiation emitted from an accelerating charged particle

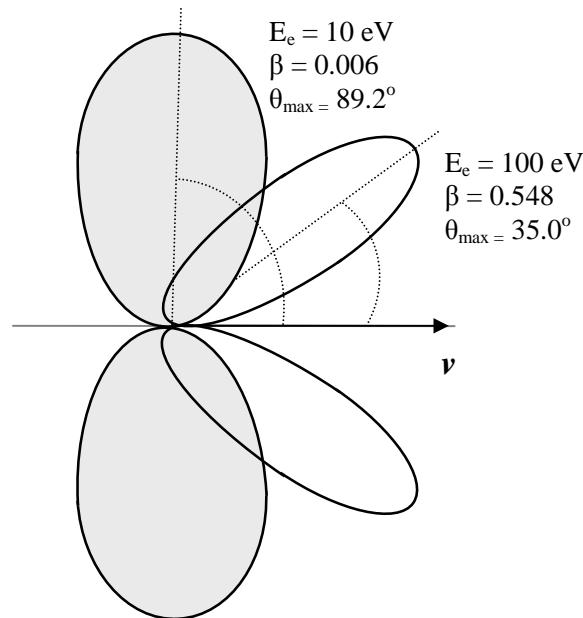


Figure caption (after 189p99): As $\beta = v/c$ increases, the radiation tips forward in the direction of motion, never emitted in the direction of \mathbf{v} , but in an ever tightening cone around it. (were \mathbf{v} is the velocity of the charge) (Figure not to scale)

Conservation of energy mandates that the energy of the emitted photon cannot be greater than the energy used to create it (188p24). In 1915, Duane and Hunt empirically showed that the shortest emitted wavelength λ_{\min} multiplied by the accelerating voltage U is constant:

$$U \lambda_{\min} \approx 1.24 \text{ E-6 Vm}, \quad \text{A.12}$$

(194) which, from the energy equation,

$$KE = eU = hc/\lambda_{\min}$$

A.13

where h is Planck's constant (194), shows that the greatest amount of energy that can be lost in a single radiative event is equal to the kinetic energy of the impinging electron, and that the Duane Hunt constant is hc/e . Radiation events of lower energy are, of course, possible; thus, the bremsstrahlung spectrum ranges from zero⁺ to the entire kinetic energy of the electron (189p97)(see Figure B.2).

The vast majority of interactions between an energetic electron and the nuclei of the absorbing media are elastic collisions (195). See Figure B.8. Since greater than 99% of the energy carried by the electrons deposits in the anode as heat, tungsten is also used as the target material due to its high melting point, (i.e. 3370°C (195)). Tungsten, with an atomic number of 74, yields substantial bremsstrahlung (as evident from Equations B.8 & B.9) as well as characteristic x-rays (i.e. high ω_K).

Figure B.8: Interactions of an impinging electron

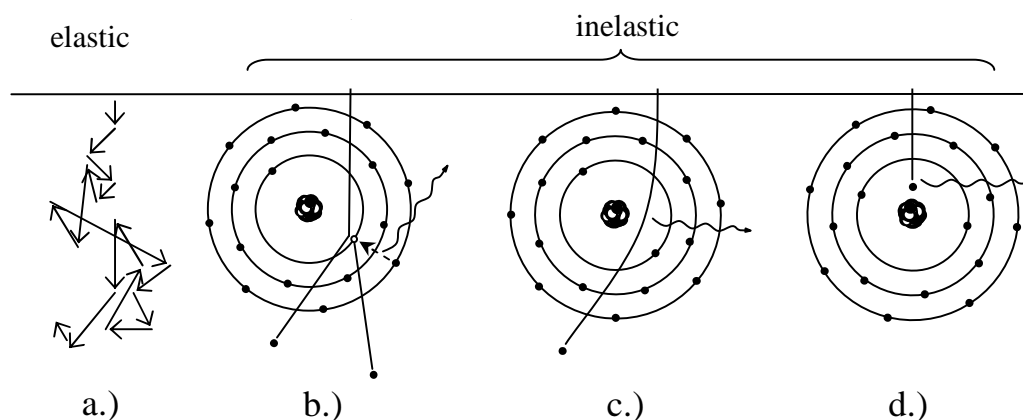


Figure caption (after (190)): More than 99 % of the electron's interactions with the anode are elastic collisions. a.) the electron's energy is transferred directly to the medium in numerous elastic collisions, causing heat. b.) Far less frequently, the electron displaces an orbital electron, resulting in the production of characteristic x-rays. c.) An encounter with the Coulombic field of an atom causes the electron to change course, thus releasing a portion of its kinetic energy as a photon. d.) A close encounter with the atom stops the electron; the entire kinetic energy of the electron is radiated away.

The fluence from the x-ray tube is polychromatic and will vary from tube to tube as well as in time; the variables include the current through the filament, the voltage across the tube, the nature of the power supply, component materials, quality of the vacuum, anode and cathode configuration, tube housing, filtration, etc (195). It turns out that the biological effectiveness of x-rays is relatively insensitive to their energy (188p270), rather it is the penetrative power of the beam, referred to as its *quality*, that is of primary interest (195). Thus, instead of describing the nature of each beam by its unique spectrum, just its depth of penetration into some homogeneous material is often quoted. For diagnostic x-rays, the quality is expressed by the thickness of material (typically millimeters of aluminum) needed to reduce the fluence of the beam by one half, called the *half value layer* (HVL) (189p238).

Photon Interactions with matter

Incident x-rays pass with random trajectories into and through the cross sectional area of any material in their path. The expected number of interactions p between an x-ray and the absorbing material is proportional to the area (or effective area) occupied by each atom, referred to as the *cross section* of the atom μ_a . Mathematically,

$$p = N_a \mu_a \cdot x, \quad \text{B.14}$$

where N is the population of atoms per unit volume of the target, and x is the thickness of the target (196). Each possible interaction between an x-ray and the atoms in its path has its own probability of occurrence, and thus, its own cross section. Possible interactions between an incident x-ray and the absorbing material depend on the energy of the photon and on the atomic number of the material. These interactions include:

Classical scatter – the elastic scatter of the photon off a free electron (189p189).

Rayleigh scatter – the elastic scatter of a photon off the bound electrons of an atom (189p214).

Compton scatter – the inelastic scatter of a photon off a loosely bound electron (189p193).

The photoelectric effect— the complete absorption of the photon by a tightly bound electron, resulting in the expulsion of the electron(s) from the atom (189p220).

Pair production— the complete absorption of the photon by the nucleus of the atom, resulting in the creation and emission of an electron/positron pair (189p227).

Triplet production— the complete absorption of the photon by a tightly bound electron, resulting in the expulsion of the electron from the atom as well as the creation and emission of an electron/positron pair (189p227).

Photodisintegration –the complete absorption of the photon by the nucleus of an atom, triggering some form of nuclear decay, typically the emission of a single neutron. (189p235)

For the photon energies associated with radiological imaging, only Rayleigh, Compton, and photoelectric interaction are significant (189p242).

Rayleigh Scatter

Rayleigh scatter occurs when a photon interacts with the atom as a whole (188p172,189p188). However, it is instructive to first discuss the classical derivation of a scattering event off a single, free electron.

Consider a photon with an electric field E_1 which, when interacting with a free electron, is absorbed, and having transferred all its energy to the electron, sets up a resonance in the charged particle with a force of

$$m_e a_1 = eE_1 = eE_o \sin wt, \quad \text{B.15}$$

where w is the frequency of oscillation of the electron around its mean position, and t is time (189p189). During oscillation, the charge experiences acceleration

$$a_1 = \frac{e}{m_e} E_o \sin wt. \quad \text{B.16}$$

See Figure B.11. The accelerating charge emits radiation, as in Equation B.5, which, with the substitution of Equation A.16 for a , and e for q , becomes

$$E_1' = \frac{1}{4\pi\epsilon_0} \frac{e}{rc^2} \left(\frac{e}{m_e} E_o \sin wt \right) \sin \Theta, \quad \text{B.17}$$

where Θ is the angle between the emission vector \mathbf{r} and the polarization vector \mathbf{a} of the incident photon from Figure B.9 (189p191). Noting that $1/(4\pi\epsilon_0)(e^2/m_e c^2)$ is the classical radius of the electron r_o ($r_o = 2.81795\text{E-}15$ m) (188p168), Equation B.17 may be more simply expressed as

$$E_1' = \frac{r_o}{r} E_o \sin wt \sin \Theta. \quad \text{B.18}$$

(188p169) The emission of radiation dissipates the electron's kinetic energy until it is once again "at rest" (188p171).

Figure B.9: Vector diagram of the classical scatter of a photon off a free electron

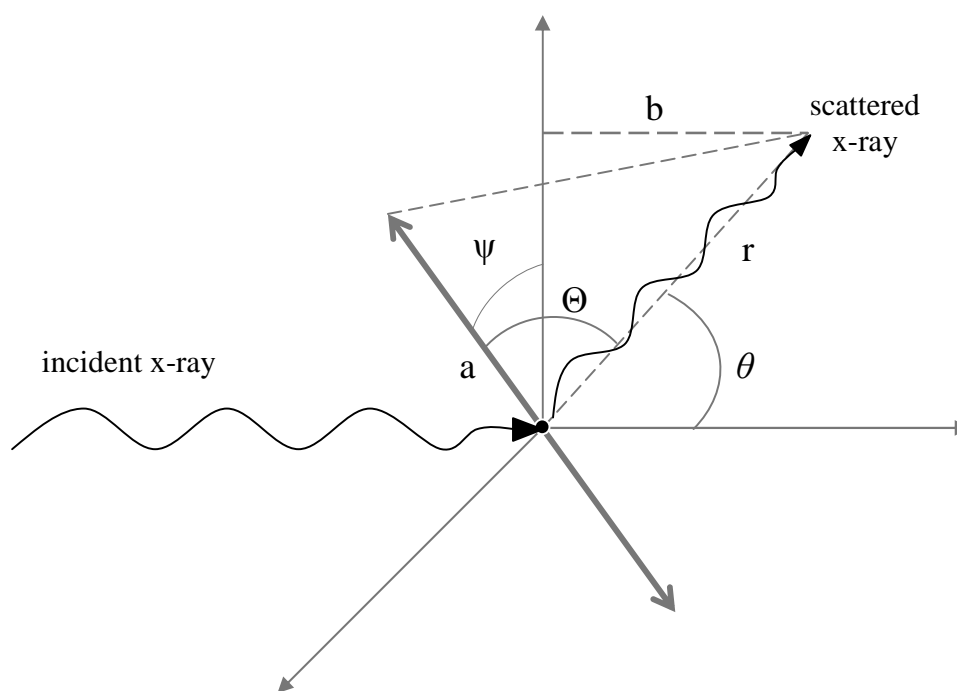


Figure caption (after (189p191))Diagram of classical scatter: a photon is absorbed by a free electron (depicted here at the origin), setting-up a resonance which radiates the absorbed energy away as a scattered photon. The relationship between the scattering angle θ and the polarization angle ψ can be determined from the geometry: $\cos\Theta = (a/r)$, $\sin\theta = (b/r)$, and $\cos\psi = (a/b)$, giving $\cos\Theta = \sin\theta\cos\psi$ and $\sin^2\Theta = 1 - \sin^2\theta\cos^2\psi$ (P191).

The probability of the re-emission of the incident photon into a solid angle $d\Omega$, referred to as the differential *classical scattering cross section* per electron per unit solid angle $d_e\sigma_o/d\Omega$ (188p170), is found from the time-averaged ratio of intensities (radiation-out divided by the radiation-in) multiplied by the area differential, i.e.

$$d_e \sigma_o = \frac{\bar{I}_{out}}{\bar{I}_{in}} dA . \quad \text{B.19}$$

(189p190). From Equations B.9, B.15 and B.18, and noting that the average of $\sin^2 wt = 1/2$,

$$\bar{I}_{in} = \epsilon_o c \bar{E}_1^2 = \epsilon_o c E_o^2 (\sin^2 wt)_{ave} = \frac{1}{2} \epsilon_o c E_o^2 \quad \text{B.20}$$

and

$$\bar{I}_{out} = \epsilon_o c \bar{E}_1'^2 = \epsilon_o c E_o^2 \frac{r_o^2}{r^2} (\sin^2 wt)_{ave} (\sin^2 \Theta)_{ave} = \frac{1}{2} \epsilon_o c E_o^2 \frac{r_o^2}{r^2} (\sin^2 \Theta)_{ave} \quad \text{B.21}$$

(189p190). With $dA = r^2 d\Omega$, Equation B.19 becomes

$$d_e \sigma_o = \frac{\frac{1}{2} \epsilon_o c E_o^2 \frac{r_o^2}{r^2} (\sin^2 \Theta)_{ave}}{\frac{1}{2} \epsilon_o c E_o^2} r^2 d\Omega , \quad \text{B.22}$$

and reduces to

$$\frac{d_e \sigma_o}{d\Omega} = r_o^2 (\sin^2 \Theta)_{ave} . \quad \text{B.23}$$

(189p190). Noting that the emitted radiation is unpolarized, to find the average value of $\sin^2 \Theta$, integrate over the polarization angle ψ from 0 to 2π to get

$$(\sin^2 \Theta)_{ave} = \frac{1}{2} (1 + \cos^2 \theta) , \quad \text{B.24}$$

where θ is the scattering angle between the incident and reemitted photons (189p191). The relationship between Θ and ψ is depicted in Figure B.9. This gives

$$\frac{d_e \sigma_o}{d\Omega} = \frac{1}{2} r_o^2 (1 + \cos^2 \theta) \quad \text{B.25}$$

(189p191). In order to calculate the total probability of the scattering event, $d_e \sigma_o / d\Omega$ must be integrated over all scattering angles. To find the differential classical cross section per electron per unit scattering angle, $d_e \sigma_o / d\theta = (d_e \sigma_o / d\Omega) (d\Omega / d\theta)$, and given that $d\Omega / d\theta = 2\pi \sin \theta$,

$$\frac{d_e \sigma_o}{d\theta} = r_o^2 \pi \sin \theta (1 + \cos^2 \theta) . \quad \text{B.26}$$

(188p169). A graph of both $d_e\sigma_o/d\Omega$ and $d_e\sigma_o/d\theta$ vs θ is shown in Figure A.10. The resulting total classical scattering cross section per electron ${}_e\sigma_o$, found by integrating Equation A.26 over all scattering angles, essentially, finding the area under the curve in Figure A.10, is constant ${}_e\sigma_o = 66.5 \text{ E-}30 \text{ m}^2$ (188p171). The lack of an energy dependence shows that there is no change in energy between the incident and reemitted photons (i.e. the scattering event is elastic) (189p193).

Figure B.10: The classical differential cross section per electron (per unit scattering angle and per unit solid angle) plotted against scattering angle

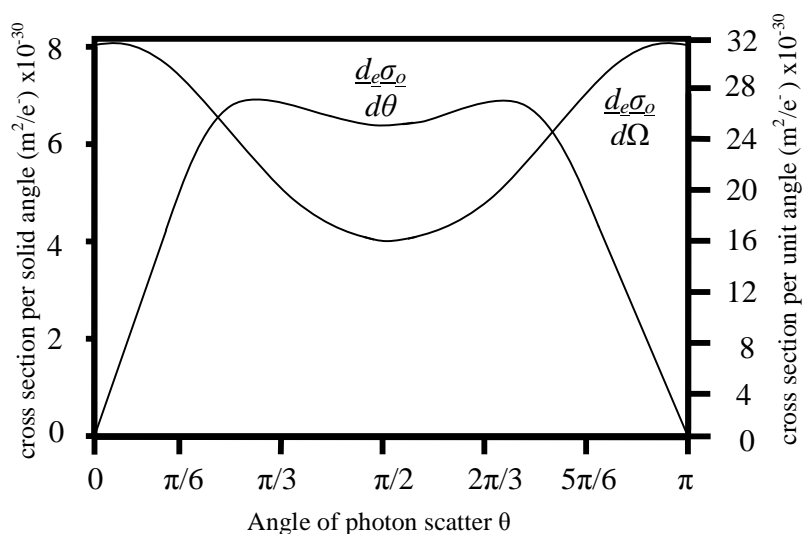


Figure caption (after 188p171) Radiation is emitted in every direction. At $\theta = 0$ or π , $d_e\sigma_o/d\Omega = r_o^2 = 7.94 \text{ E-}30 \text{ (m}^2/\text{e}^- \text{ steradian)}$, and at $\pi/2$, half that, indicating that twice as much radiation is scattered either forward or backwards than at right angles to the incident photon. To derive the total probability of the scattering event, $d_e\sigma_o/d\theta$ is integrated over all scattering angles, giving $66.5\text{E-}30 \text{ m}^2$. ($d_e\sigma_o/d\theta$ gives the fraction of incident radiation scattered into the cone contained between θ and $\theta+d\theta$.)

Moving to the case where all of the atomic electrons are involved in the scattering event (i.e. Rayleigh scattering), the classical coefficient must be modified to account for the atom's complete orbital structure. The atomic structure is described by its form factor $F(x, Z)$ (197); here again Z is the atomic number of the atom, and the term x is the momentum transfer variable, defined as

$$x = \sin(\theta/2) / \lambda \quad , \quad \text{B.27}$$

where λ is the wavelength of the incident x-ray (189p215). The form factor is, understandably, an extremely complex function and can only be solved analytically for the hydrogen atom –all other atoms require approximations and atomic modeling (189p215). Now at last, we come to the mathematical definition of the Rayleigh scattering. The differential Rayleigh cross section per unit solid angle is simply

$$\frac{d_a\sigma_R}{d\Omega} = \frac{d_e\sigma_o \{F(x, Z)\}^2}{d\Omega} \quad \text{B.28}$$

The subscript 'a' denotes that the cross section is per atom. Likewise, the differential Rayleigh cross section per unit scattering angle θ may be found by

$$\frac{d_a \sigma_R}{d\theta} = \frac{d_e \sigma_0}{d\theta} \{F(x, Z)\}^2 = r_0^2 \pi \sin \theta (1 + \cos^2 \theta) \{F(x, Z)\}^2 \quad \text{B.29}$$

(189p215) Since the momentum transfer factor x is inversely proportional to the incident photon's wavelength λ (Equation B.27), Rayleigh scattering is energy dependent as well as Z dependent. The complex nature of these dependences can be seen in Figure B.11, which shows the Rayleigh differential cross section with respect to scattering angle for Hydrogen and Carbon absorbers, respectively, plotted against scattering angle for several incident photon energies. Also plotted are the corresponding differential classical cross sections per atom, simply ${}_a\sigma_o = Z_e \sigma_o$.

From Figure B.11, it is evident that the Rayleigh scattering is not symmetric about $\pi/2$, but especially for high energies, favors forward scattering. The characteristic angle of Rayleigh scattering θ_R is defined as the half-angle of the cone containing 75% of the scattered photons, and is estimated by (189p216)

$$\theta_R = 2 \sin^{-1} \left(\frac{0.026 m_e c^2 Z^{1/3}}{h\nu} \right). \quad \text{B.30}$$

For the extreme case of only a single orbital electron, as the energy of the incident photon decreases, the Rayleigh differential cross section approaches the classical one. However, for $Z > 1$, incorporation of the form factor increases the Rayleigh differential cross section well above the classical case (189p217).

The total Rayleigh scattering cross section ${}_a\sigma_R$ can be found by integrating Equation B.29 over all scattering angles (189p215). As incident photon energies increase, the Rayleigh cross section decreases rapidly, and for low atomic number materials, such as soft tissues, is negligibly low for energies above 1 MeV (188p150). (See Figure B.11.)

Figure B.11: The effects of incident photon energy and Z of the absorber on the Rayleigh differential cross section per unit scattering angle

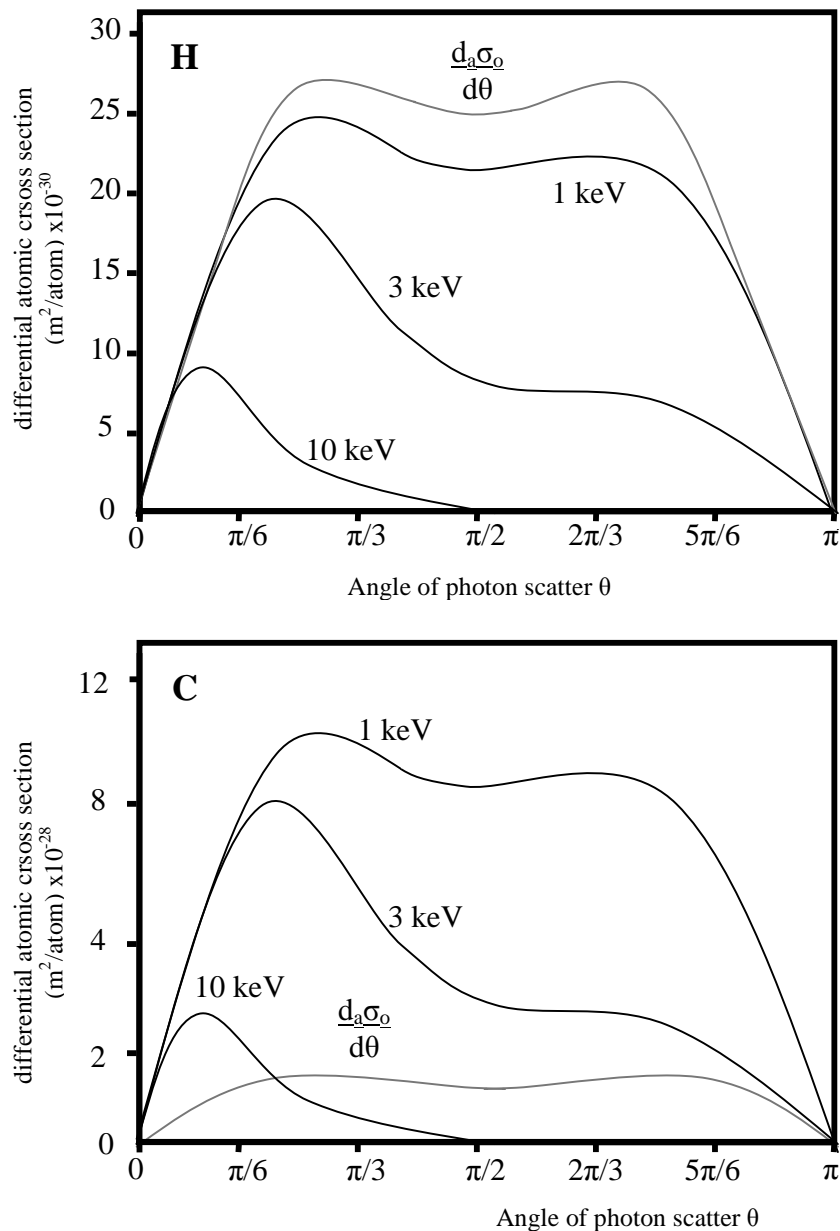


Figure caption (189p217) Top: For H, ${}_a\sigma_o = {}_e\sigma_o$, and as $h\nu \rightarrow 0$, ${}_a\sigma_R \rightarrow {}_a\sigma_o$, but for atoms with more complex orbital structure, ${}_a\sigma_R$ never approaches ${}_a\sigma_o$. Bottom: The C atom shows the general case: as photon energy increases, the cross section decreases and the scattered radiation becomes decidedly forward peaked.

Compton Scatter:

Compton scatter describes an inelastic collision between a photon and a loosely bound electron. Having transferred a portion of its energy to the electron, the scattered

photon leaves the interaction with diminished energy while the electron recoils (188p174). See Figure B.12.

Figure B.12: Diagram of Compton scatter

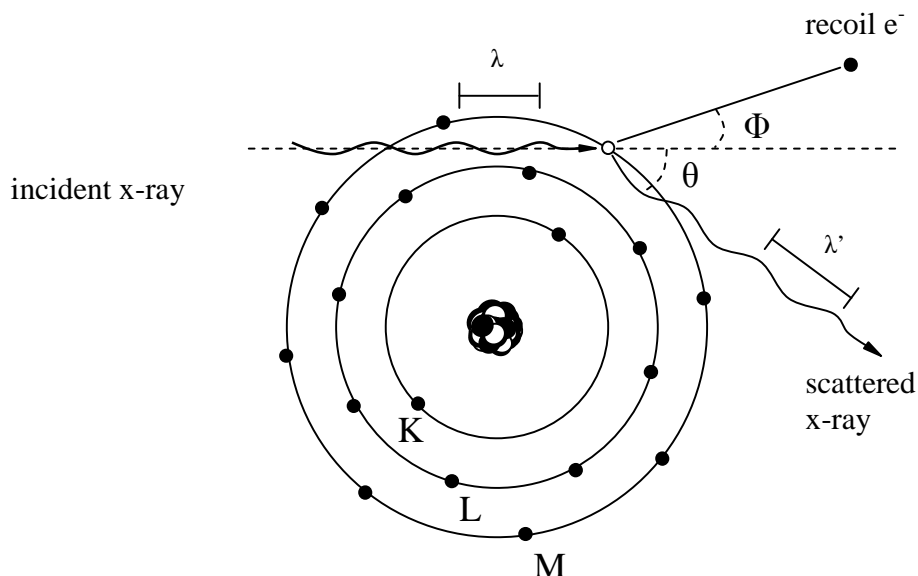


Figure caption (after (190)): An incident photon interacts with bound electron, and is scattered. The scattered photon is of a lower energy than the incident photon, having transferred a portion of its momentum to the recoiling electron.

If one assumes that the electron is free and stationary, it is a straightforward derivation to obtain the post collision energies using the conservation of momentum and energy:

$$E_e = \frac{h\nu\alpha(1 - \cos\theta)}{1 + \alpha(1 - \cos\theta)} \quad \text{B.31}$$

$$h\nu' = h\nu \frac{1}{1 + \alpha(1 - \cos\theta)} \quad \text{B.32}$$

where E_e and $h\nu'$ are the energies of the electron and photon after the collision, and $\alpha = h\nu/(m_e c^2)$, where m_e is the mass of the electron (188p174). The relationship between the electron recoil angle Φ and the scatter angle θ is

$$\cot\varphi = -(1 + \alpha) \tan\left(\frac{\theta}{2}\right). \quad \text{B.33}$$

(196). In the case where the incident photon makes a 'direct hit' on an electron, the photon will be scattered backwards at an angle of $\theta = 180^\circ$. This results in the maximum energy transfer to the electron and the minimum energy escaping with the scattered photon (188p175). A classical description of such a collision tells us nothing of the probability of such an event occurring. For this, a quantum mechanical treatment is necessary. In 1929, Oskar Klein and Yoshio Nishina undertook the task of deriving the differential cross section of Compton scattering $d_e\sigma_C/d\Omega$ (189p200) (Note the subscript

'e', indicating the cross section is per electron). Here again, the new cross section can be expressed in terms of the classical one, this time, by the inclusion of the Klein-Nishina form factor F_{KN}

$$\frac{d_e \sigma_C}{d\theta} = \frac{d_e \sigma_0}{d\theta} (F_{KN}) = r_0^2 \pi \sin \theta (1 + \cos^2 \theta) F_{KN}, \quad \text{B.34}$$

were

$$F_{KN} = \left[\frac{1}{1 + \alpha(1 - \cos \theta)} \right]^2 \left\{ \frac{1 - (\alpha(1 - \cos \theta))^2}{(1 + \alpha(1 - \cos \theta))(1 + \cos^2 \theta)} \right\}. \quad \text{B.35}$$

(189p200). There is no Z dependence in Equation A.35 since the electron is assumed to be free. Thus, the probability of a Compton interaction is independent of the absorber material. The inclusion of $\alpha = h\nu/m_e c^2$, however, gives a clear energy dependence to $d_e \sigma_C/d\Omega$, which is illuminated in Figure B.13.

Figure B.13: The affects of incident photon energy on the Compton differential cross section per unit solid angle

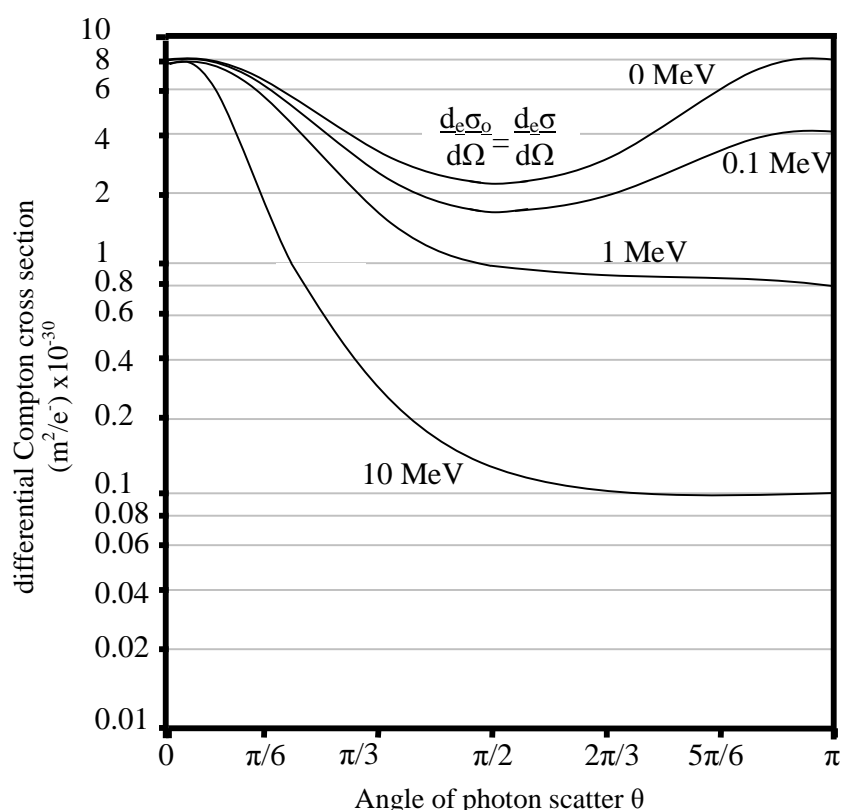


Figure caption (After 188p177): The Compton differential cross section equals the classical cross section only for zero energy photons. As the photon's energy increases, the larger the scattering angle (i.e. interactions where the recoiling electron receives a significant portion of the incident photon's energy) the lower the cross section.

Again, the classical differential cross section is included for reference, and, as with the Rayleigh differential cross section for a hydrogen atom, as the energy of the incident photon goes to zero, $d_e\sigma_C/d\Omega \rightarrow d_e\sigma_o/d\Omega$. To find the total probability of a Compton scattering event, ${}_e\sigma_C$, Equation B.34 must be integrated over all scattering angles. The result is

$${}_e\sigma_C = \frac{3}{4} {}_e\sigma_o \left\{ \left(\frac{(1+\alpha)}{\alpha^2} \right) \left(\frac{2(1+\alpha)}{1+2\alpha} - \frac{\ln(1+2\alpha)}{\alpha} \right) + \frac{\ln(1+2\alpha)}{2\alpha} - \frac{(1+3\alpha)}{(1+2\alpha)^2} \right\} \quad \text{B.36}$$

(188p178).

The obvious flaw, however, is that electrons within a material are not truly free, nor are they stationary. An accurate account of the electron's binding energy entails knowledge of its wave function, thus, for anything other than the simplest of atomic structures, an approximate solution must suffice (188p181). The probability of a Compton scattering event off a bound electron ${}_a\sigma_{inc}$ (the subscript 'inc' refers to the fact that, unlike Rayleigh scattering, this is an incoherent scattering event) is expressed in differential form as two separate probabilities

$$\frac{d_a\sigma_{inc}}{d\theta} = \frac{d_e\sigma_C}{d\theta} S(x, Z). \quad \text{B.37}$$

The probability $d_e\sigma_C/d\theta$ describes, as we have just seen, the probability that a photon will scatter off a free electron through an angle θ . The second factor in Equation A.37 $S(x, Z)$, called the incoherent scattering function (188p182), is the probability that the recoiling electron will escape its binding energy and leave the atom with energy E_e (188p181). Here again, x is the momentum transfer variable, equal to $\sin(\theta/2)/\lambda$. Using a quantum mechanical treatment, John Hubbell derived extensive tables of $S(x, Z)$ (197).

The integral of this differential over all angles θ cannot be solved in closed form (188p182); thankfully Hubbell also calculated ${}_a\sigma_{inc}$ for Z from 1 to 100 (197). Figure B.16 shows the angular distribution of the several differential cross sections discussed: the classical $d_e\sigma_o/d\theta$, coherent scatter (Rayleigh) $d_a\sigma_R/d\theta$, incoherent scatter off a free electron (Compton/ Klein-Nishina) $d_e\sigma_C/d\theta$, and incoherent scatter off a bound electron $d_a\sigma_{inc}/d\theta$.

Figure B.14: The Classical, Rayleigh, Compton, and incoherent differential cross sections per unit scattering angle plotted against the scattering angle for carbon and 10 keV photons

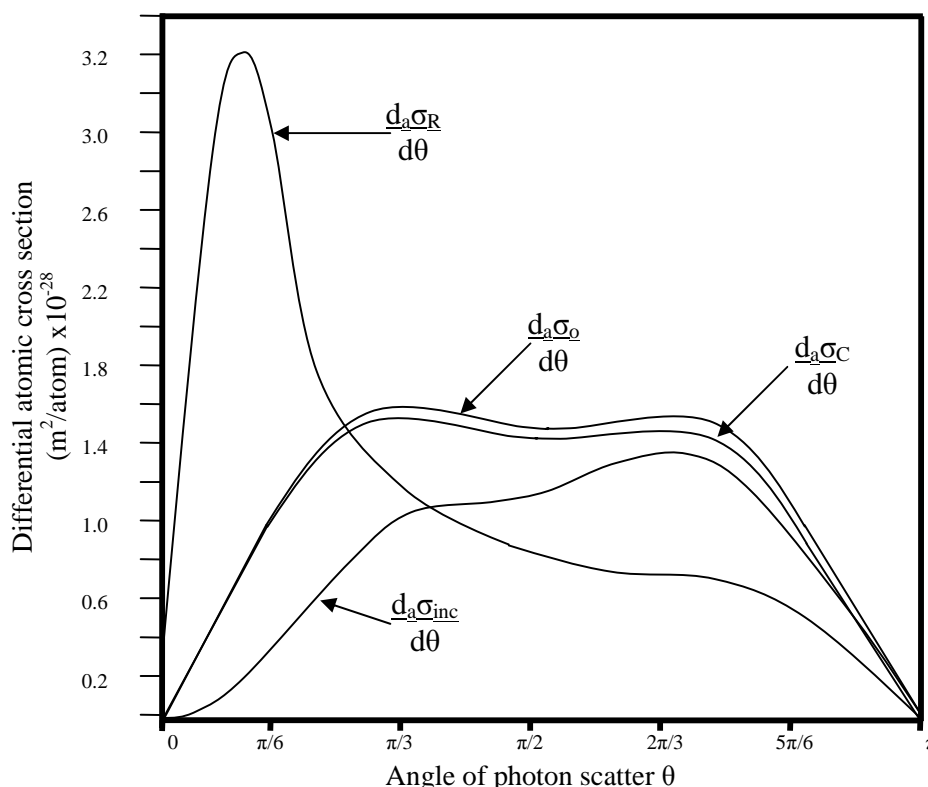


Figure caption (after 188p183): The differential cross sections for coherent and incoherent scattering events, where $d_a\sigma_o/d\theta$ and $d_a\sigma_c/d\theta$ are simply the differentials per electron multiplied by the atomic number of carbon $Z = 6$. The $d_a\sigma_o/d\theta$ graph shows the angular probability of a scattering event of a free electron with no energy transfer. The $d_a\sigma_R/d\theta$ graph is also for a scattering event without energy transfer, however the constructive interference of the atom's electrons create a coherent scattering event. The $d_a\sigma_c/d\theta$ give the angular probability of a scattering event off a free electron with energy transfer, and $d_a\sigma_{inc}/d\theta$ shows the angular probability if the electron is not free.

Photoelectric effect

In the photoelectric effect, the photon interacts with the whole atom. The entire energy of the photon is absorbed and the atom emits one or more electrons to dissipate the acquired energy. The kinetic energy KE of the exiting electron is equal to the photon energy $h\nu$ minus the binding energy of the electron shell E_B (189p224)

$$KE = h\nu - E_B. \quad \text{B.38}$$

If only a single electron is emitted, the atom remains in an excited state with excess energy

$$E = h\nu - KE. \quad \text{B.39}$$

Remaining in an excited state leaves a vacancy in the orbital, which, if filled with an electron from a higher orbital, results in either an emission of a characteristic photon or

an Auger electron (189p224), reducing the atom's energy even further. A cascade of Auger electrons and characteristic x-rays diminishes the excitation of energy of the atom

$$E = h\nu - \sum_1^i KE_i - \sum_1^k h\nu_k, \quad \text{B.40}$$

where $\sum KE_i$ is the sum of the energies of all the expelled electrons, and $\sum h\nu_k$ is the sum of the emitted photon energies. As E approaches zero, the atom returns to its original energy state, thus the amount of energy leaving the interaction site ranges from $(h\nu - E_B)$ to $h\nu$. It is important to note for both radiological imaging and dosimetry, that the characteristic photons of low Z organic materials usually deposit their energy at the interaction site (i.e. within the dimensions of a human cell) (188p167).

Returning again to the first ejected electron, as with bremsstrahlung, the angular distribution of photoelectrons is energy dependant. For low incident photon energies, the peak in emissions approaches 90° , but moves progressively to lower angles as $h\nu$ increases (189p223).

The photoelectric cross section per atom ${}_a\tau$ for water and lead are graphed for energies 10 keV to 10 MeV in Figure 15. The spikes in the lead graph are called absorption edges, and correspond to the binding energies of the atom's L and K orbitals. Absorption edges result from the x-ray's ability to ionize that orbital; at photon energies just slightly below the binding energy of the orbital, the photon cannot overcome the orbital's grip on the electron. Yet, once $h\nu = E_B$, the cross section graph spikes, indicating absorption of the photon is most effective when its energy is just capable of ionizing the orbital (188p148). Apart from the spikes, the probability of a photoelectric interaction drops steadily with increasing photon energies. For lead, the sudden ability to ionize the two K shell electrons increases the probability of a photoelectric interaction by a factor of 5 over all 16 electrons of the L and M shells combined, indicating that the inner shells contribute more significantly to photoelectric absorption (188p148).

There are distinctive regions in the ${}_a\tau$ energy dependency: the area in the vicinity of the spikes, regions without spikes at non-relativistic energies, and at relativistic energies (189p222). In the region of the absorption edges, prediction of ${}_a\tau$ is uncertain (189p222). For energies below about 1 MeV but removed from the spikes, the slope of ${}_a\tau$ vs. $h\nu$ is essentially linear on a log scale, and falls by approximately $h\nu^{-2.6}$ (188p146). It is in these regions that the Z dependency is obvious. Higher Z materials hold onto their K orbital electrons much tighter! Just beyond the absorption edges, the photoelectric cross section ${}_a\tau_K$ may be approximated by

$${}_a\tau_K = \alpha^4 {}_e\sigma_0 Z^n \sqrt{\frac{37}{\epsilon^7}}, \quad \text{B.41}$$

where here, α is the fine structure constant ($\alpha = e^2/(2hc\epsilon_0) \approx (1/137)$), ϵ is the normalized photon energy (i.e. $\epsilon = h\nu/(m_e c^2)$), and finally, n is the power of the Z dependency which varies with photon energy from $n = 4$ to $n = 4.6$ (189p222). The region described by Equation B.41 constitutes the entire portion of the ${}_a\tau$ vs energy graph for water in Figure B.15. At around 1 MeV, the slopes of both graphs become shallower, gradually approaching an energy dependence of $h\nu^{-1}$. In this region where $\epsilon \gg 1$, ${}_a\tau_K$ is approximated by

$${}_a\tau_K = \frac{1.5}{\varepsilon} \alpha^4 \sigma_0 Z^5.$$

B.42

(189p223).

Figure B.15: The photoelectric cross section for water and lead plotted against the incident photon energy

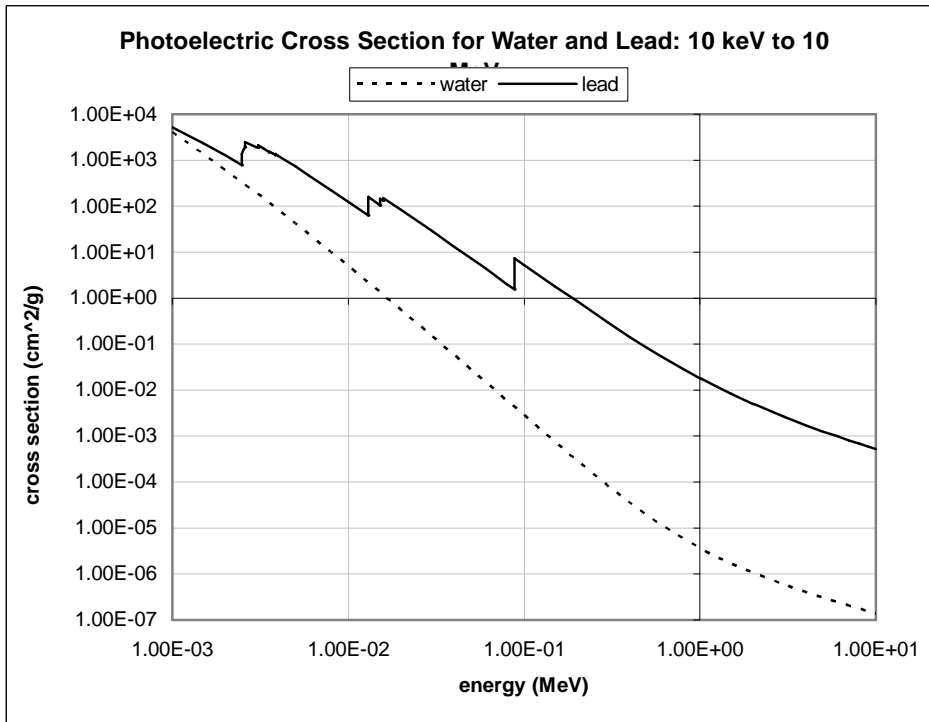


Figure caption: (graphed with values from the XCOM data base (198)) At lower energies, the absorption edges of the M orbitals would also be noticeable.

Linear Attenuation Coefficient

Although the possible fates of an x-ray entering an object are many, the situation is simple –either the photon passes through the material and out the other side, or it interacts with it. The expected number of *any* interaction p is the sum of the expected number of each possible interaction, i.e. Equation B.14 becomes

$$p = (N_a \sigma_R x) + (N_a \sigma_{inc} x) + (N_a \tau x) \quad \text{B.43}$$

where N and x , again, are the number atoms per unit volume of the target and x is its thickness, respectively. Thus,

$$p = N ({}_a\sigma_R + {}_a\sigma_{inc} + {}_a\tau) x, \quad \text{B.44}$$

where it becomes evident that

$${}_a\mu = {}_a\sigma_R + {}_a\sigma_{inc} + {}_a\tau. \quad \text{B.45}$$

(189p243). Figure B.16 shows the total cross section along with its constituent cross sections.

Figure B.16: The total atomic cross sections for Water and Lead plotted against the incident photon's energy

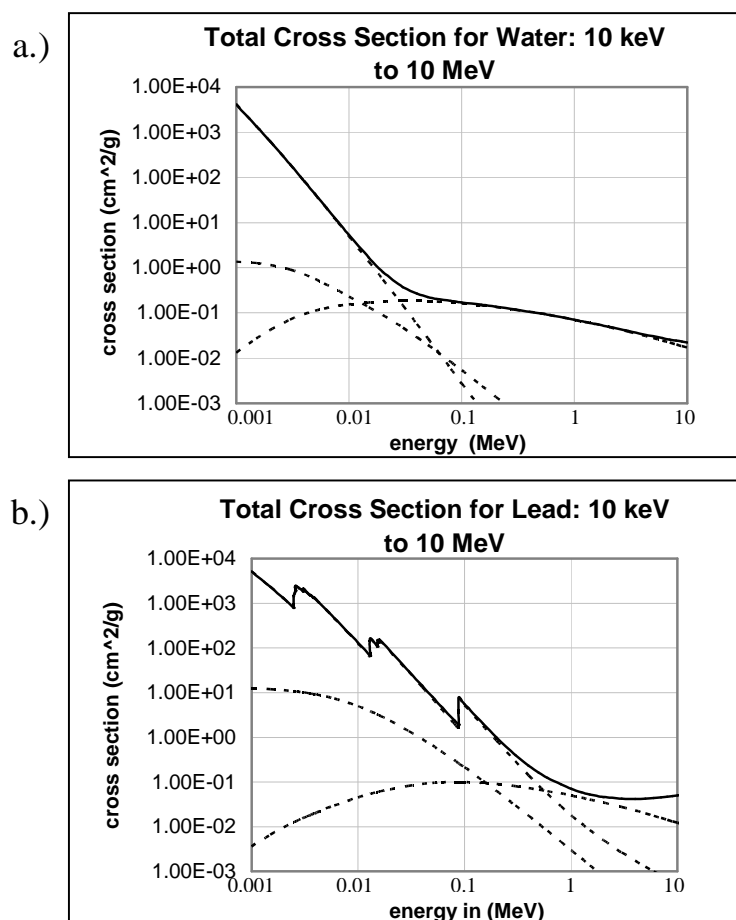


Figure caption: The total atomic cross section for a.) water and b.) lead at energies ranging from 10 to 10 MeV (graphed with values from the XCOM data base (198)).

The number of atoms per unit volume N is a function of the object's density ρ

$$N = \rho A / N_A, \quad \text{B.46}$$

where A is the material's atomic mass and N_A is Avogadro's number (189p243). The product $N_a\mu$ is called the *linear attenuation coefficient* and is denoted as μ , without subscript (188p134).

$$\mu = \sigma_R + \sigma_{inc} + \tau. \quad \text{B.47}$$

The change in photon fluence due to attenuation in a medium is proportional to both the number of photons in the beam and the expected number of interactions with the medium

$$d\phi = -\phi p \quad \text{B.48}$$

where the negative sign indicates that the fluence is reduced by interactions with the absorbing medium. By substitution of Equation B.14, this becomes

$$d\phi = -\phi N_a \mu x = -\phi \mu x. \quad \text{B.49}$$

Integrating Equation B.49 gives

$$\phi = \phi_o e^{-\mu x} \quad \text{B.50}$$

where ϕ_o is the incident influence, and ϕ is what remains of the fluence after attenuation by the absorber (196). Thus, the significance of the coefficient is that it allows the differential equation for the attenuation of a photon fluence ϕ to be integrated (196).

An inspection of Equations B.45-47 reminds us that μ is a function of the energy of the photon fluence as well as both the atomic number and density of the attenuating medium. Therefore, Equation B.50 only holds for a monochromatic beam and for a homogenous absorbing material. When this is the case, however, μ can be measured directly with the aid of judicious collimation known as *narrow beam geometry*; see Figure B.17 (189p237).

Figure B.17: Narrow beam geometry

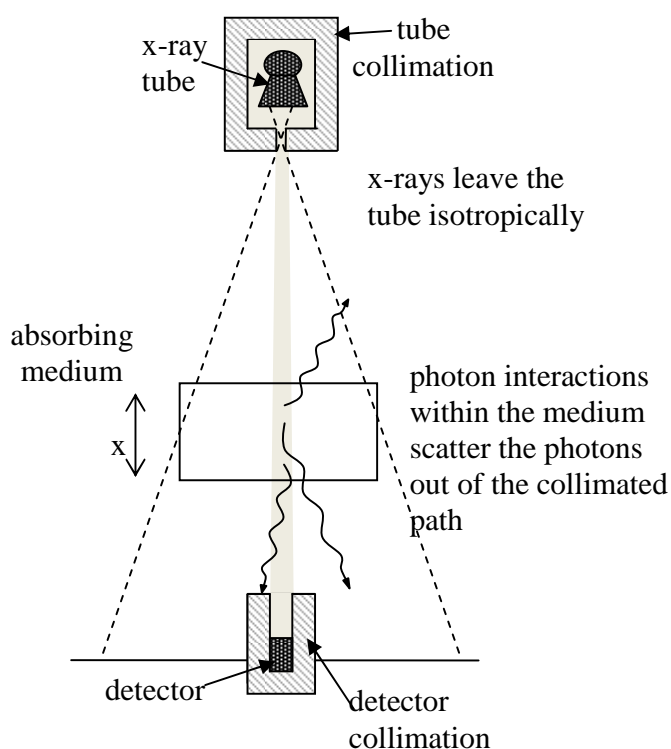


Figure caption: With narrow beam geometry, only x-rays that have not undergone an interaction are allowed to reach the detector. In an x-ray tube, the photons are not monochromatic, however, the beam's *effective energy* (defined by its *quality*) can be used.

Ideally, narrow beam geometry allows only those x-rays which have passed through the object without interaction of any kind to be detected, and the fluence of photons on the other side ϕ is measured. With knowledge of the photon fluence without an absorbing object in its path, ϕ_0 , μ can be easily solved for (189p237).

Radiological images are formed by the spatial variation of x-ray fluence detected on the exiting side of an absorbing object. Thus, it is the exiting fluence ϕ , i.e. the degree and variation of attenuation of the incident photon beam, which communicates information in the radiological exam. It must be stressed that, ideally, only photons which have survived the journey without interaction with the object, called *primaries*, communicate this information, namely the probability of surviving the journey (199p5).

X-ray formation and its interactions with matter are random events governed by Poisson statistics (165p3), thus if $\mu x = p$ is the expected number of interactions between the photon and the absorbing medium, then $e^{-\mu x}$ is the probability of no interaction (i.e. $A = P(0 | \mu x) = (\mu x)^0 / 0! * e^{-\mu x} = e^{-\mu x}$). From Equation B.50, this survival probability $A = e^{-\mu x}$ is equal to the fraction of photons that survive the journey to the detector ϕ / ϕ_0 . Mathematically, A is a function of both the photon's path and its energy, and is described by the weighted sum of all the linear attenuation coefficients along the path of the photon from the source \mathbf{r} to the detector \mathbf{r}' (i.e. $\mu(E) |\mathbf{r}' - \mathbf{r}|$) (see Figure B.18)

$$A(\bar{r}, \bar{r}', E) = e^{-\int_{\bar{r}}^{\bar{r}'} \mu(E) ds} \quad \text{B.51}$$

where E is the photon beam energy, and \mathbf{r} and \mathbf{r}' are the position vectors of the source and detector element, respectively (199p16).

Figure B.18: Geometry of an x-rays path through an absorbing medium

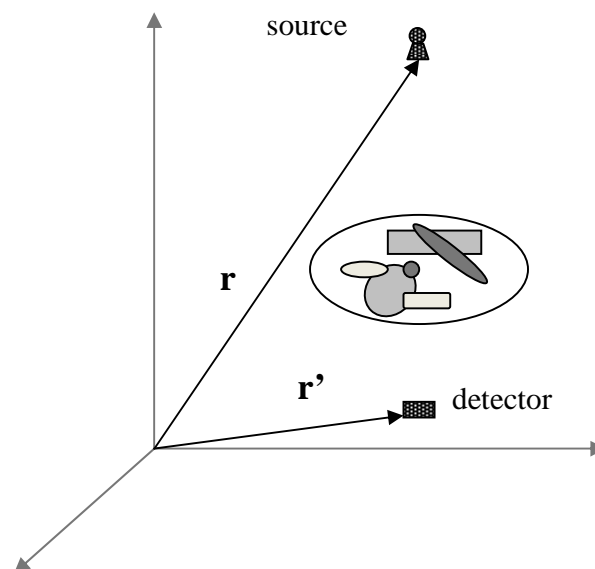


Figure caption: Each photon traverses some path from the source to the detector. Its probability of interaction depends of the distribution of materials in its path.

Of course, the photons leaving the target of an x-ray tube are not monoenergetic, nor are typical patients undergoing radiological exams homogeneous. Addressing the

issue of nonhomogeneity first, $\mu(E)|\mathbf{r}'-\mathbf{r}|$ must be integrated along the path of the x-rays from the source to the detector (199p16). The ratio of the x-ray beam's attenuation is then

$$\varphi / \varphi_0 = A(\bar{r}, \bar{r}', E) = e^{-\int_0^{|\bar{r}'-\bar{r}|} \mu(\bar{r} + ((\bar{r}' - \bar{r}) / |\bar{r}' - \bar{r}|)\xi, E) d\xi}, \quad \text{B.52}$$

where ξ is an increment of distance along the path between the source and the detector. When the beam also contains photons of varying energy, the beam as well as the linear attenuation coefficients along the path of the beam must be integrated over the range of energies, i.e. from 0 to $h\nu_{max}$ (165p2).

$$\frac{\varphi}{\varphi_0} = \frac{\int_0^{h\nu_{max}} \varphi_0(E) A(\bar{r}, \bar{r}', E) dE}{\int_0^{h\nu_{max}} \varphi_0(E) dE}. \quad \text{B.53}$$

Contrast, which allows us to perceive the information of the radiological exam by distinguishing one region from another, is defined as

$$C = \frac{(\varphi_A - \varphi_B)}{\varphi_A}, \quad \text{B.54}$$

where the subscripts A and B refer to fluence detected at different locations in the image (165p5). It is clear that contrast depends on the linear attenuation coefficients of the object being investigated. Both coherent and incoherent scattered photons, called *secondaries*, are not true survivors of the journey, and so if detected, are presumed to be primaries, and only obfuscate the information of the radiological exam (199p15).

Figure B.19: The total atomic cross sections of water and air for energies between 1 keV and 100 keV

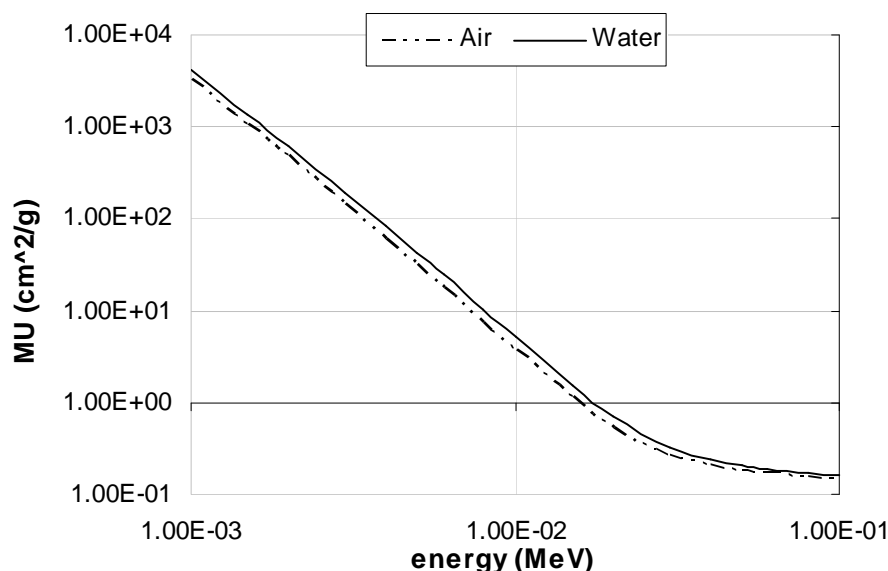


Figure caption: The total atomic cross sections for water and air plotted with values from the XCOM data base (198) (air is approximated by N₂). Most of the body's tissues have similar cross sections to water. The lungs, however, which contain a significant amount of air even at end exhale, provide excellent radiological contrast (despite the apparent proximity of the two graphs).

CT#

In radiological exams, the exact distribution of linear attenuation coefficients is not known, but inferred from the measured values ϕ and ϕ_0 . Also, the exact spectrum of the x-ray tube is not known. Instead, the *effective energy* of the x-rays is used. This effective energy is the energy of a monochromatic beam with the same quality as the tube's polychromatic spectrum. Recall, the quality of a beam is described by the HVL in aluminum, i.e.

$$\phi/\phi_0 = 1/2 = e^{-\mu(x=\text{HVL})}. \quad \text{B.55}$$

Since all the discernable information from a radiological exam is due to the linear attenuation coefficients of the object, the goal of a CT scan is to create a map the object's μ distribution, i.e. $\mu[x,y]$ (144). The pixel values of a CT image are defined as

$$\text{CT\#} = \left(\frac{\mu_m - \mu_{\text{water}}}{\mu_{\text{water}}} \right) \cdot 1000 \text{ HU} \quad \text{B.56}$$

with units of *Hounsfield units* (HU). Here, the measured linear attenuation coefficients μ_m are normalized to that of water μ_{water} for a particular CT tube's x-ray spectrum. This removes the energy dependence of μ from the unit. Thus, in all CT machines, the CT# for water is equal to 0 HU, and for air, with a μ_{air} essentially equal to 0, the CT# is -1000 HU (143).